Degradation of Ceramic Surfaces and its Mitigation: From Electric Propulsion to Cultural Heritage

Thesis by

Celia S. Chari

In Partial Fulfillment of the Requirements for

the Degree of

Doctor of Philosophy in Materials Science

CALIFORNIA INSTITUTE OF TECHNOLOGY

Pasadena, California

2023

Defended August 11, 2022

Celia S. Chari
ORCID: 0000-0001-6404-4203

ACKNOWLEDGEMENTS

Throughout my time at Caltech, I have come across countless passionate, intelligent, and kind-hearted people who, perhaps unknowingly, have enriched not just my research but also my life. Without their support, I would not be where I am today.

First, I would like to thank my advisor, Prof. Katherine T. Faber, for her incredible mentorship and support. Thank you so much for always believing in me and my multi-tasking abilities! Your knowledge, enthusiasm, and trust have been the foundation of my doctoral work, providing me with stability to pursue new research ideas that have flourished into the work presented here today. Thank you for opening so many doors for my career and always having my best interest in mind. It has been an absolute joy working with you and your group.

Next, I would like to thank Prof. Brent T. Fultz, Prof. Guruswami (Ravi) Ravichandran, Prof. George R. Rossman, and Dr. Bryan W. McEnerney for being on my thesis committee, for your encouragement throughout the years, for reviewing my thesis, and lastly for your invaluable advice.

Thank you also to my many collaborators, including Dr. Bryan W. McEnerney, Dr. Rich R. Hofer, and Dr. Colleen M. Marrese-Reading from the Jet Propulsion Laboratory, Dr. James A. Wollmershauser and Dr. Ed P. Gorzkowski from the Naval Research Laboratory, Dr. Anikó Bezur from Yale's Institute for the Preservation of Cultural Heritage, Dr. Zeev Rosenzweig, Dr. Joseph Bennett, and Dr. Jessica Heimann from the University of Maryland, Baltimore County, and Dr. Glenn Gates from the Walters Art Museum. I could not have asked for better researchers to collaborate with.

I would also like to thank the following scientists at Caltech for their time and support over the years: Prof. George R. Rossman, Dr. Chi Ma, and Mark Garcia from the Geological and Planetary Science Division; Dr. Bruce Brunschwig and Jake Evans from the Molecular Materials Resource Center; Dr. Matthew Hunt, Dr. Miguel Caban-Acevedo, and Dr. Rebecca Gallivan from The Kavli Nanoscience Institute. Your expertise and advice were fundamental to this work and are greatly appreciated.

I would like to gratefully acknowledge Zonta International for their support through the Amelia Earhart Fellowship. It has been incredible to be a part of such an inspiring community of aerospace engineers and women's rights advocates.

I would also like to give a big thank you to all members of the Faber group, past and present, who have been both my collaborators and my family during my time at Caltech. In part, this includes Dr. Matthew Johnson, Dr. Xiaomei Zeng, Dr. Wei-Lin Tan, Dr. Neal Brodnik, Dr. Nori Arai, Dr. Claire Kuo, Dr. Benjamin Herren, Vince Wu, Laura Quinn, Sara Gorske, Kevin Yu, and also my former SURF students Zane Taylor and Tomas Grossmark. I am incredibly lucky to have had your support and comradery over the years, and to continue being a part of the Faber group family.

I would like to thank Christy Jenstad, Jennifer Blankenship, Katie Pichotta, and Angie Riley for all your encouragement, advice, and genuine care for not just me, but for all of the students in the department. You are real-life fairy godmothers.

Thank you to everyone in my materials science cohort, my fellow delegates at the President's Council of Student Advisors of the American Ceramic Society, and my dearest friends: Andrei Ruskuc, Ciara Maguire, Iwan Blake, Anna Gavigan, Edie Davis, and Meadhbh Larkin-Woulfe. Our friendships will always be a light in my life.

Lastly, I would like to thank my loved ones. Will, thank you for all your love, companionship, and for always being my biggest cheerleader. To my mama and papa, Isabel and Raj, thank you for your unconditional love and support. After a lifetime of book dedications, I can finally dedicate my work to you.

-Celia

ABSTRACT

Ceramics have played an evolving role throughout human history, with the earliest known fired clay figurines dating back to 29,000-25,000 BCE in what is today the Czech Republic. Such examples of porous, low-fired potteries transitioned into vitreous and heat-resistant porcelain with the advancements of kiln technologies, which steadily grew to reach temperatures up to 1270 °C by the time of the Song Dynasty (960-1279 CE). In the modern-age, furnaces technologies have become exceedingly more sophisticated, reaching ultra-high temperatures of up to 3000 °C with dedicated calibration systems. With the advancement of firing technologies came the advancement of materials processing methods, which have transformed the role of ceramics in everyday applications: from ceramic fibers used in tennis racquets, to ceramics used in space shuttle tiles and even in artificial joints. Indeed, ceramics are candidate solutions to the most stringent material problems faced today, including high-temperature applications like electric propulsion and turbine engine systems. However, in order to improve the long-term use and sustainability of ceramics, it is essential to evaluate both their performance and their eventual degradation from mechanical wear and chemical erosion.

This work explores the processing-microstructure-performance relationship of ceramics to better understand the performance and degradation mechanisms of ceramic surfaces. This relationship is investigated using a series of material case studies, including (i) advanced high-temperature ceramics composed of h-BN rich composites, and (ii) historic ceramics, ranging from low-fired pottery to porcelain. Details are provided for the design and manufacturing of novel high-performing ceramics, while simultaneously referring to ceramics of the past to understand how their surfaces have altered over their lifetime. Highlights of this work include the innovative use of carbothermic reactions to create h-BN surface layers for electric propulsion; self-healing strategies from AlN/BN composites; DFT-supported analysis of pottery corrosion in acidic soils; and nanoscale processing of historic porcelain glazes. These analyses provide us with an opportunity to learn from materials of the past to create more sustainable materials for the future, with an emphasis on ways of mitigating degradation by controlling processing conditions and environmental exposures.

PUBLISHED CONTENT AND CONTRIBUTIONS

C. S. Chari, B. W. McEnerney, R. R. Hofer, C. M. Marrese-Reading, R. Lobbia, J. A. Wollmershauser, E. P. Gorzkowski, K. T. Faber (n.d.). Effects of Plasma Exposure on Graphite/h-BN Bimaterials for Hall-Effect Thrusters. In: *In Preparation*.
C.S.C led the sample preparation, characterization, and writing of the manuscript.

C. S. Chari, B. W. McEnerney, R. R. Hofer, J. A. Wollmershauser, E. P. Gorzkowski, K. T. Faber (n.d.). High-temperature Carbothermal Synthesis and Characterization of Graphite/h-BN Bimaterials. In: *Under review*.
C.S.C led the experimental work and writing of the manuscript.

C. S. Chari[*], J. E. Heimann[*], Z. Rosenzweig, J. W. Bennet, K. T. Faber (n.d.). From Acidic Soil to Acid Rain: Chemical Transformations of 2D Clay Mineral Surfaces from Sulfuric Acid Exposure. In: *Under review*.
C.S.C is a co-first author of this work, leading the experimental studies and writing of the manuscript.

C. S. Chari, Z. W. Taylor, A. Bezur, X. Sujing, K. T. Faber, Nanoscale engineering of gold particles in 18th century Böttger lusters and glazes, Proceedings of the National Academy of Sciences. 119 (2022) e2120753119. https://doi.org/10.1073/pnas.2120753119.
C.S.C led the recreation experiments and spear-headed the writing of the manuscript.

C. S. Chari, K. T. Faber, Oxidation resistance of AlN/BN via mullite-type $Al_{18}B_4O_{33}$, Journal of the European Ceramic Society. 42 (2022) 3437–3445. https://doi.org/10.1016/j.jeurceramsoc.2022.02.037.
C.S.C led the experimental work and writing of the manuscript.

TABLE OF CONTENTS

LIST OF ILLUSTRATIONS

LIST OF TABLES

C h a p t e r 1

INTRODUCTION

1.1 Ceramics Throughout History

Materials have played a defining role in the advancement of human civilization. Take for example the evolution of the ordinary hunting tool. Initially crafted from stone and bone in the Paleolithic, it was later replaced by bronze and iron with the progression of metallurgical technologies spanning up to 1200 BCE [1]. The role of ceramics has similarly evolved throughout human history, with the earliest known fired clay objects being from 29,000 to 25,000 BCE. An example of this is the *Venus of Dolní Věstonice* seen in Figure 1.1. Interpreted as a symbol of fertility, this figurine was uncovered in what is now known as modern-day Czech Republic.

Figure 1.1. Image of Venus of Dolní Věstonice. Original image of object by Don Hitchcock, published by Jessica Liew, and under the Creative Commons BY-NC-SA 4.0 International License.

Records on the fabrication method and technologies used to create the figurine became lost over time. However, by carefully evaluating the object using scientific analyses, details on the sintering mechanism of the *Venus of Dolní Věstonice* were discovered, providing context on the kiln technologies of the time [2]. Vandiver et al. created replications of the figurines using loess (a clastic sediment) retrieved from the same geographic location as

the original object [2]. Using a combination of microscopy, chemical analyses, fractography and thermal shock analyses, Vandiver et al. established that the firing temperature of the highly porous clay figurines was between 500 °C and 800 °C, indicative of early versions of earthenware.

Unlike degradable organics, the relative durability of ceramics makes this material essential for understanding the technologies of ancient civilizations and their progression into the advanced ceramic world that we are familiar with today. Nevertheless, as we move forward it is worth remembering that ceramics are not immune to chemical and mechanical degradation, and that their microstructure, composition, and mechanical properties can still be impacted by environmental changes and wear over time. This thesis seeks to investigate the relationship between ceramics and their surface characteristics, their processing and use and ultimately, their degradation in order to better understand the performance of both modern-day advanced ceramics as well as historic ceramics, and to aid in their sustainability.

1.2 Processing Methods for Ceramics

1.2.1 Historic Ceramics

Early ceramics, from about 2200 BCE to the 20th century, can be broadly categorized into one of the following types: earthenware (a type of low-fired pottery), stoneware, and porcelain. This classification largely depends on the firing temperature of the piece, a fundamental factor that influences the chemical and microstructural composition of the ceramic. The ingredients used in the production of ceramics largely consisted of naturally derived aluminosilicate minerals, such as clays, feldspar, and mica, as well as silicates like quartz [3]. Kaolinite ($Al_2Si_2O_5(OH)_4$) in particular is a clay mineral that is an essential ingredient in pottery making. It is a phyllosilicate that facilitates the clay-forming and molding process for the artist, due to its sheet-like, highly absorbent structure that allows sheets to slip past each other when the clay is moistened, as a result of water molecule incorporation in between the aluminosilicate layers. Once dried, the sheets become bonded

to each other through hydrogen bonds, allowing the piece to maintain its shape for the firing step.

Quite different to modern day furnaces equipped with electronic control systems, kiln technologies originated from hand-crafted underground trenches and pit fires. For example, during the Song dynasty in the 12th century, dragon kilns were built on hillsides, measuring around 30 m in length and 2 m in width [3]. The kiln's firebox was located on the lower end of the hill, allowing heat to rise to the top of the sloping kiln. The insides of the kiln were filled with lined up saggar-enclosed pieces, positioned within set distances from the firebox depending on their desired firing temperature.

Figure 1.2. Photograph of excavated floor of a dragon kiln from the Southern Song dynasty, Hangzhou, China. Published by Michael Gunther, and under the Creative Commons BY-SA 4.0 International License.

Calibration of firing temperatures was rather rudimentary and relied on the craftsmen's expertise, or by tracking the color of the burning flame. For reference, low-fired pottery, porous in appearance, is produced at temperatures below 1000 °C, while increasingly dense and vitreous bodies, like porcelain, can be made at firing temperatures approaching 1400 °C where clay decomposes into mullite and silica glass. Reducing atmospheres during firing could be achieved by burning rosemary or smoking substances that would enable a

non-oxidizing environment, a technique that was widely used to produce lustrous ceramic surfaces from as far back as ninth century CE Mesopotamia [4,5], demonstrating the historic ingenuity of ceramic processing technologies.

1.2.2 Advanced Ceramics

In the modern age, the necessity for high-temperature resistant and functional materials has transformed the role of ceramics in everyday applications: from ceramic fibers used in tennis racquets [6], to ceramics used in space shuttle tiles [7] and even in artificial joints [8]. Each application requires its own portfolio of material properties and demands, which can be fulfilled by the choice of chemistry, processing method, microstructure, and defects. As such, a palette of ceramic options and combinations can be considered as candidate solutions to the most stringent material problems faced today.

1.2.2.1 High-temperature Ceramic Coatings

One such challenge is the development of high-temperature ceramic coatings, which are typically desired to protect substrates from oxidation or corrosion or to provide a functional element to the surface of a material. Such high-temperature coatings are particularly necessary for protecting materials rich in carbon, such as C/C composites [9], composites reinforced by carbon fibers [10], and graphite substrates [11], which can easily oxidize at temperatures above 400 °C. In the past, these protective coatings have been produced from plasma-sprayed material combinations of SiO_2 [12–14], SiC [13], ZrO_2 [12] and Al_2O_3 [13,14], which have proven to mitigate oxidation up to 1800 °C [10], by acting as a resistant barrier that limits the diffusion of O_2 to the substrate. Additionally, ceramic coatings can provide a functional component to the material. An example is coatings of hexagonal boron nitride (h-BN), frequently used in SiC/SiC ceramic matrix composites as an interphase material that toughens the composite by facilitating crack deflection towards the h-BN coating and not the reinforcing fibers. This oxidation resistant, dielectric ceramic coating is typically prepared via chemical vapor infiltration [15], or atomic layer deposition [16], to produce coatings on the order of 1 to 100 nm in thickness.

1.2.2.2 Ceramic Composites

Apart from coatings, a separate way of combining one or more ceramic materials is through the preparation of ceramic composites. Such materials usually comprise of a base matrix material and a reinforcement material. In the case of SiC/SiC ceramic matrix composites, the matrix material is SiC, and the reinforcement are acicular SiC fibers, shown in Figure 1.3. In fact, fibers [17], whiskers [18,19], or nanotubes [20] are typically featured as reinforcement fillers in composites due to their high aspect ratio that enable their high load bearing capacity, further shown in Figure 1.3.

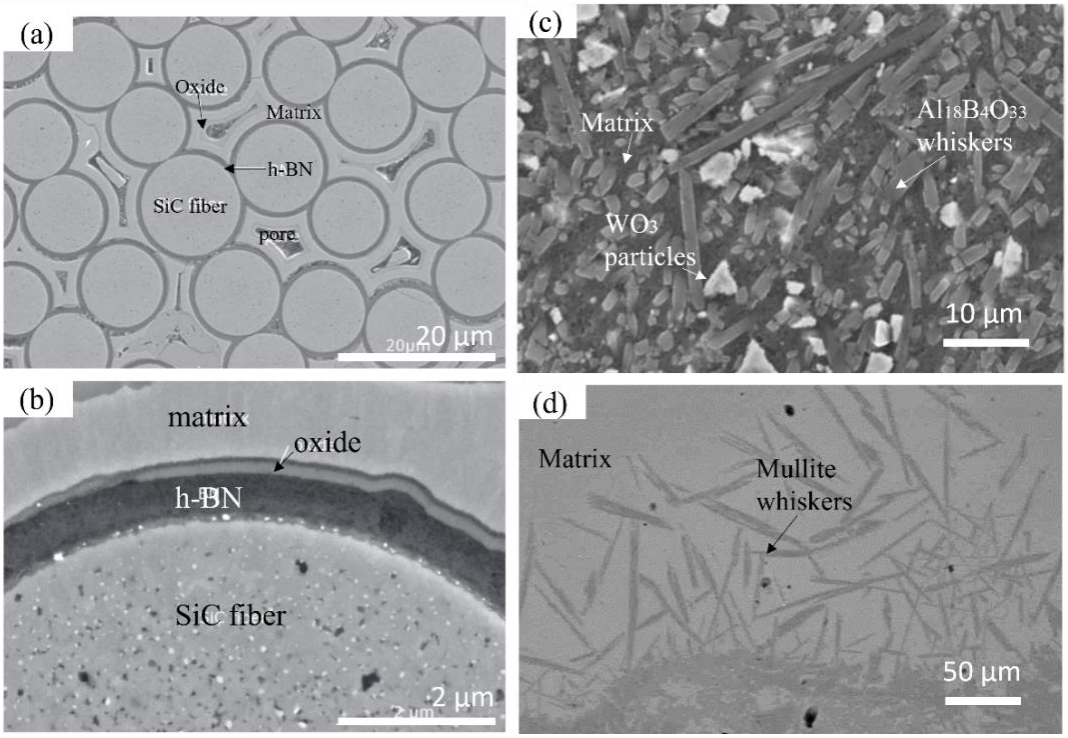

Figure 1.3. Examples of ceramic composites: a) Micrograph of oxidized SiC/SiC ceramic matrix composite, showing SiC fiber and SiC matrix with h-BN interphase, b) close-up showing borosilicate oxide. Reprinted with permission from Opila et al.[17]*, © John Wiley and Sons (2015). c) Micrograph of aluminum matrix reinforced with $Al_{18}B_4O_{33}$ whiskers and WO_3 particles. Reprinted with permission from Feng et al.*[19]*, © Elsevier (2009). d) Micrograph of silica matrix reinforced with mullite ($Al_6Si_2O_{13}$) whiskers, from porcelain sample prepared by C. S. Chari. Printed as an original by C. S. Chari.*

Apart from mechanical reinforcement, composites can also be used to improve the electrical conductivity of materials, as was seen with silicon oxycarbide ceramics reinforced by carbon nanotubes [20], and also the machinability of materials, as was seen with AlN composited with h-BN [21]. In the latter case, the inclusion of the lubricant h-BN lowers the toughness and compliance of AlN, making it more accessible to work with and more economical to manufacture than bulk AlN. Thus, ceramic composites are an effective way of combining the properties of several materials into one, creating a tailored product for a specific purpose.

1.3 Performance and Degradation of Ceramic Surfaces

1.3.1 Mechanical Erosion and Wear

Erosion in ceramic materials can develop from wear after repeated exposures to extreme environments. Due to its brittleness, microcracks can form on a ceramic surface and propagate as well as extend through the material, forming a detrimental network of cracks that can lead to the removal of material from the surface.

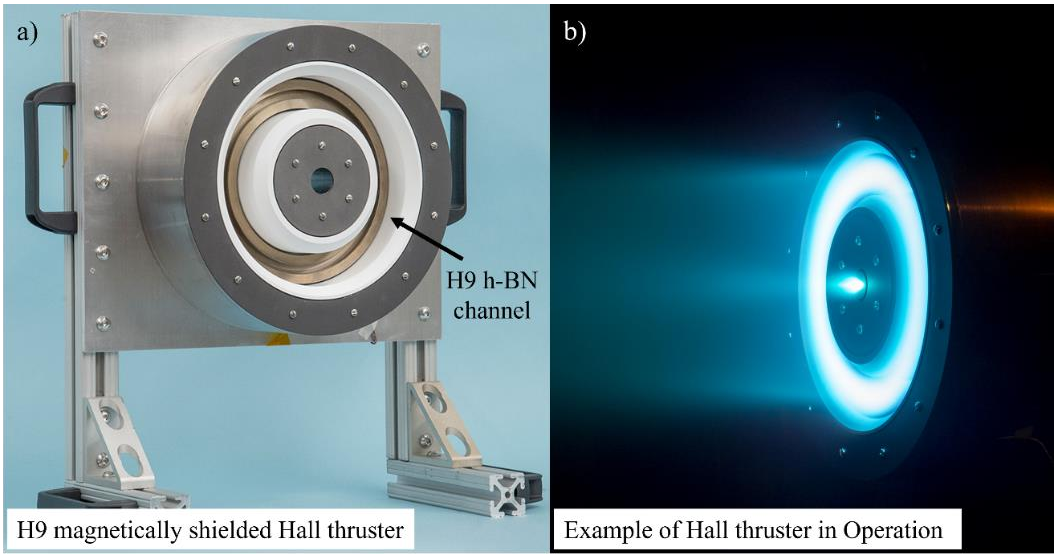

Figure 1.4. Examples of a H9 Hall thruster made of h-BN a) shown without a cathode, illustrating location of thruster channels, b) in operation at the Jet Propulsion Laboratory. Reprinted with permission from R. R. Hofer et al.[22]*, © NASA/JPL-Caltech.*

Advanced ceramics used in electric propulsion are subject to such mechanical damage during propulsion environments. Hall-effect thrusters used in electric spacecraft propulsion systems operate using Xe as a propellant, seen in Figure 1.4 [23]. The lifetime of materials used in walls of thruster channels is determined by their ability to survive exposures to such plasma environments, were Xe neutrals and ions can impinge the surface of channels and physically erode the material through grain detachment and spallation [24,25]. Additionally, such high-energy plumes can also contain metal atoms (e.g., from Mo shields) that contribute to further impingement and wear of the channel material [26]. Thermal shock is also a cause of concern in high-temperature applications, where large temperature gradients can lead to the expansion of pre-existing cracks on the surface, accelerating material failure [27].

Mechanical erosion is also frequently seen in ancient ceramics uncovered from archaeological excavations, predominantly in unglazed earthenware. These porous structures are capable of retaining dissolved salts and water when exposed to humid environments over prolonged times, such as humid soils or air. This can be detrimental to earthenware objects for two reasons. First, infiltrated salt solutions can cause the weakly sintered ceramic to rehydroxylate back into clay, further damaging the already delicate structure [28]. Second, when removed from the humid environment, the evaporation of water can cause salts to become trapped inside the pores, where they can recrystallize and cause damage from their volume expansion, leading to the formation of internal cracks [28]. Additionally, efflorescence can occur in porous objects, where salts from ceramic structures (e.g., $CaCl_2$) can dissolve in water and migrate to the surface of the ceramic, altering both the chemical and mechanical properties of the object internally [29].

1.3.2 Chemical Erosion

Apart from mechanical wear, a significant contribution to the erosion of ceramics originates from chemical alterations of their surfaces. For advanced ceramics in high-temperature environments, the oxidation resistance of the material is an important property of non-oxide ceramics like SiC, AlN and BN. For example, SiC is susceptible to oxidation above 800 °C, where it can start to react into SiO_2, forming an oxide layer that alters the material properties at the surface, which can be detrimental to its function [30].

Additionally, in ceramic composites were more than one non-oxide is present, for example SiC/BN/SiC systems, the oxidation products can react with each other to form borosilicate glasses that chemically alter and disturb the system, seen in Figure 1.3. More precisely, the enhanced oxidant permeability in borosilicate glasses has been shown to accelerate the oxidation of the composite [17,31]. However, from a different perspective, some studies have suggested that the creation of such oxides can actually benefit the system and facilitate crack healing. For example, in SiC/B_4C composites it was found that pre-existing cracks at the material's surface could be filled with borosilicate glass upon oxidation. The glass was found to infiltrate the cracks upon cooling, self-sealing the fractured composite and improving its mechanical properties by acting as a load bearing material [32].

In response to preventing the high-temperature oxidation of non-oxides, there has been considerable progress made in the development of barrier coatings. Such coatings can be applied on the surface of ceramic substrates to protect them from extreme temperatures (i.e., thermal barrier coatings) and harsh environments (i.e., environmental barrier coatings). For SiC, these coatings are typically made from silicate-based materials (e.g., mullite [33,34], barium-strontium-aluminosilicates [34], ytterbium silicates [35]), with compatible coefficients of thermal expansion to the underlying substrate. Similar in concept to glazes in historic ceramics, which were not just decorative but also practical, the Si-rich layer acts as a protective coating that extends the lifetime of the object and seals the material from threatening pollutants.

The most damaging environmental pollutants that are exposed to statues and buried objects in an archaeological context are undoubtedly S-rich species derived from acid rain or acidic soils. This is especially true for calcareous ceramics, rich in lime [36]; they can react with the pollutants to form gypsum ($CaSO_4$), which easily peels off the surface, weathering the ceramic surface. Other factors like porosity and humidity can further contribute to the corrosion rate, accelerating the degradation of ceramic objects. A careful control of pH and humidity is therefore essential for conserving and treating ceramic surfaces and mitigating their chemical degradation.

1.4 Thesis Outline

This thesis seeks to better understand how different processing methods can play a vital role in defining the performance and degradation mechanisms of ceramic surfaces. This is achieved by primarily studying chemical and mechanical interactions occurring on ceramic surfaces during their synthesis and/or during environmental exposures. In this work, this concept is explored using four distinct case studies on (i) advanced high-temperature ceramics composed of h-BN rich composites, and (ii) historic ceramics, including low-fired pottery and porcelain. These analyses provide us with an opportunity to learn from materials of the past to create more sustainable materials for the future.

First focusing on advanced ceramics, Chapter 2 describes the high-temperature carbothermic synthesis of graphite/h-BN layered composites, which are materials that are dielectric and emissive at their surface due to the functional inclusion of h-BN layers. The study concentrates on the processing-microstructure relationship of these bimaterials, which is further informed by the underlying thermochemistry of the carbothermic reaction. In Chapter 3, graphite/h-BN bimaterials are assessed for potential use as channel wall materials for Hall-effect thrusters. The performance of the bimaterial is tested under plasma exposures, and links are made between carbothermic processing methods and the mechanical erosion of the surface. Additionally, the resistivity, emissivity, and thermal cycling of graphite/h-BN bimaterials is evaluated. Chapter 4 focuses on an additional h-BN-based ceramic: AlN/h-BN composites. The oxidation behavior of AlN/h-BN is investigated in detail, contrasted to that of AlN and B_2O_3-coated AlN. The chemical degradation of the composite in high-temperature environments is analyzed, shedding light on the role of $Al_{18}B_4O_{33}$ crystals on the temporary oxidation resistance and healing abilities of the composite.

Moving onto historic ceramics, Chapter 5 focuses on the degradation mechanism of aluminosilicates in acidic environments, expanding on the literature's current understanding of how low-fired pottery is affected by environmental pollutants like H_2SO_4 and SO_2, commonly found in acidic soils or acid rain. Surface sensitive techniques, including X-ray photoelectron spectroscopy and Fourier transform infrared spectroscopy, are used to investigate chemical erosion experimentally. Density functional theory and a

thermodynamics model are performed to corroborate observations computationally. Connections are made between firing conditions and material degradation, exemplifying the importance of processing methods in the design of sustainable materials that can be conserved for the future. Chapter 6 focuses on the synthesis of silica-based luster glazes developed in the Meissen Manufactory during the 18th century. Comparing two famous Au-based purple colorants of that time, *Böttger luster* and *Purple of Cassius*, details are revealed on how different processing methods led to distinct surface nanostructures that governed the optical properties of the glazes, providing an example of how innovative and sustainable materials can be created using modern technologies inspired by the past. Finally, conclusions and suggestions for future work are presented in Chapter 7.

References

[1] Materials and man's needs: Materials science and engineering -- Volume I, The history, scope, and nature of materials science and engineering, National Academies Press, Washington, D.C., 1975. https://doi.org/10.17226/10436.

[2] P.B. Vandiver, O. Soffer, B. Klima, J. Svoboda, The origins of ceramic technology at Dolni Věstonice, Czechoslovakia, Science. 246 (1989) 1002–1008.

[3] W.D. Kingery, P.B. Vandiver, Ceramic masterpieces, The Free Press, New York NY, 1986.

[4] Chari Celia S., Taylor Zane W., Bezur Anikó, Xie Sujing, Faber Katherine T., Nanoscale engineering of gold particles in 18th century Böttger lusters and glazes, Proceedings of the National Academy of Sciences. 119 (2022) e2120753119. https://doi.org/10.1073/pnas.2120753119.

[5] P. Colomban, The use of metal nanoparticles to produce yellow, red and iridescent colour, from bronze age to present times in lustre pottery and hlass: solid state chemistry, spectroscopy and nanostructure, Journal of Nano Research. 8 (2009) 109–132. https://doi.org/10.4028/www.scientific.net/JNanoR.8.109.

[6] T.Y. Chen, C.Y. Chen, D.C. Lin, C. Huang, Vibrational analysis of tennis racquet composite grips with ratios of carbon and glass fibres, ISBS - Conference Proceedings Archive. (2000). https://ojs.ub.uni-konstanz.de/cpa/article/view/2254 (accessed June 21, 2022).

[7] T.E. Steyer, Shaping the future of ceramics for aerospace applications, International Journal of Applied Ceramic Technology. 10 (2013) 389–394. https://doi.org/10.1111/ijac.12069.

[8] C. Piconi, W. Burger, H.G. Richter, A. Cittadini, G. Maccauro, V. Covacci, N. Bruzzese, G.A. Ricci, E. Marmo, Y-TZP ceramics for artificial joint replacements, Biomaterials. 19 (1998) 1489–1494. https://doi.org/10.1016/S0142-9612(98)00064-7.

[9] X. Jin, X. Fan, C. Lu, T. Wang, Advances in oxidation and ablation resistance of high and ultra-high temperature ceramics modified or coated carbon/carbon composites, Journal of the European Ceramic Society. 38 (2018) 1–28. https://doi.org/10.1016/j.jeurceramsoc.2017.08.013.

[10] Y. Arai, R. Inoue, K. Goto, Y. Kogo, Carbon fiber reinforced ultra-high temperature ceramic matrix composites: A review, Ceramics International. 45 (2019) 14481–14489. https://doi.org/10.1016/j.ceramint.2019.05.065.

[11] A.A. Mashnitskii, T.V. Andreeva, T.V. Dubovik, High-temperature graphite protective coatings, Refractories. 12 (1971) 728–730. https://doi.org/10.1007/BF01285611.

[12] J.-F. Huang, X.-R. Zeng, H.-J. Li, X.-B. Xiong, G. Sun, ZrO_2–SiO_2 gradient multilayer oxidation protective coating for SiC coated carbon/carbon composites, Surface and Coatings Technology. 190 (2005) 255–259. https://doi.org/10.1016/j.surfcoat.2004.02.014.

[13] H. Jian-Feng, Z. Xie-Rong, L. He-Jun, X. Xin-Bo, H. Min, Mullite-Al_2O_3-SiC oxidation protective coating for carbon/carbon composites, Carbon. 41 (2003) 2825–2829. https://doi.org/10.1016/S0008-6223(03)00397-X.

[14] F. Smeacetto, M. Ferraris, M. Salvo, Multilayer coating with self-sealing properties for carbon–carbon composites, Carbon. 41 (2003) 2105–2111. https://doi.org/10.1016/S0008-6223(03)00228-8.

[15] R. Naslain, Design, preparation and properties of non-oxide CMCs for application in engines and nuclear reactors: An overview, Composites Science and Technology. 64 (2004) 155–170. https://doi.org/10.1016/S0266-3538(03)00230-6.

[16] S.K. Bull, T.A. Champ, S.V. Raj, R.C. O'Brien, C.B. Musgrave, A.W. Weimer, Atomic layer deposited boron nitride nanoscale films act as high temperature hydrogen barriers, Applied Surface Science. 565 (2021) 150428. https://doi.org/10.1016/j.apsusc.2021.150428.

[17] E.J. Opila, R.C. Robinson, M.J. Verrilli, Borosilicate glass-induced fiber degradation of SiC/BN/SiC composites exposed in combustion environments, International Journal of Applied Ceramic Technology. 13 (2016) 434–442. https://doi.org/10.1111/ijac.12499.

[18] J. Hu, W.D. Fei, C. Li, C.K. Yao, Interfacial reaction in alumina borate whisker reinforced aluminium composite, Journal of Materials Science Letters. 13 (1994) 1797–1799. https://doi.org/10.1007/BF00776362.

[19] Y.C. Feng, L. Geng, G.H. Fan, A.B. Li, Z.Z. Zheng, The properties and microstructure of hybrid composites reinforced with WO_3 particles and $Al_{18}B_4O_{33}$ whiskers by squeeze casting, Materials & Design. 30 (2009) 3632–3635. https://doi.org/10.1016/j.matdes.2009.02.020.

[20] C.T. Kuo, K.T. Faber, Permeable carbon nanotube-reinforced silicon oxycarbide via freeze casting with enhanced mechanical stability, Journal of the European Ceramic Society. 40 (2020) 2470–2479. https://doi.org/10.1016/j.jeurceramsoc.2019.12.059.

[21] C.S. Chari, K.T. Faber, Oxidation resistance of AlN/BN via mullite-type $Al_{18}B_4O_{33}$, Journal of the European Ceramic Society. 42 (2022) 3437–3445. https://doi.org/10.1016/j.jeurceramsoc.2022.02.037.

[22] R.R. Hofer, S.E. Cusson, R.B. Lobbia, A.D. Gallimore, The H9 magnetically shielded Hall thruster, in: 35th International Electric Propulsion Conference, IEPC-2017-232, Altanta, GA, 2017: p. 18.

[23] J.T. Yim, M.L. Falk, I.D. Boyd, Modeling low energy sputtering of hexagonal boron nitride by xenon ions, Journal of Applied Physics. 104 (2008) 123507. https://doi.org/10.1063/1.2987090.

[24] Y. Garnier, V. Viel, J.-F. Roussel, J. Bernard, Low-energy xenon ion sputtering of ceramics investigated for stationary plasma thrusters, Journal of Vacuum Science & Technology A: Vacuum, Surfaces, and Films. 17 (1999) 3246–3254. https://doi.org/10.1116/1.582050.

[25] Y. Garnier, V. Viel, J.F. Roussel, D. Pagnon, L. Magne, M. Touzeau, Investigation of xenon ion sputtering of one ceramic material used in SPT discharge chamber, in: 26th International Electric Propulsion Conference, IEPC Paper 1999-083, Kitakyushu, Japan, 1999.

[26] M.W. Crofton, J.A. Young, Low energy Xe^+ sputter yields for alumina, Hiperco 50, and boron nitride, American Institute of Physics Advances. 11 (2021) 125126. https://doi.org/10.1063/5.0067346.

[27] K.T. Faber, M.D. Huang, A.G. Evans, Quantitative studies of thermal shock in ceramics based on a novel test technique, Journal of the American Ceramic Society. 64 (1981) 296–301. https://doi.org/10.1111/j.1151-2916.1981.tb09606.x.

[28] P. Vandiver, Corrosion and conservation of ancient glass and ceramics, in: Corrosion of Glass, Ceramics and Ceramic Superconductors, Noyes Publications, Park Ridge, NJ, 1992.

[29] A. Boccia Paterakis, M. Steiger, Salt efflorescence on pottery in the Athenian Agora: A closer look, Studies in Conservation. 60 (2015) 172–184. https://doi.org/10.1179/2047058413Y.0000000113.

[30] B.E. Deal, A.S. Grove, General relationship for the thermal oxidation of silicon, Journal of Applied Physics. 36 (1965) 3770–3778. https://doi.org/10.1063/1.1713945.

[31] G.N. Morscher, D.R. Bryant, R.E. Tressler, Environmental durability of BN-based interphases (for SiC_f/SiC_m composites) in H_2O containing atmospheres at intermediate temperatures, in: Proceedings of the 21st Annual Conference on Composites, Advanced Ceramics, Materials, and Structures—A: Ceramic Engineering and Science Proceedings, John Wiley & Sons, Ltd, 1997: pp. 525–534. https://doi.org/10.1002/9780470294437.ch58.

[32] X. Luan, Y. Zou, X. Hai, H. Bai, Q. Zhang, R. Riedel, L. Cheng, Degradation mechanisms of a self-healing $SiC_{(f)}/BN_{(i)}/[SiC\text{-}B4C]_{(m)}$ composite at high temperature under different oxidizing atmospheres, Journal of the European Ceramic Society. 38 (2018) 3804–3813. https://doi.org/10.1016/j.jeurceramsoc.2018.05.001.

[33] K.N. Lee, Current status of environmental barrier coatings for Si-based ceramics, Surface and Coatings Technology. 133–134 (2000) 1–7. https://doi.org/10.1016/S0257-8972(00)00889-6.

[34] K.N. Lee, D.S. Fox, J.I. Eldridge, D. Zhu, R.C. Robinson, N.P. Bansal, R.A. Miller, Upper temperature limit of environmental barrier coatings based on mullite and BSAS, Journal of the American Ceramic Society. 86 (2003) 1299–1306. https://doi.org/10.1111/j.1151-2916.2003.tb03466.x.

[35] K.N. Lee, D.S. Fox, N.P. Bansal, Rare earth silicate environmental barrier coatings for SiC/SiC composites and Si_3N_4 ceramics, Journal of the European Ceramic Society. 25 (2005) 1705–1715. https://doi.org/10.1016/j.jeurceramsoc.2004.12.013.

[36] I.C. Freestone, Post-depositional changes in archaeological ceramics and glasses, in: Handbook of Archaeological Sciences, John Wiley & Sons, Ltd., 2001: pp. 615–626.

Chapter 2

SYNTHESIS AND CHARACTERIZATION OF GRAPHITE/HEXAGONAL BORON NITRIDE BIMATERIALS

The contents of this chapter are part of a manuscript in preparation titled "High-temperature Carbothermal Synthesis and Characterization of Graphite/h-BN Bimaterials" by C.S. Chari, B. W. McEnerney, R. R. Hofer, J. A. Wollmershauser, E. P. Gorzkowski, and K.T. Faber. In this work, C.S. Chari led the experimental work, with the assistance of J. A. Wollmershauser and E. P. Gorzkowski from the Naval Research Laboratory, who helped prepare samples. Faber supervised the experimental work. All authors were involved in designing the work and preparing the manuscript.

2.1 Introduction

Hexagonal boron nitride (h-BN) is one of many boron nitride polymorphs, and is widely valued for its dielectric properties, emissivity, and oxidation resistance up to 1000 °C [1]. Structurally, h-BN is composed of alternating B and N atoms arranged in a two-dimensional hexagonal structure, achieved when BN is crystallized past 1600 °C at ambient pressures [2,3]. The highly anisotropic sheets of h-BN are bound together by weak van der Waals forces, making this material lubricating, with an elastic modulus in the c-direction significantly lower than in the a-direction [4]. It can be synthesized from boria (B_2O_3) through several high-temperature routes, including by reacting the oxide with N-containing compounds [5–8] (e.g., NH_3, $CO(NH_2)_2$, as described in Appendix A), or via carbothermic reactions in nitriding atmospheres [9–14]. The thermal shock resistance of h-BN has made it sought-after for nuclear and aerospace applications; for example, it is used in the discharge chamber of Hall effect thrusters in electric propulsion (EP) systems [15]. Additionally, its elastic properties have made h-BN a standard in the combustion engine industries, where it is featured in SiC/BN/SiC ceramic-matrix composites to facilitate crack deflection [16,17]. Despite these desirable properties, h-BN is expensive to process and difficult to machine into complex shapes due to its brittle nature.

Graphite is isostructural with h-BN. It has a comparable coefficient of thermal expansion to h-BN [18], but unlike h-BN, graphite is electrically conductive and starts to oxidize at temperatures as low as 400 °C [19], making it unsuitable for some high-temperature applications. Nevertheless, it is more compliant, easier to machine, and less prone to fracture than h-BN, making it more economical to manufacture and process. It also has an even greater resistance to thermal shock than h-BN [20], which could be attractive for aerospace and automotive applications were it not for its tendency to oxidize so readily.

Coupling the disparate properties of the two materials is possible when they are made into a single bimaterial composed of a graphite core and a h-BN exterior. In fact, h-BN can be grown directly on graphite samples through the high-temperature carbothermic reaction of B_2O_3 in nitrogen, which converts the surface of graphite into h-BN [9,12]. The graphite body is completely enclosed by a layer of h-BN that is dielectric, emissive, and resistant to oxidation. In this way, the h-BN layer can protect the internal graphite from degradation under high-temperature environments, making this bimaterial an innovative candidate for applications functioning between 400 °C and 1000 °C, while still retaining the machinability and fracture resistance of the graphite body.

High-temperature methods for synthesizing graphite/h-BN bimaterials have been reported in the past [9,12]. However, these studies have not characterized the microstructure or interface of the layered bimaterials in any detail. The present study aims to investigate the processing-microstructure relationship of graphite/h-BN bimaterials, to understand how carbothermal synthesis conditions can control the thickness and microstructure of the h-BN layer; properties that could influence the emissivity and electrical conductivity of the bimaterial at its surface, of importance to applications like electric propulsion. Additionally, this study seeks to understand the chemical and mechanical properties of the interface between graphite and the h-BN layer to further evaluate the adhesion between the layers. A detailed evaluation is provided to understand how both the reactive phases of B_2O_3, liquid-phase and vapor-phase, can influence the size and composition of the interfacial region as well as the properties of the h-BN layer.

2.2 Materials & Methods

2.2.1 Graphite/h-BN Synthesis

2.2.1.1 h-BN Precursor Powders

High-temperature carbothermal reduction reactions, also known as carbothermic reactions, were used to convert surfaces of bulk graphite bodies, both rectangular and cylindrical coupons, to hexagonal boron nitride (h-BN) layers. To prepare the precursor powders, 9.89 g of boric acid (H_2BO_3, Sigma Aldrich) was mixed with 0.74 g of h-BN (IDL-500, Saint-Gobain). The blend of powders was then melted in an Al_2O_3 crucible at 800 °C for 30 min using a high-temperature box furnace (CM Rapid Temp). This step allowed the boric acid to dehydrate into glassy B_2O_3 before the h-BN-forming reaction was carried out, limiting the effects of water vapor on the porosity and growth of the h-BN layer. Temperatures higher than 800 °C were avoided to prevent B_2O_3 from reacting with the Al_2O_3 crucible to generate aluminum borate [21]. The heating and cooling rates were both 3 °C/min. After heating, the B_2O_3-rich precursor powders were removed from the crucible and ground to particles of 1 µm in diameter or less, the latter which was determined by using a sieve to help screen the particle size.

2.2.1.2 Carbothermic Reactions

Approximately 4 g of the B_2O_3-rich precursor powders were placed inside a boron nitride crucible. Three rectangular graphite strips (G540, Tokai Carbon) were then placed atop the powders. Each 30 mm × 2 mm × 6 mm strip weighed approximately 4.3 g. The 30 mm × 6 mm face of each strip was in contact with the precursor powders while the opposite 30 mm × 6 mm face was exposed to B_2O_3 vapors. A boron nitride lid was then placed over the crucible with a visible gap between the lid and the crucible wall. This set-up permitted the flow of nitrogen gas into the crucible, while still ensuring a high concentration of B_2O_3 vapor within the crucible's enclosure. The h-BN forming carbothermic reaction is described in Eqn. 2.1.

$$B_2O_{3(l)} + 3C_{(s)} + N_{2(g)} \rightarrow 2BN_{(s)} + 3CO_{(g)} \quad (2.1)$$

The standard Gibbs Free Energy change in Joules for Eqn. 2.1 was calculated to be $\Delta G^{o}_{(2.1)} = 2{,}550 - (130 \times T)$ using thermochemical data from Chase [22].

The lidded crucible and its contents were placed in a high-temperature tube furnace with flowing nitrogen gas (UHP200, Airgas) to synthesize h-BN. A Carbolite CTF 17/300 Tube Furnace was used for syntheses taking place at 1600 °C. The holding times ranged from 3 h to 12 h. The heating rate was 3 °C/min up to 900 °C, then 2 °C/min up to the target temperature, while the cooling rate was 1 °C/min until 1100 °C, then 2 °C/min to room temperature. An MTI GSL-1800X tube furnace with a SiC tube (Saint Gobain) and a Eurotherm 3504 controller was used for syntheses taking place at 1650 °C and 1700 °C. The temperature was calibrated for the SiC tube with a B-type thermocouple resting on an empty BN crucible with the same gas flow rate used in the experiments. The holding times at each temperature ranged from 8 h to 18 h. With the 1650 °C and 1700 °C temperature reactions, the SiC tube furnace was not able to reach the target temperature as quickly, therefore the heating rate used was 3 °C/min up to 900 °C, then ~2 °C/min up to the target temperature. Additionally, the cooling rate was 1 °C/min until 1100 °C, then 2 °C/min to room temperature.

After the carbothermic reaction, the graphite/h-BN bimaterials were removed from the crucible. The surrounding precursor powders fully converted into lubricating h-BN powders after the reaction, which facilitated the removal of the samples. Excess powders were washed off the bimaterials with deionized water, revealing ceramic h-BN layers over the graphite bodies.

Additionally, the boron carbide forming carbothermic reaction described in Eqn. 2.2 was also investigated to gain a better understanding of the mechanisms involved in h-BN formation.

$$2B_2O_{3(l)} + 7C_{(s)} \rightarrow B_4C_{(s)} + 6CO_{(g)} \qquad (2.2)$$

The standard Gibbs Free Energy change in Joules for Eqn. 2.2 was calculated to be $\Delta G^{o}_{(2.2)} = 946{,}000 - (605 \times T)$ using thermochemical data from Chase [22].

Flowing argon gas (AR200, Airgas) was used during the boron carbide forming reaction, taking place at 1600 °C by holding for 12 h.

2.2.2. Characterization

Scanning electron microscopy and energy dispersive X-ray spectroscopy (SEM-EDS, ZEISS 1550VP FESEM, Carl Zeiss Microscopy GmbH, Jena, Germany) were used to study the microstructure of the bimaterials and synthesized h-BN layers. The diffusion profiles of the interface of graphite/h-BN were obtained using EDS line scans comprising of at least 100 data points per line, each of which was drawn perpendicular to the layers of each bimaterial sample. The h-BN layer thicknesses were measured using an optical microscope and the image-processing tool ImageJ (National Institutes of Health). An average of 15 thickness measurements were carried out for each sample over lengths up to 6 mm, with measurements being made in evenly spaced intervals. The reported values of the h-BN layer thickness were determined using number averaging, with the error term representing one standard deviation. A camera was used to photograph the bimaterials on the macroscale (Nikon D7500, AF-S Micro Nikkor 40mm Lens, Nikon, Tokyo, Japan). X-ray powder diffraction (XRD, PANalytical X'Pert Pro) and transmission electron microscopy (TEM, TF-30, Tecnai) were also carried out to characterize the bimaterials and h-BN layers, respectively.

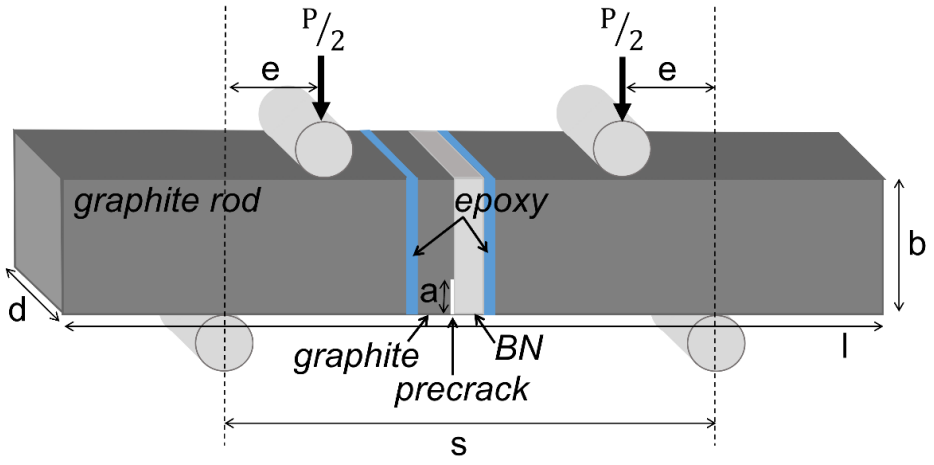

Figure 2.1. Single-edge notched beam test used on the bimaterial to investigate the interfacial fracture toughness of h-BN/graphite.

Single-edge-notch-beam (SENB) tests were carried out to measure the fracture toughness of the bimaterial interface [23,24]. A 4-point-bend test set-up, with an outer span of 40 mm and an inner span of 20 mm, was mounted in an Instron 5982 mechanical testing frame (Instron Corporation, Norwood, MA), operated at a cross-head rate of 0.5 mm/min. Figure 2.1 illustrates the beam geometry and test set-up, where *s* is 40 mm, *e* is 10 mm, and the dimensions of the beam ($l \times d \times b$) are approximately $50 \times 2 \times 8$ mm^3. The beams were fabricated by sandwiching a graphite/h-BN coupon between two graphite rods of dimension $20 \times 2 \times 8$ mm^3 using epoxy (J-B Weld). The precrack notch was prepared using a 0.3 mm thick razor and an optical microscope. Of the SENB tests, four pure graphite specimens were to study the substrate; four pure h-BN specimens were to evaluate a commercial grade of binderless h-BN (AX05, Saint-Gobain); eight h-BN/graphite biomaterial specimens were to examine bimaterials synthesized at 1700 °C for 18 h. Of the latter eight, four were from graphite/h-BN coupons produced from liquid-phase B_2O_3, while four were from graphite/h-BN coupons created from vapor-phase B_2O_3.

2.3 Results & Discussion

2.3.1 Carbothermic Development of h-BN Layer

The graphite/h-BN bimaterial, shown in Figure 2.2a, consists of a graphite body with a carbothermic reduction-produced h-BN ceramic layer, synthesized at 1600 °C. A cross-sectional view of the bimaterial, shown in the SEM-EDS map of Figure 2.2b, confirmed that the outer layer was rich in B and N, and indicated a rough graphite/h-BN interface with a complex chemistry, showing signs of a second B-rich material below the h-BN layer. Diffraction patterns and transmission electron micrographs, shown in Figure 2.2c-d, were used to confirm the phase of the synthesized BN layer, indicating that it crystallized into h-BN past 1600 °C as expected from phase diagrams in the literature [2].

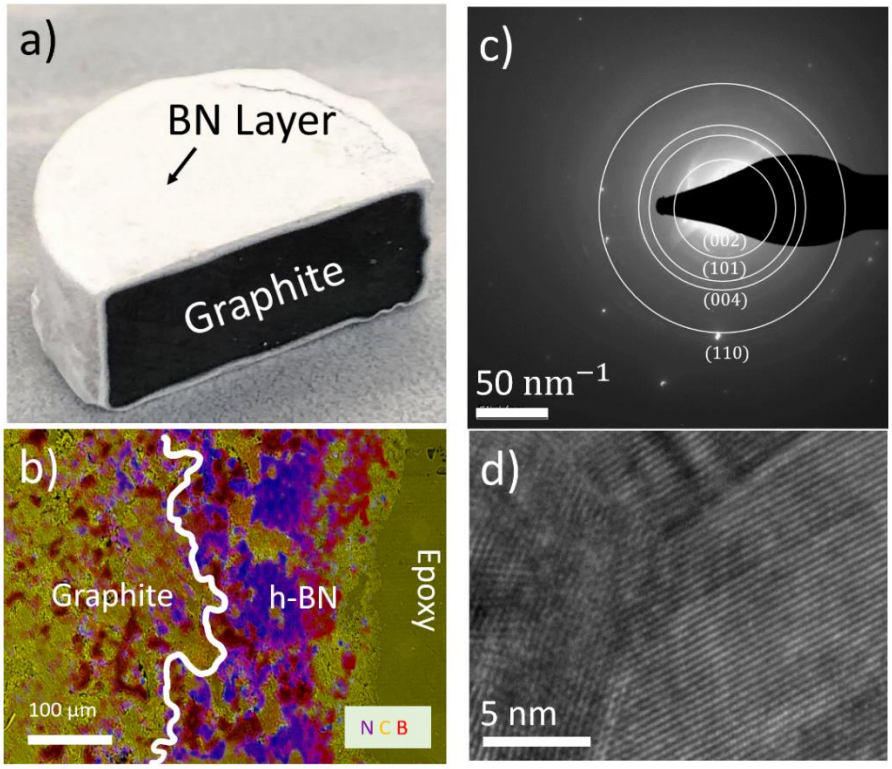

Figure 2.2. Development of h-BN layer: a) Bimaterial cylinder of graphite and h-BN processed at 1600 °C, b) SEM-EDS map showing cross-sectioned view of the rough interface between the h-BN layer and graphite of a), c) diffraction pattern (ring pattern) of polycrystalline h-BN layer synthesized at 1600 °C, confirming polycrystalline hexagonal phase, d) transmission electron micrograph of h-BN layer from b).

The carbothermic reaction used to synthesize the graphite/h-BN bimaterial is described in Eqn. 2.1. The B_2O_3-rich precursor powders reacted with the surface of the graphite bodies, converting the outer layer of graphite into h-BN with the release of CO. In this way, the h-BN layers could be grown directly from the graphite sample, ensuring better adhesion and thicker layers (on the order of hundreds of microns) than the thickness expected by other methods such as chemical vapor deposition [25] or atomic layer deposition [26].

The surface microstructure of the h-BN layer was studied using scanning electron microscopy, shown in Figure 2.3a-f, where it was found that altering the time and temperature of the carbothermic reaction changed the microstructure of the h-BN layer's surface.

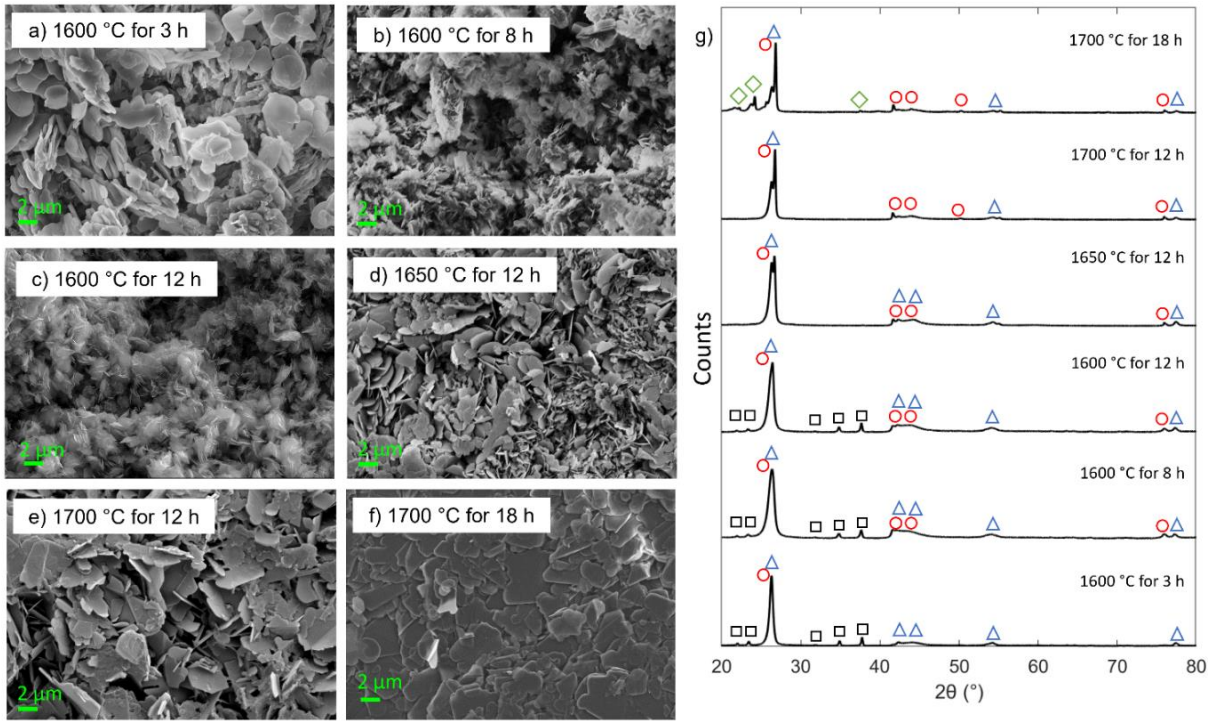

Figure 2.3. h-BN layer grown at 1600 °C-1700 °C, over 3 h, 8 h, or 12 h: a-f) microstructures, g) accompanying XRD spectra of bimaterials shown on the left, showing presence of BN (○), graphite (△), boron carbide (□) and carbon nitride (◊).

For example, Figure 2.3a shows the microstructure of a h-BN layer grown at 1600 °C for 3 h, revealing large, coarse flakes. The corresponding XRD spectrum in Figure 2.3g indicates that the bimaterial contains only minor amounts of h-BN but abundant amounts of crystalline graphite and boron carbide. In contrast, increasing the time of the reaction at 1600°C as shown in Figures 3b-c results in progressively smaller h-BN flakes, phase confirmed in Figure 2.3g. These flakes are sintered together to form a porous structure, potentially due to the evolution of CO gas from Eqn. 2.1. The strong presence of h-BN indicates that 8 h and 12 h at 1600 °C was sufficient for B_2O_3, C and N_2 to react completely, with BN crystallizing into a hexagonal, two-dimensional structure. Nevertheless, it should be noted that boron carbide is also present in specimens synthesized at 1600 °C.

Based upon estimated X-ray penetration depths in B, C and N, our XRD observations indicate that the boron carbide detected is located within the first couple of hundred microns of the bimaterial [27]. This could be attributable to a second carbothermic reaction

taking place in the absence of nitrogen, seen in Eqn. 2.2, where B_2O_3 can react with graphite at high temperatures to form boron carbide. During the bimaterial synthesis, the B_2O_3-rich precursors melt into a liquid within the crucible that can penetrate the graphite bodies. It is likely that boron carbide develops below the h-BN layer, where B_2O_3 has reacted with graphite in areas inaccessible to nitrogen gas. Referring to the SEM-EDS map in Figure 2.2b, the boron infiltration previously observed below the h-BN layer could be due to the development of boron carbide near the interface. The origins of boron carbide formation will be revisited in later parts of the discussion.

As seen in Figures 2.3d-f, increasing the temperature of the carbothermic reaction to 1650 °C and 1700 °C appears to densify the microstructure of the h-BN layer. As a result, the target temperature of the carbothermic reactions was chosen to be either 1650 °C or 1700 °C in subsequent sections of this study. The diffraction spectra reported in Figure 2.3g suggest that boron carbide is not observed at 1650 °C or 1700 °C: note that both h-BN and graphite are visible, suggesting boron carbide is not at all present at the interface. Also worth noting, carrying out the carbothermic reaction at 1700 °C for 18 h can produce residual carbon nitrides on the samples. These can be removed from the bimaterial by sonicating the sample in deionized water. While precautions should be taken when handling such toxic residues, these residues are not detrimental to the function of the h-BN layer.

2.3.2 The Role of the B_2O_3 Phase in h-BN Formation

Throughout the high-temperature carbothermic reaction, B_2O_3 is present as both a liquid-phase and a vapor-phase oxide [12,13,28–30]. Both phases can participate in the h-BN forming carbothermic reaction, making it essential to investigate how the B_2O_3 reacting phase influences the microstructure and thickness of the synthesized h-BN layer, as well as the interface of the bimaterial. These concepts are demonstrated in Figure 2.4a-b, where graphite samples can develop h-BN layers on their surface regardless of whether the graphite faces are in contact with the precursor powders or not. Liquid-phase B_2O_3 originates from the melted precursor powders that accumulate at the bottom of the crucible, while the vapor-phase B_2O_3 volatilizes to the top of the crucible where it is partially trapped by the lid and can thus react with the exposed graphite surfaces.

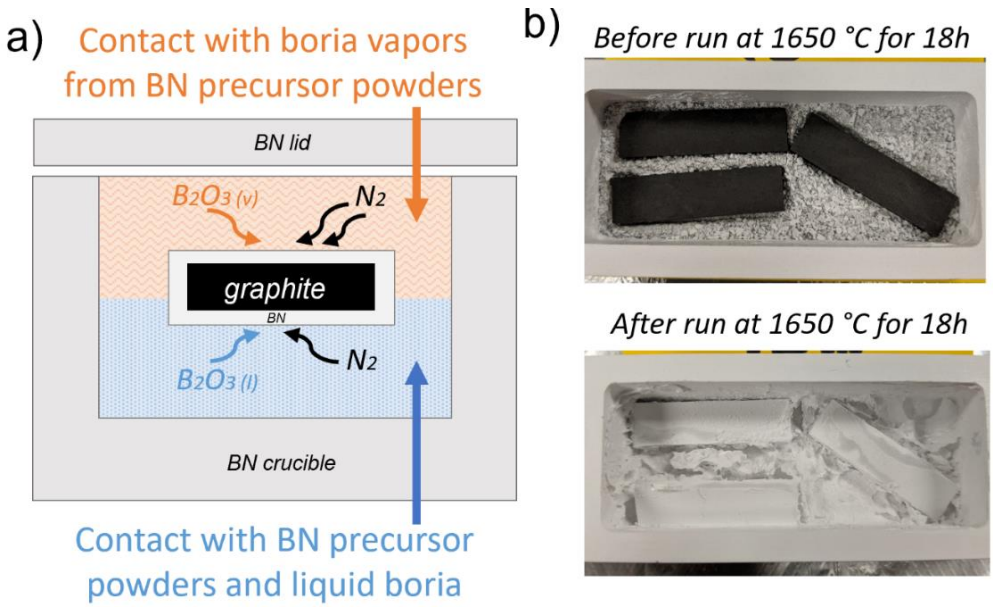

Figure 2.4. Carbothermic reaction: a) Illustration showing the conversion of graphite into h-BN by both liquid-phase B_2O_3 from melted precursor powders (blue) and by vapor-phase B_2O_3 from the high-temperature evaporation of the precursor powders (orange). b) Example of materials prior to carbothermic reaction at 1650 °C for 18 h (top), and after reaction (bottom).

2.3.2.1 Vapor-Phase Carbothermic Reactions

The most widely established mechanism for the carbothermic formation of h-BN is based on the vapor-phase reduction of B_2O_3 into BO or metallic B, which consequently reacts with N_2 to produce the nitride[12,30]. This mechanism can be summarized by a series of independent chemical reactions, as listed by Aydoğdu *et al*.[12], seen below in Eqns. 2.3 to 2.6.

$$B_2O_{3(l)} + 2C_{(s)} \rightarrow 2BO_{(g)} + CO_{(g)} \quad (2.3)$$

$$B_2O_{3(l)} + 3C_{(s)} \rightarrow 2B_{(g)} + 3CO_{(g)} \quad (2.4)$$

$$B_2O_{3(l)} \rightarrow B_2O_{3(g)} \quad (2.5)$$

$$2B_{(g)} + \frac{1}{2}N_{2(g)} \rightarrow BN \quad (2.6)$$

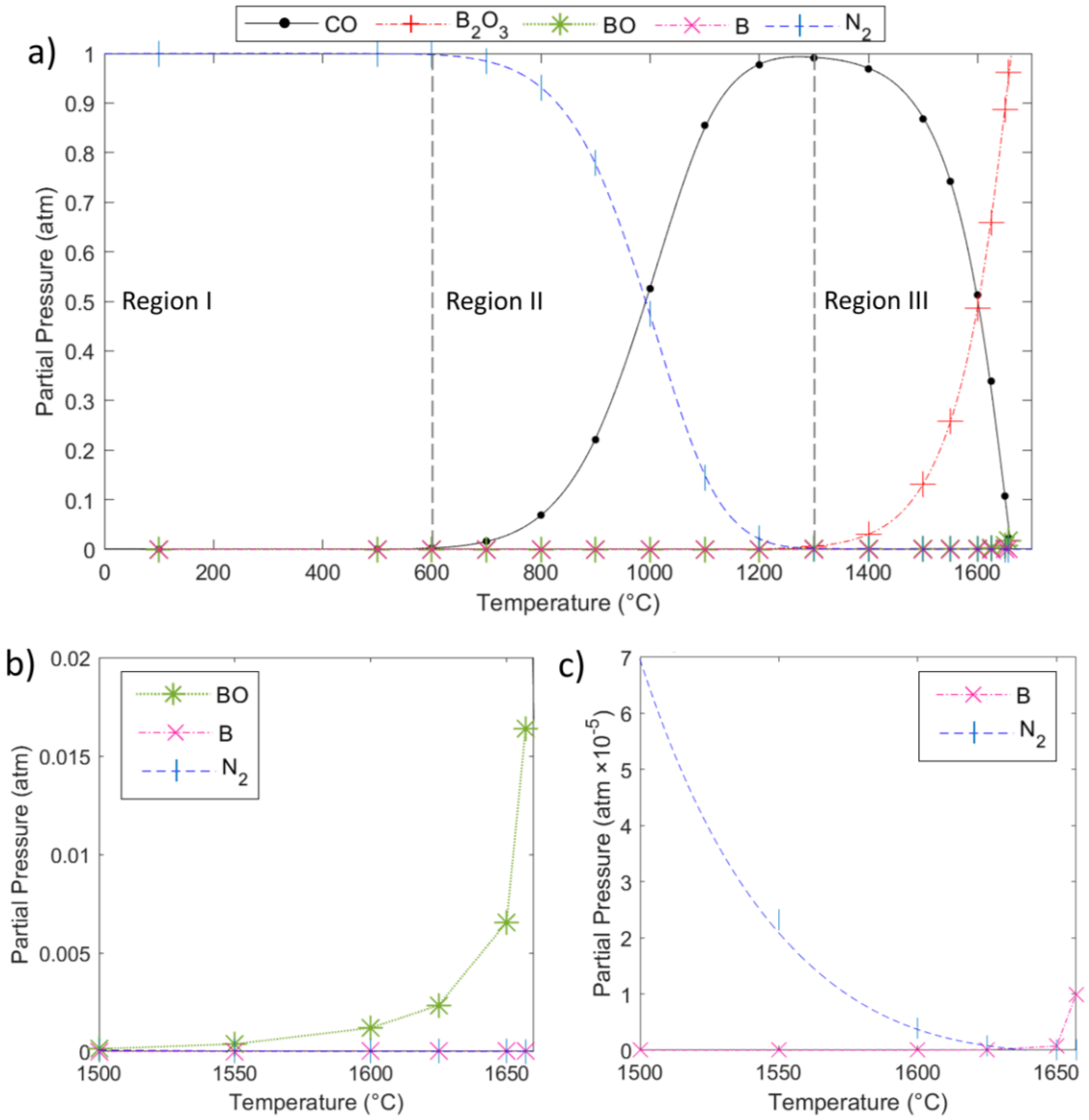

Figure 2.5. Equilibrium partial pressure of CO, BO, B, B_2O_3 and N_2 in a closed system as a function of temperature: a) showing three distinct regions largely populated by N_2, CO, and B_2O_3, respectively. b) Close-up of a) showing increase in P_{BO} with temperature. c) Close-up of a) showing increase in P_B with temperature.

The equilibrium partial pressures of the gaseous species in a closed system can be estimated by determining the equilibrium constants, *K*, of these reactions. The standard Gibbs Free Energy change in Joules for Eqns. 2.3 to 2.6 are as follows: $\Delta G^{o}_{(2.3)} = 1{,}106{,}840 -$

$(473.42 \times T)$, $\Delta G^{o}_{(2.4)} = 2{,}025{,}980 - (763 \times T)$, $\Delta G^{o}_{(2.5)} = 359{,}995 - (186.2 \times T)$, $\Delta G^{o}_{(2.6)} = -820{,}780 + (235.43 \times T)$. Note that $\Delta G^{o}_{(2.3)}$, $\Delta G^{o}_{(2.4)}$ and $\Delta G^{o}_{(2.6)}$ were taken from Aydoğdu *et al*. [12] from data compiled by Turkdogan[31], while $\Delta G^{o}_{(2.5)}$ was taken from Yoon *et al*. [30]. Equilibrium constants could then be calculated at a given temperature through the following relationship: $K_{(i)} = \exp\left(-{}^{\Delta G^{o}_{(i)}}/_{T}\right)$. The equilibrium partial pressures were thus calculated by finding the simultaneous solution of the following equations: $K_{(2.3)} = P_{BO}^{2} \times P_{CO}$, $K_{(2.4)} = P_{B}^{2} \times P_{CO}^{3}$, $K_{(2.5)} = P_{B_2O_3}$, and $K_{(2.6)} = \frac{1}{P_B \times {P_{N_2}}^{1/2}}$, where $P_{CO} + P_B + P_{BO} + P_{N_2} + P_{B_2O_3} = 1$.

The equilibrium partial pressures P_{CO}, P_B, P_{BO}, P_{N_2} and $P_{B_2O_3}$ at 1500 °C were reported by Aydoğdu *et al*. [12]. Moving beyond their study, we seek to gain a better understanding of the carbothermic formation of h-BN over a wider temperature range, from 100 °C to near 1700 °C. Figure 2.5a summarizes the calculated data, where the effect of temperature on each partial pressure reveals the most prevalent vapors at each point of the h-BN synthesis. From this, we can distinguish three distinct regions in the formation of h-BN.

Region I defines the system before the carbothermic reaction commences, indicating that the closed crucible is filled only with N_2 vapors. Starting at 600 °C, the rise in CO from Eqns. 2.3 and 2.4 indicates the early stages of the carbothermic reaction. This defines the start of Region II, where we also see a gradual decrease in P_{N_2} as boron nitride starts to form. The equilibrium partial pressure of B_2O_3 indicates that its vapor-phase does not evolve until Region III is reached, at temperatures greater than 1300 °C. Within this region, an exponential rise in $P_{B_2O_3}$ can be seen with increasing temperature. Specifically, $P_{B_2O_3}$ increases by 0.41 atm as the temperature rises from 1600 °C to 1650 °C. Figures 2.5b-c similarly reveal that P_B and P_{BO} rise steeply past 1650 °C. Although B and BO vapors do not appear to dominate the system as strongly as B_2O_3, they still play an important role in h-BN formation as seen in Eqn. 2.6. These findings indicate that B-rich vapor-phases dominate the gaseous system above 1650 °C.

Using the ideal gas law, the data in Figure 2.5 can also be expressed in terms of mol % and wt% to gain insight into the relative concentrations of the vapor-phases. These data are shown in Figures A.2 and A.3 in Appendix A.

2.3.2.2 Liquid-Phase Carbothermic Reactions

The liquid-phase carbothermic formation of h-BN has been discussed in the past [9,12], however not as extensively as the analogous vapor-phase reaction. One reason could be due to the gaseous nature of a key reactant in nitride formation: N_2. Our results in Section 2.4 and the behavior seen in Region II in Figure 2.5a both demonstrate that liquid-phase carbothermic reactions do indeed occur. Naturally, this brings up the question of how easily N_2 dissolves in liquid B_2O_3 for h-BN to successfully form.

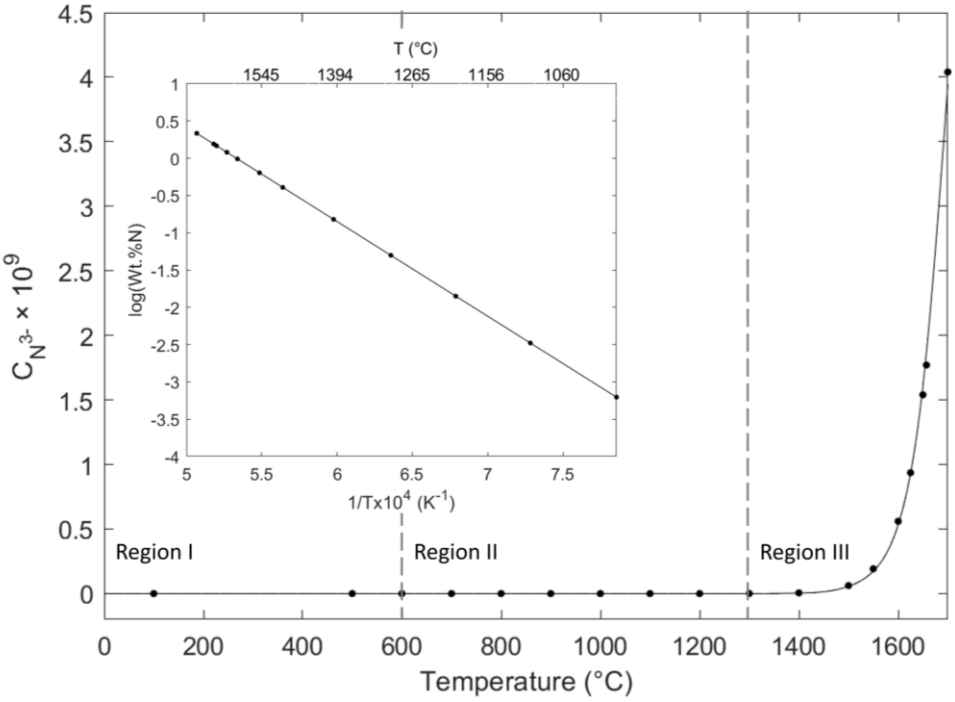

Figure 2.6. Nitride capacity as a function of temperature, showing chemical dissolution of nitrogen in the melt is favored in Region III. Inset shows solubility of nitride in the melt as a function of temperature; data for T > 1550 °C were extrapolated from Wakasugi's original work [32].

Wakasugi *et al.* have published extensively [32,33] on the physical and chemical dissolution of N_2 in pure molten B_2O_3 as well as in B_2O_3 melts containing oxides, SiO_2,

and an array of dopants like Al_2O_3, Y_2O_3 and La_2O_3. They describe the chemical dissolution of N_2 in pure molten B_2O_3 by Eqn. 2.7, also expressed by Eqn. 2.8 in terms of the oxygen and nitrogen ions in the glass melt, O^{2-} and N^{3-}, respectively. It should be noted that reducing atmospheres favor the dissolution of nitrogen into the melt, meaning that Eqns. 2.7 and 2.8 are likely promoted in the carbothermic reduction reactions described in our study [32].

$$\frac{1}{2}N_{2(g)} + \frac{1}{2}B_2O_{3(l)} \rightarrow BN_{(s)} + \frac{3}{4}O_{2(g)} \tag{2.7}$$

$$\frac{1}{2}N_{2(g)} + \frac{3}{2}O^{2-} \rightarrow N^{3-} + \frac{3}{4}O_2 \tag{2.8}$$

The standard Gibbs Free Energy change in Joules for Eqn. 2.7 is $\Delta G^o_{(7)} = 364{,}000 - (17.4 \times T)$, where $K_{(7)} = \frac{{P_{O_2}}^{3/4}}{{P_{N_2}}^{1/2}}$.

Wakasugi *et al.* refer to the term *nitride capacity*, $C_{N^{3-}}$, as a way of describing the capability of a melt to chemically dissolve nitrogen, where pure molten B_2O_3 has the highest nitride capacity of all B_2O_3 bearing melts. This term is defined as $C_{N^{3-}} = (\text{Wt\% N}) \times K_{(7)}$, where Wt% N describes the solubility of the nitride in the melt, a property that increases with rising temperature and rising P_{N_2}, and $K_{(7)}$ is the equilibrium constant for Eqn. 2.7 [32]. In this analysis, the data used for Wt% N in molten B_2O_3 were extrapolated from Wakasugi *et al.* [32], shown in the inset of Figure 2.6.

Figure 2.6 illustrates how $C_{N^{3-}}$ changes with temperature, indicating that the nitride capacity is increased in Region III. This increase also coincides with the decrease in N_2 vapor pressure seen in Figure 2.5a within this region, indicating that within a closed system the loss of N_2 vapor is from a combination of h-BN formation and N_2 dissolution into the melt. Our liquid-phase carbothermic reactions carried out at 1600 °C, 1650 °C and 1700 °C appear to contain sufficient nitrogen in the melt for the h-BN forming carbothermic reaction to successfully occur, as our results in Figures 2.3 and 2.4 indicate. In fact, since

$C_{N^{3-}}$ increases exponentially with temperature in Region III, it could also explain why boron carbide is usually seen in bimaterials synthesized at 1600 °C (where relatively lower levels of nitrogen in the melt cause Eqn. 2.2 to take place along with Eqn. 2.1) and not at 1700 °C (where the chemical dissolution of N_2 is at its highest, causing Eqn. 2.1 to occur alone without boron carbide formation).

2.3.2.3 Comparison of Vapor-Phase and Liquid-Phase Process

Irrespective of phase, we see that B_2O_3 reacts with the surface of the graphite samples and converts it into a layer of h-BN. The surface microstructures and thicknesses of these h-BN layers are compared in Figure 2.7a-b for the two reacting phases of B_2O_3.

In the vapor-phase B_2O_3 reactions, the inset in Figure 2.7a shows that the h-BN layer is not visible on the macroscale when the carbothermic reaction takes place at 1650 °C for 8 h. On the microscale, some small flakes are visible, however their concentration is too low to be identified through X-ray diffraction, as seen in Figure 2.7c, where only graphite can be recognized. When the reaction time is raised to 18 h, the h-BN layer thickness increases to 72 ± 19 µm, as seen in Figure 2.7b. The corresponding microstructure consists of sintered h-BN flakes. X-ray diffraction patterns in Figure 2.7c confirm that these bimaterials are composed of graphite and h-BN, with no signs of boron carbide. Note that the absence of boron carbide is likely due to the abundance of N_2 gas in the vapor-phase reaction, which is more accessible to the graphite surface than the dissolved nitrogen in the liquid-phase carbothermic reaction. When the reaction time is 8 h or 12 h long at 1700 °C, the h-BN layer thickness reaches 70 ± 14 µm, similar to the value seen with reactions that are 18 h long at 1650 °C. The surface microstructure of the h-BN layer appears visibly denser when synthesized at 1700 °C for 18 h, showing compacted h-BN flakes.

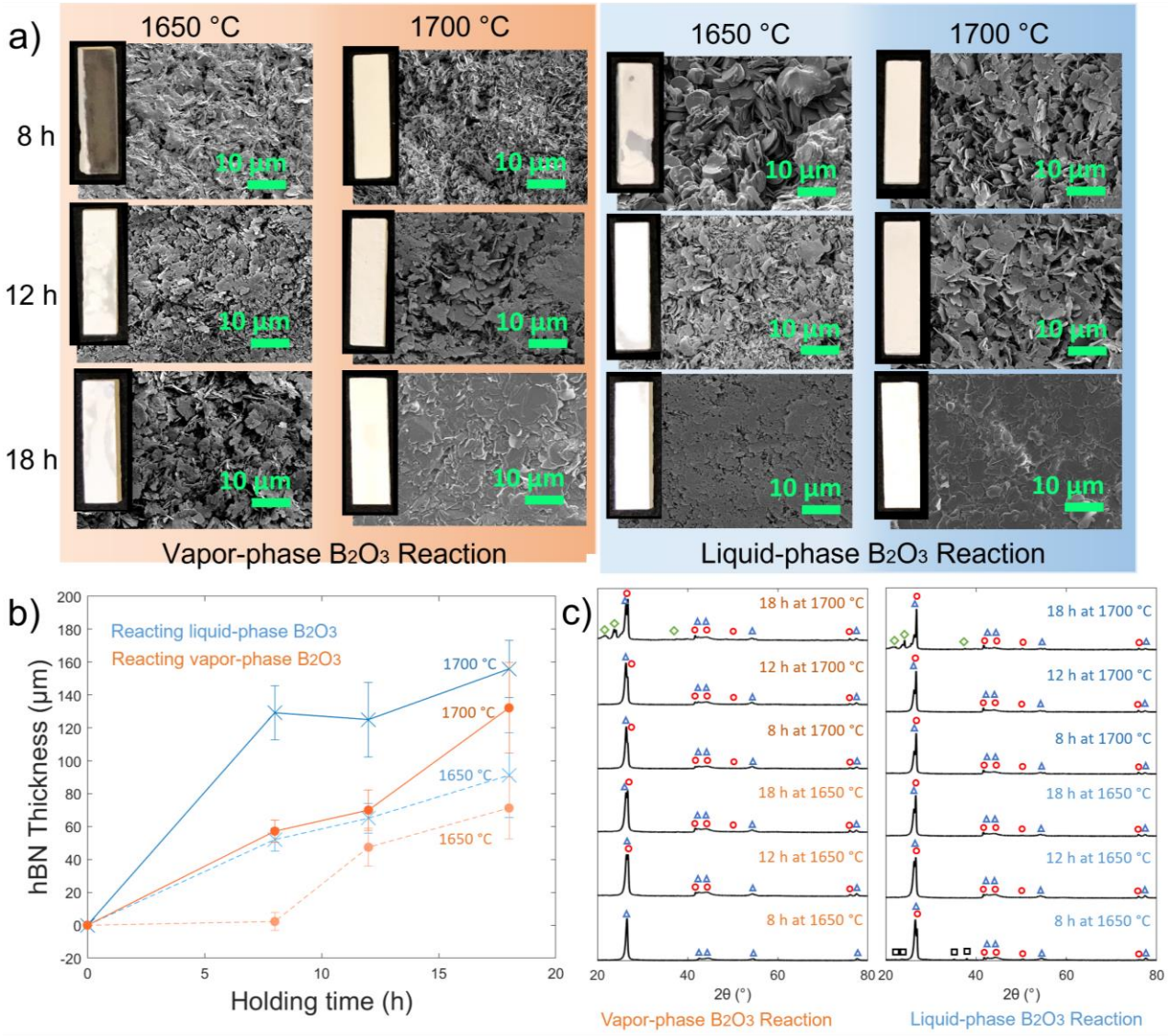

Figure 2.7. Effect of carbothermic processing conditions on bimaterial: a) Microstructure of h-BN layer of bimaterials synthesized at 1650 °C or 1700 °C, showing surface of h-BN layers that grew from vapor-phase B_2O_3 (orange) and liquid-phase B_2O_3 (blue). Insets show photographs of the surface of graphite/h-BN bimaterials. b) Thickness of h-BN layer as a function of reaction temperature and holding time, for both liquid and vapor phases of B_2O_3. c) XRD spectra of bimaterials featured in a), showing presence of h-BN (○), graphite (△), boron carbide (□) and carbon nitride (◊). Micrographs and XRD spectra of liquid-phase reactions occurring at 1650 °C for 12 h, 1700 °C for 12 h, and 1700 °C for 18 h were previously featured in Figure 2.3g. They are reincluded in this figure for comparative purposes.

For liquid-phase B_2O_3 reactions, the inset in Figure 2.7a shows that the reactions taking place at 1650 °C for 8 h result in nonuniform h-BN layers composed microscopically of coarsely stacked h-BN flakes surrounded by large amounts of unreacted B_2O_3. Figure 2.7b shows that this h-BN layer is approximately 52 ± 7 μm. Furthermore, the corresponding XRD spectrum in Figure 2.7c indicates that h-BN, graphite, and boron carbide are present in this sample. The carbide phase in the bimaterial disappears when the reaction time is increased up to 12 h and 18 h, pointing to limited nitrogen dissolution in the melt over shorter reaction times like 8 h. Prolonging the reaction time also thickens the h-BN layers up to 92 ± 26 μm. We also see that increasing the reaction temperature to 1700 °C results in h-BN layers that are considerably thicker, up to 156 ± 18 μm, which do not contain boron carbide. The densest and thickest h-BN layers studied were synthesized at 1700 °C over 18 h.

As illustrated in Figure 2.7b, the main difference between h-BN layers formed from liquid-phase and vapor-phase B_2O_3 is the thickness of the layer. However, it is important to note that, with a careful control of the carbothermic reaction time and temperature, a range of different h-BN layer thicknesses and microstructures can be achieved, regardless of the reacting phase of B_2O_3. From the perspective of scaling-up the carbothermic reaction to produce larger and more complex bimaterial samples, the vapor-phase process is particularly attractive as it can convert surfaces that are not directly in contact with a precursor melt.

2.3.3 Graphite/h-BN Bimaterial Interfaces

2.3.3.1 Diffusion Profiles at the Interface

Diffusion profiles, calculated by analyzing the cross-sections of samples through SEM-EDS, can illuminate the chemical composition of the graphite/h-BN interface. Predominantly, the diffusion of B-species into graphite and C-species into the h-BN layer were examined. Figure 2.8 summarizes the profiles of bimaterials synthesized from both liquid-phase and vapor-phase B_2O_3, with close-ups of the figure provided in Appendix A.

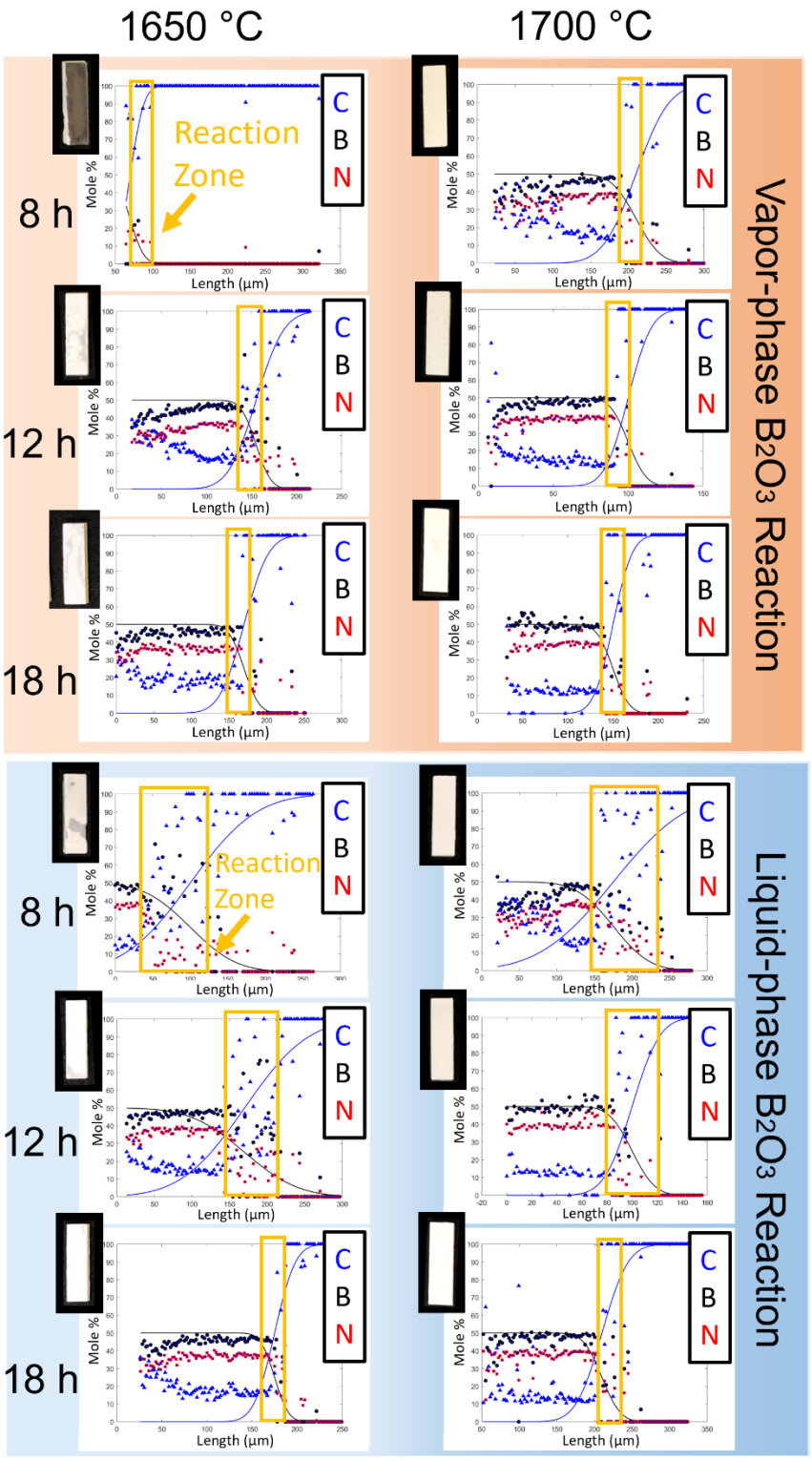

Figure 2.8. Diffusion profile showing elemental composition (mole %) of the interface for both vapor-phase B_2O_3 (orange) and liquid-phase B_2O_3 (blue) developed h-BN. Insets show photographs of the surface of graphite/h-BN bimaterials.

The size of the interfacial region varies greatly depending on the reacting phase of B_2O_3 in Eqn. 2.1. Bimaterials synthesized from vapor-phase B_2O_3 have narrow interfacial regions that can be up to 45 µm thick. Irrespective of the reaction temperature and time, the size of the interface remains consistent throughout all samples. With vapor-phase B_2O_3, the vapors condense onto the exposed graphite surfaces and react with them as shown in Eqn. 2.1, producing h-BN layers that are slightly thinner than those produced in liquid-phase oxide reactions, with a much smoother interface.

In contrast, bimaterials synthesized from liquid-phase B_2O_3 have interfacial regions as large as 100 µm thick. The diffuse interface seen in these bimaterials is likely due to the highly concentrated liquid-phase B_2O_3 penetrating the graphite body. The most dispersed interface is seen when the reaction is carried out for 8 h at 1650 °C, which shows evidence of boron carbide formation in this sample, as was previously seen with X-ray spectra (Figure 2.7c) and supported by the SEM-EDS map in Figure 2.2b. As the temperature and reaction time increase, the size of the interfacial region decreases significantly; the interface between the layers becomes better defined as Eqn. 2.1 progresses.

Our observations on the position of the reaction zone front are supported by calculated effective diffusivity constants, D_{eff}, which were estimated based on the profiles shown in Figure 2.8, using Eqn. 2.9

$$\frac{c(x)}{c_0} = \frac{1}{2}\left[1 + erf\left(\frac{x}{\sqrt{4D_{eff}t}}\right)\right] \tag{2.9}$$

where $\frac{c(x)}{c_0}$ is the relative concentration of each diffusive species (both C and B) over a distance x for a given time *t*. The effective diffusivities for bimaterials produced from liquid-phase B_2O_3 at 1650 °C and 1700 °C are on the order of $1 \times 10^{-10}\ \frac{cm^2}{s}$. In contrast, bimaterials synthesized from vapor-phase B_2O_3 have effective diffusivities on the order of $1 \times 10^{-11}\ \frac{cm^2}{s}$.

2.3.3.2 Boron Carbide Formation at the Interface

Our studies have indicated that boron carbide initially develops within the bimaterial as a result of Eqn. 2.2, in the absence of nitrogen. To confirm this, the carbothermic reaction

was carried out at 1600 °C for 12 h in an argon atmosphere, using the same set-up as described in Section 2. The X-ray diffraction patterns in Figure 2.9a detail the results of this experiment, showing that bimaterials synthesized in argon are composed of graphite and boron carbide, supportive of the reaction described by Eqn. 2.2. In contrast, when the same reaction is carried out in nitrogen, h-BN is identified along with boron carbide and graphite, consistent with both Eqns. 2.1 and 2.2. The identified boron carbide in the latter likely formed in regions inaccessible to nitrogen gas, such as that below the h-BN layer near the interface with graphite.

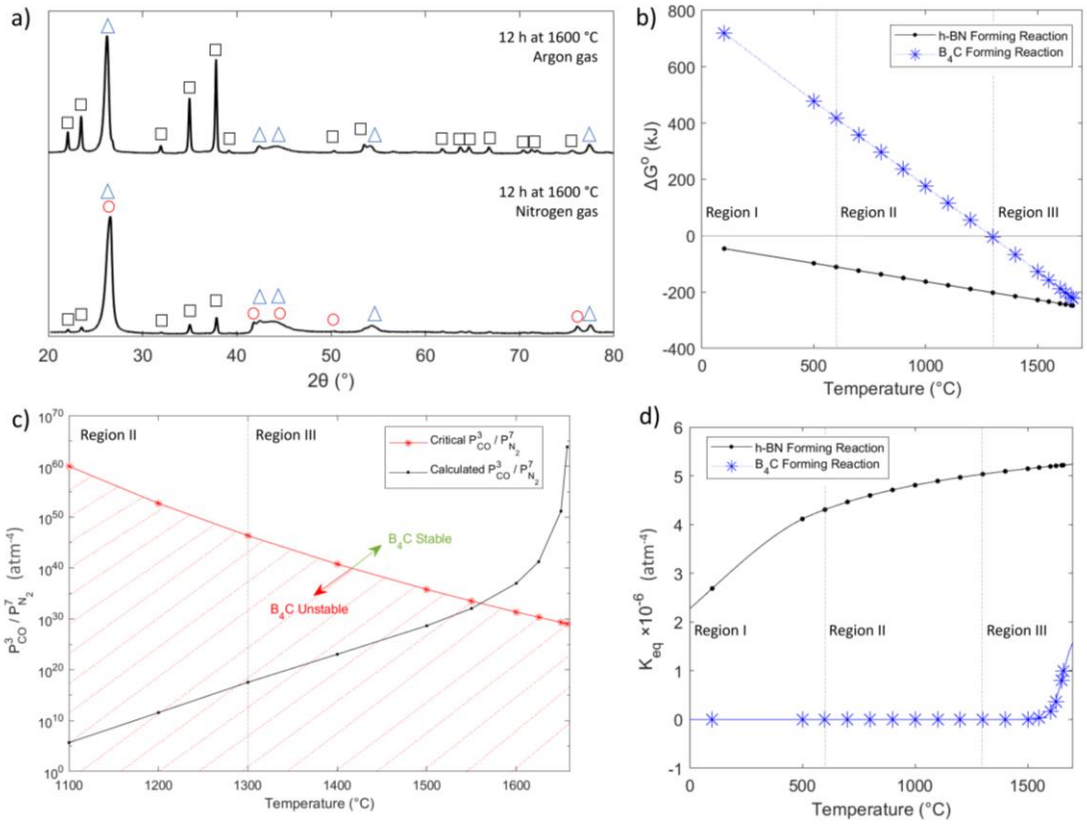

Figure 2.9. Boron carbide formation: a) XRD patterns of bimaterials synthesized under the same temperature profiles in both flowing argon and nitrogen gas, demonstrating the formation of boron carbide in the absence of nitrogen, showing presence of BN (○), graphite (△), and boron carbide (□) under nitrogen flow. b) Gibbs free energy change as a function of temperature for Eqns. 2.1 and 2.2, c) Plot showing critical ratio needed for Eqn. 2.10 to take place alongside calculated data from the system described in Figure 2.5a, d) Equilibrium constants as a function of temperature for Eqns. 2.1 and 2.2.

Figure 2.9b shows the Gibbs free energy change as a function of temperature for Eqns. 2.1 and 2.2, showing that it is energetically favorable for Eqn. 2.1 to take place over Eqn. 2.2. In fact, unlike the h-BN forming carbothermic reaction, the boron carbide forming reaction requires temperatures higher than 1300 °C to occur spontaneously. Figure 2.9d shows the equilibrium constant for Eqns. 2.1 and 2.2 as a function of time, and interestingly suggests that the carbide in Eqn. 2.2 is most likely to form at temperatures greater than 1550 °C.

The stability of boron carbide and its role in the h-BN-forming carbothermic reaction has been discussed previously [12,13]. It is widely concluded that the carbide is a product of Eqn. 2.2, and that it can act as an intermediate phase in the production of h-BN. However, the stability of boron carbide and its ability to convert into h-BN depends on the relative ratio of P_{CO} to P_{N_2}. The conversion of boron carbide into h-BN can be described by:

$$3B_4C_{(s)} + B_2O_{3(l)} + 7N_{2(g)} \rightarrow 14BN_{(s)} + 3CO_{(g)} \qquad (2.10)$$

The standard Gibbs Free Energy change in Joules for Eqn. 2.10 was calculated to be $\Delta G^o_{(10)} = -2{,}820{,}000 - (-906 \times T)$ using thermochemical data from Chase [22].

Thus, we can use the equilibrium constant of Eqn. 2.10 to determine the critical ratio, $\left(\frac{{P_{CO}}^3}{{P_{N_2}}^7}\right)_{crit}$, needed for the reaction to occur. For a given temperature, if $\frac{{P_{CO}}^3}{{P_{N_2}}^7} < \left(\frac{{P_{CO}}^3}{{P_{N_2}}^7}\right)_{crit}$ then boron carbide is unstable, and Eqn. 2.10 can proceed. In contrast, if $\frac{{P_{CO}}^3}{{P_{N_2}}^7} > \left(\frac{{P_{CO}}^3}{{P_{N_2}}^7}\right)_{crit}$, boron carbide is stable and will not convert to h-BN. Figure 2.9c illustrates how the critical ratio changes with temperature and compares it to the calculated ratio from the closed system described in Figure 2.5a. The two plots intersect just over 1550 °C, suggesting that boron carbide synthesized at 1600 °C or higher is energetically stable, and will not convert to h-BN. This is supported by Figure 2.9d, which shows that the carbothermic formation of boron carbide readily occurs at temperatures greater than 1550 °C.

Given the stability of the carbide phase under the conditions described, a crucial way to avoid boron carbide from forming in the bimaterial is to ensure that enough nitrogen is accessible to facilitate Eqn. 2.1, or alternatively Eqn. 2.10, both in the liquid-phase and vapor-phase reactions. One solution is to choose a high synthesis temperature, like 1700 °C, and a high holding time, like 18 h, to ensure that sufficient nitrogen can dissolve into the B_2O_3 melt (Figure 2.6), and to maximize the amount of vapor-phase B_2O_3 in the crucible (Figure 2.5a). Rationally, our experimental set-up (described in Materials & Methods) differs from the closed system described in Figure 2.5, since a constant stream of N_2 gas flows into the system throughout the bimaterial synthesis. This replenishment of N_2 throughout the carbothermic reaction should also help minimize boron carbide formation.

2.3.3.3 Interfacial Fracture Toughness

To quantify the adhesion of the h-BN layer on the graphite body, and further probe the properties at the interface of the bimaterial, single-edge-notch beam (SENB) tests were carried out to measure the interfacial fracture toughness. This technique was preferred over other methods involving indentation due to the lubricating, plate-like nature of h-BN and graphite, which densify upon indentation and do not reveal clean indents. Figure 2.1 and Figure 2.10a illustrate the SENB test set-up. Fracture toughness, K_{Ic}, is calculated using Eqn. 2.11 [23,24].

$$K_{Ic} = \frac{3Pe\sqrt{a}}{db^2}\left[1.99 - 2.47\left(\frac{a}{b}\right) + 12.97\left(\frac{a}{b}\right)^2 - 23.17\left(\frac{a}{b}\right)^3 + 24.80\left(\frac{a}{b}\right)^4\right] \qquad (2.11)$$

where P is the load to failure, a is the precrack length, b is the height of the beam, d is the width, and e is fixed at 10 mm for this configuration, with requirements for the beam dimensions shown in Eqns. 2.12 to 2.16.

$$\frac{s-2e}{b} > 2 \tag{2.12}$$

$$\frac{s}{b} \geq 2 \tag{2.13}$$

$$l \geq 4.2b \tag{2.14}$$

$$0 < \frac{a}{b} < 0.6 \tag{2.15}$$

$$2 \leq \frac{b}{d} \leq 8 \tag{2.16}$$

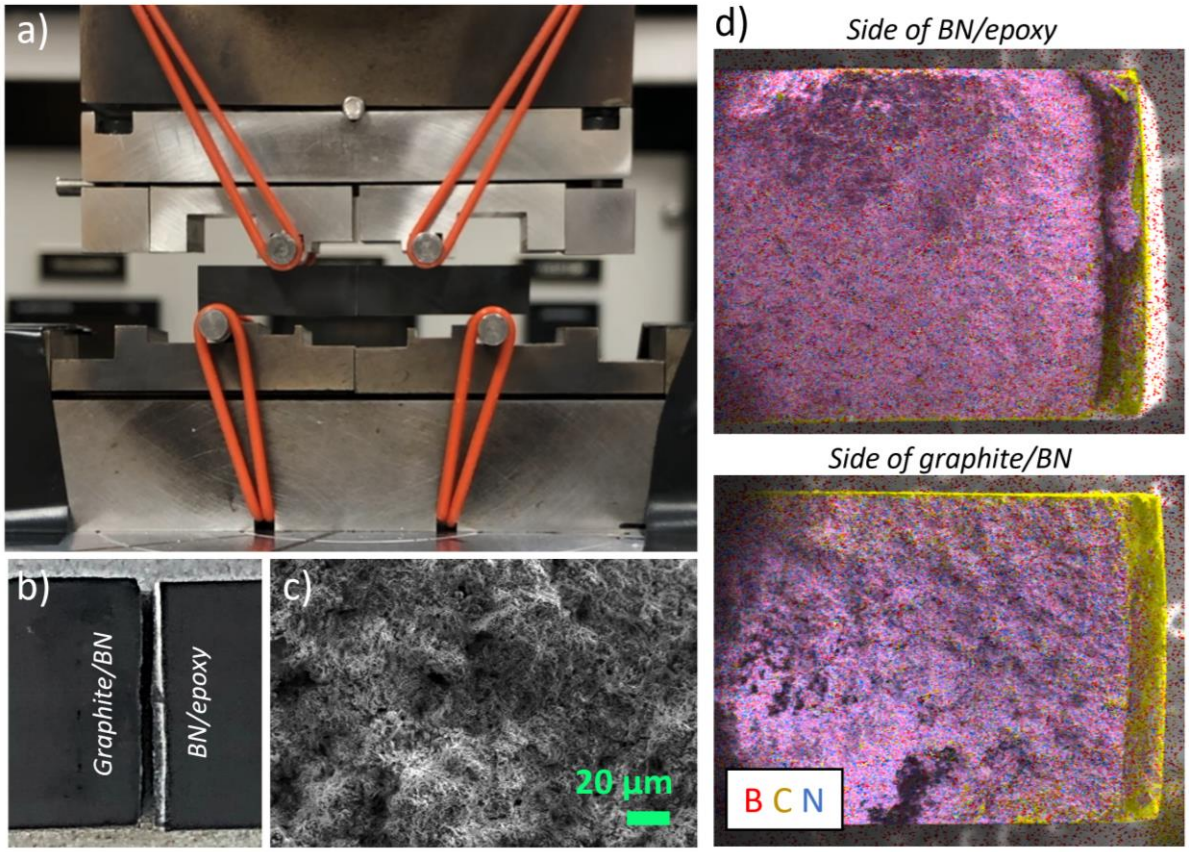

Figure 2.10. Fracture toughness measurements: a) Set-up for 4-point bending for single-edge-notched-beam (SENB) test. b) Example of failed beam, showing fracture through the h-BN layer. c) Microstructure of mode I fracture surface, illustrating the porosity of the h-BN layer. d) SEM-EDS maps of the mode I fracture surfaces, confirming that failure occurred through the porous h-BN layer.

The fracture toughness of the graphite substrate was measured to be 0.96 ± 0.07 MPa$\sqrt{m}$. The fracture toughness of a commercial grade of binderless h-BN (AX05, Saint-Gobain) was measured for comparison, and found to be 0.66 ± 0.10 MPa$\sqrt{m}$. The fracture toughness of the porous h-BN layer synthesized at 1600 °C for 12 h (shown in Figure 2.3c) was measured to be 0.12 ± 0.06 MPa$\sqrt{m}$. The following measurements are for samples synthesized at 1700 °C for 18 h.

Fracture toughness of bimaterials derived from both liquid-phase and vapor-phase B_2O_3 synthesized at 1700°C for 18 h were found to be lower than that of pure binderless h-BN. It was found that the average interfacial fracture toughness for bimaterials synthesized from liquid-phase B_2O_3 was 0.42 ± 0.14 MPa$\sqrt{m}$, statistically similar to samples synthesized from vapor-phase B_2O_3 which was 0.39 ± 0.09 MPa$\sqrt{m}$.

Figure 2.10b-d shows examples of the fracture toughness test results for liquid-phase grown graphite/h-BN bimaterials (1700 °C over 18 hours), demonstrating that the material failed within the h-BN layer, as was the case with all samples. The microstructure in Figure 2.10c reveals porosity within the h-BN layer, where pores approximating 20 μm in size could have emerged from trapped CO as a consequence of Eqn. 2.1. Although increasing the temperature and holding time of the carbothermic reaction appeared to densify the h-BN layer at the surface, seen in Figures 2.3 and 2.7, it did not fully densify the structure internally, resulting in internal pores that facilitated crack deflection. An observation related to the internal pores is that positioning the precrack closer to the h-BN layer resulted in a fracture toughness of 0.28 ± 0.02 MPa$\sqrt{m}$, while having a precrack closer to the uneven interface with graphite resulted in a fracture toughness of 0.53 ± 0.05 MPa$\sqrt{m}$. This may suggest that the microstructure and porosity may not be uniform through the thickness of the h-BN layer, and that methods to rid the system of internal porosity should be a focus of subsequent research.

Relative to graphite, the low toughness of the h-BN layer ensures that the bimaterial will always fail within the outer layer, and that we see no evidence for a preferred deflection path towards the interface. The results suggest that the interface toughness is greater than

that of the h-BN, such that the graphite body will remain protected by a layer of h-BN and continue functioning as a bimaterial.

2.4 Summary

To create graphite/h-BN bimaterials, a carbothermal synthesis process was developed where the bimaterials consist of graphite bodies covered by an exterior ceramic layer of h-BN. The surface of the graphite substrate is converted to h-BN during the high-temperature carbothermic reduction of B_2O_3 into h-BN within nitrogen environments. This results in a h-BN layer up to 156 ± 18 µm thick, of varied microstructure depending on the reaction temperature and holding time, shedding light into the processing-microstructure relationship of this synthesis method. Densification was improved by increasing the reaction temperature to 1700 °C, and by increasing the holding time to 18 h.

The phase of the reacting B_2O_3 was found to play a role in the growth and thickness of the h-BN layer, with liquid-phase B_2O_3 producing the thickest layers and roughest interfaces compared to vapor-phase B_2O_3. Differences between the two phases were mainly due to relative concentrations of B_2O_3 and N_2, as determined by the partial pressures of the reacting vapors and the dissolution of N_2 into the B_2O_3 melt. Notably, the effectiveness of the vapor-phase at converting graphite surfaces is a promising result for scaling-up the reaction to produce larger sized and complex-shaped bimaterials.

The interface of the bimaterial was studied in detail. An alternate carbothermic reaction was shown to take place in the absence of nitrogen, producing boron carbide from the carbothermal reduction of B_2O_3. Thermochemical analysis showed that the h-BN forming reaction is energetically more favorable than the boron carbide forming reaction. Nevertheless, our studies showed that the stability of boron carbide relies on the equilibrium partial pressures of CO and N_2, as well as the temperature of the reaction. To avoid the formation of boron carbide in the bimaterials, it was found that increasing the reaction temperature to 1700 °C maximized the dissolution of N_2 into the melt and promoted h-BN production.

The mechanical properties of the bimaterial remained constant regardless of the reacting phase of B_2O_3. The interfacial fracture toughness showed no statistical difference between bimaterials developed from vapor-phase or liquid-phase B_2O_3, with the bimaterial failing repeatedly within the h-BN layer. Internal pores promoted fracture through the outer h-BN layer, avoiding crack deflection toward the interface, which points to a promising adhesion between h-BN and graphite.

Compared to bulk h-BN, the graphite-bodied h-BN bimaterial is more economic to process for industrial applications, while still retaining the properties of h-BN at the surface. In particular, the design of the layered bimaterial ensures that fracture will occur through the h-BN layer, while protecting the bulk material structure and its interface with h-BN. This is a principal finding, given that bulk h-BN is notoriously brittle, while the bimaterial in comparison is protected by the graphite/h-BN interface. Overall, by understanding the underlying thermochemistry and kinetics of the governing reactions, it is possible to optimize the conditions of the carbothermal synthesis for the desired bimaterial to produce tailored h-BN layer thicknesses, microstructures, and interfacial properties.

References

[1] N. Jacobson, S. Farmer, A. Moore, H. Sayir, High-temperature oxidation of boron nitride: i, monolithic boron nitride, Journal of the American Ceramic Society. 82 (2004) 393–398. https://doi.org/10.1111/j.1551-2916.1999.tb20075.x.

[2] V.L. Solozhenko, V.Z. Turkevich, W.B. Holzapfel, Refined phase diagram of boron nitride, The Journal of Physical Chemistry B. 103 (1999) 2903–2905. https://doi.org/10.1021/jp984682c.

[3] M. Hubáček, M. Ueki, T. Sato, V. Brožek, High-temperature behaviour of hexagonal boron nitride, Thermochimica Acta. 282–283 (1996) 359–367. https://doi.org/10.1016/0040-6031(96)02884-5.

[4] Z. Zhang, X. Duan, B. Qiu, Z. Yang, D. Cai, P. He, D. Jia, Y. Zhou, Preparation and anisotropic properties of textured structural ceramics: A review, Journal of Advanced Ceramics. 8 (2019) 289–332. https://doi.org/10.1007/s40145-019-0325-5.

[5] T.E. O'Connor, Synthesis of boron nitride, Journal of the American Chemical Society. 84 (1962) 1753–1754. https://doi.org/10.1021/ja00868a065.

[6] J. Thomas, N.E. Weston, T.E. O'Connor, Turbostratic boron nitride, thermal transformation to ordered-layer-lattice boron nitride, Journal of the American Chemical Society. 84 (1962) 4619–4622. https://doi.org/10.1021/ja00883a001.

[7] E. Medvedovski, Preparation of boron nitride-based coatings through thermal diffusion process, Advances in Applied Ceramics. 117 (2018) 221–230. https://doi.org/10.1080/17436753.2017.1397938.

[8] M. Hubáček, M. Ueki, Chemical reactions in hexagonal boron nitride system, Journal of Solid State Chemistry. 123 (1996) 215–222. https://doi.org/10.1006/jssc.1996.0171.

[9] A.A. Mashnitskii, T.V. Andreeva, T.V. Dubovik, High-temperature graphite protective coatings, Refractories. 12 (1971) 728–730. https://doi.org/10.1007/BF01285611.

[10] T.S. Bartnitskaya, M.V. Vlasova, V.I. Lyashenko, T.I. Serebryakova, I.I. Timofeeva, T.V. Tomila, Formation of highly disperse boron nitride in carbothermal reduction in the presence of lithium compounds, Powder Metallurgy and Metal Ceramics. 32 (1993) 63–72. https://doi.org/10.1007/BF00559737.

[11] T.S. Bartnitskaya, V.I. Lyashenko, A.V. Kurdyumov, N.F. Ostrovskaya, I.G. Rogovaya, Effect of lithium on structure formation of graphite-like boron nitride with carbothermal synthesis, Powder Metallurgy and Metal Ceramics. 33 (1995) 335–340. https://doi.org/10.1007/BF00559576.

[12] A. Aydoğdu, N. Sevinç, Carbothermic formation of boron nitride, Journal of the European Ceramic Society. 23 (2003) 3153–3161. https://doi.org/10.1016/S0955-2219(03)00092-X.

[13] H.E. Çamurlu, N. Sevinç, Y. Topkaya, Role of boron carbide in carbothermic formation of hexagonal boron nitride, Journal of Materials Science. 41 (2006) 4921–4927. https://doi.org/10.1007/s10853-006-0339-6.

[14] S.N. Pikalov, Mechanism of formation of graphitelike boron nitride in the carbothermal process, Soviet Powder Metallurgy and Metal Ceramics. 27 (1988) 404–406.

[15] R.R. Hofer, S.E. Cusson, R.B. Lobbia, A.D. Gallimore, The H9 Magnetically Shielded Hall Thruster, in: 35th International Electric Propulsion Conference, IEPC-2017-232, Altanta, GA, 2017: p. 18.

[16] B.W. Sheldon, E.Y. Sun, S.R. Nutt, J.J. Brennan, Oxidation of BN-coated SiC fibers in ceramic matrix composites, Journal of the American Ceramic Society. 79 (1996) 539–543. https://doi.org/10.1111/j.1151-2916.1996.tb08163.x.

[17] E.J. Opila, R.C. Robinson, M.J. Verrilli, Borosilicate glass-induced fiber degradation of SiC/BN/SiC composites exposed in combustion environments, International Journal of Applied Ceramic Technology. 13 (2016) 434–442. https://doi.org/10.1111/ijac.12499.

[18] B. Yates, M.J. Overy, O. Pirgon, The anisotropic thermal expansion of boron nitride, The Philosophical Magazine: A Journal of Theoretical Experimental and Applied Physics. 32 (1975) 847–857. https://doi.org/10.1080/14786437508221624.

[19] L. Xiaowei, R. Jean-Charles, Y. Suyuan, Effect of temperature on graphite oxidation behavior, Nuclear Engineering and Design. 227 (2004) 273–280. https://doi.org/10.1016/j.nucengdes.2003.11.004.

[20] Z. Zhang, C. Wei, R. Liu, Y. Wu, D. Li, X. Ma, L. Liu, P. Wang, Y. Wang, Experiment and simulation analysis on thermal shock resistance of laminated

ceramics with graphite and boron nitride interfaces, Ceramics International. 47 (2021) 11973–11978. https://doi.org/10.1016/j.ceramint.2021.01.039.

[21] C.S. Chari, K.T. Faber, Oxidation resistance of AlN/BN via mullite-type $Al_{18}B_4O_{33}$, Journal of the European Ceramic Society. 42 (2022) 3437–3445. https://doi.org/10.1016/j.jeurceramsoc.2022.02.037.

[22] M.W. Chase Jr., NIST-JANAF Themochemical Tables, Fourth Edition, American Chemical Society, 1998.

[23] J. Srawley, W. Brown, Fracture toughness testing methods, in: Fracture Toughness Testing, National Aeronautics and Space Administration, 1965.

[24] G. Kleer, R. Schonholz, W. Doll, S. Sturlese, Interface crack resistance of zirconia base thermal barrier coatings, in: High Performance Ceramic Films and Coatings, 1991: pp. 329–328.

[25] L. Song, L. Ci, H. Lu, P.B. Sorokin, C. Jin, J. Ni, A.G. Kvashnin, D.G. Kvashnin, J. Lou, B.I. Yakobson, P.M. Ajayan, Large scale growth and characterization of atomic hexagonal boron nitride layers, Nano Letters. 10 (2010) 3209–3215. https://doi.org/10.1021/nl1022139.

[26] H. Park, T.K. Kim, S.W. Cho, H.S. Jang, S.I. Lee, S.-Y. Choi, Large-scale synthesis of uniform hexagonal boron nitride films by plasma-enhanced atomic layer deposition, Scientific Reports. 7 (2017) 40091. https://doi.org/10.1038/srep40091.

[27] B.D. Cullity, Elements of X-ray diffraction, Addison-Wesley Publishing Company, 1956.

[28] H. Hatta, T. Sohtome, Y. Sawada, A. Shida, High temperature crack sealant based on SiO_2-B_2O_3 for SiC coating on carbon–carbon composites, Advanced Composite Materials. 12 (2003) 93–106. https://doi.org/10.1163/156855103772658498.

[29] S.J. Yoon, A. Jha, Vapour-phase reduction and the synthesis of boron-based ceramic phases, Journal of Materials Science. 31 (1996) 2265–2277. https://doi.org/10.1007/BF01152935.

[30] S.J. Yoon, A. Jha, Vapour-phase reduction and the synthesis of boron-based ceramic phases, Journal of Materials Science. 30 (1995) 607–614. https://doi.org/10.1007/BF00356318.

[31] E.T. Turkdogan, Physical chemistry of high temperature technology, Academic Press Inc, New York, 1980.

[32] T. Wakasugi, F. Tsukihashi, N. Sano, Thermodynamics of nitrogen in B_2O_3, $B_2O_3SiO_2$, and B_2O_3CaO systems, J American Ceramic Society. 74 (1991) 1650–1653. https://doi.org/10.1111/j.1151-2916.1991.tb07154.x.

[33] T. Wakasugi, F. Tsukihashi, N. Sano, The solubilities of BN in B_2O_3 bearing melts, Journal of Non-Crystalline Solids. 135 (1991) 139–145. https://doi.org/10.1016/0022-3093(91)90414-2.

Chapter 3

EVALUATION OF GRAPHITE/HEXAGONAL BORON NITRIDE BIMATERIALS FOR ELECTRIC PROPULSION

The contents of this chapter are part of a manuscript in preparation titled "Effects of Plasma Exposure on Graphite/h-BN Bimaterials for Hall-Effect Thrusters" by C.S. Chari, B. W. McEnerney, R. R. Hofer, C. M. Marrese-Reading, R. Lobbia, J. A. Wollmershauser, E. P. Gorzkowski, and K.T. Faber. In this work, R. R. Hofer and C. M. Marrese-Reading led the initial resistivity and thermal cycle tests conducted at the Jet Propulsion Laboratory. R.R. Hofer led the H9C thruster tests carried out at the Jet Propulsion Laboratory, with the help of R. Lobbia. Additionally, B. W. McEnerney led the emissivity tests conducted at the Jet Propulsion Laboratory. All other experimental work was led by C.S. Chari, with the assistance of J. A. Wollmershauser and E. P. Gorzkowski from the Naval Research Laboratory who helped prepare samples. Faber supervised the experimental work. C.S. Chari, B. W. McEnerney, R. R. Hofer and K.T. Faber were involved in designing the work and preparing the manuscript.

3.1 Introduction

Electric spacecraft propulsion systems utilize Hall-effect thrusters to generate thrust through the acceleration of an ionized propellant, such as xenon, that can be referred to as plasma [1]. The state-of-the-art material used for thruster channels by leading space missions is hexagonal boron nitride (h-BN). It is a chemically inert high-temperature ceramic with a low dielectric constant and high electrical resistivity, which are properties required for the operation of Hall-thrusters [2]. The material is easy to fabricate and machine into complex designs, which has made it a popular insulating material in aerospace and nuclear applications [2]. Despite its attractive properties, the brittleness of bulk h-BN has caused concerns for its performance in electric propulsion.

A novel material, previously described in Chapter 2, is proposed as a candidate wall material for Hall-effect thrusters. It is a graphite/h-BN bimaterial, consisting of a structural body of graphite with a converted surface layer of h-BN, developed from the carbothermic

reaction of B_2O_3 in nitrogen. The material couples the dielectric behavior and low emissivity of h-BN with the thermal shock resistance and machinability of graphite, making it an ideal material for spacecraft propulsion. It can be synthesized from liquid-phase and vapor-phase carbothermic reactions, resulting in h-BN layers on the order of hundreds of microns in thickness. Detailed reports have been made on the synthesis and characterization of such bimaterials, however its performance during plasma exposures has yet to be evaluated. Here, we report the behavior of graphite/h-BN bimaterials in thruster environments.

The lifetime of Hall-effect thrusters is determined by the sputtering of the discharge channel walls due to ion bombardment from the propellant [2–9]. Additionally, metal atoms may also be suspended in the plume and deposit onto the channel walls, affecting the wall material properties [10]. As such, it is critical to understand how graphite/h-BN bimaterials respond to exposures from the discharge plasma to learn how they can erode over time, bearing in mind that their desired operational time is between thousands to tens of thousands of hours [2].

The present study seeks to uncover the performance of graphite/h-BN bimaterials in Hall-effect thrusters operating with xenon propellant, with samples located both on the chamber walls and directly in front of the plume. Intrinsic material properties for electric spacecraft propulsion are assessed, including emissivity and resistivity. Material erosion is evaluated by monitoring changes in surface roughness, microstructure, chemical and structural composition, as well as h-BN thickness, before and after the plasma exposures. The importance of the phase of the h-BN forming carbothermic reactions on the performance of the bimaterial is discussed in detail, comparing h-BN layers developed from liquid-phase and vapor-phase carbothermic reactions.

3.2 Materials & Methods

3.2.1 Graphite/h-BN Synthesis

Bimaterials were prepared following the high-temperature carbothermal synthesis method described in Chapter 2. Precursor powders were first prepared by mixing 9.89 g of boric

acid (H_2BO_3, Sigma Aldrich) with 0.74 g of h-BN (IDL-500, Saint-Gobain), and melting them in an Al_2O_3 crucible at 800 °C for 30 min using a high-temperature box furnace (CM Rapid Temp). The melt was then removed from the crucible and ground to particles of 1 μm in diameter or less, the latter which was determined by using a sieve to help screen the particle size. Approximately 4 g of said powders were placed inside a boron nitride crucible. Three rectangular graphite strips (G540, Tokai Carbon) were placed over the powders, where each 30 × 2 × 6 mm^3 strip weighed approximately 4.3 g. A boron nitride lid was placed over the crucible as described in Chapter 2. The lidded crucible was then placed in a high-temperature tube furnace (MTI GSL-1800X with a Eurotherm 3504 controller) with flowing nitrogen gas (UHP200, Airgas). The h-BN layers were synthesized at 1700 °C, with a holding time of 18 h at the target temperature. The temperature was calibrated for the SiC tube with a B-type thermocouple resting on an empty BN crucible with the same gas flow rate used in the experiments.

3.2.2 Testing Chamber Set-up

Bimaterial samples were mounted on a H9C thruster using two strips of Mo shields (total initial thickness of Mo was 200 μm) to secure the samples in place. Two environments were investigated, referred to as the *thruster* environment and *downstream* environment, illustrated in Figure 3.1.

The *thruster* exposed samples were mounted to the inner front pole of the thruster, between the inner diameter of the channel. The temperature of these samples was monitored using an infrared camera (FLIR 655) through a ZnSn viewport [11]. The pressure in the thruster was on the order of 1×10^{-3} torr, however the pressure experienced by the samples is thought to be lower due to plume expansion. The *downstream* exposed samples were mounted in the plume of the thruster exhaust, located 1 m from the thruster exit plane. This environment is harsher than the operative thruster environment, dominated by Xe neutrals and ions, with a pressure of 1×10^{-5} torr during thruster operation. The temperature of the downstream samples was monitored using thermocouples. The chamber has a finite pumping speed and non-zero leak rate, so it will always reach a minimum base pressure (10^{-7} torr) that balances those conditions. That base pressure is composed of air and water. It is important to note that both the *thruster* and *downstream* environments were chemically

inert, however low-levels of O_2 (from air) and H_2O are expected to be present in the chamber as a result of the base pressure.

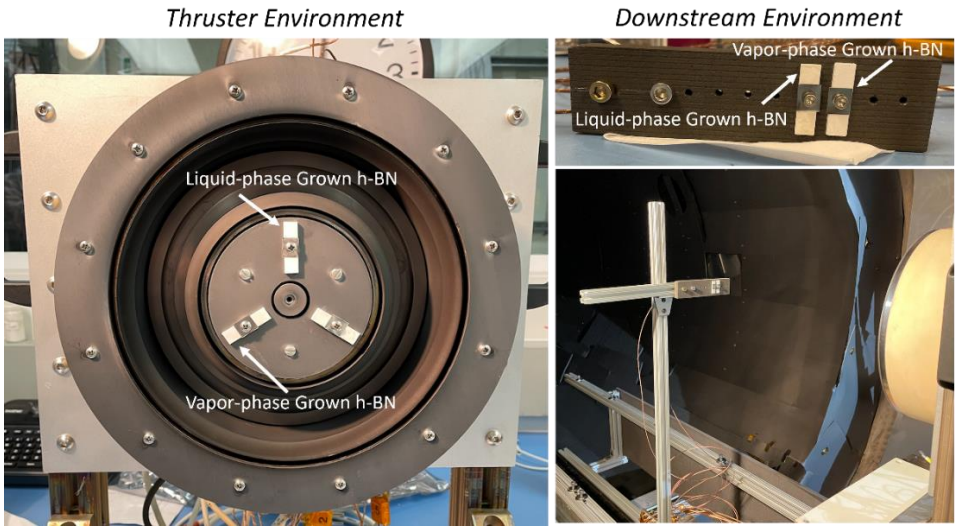

Figure 3.1. Set-up of H9C thruster and mounted samples showing thruster exposure (left) and downstream exposure (right).

Temperatures detected on *thruster* exposed samples never surpassed 267 °C, and *downstream* exposed samples never surpassed 240 °C. Nevertheless, higher effective temperatures, localized at the very surface of the bimaterial, are expected from ion bombardment. The exposed bimaterials were subject to seven cycles of increasing voltage ranging from 300 V to 500 V; exposure times are further described in Table 3.1. The total exposure time was just under 11 hours.

Table 3.1. Overview of exposure time for each chamber testing conditions.

Cycle	300 V / < 15 A	300 V / 15 A	400 V / 15 A	500 V / 15 A	Total operational time [min]
1	30	15	25	90	160
2	6	3	3	120	132
3	6	2	2	60	70
4	6	2	2	60	70
5	6	2	2	60	70
6	6	2	2	60	70
7	6	2	2	60	70

3.2.3 Characterization

Prior to the plasma exposure, the emissivity (Surface Optics ET-100) of graphite/h-BN bimaterials was evaluated. The resistivity was also assessed by sandwiching the samples between 1mm-thick Grafoil sheets and placing a stainless-steel shim stock electrode on one side using spring washers to avoid over-tightening and cracking the h-BN layer. The voltage was then ramped from 0 to 600 V and the leakage current was measured at several voltage levels. A Keithley 2470 Sourcemeter (ID5109356) was used to apply the voltage and measure the current. Vacuum thermal cycle tests were carried out by heating the samples up to 250 °C at a rate of 3.75 °C/min, holding at 250 °C for 30 min, cooling down and repeating 9 more cycles for a total of 10 cycles. After cycling, samples were inspected using an optical microscope and through scanning electron microscopy.

Oxidation tests were carried out using a high-temperature box furnace (CM Rapid Temp) in stagnant air over temperatures changing from 200 °C to 1000 °C. Samples analyzed in the oxidation tests were: bulk graphite (ZXF-5Q, POCO); bulk h-BN (AX05, Saint-Gobain); bimaterials made through the carbothermal synthesis of h-BN from graphite (POCO, ZXF-5Q) at 1600 °C for 12 h in nitrogen. After the heat treatments, the weight loss of the samples was measured using an analytical balance.

Following the plasma exposure, profilometry (Nanovea ST-400 with CL3+ MG140 optics, 1mm range, 20 μm lateral resolution, ±200 nm height accuracy) was used to evaluate the erosion of the h-BN layer. A camera was used to photograph the bimaterials on the macroscale (Nikon D7500, AF-S Micro Nikkor 40mm Lens, Nikon, Tokyo, Japan). Scanning electron microscopy and energy dispersive X-ray spectroscopy (SEM-EDS, ZEISS 1550VP FESEM, Carl Zeiss Microscopy GmbH, Jena, Germany) were used to study the microstructure and chemical composition of the bimaterials pre- and post-testing. X-ray powder diffraction (XRD, PANalytical X'Pert Pro) was used to monitor changes in the structural composition after testing. The thickness of the h-BN layers was evaluated using an optical microscope and the image-processing tool ImageJ (National Institutes of Health). On average, 15 thickness measurements were made for each sample in evenly spaced intervals, over lengths up to 6 mm. Reported values of h-BN layer thickness were

calculated using number averaging, with the error term representing one standard deviation.

3.3 Results and Discussion

3.3.1 Pre-Thruster Exposure Characterization

3.3.1.1 Emissivity

The emissivity of graphite/h-BN bimaterials was evaluated and compared to bulk h-BN. It was found that bimaterials had an emissivity of 0.829 ± 0.029, irrespective of whether the h-BN layer developed from liquid-phase B_2O_3 or vapor-phase B_2O_3. Controls of bulk h-BN had an emissivity of 0.898 ± 0.002, which was found to be comparable to our h-BN layered graphite.

3.3.1.2 Resistivity and Thermal Cycle Tests

The resistivity of the graphite/h-BN bimaterials was determined by measuring the leakage current through the h-BN layer on graphite at an applied voltage of up to 600 V. Results are summarized in Table 3.2. The resistivity of the bimaterials is comparable to that of bulk h-BN, which is reported as being > 10^{14} Ohm-cm at room temperature (AX05, Saint-Gobain) [12].

Table 3.2. Leakage current with voltage of graphite/h-BN bimaterials.

Applied Voltage (V)	Leakage Current (nA)	Resistance (Ohms)	Resistivity (Ohm-cm)
0	0.00025		
1	0.00093	1.08×10^{12}	2.50×10^{14}
10	0.0001	1.00×10^{13}	2.32×10^{15}
50	0.0015	3.33×10^{13}	7.75×10^{15}
100	0.002	5.00×10^{13}	1.16×10^{16}
200	0.0028	7.14×10^{13}	1.66×10^{16}
300	0.172	1.74×10^{12}	4.05×10^{14}
400	0.323	1.24×10^{12}	2.88×10^{14}
500	0.555	9.01×10^{11}	2.09×10^{14}
600	0.758	7.92×10^{11}	1.84×10^{14}

The graphite/h-BN bimaterials were also subject to vacuum thermal cycle tests. It was found that the bimaterial did not develop any damage from this test, as there were no signs of cracking or spallation following the repeated thermal exposures. Details are further described in Section A.5 of Appendix A.

3.3.1.3 Oxidation Resistance

The multifunctionality of graphite/h-BN bimaterials can be further analyzed by testing its oxidation behavior, to see how it behaves compared to bulk graphite and bulk h-BN. This was assessed by monitoring the weight loss of coupons exposed to different oxidative environments:

$$\text{Weight Loss (\%)} = \frac{m_0 - m_f}{m_f} \times 100 \tag{3.1}$$

where m_0 is the mass of the coupons prior to oxidation, and m_f is the mass of the coupons after.

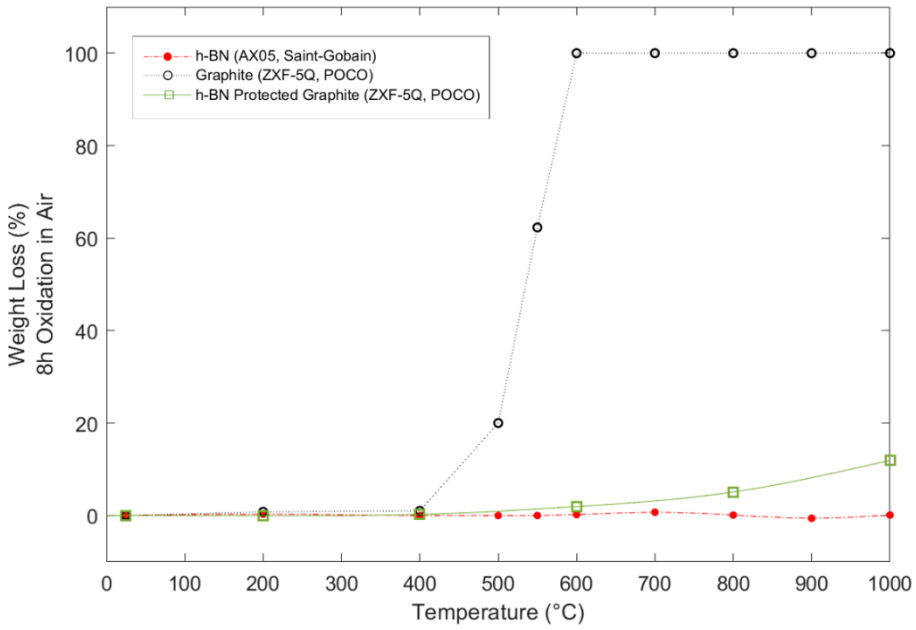

Figure 3.2. Weight loss (%) of coupons exposed to stagnant air at temperatures ranging from 200 °C to 1000 °C, showing coupons of graphite (○), h-BN (□), and graphite/h-BN bimaterials (●).

Figure 3.2 confirms that graphite is susceptible to oxidation starting at 400 °C, with samples completely oxidizing into $CO_{(g)}$ at temperatures past 600 °C. Thruster environments typically function below 600 °C in predominantly chemically inert atmospheres, although O_2 and H_2O are expected to be present in the exposure environment, which could cause candidate materials made of graphite to oxidize and volatilize. Samples of graphite protected by a layer of h-BN were subsequently studied by monitoring the oxidation resistance of graphite/h-BN bimaterials, as seen in Figure 3.2. It was found that the bimaterials were resistant to oxidation up to 600 °C, after which a measurable weight loss was observed due to the oxidation of h-BN into B_2O_3 vapor. It should be noted that the graphite bodies remained protected by h-BN layers at temperatures below 1000 °C. At 1000 °C, the graphite body became exposed due to the complete oxidation of h-BN into B_2O_3 vapor. The oxidation resistance of bulk h-BN is shown for comparison, demonstrating that the weight of h-BN coupons remains approximately constant throughout all oxidation tests carried out until 1000 °C. There is a slight weight gain visible at 800 °C due to the oxidation of h-BN into B_2O_3 liquid, which eventually evaporates as B_2O_3 vapor at 1000 °C leading to a weight loss.

Figure 3.2 shows similar oxidation behavior between bulk h-BN and graphite/h-BN bimaterials at temperatures below 600 °C, suggesting that the bimaterials can survive the working temperatures of Hall thrusters, without being affected by O_2 and H_2O in the environment. Differences between bulk h-BN and graphite/h-BN bimaterials at temperatures from 800 °C to 1000 °C are likely to due to the porosity of the nitride layer in the bimaterial. The pores facilitate the transport of O_2 into h-BN and its interface with graphite, enabling its oxidation in contrast to the much denser bulk h-BN material.

3.3.2 Performance of Liquid-Phase Produced Bimaterials

3.3.2.1 Roughness and Thickness of h-BN Layer

Surface roughness was measured using a profilometer to quantify the height difference between the virgin h-BN layer, protected by the Mo shield, and the plasma-exposed h-BN layer. It was found that the bimaterials developed from liquid-phase B_2O_3 had a step height

of 8.13 µm after being exposed to *thruster* environments, which is within flatness noise of the original surface and does not point to significant erosion. This large flatness noise, a sign of surface irregularities, is typical for liquid-phase developed bimaterials, as previously reported by in Chapter 2. In contrast, after exposures to *downstream* environments the step height measured was 48.6 µm, pointing to a significantly greater erosion rate from the plasma plume.

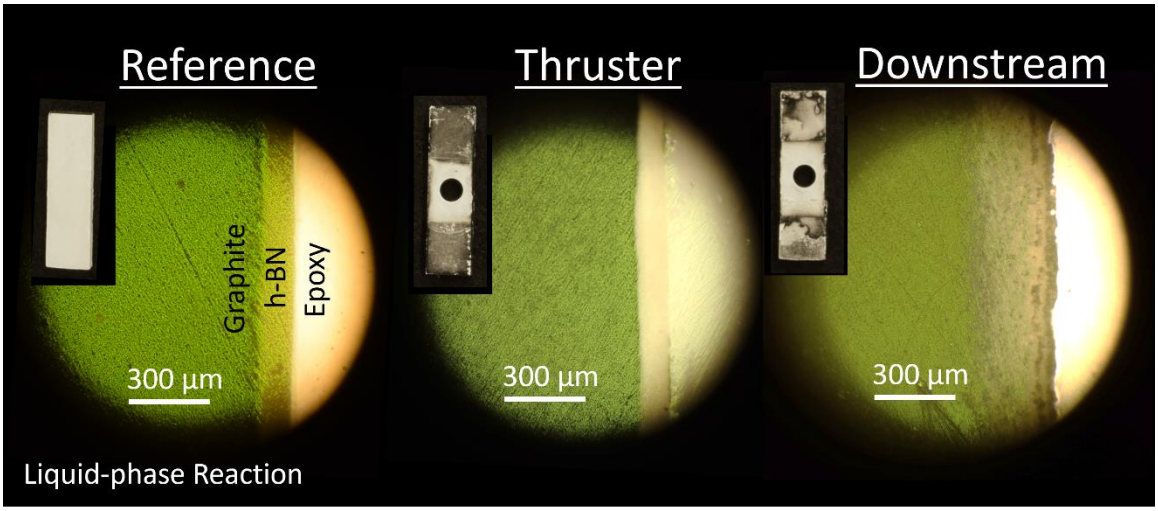

Figure 3.3. Optical microscope images of cross-sectioned samples developed from liquid-phase B_2O_3, showing: reference, sample after thruster exposure, sample after downstream exposure. Insets show photographs of bimaterial samples.

Figure 3.3 shows cross-sections of the reference and exposed samples to illustrate the similarities in the h-BN thickness of samples before and after exposure to *thruster* environments. In contrast, looking at the surface roughness of samples from *downstream* environments, the h-BN layer appears to be more porous and damaged than the pristine reference material with a diffuse interface that points to chemical changes into the h-BN layer during the exposure. This could have affected the size of the interfacial reaction zone.

Cross-sectioned samples of the bimaterials were additionally studied using energy dispersive X-ray spectroscopy to better identify the thickness changes of the h-BN layer, shown in Figure 3.4.

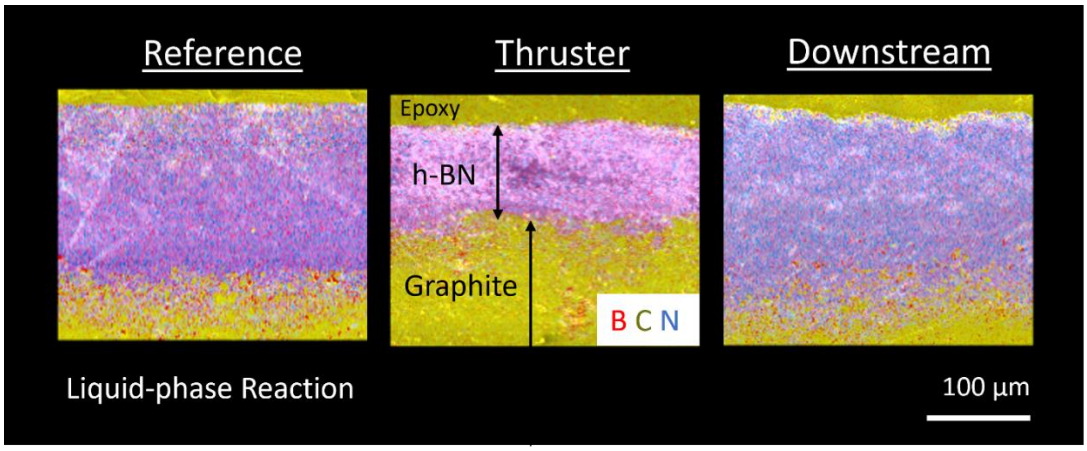

Figure 3.4. SEM-EDS maps showing elemental composition of cross-sectioned samples synthesized from liquid-phase carbothermic reaction. Maps show h-BN layer (purple) over graphite (yellow, under h-BN).

It was found that, compared to pristine reference samples, liquid-phase produced h-BN layers in *thruster* environments show a 28 ± 21 µm decrease in h-BN thickness. In *downstream* environments, the thickness of the h-BN layer increases by 108 ± 29 µm. Discrepancies between these results and the profilometry data could arise from the surface irregularities and porosities seen on the surface of such samples (Figure 3.5). The increase in h-BN thickness could be due to the exiting h-BN flakes, which remain attached to the surface as the layer is being bombarded by plasma, creating a tower-like structure that forms a thicker, yet more porous, h-BN layer.

3.3.2.2 Microstructure

The surface microstructure of the h-BN layer was studied using scanning electron microscopy, as seen in Figure 3.5. The reference sample shows the pristine h-BN surface prior to the *thruster* and *downstream* exposures. The reference microstructure is composed of densely packed h-BN flakes, with surface irregularities (visible in Figure 3.5a(i)) that are typical from liquid-phase developed bimaterials, as previously reported in Chapter 2. On a finer scale (Figure 3.5b(i)), the flat faces of the h-BN flakes appear to be oriented parallel to the surface.

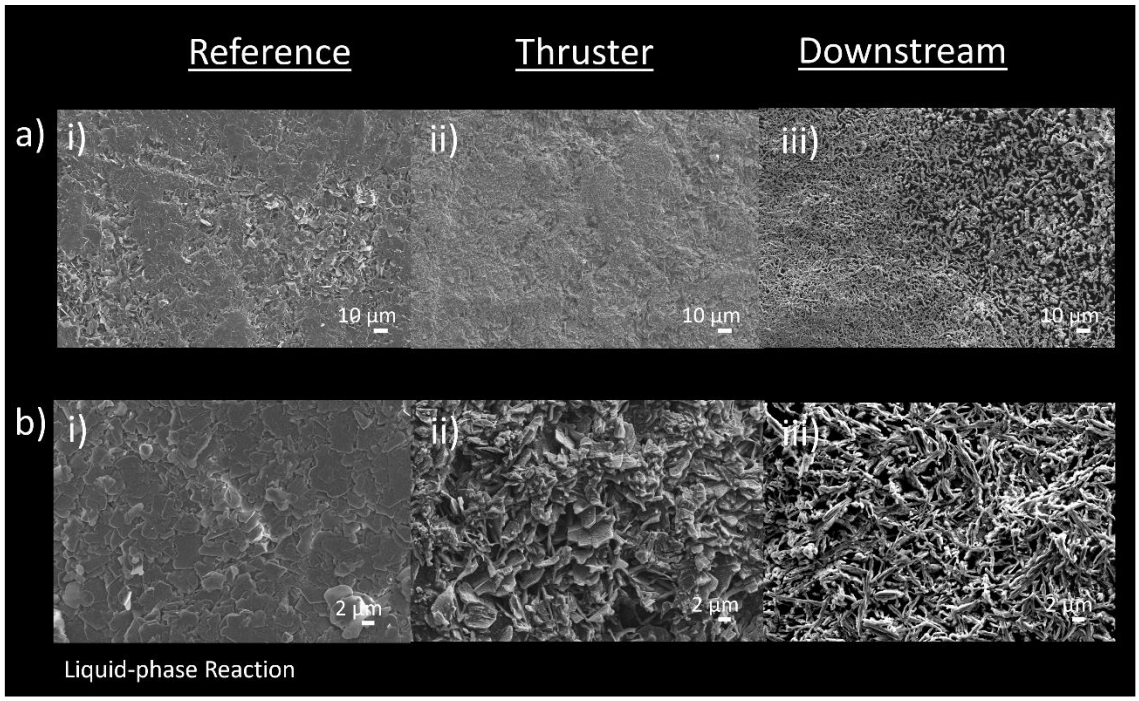

Figure 3.5. Mechanical wear of liquid-phase developed h-BN layer: a) surface microstructure of sample i) before exposure (Reference) and after ii) thruster and iii) downstream exposures; b) magnification of a).

Exposing the bimaterials to a *thruster* environment worsens the surface irregularities mentioned above (visible in Figure 3.5a(ii)). During the exposure, there is a removal of flat faces parallel to the surface, revealing randomly oriented h-BN flakes underneath (Figure 3.5b(ii)). The surface texture could have been facilitated by surface-level oxidation of the h-BN layer during the exposure (which occurs at an effective temperature of at least 1000 °C), where the liquid B_2O_3 could have further enabled the reorientation or removal of h-BN flakes. In the even harsher *downstream* environment, the surface irregularities worsen (Figure 3.5a(iii)), resulting in a porous microstructure. Within the porous framework seen in Figure 3.5b(iii), h-BN flat faces are not visible, and instead we can only see the edges of the flakes.

Starting with surface irregularities on the h-BN layer causes a ripple-effect of microstructural changes when samples are exposed to the plume. The h-BN layer experiences different erosion rates on each individual h-BN flake depending on its orientation relative to the surface. The highest erosion rate is observed when the flat faces

of the h-BN flakes are exposed (Figure 3.5b(i)), while the lowest erosion rate is seen when the edges of the flakes are exposed (Figure 3.5b(iii)). Similar observations have been reported in the literature by Garnier et al. [5,6], who noted that grains in polycrystalline samples experience local Xe ion sputtering yields that cause the grains to erode at different rates. This results in an irregular structure with depth variations, dependent on the initial orientations of the exposed grains. Given the anisotropy of h-BN flakes, it appears as if the erosion of the flake perpendicular to its basal plane is favored over the erosion of the flake parallel to its basal plane, the latter which proves to more difficult due to the higher concentration of B-N bonds in this direction, which requires high energies to break. This logic explains the morphologies seen in *downstream* environments, where only the edges (and not the flat faces) of the flakes have survived.

3.3.2.3 Chemical and Structural Composition

The chemical composition of the h-BN surface was analyzed using energy dispersive X-ray spectroscopy. Table 3.3 depicts an overview of the chemical changes that liquid-phase developed bimaterials undergo when exposed to thruster and downstream environments. Additionally, Figure 3.6 shows EDS maps of the bimaterial surface.

Table 3.3. Elemental composition (Wt.%) of surface of liquid-phase developed h-BN.

Element	Reference (Wt.%)	Thruster (Wt.%)	Downstream (Wt.%)
B	35.3	27.9	35.5
N	38.9	28.4	37.9
O	2.7	5.9	5.1
C	22.8	34	15
Mo	0	3.2	6.3
Si	0.2	0.5	0.3

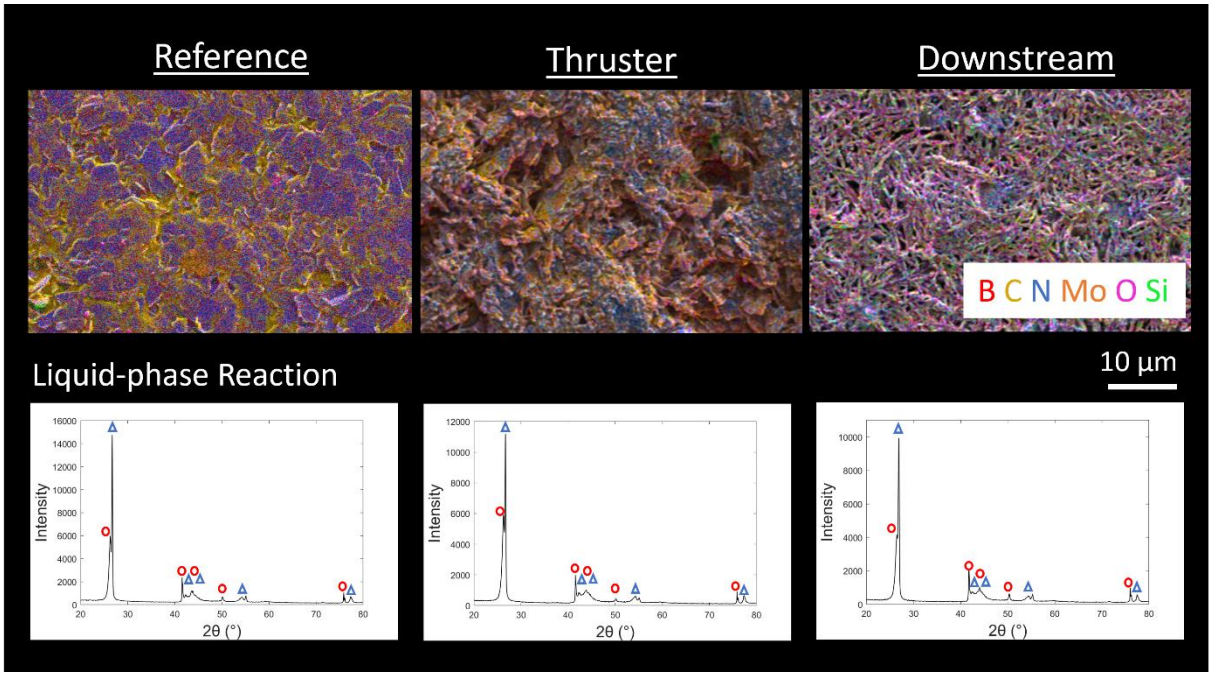

Figure 3.6. SEM-EDS maps showing elemental composition of h-BN surfaces, synthesized from liquid-phase carbothermic reactions. Corresponding XRD spectra are found below the reference (left), thruster exposed sample (middle), and downstream exposed sample (right), showing presence of h-BN (○) and graphite (△).

As expected, reference samples are largely composed of B, N, and C. Small amounts of O are typical from air contamination and local oxidation of the carbon coating used for electron imaging. Si present in the reference samples could be due to contamination during the carbothermal synthesis, which took place in a SiC tube. The EDS map in Figure 3.6 shows a significant deposition of C on the surface, indicative of the surface irregularities seen in the liquid-phase developed reference layers. The corresponding XRD spectrum indicates that the reference bimaterials are solely composed of graphite and h-BN.

Thruster and downstream samples contain varying amounts of Mo and O. Impingement from Mo originates from the Mo shields that secure the samples in place. The shields erode by 160 µm during the exposure test, and thus, Mo sputters onto the bimaterial surface, further contributing to the erosion of the bimaterial. The surface irregularities seen after the *thruster* exposures, and the open framework observed after *downstream* exposures, could facilitate the embedment of Mo into these structures. The higher detection of O in exposed samples could be due to surface-level oxidation from high-energy impacting ions.

The lower levels of O in *downstream* environments compared to *thruster* environments are likely due to the harsher plume conditions that lead to B_2O_3 volatility. XRD spectra in Figure 3.6 indicate that no new crystalline products formed during the exposures. Xe was not detected in any of the samples.

3.3.3 Performance of Vapor-Phase Produced Bimaterials

3.3.3.1 Roughness and Thickness of h-BN Layer

It was found that the bimaterials developed from vapor-phase B_2O_3 had a step height of 4.45 µm after being exposed to *thruster* environments, which is within flatness noise of the original surface. The measured flatness noise is lower than what was detected for liquid-phase grown bimaterials (~ 8.13 µm), indicating that vapor-phase grown surfaces are much smoother in comparison. After exposures to *downstream* environments the step height measured was 21.3 µm, pointing to erosion from the plasma plume. This extent of erosion is consistent with the value predicted for state-of-the-art bulk h-BN used in H9 thrusters, which is equal to 23.6 µm (for calculation please refer to Section A.6 of Appendix A). Similarities in the erosion rates suggest that the sputtering yield of the vapor-phase developed bimaterials is similar to bulk h-BN, which is 0.0208 mm^3/C at 300 V.

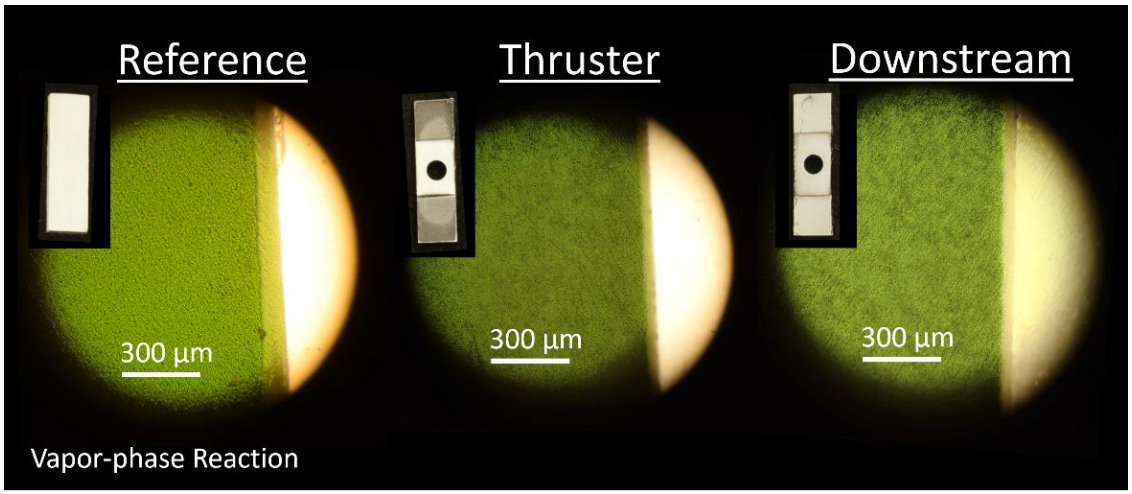

Figure 3.7. Optical microscope images of cross-sectioned samples developed from vapor-phase B_2O_3, showing: reference, sample after thruster exposure, sample after downstream exposure. Insets show photographs of bimaterial samples.

Figure 3.7 shows cross-sections of the reference and exposed samples. Through these micrographs, it is clear that the h-BN layer has eroded after being exposed to both *thruster* and *downstream* environments. The surface profiles of the layers, seen in Figure 3.7, appear to be much smoother than the liquid-phase developed bimaterials, both prior to and after the exposures. Thus, the erosion behavior observed in vapor-phase developed bimaterials is comparable to the state-of-the-art material used in H9 thrusters and is superior to that observed in liquid-phase processed bimaterials.

Cross-sectioned samples of the bimaterials were additionally studied using energy dispersive X-ray spectroscopy to better identify the thickness changes of the h-BN layer, shown in Figure 3.8. Compared to pristine reference samples, vapor-phase developed h-BN layers degrade in *thruster* environments by 68 ± 15 µm. In *downstream* environments, the h-BN layer degrades by 74 ± 16 µm compared to as-processed samples. Variations between this data and the profilometry data reported earlier could be due to surface irregularities arising from both thruster and downstream environments.

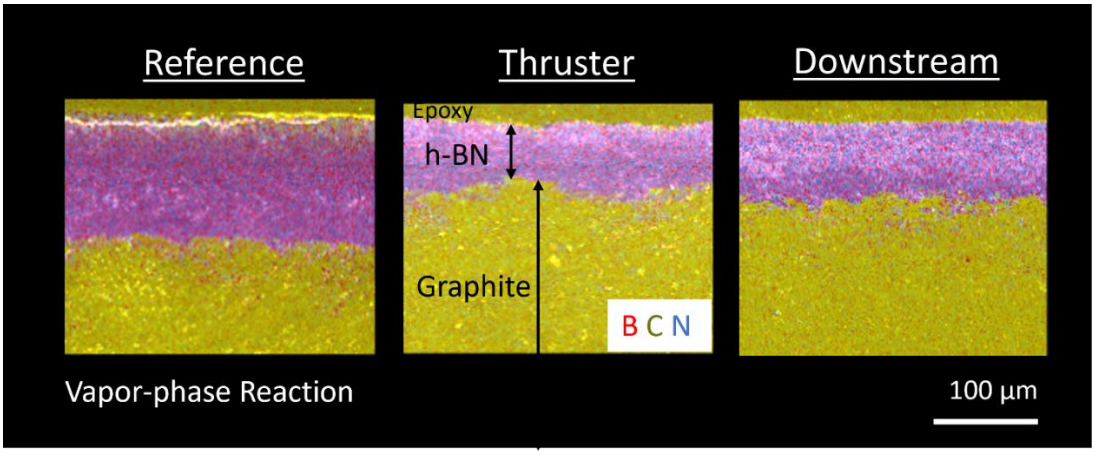

Figure 3.8. SEM-EDS maps showing elemental composition of cross-sectioned samples synthesized from vapor-phase carbothermic reaction. Maps show h-BN layer (purple) over graphite (yellow, under h-BN).

Statistically, vapor-phase developed h-BN layers exposed to *thruster* and *downstream* environments behaved with notable similarities, with the bimaterial retaining h-BN layers that are 57 ± 4 µm thick after the plasma exposures. Though thinner than the reference

material, the quality and compact structure of the h-BN flakes ensures the protection of the underlying graphite substrate, and endurance of the bimaterial in extreme environments.

3.3.3.2 Microstructure

Figure 3.9 shows the microstructures of vapor-phase developed h-BN layers. The reference sample shows the original h-BN surface prior to the thruster and downstream tests. Like in Figure 3.5a(i) and Figure 3.5b(i), the reference microstructure is composed of packed h-BN flakes. Surface irregularities are less obvious in this case than in Figure 3.5a(i), which is usual for vapor-phase developed bimaterials, as described in Chapter 2.

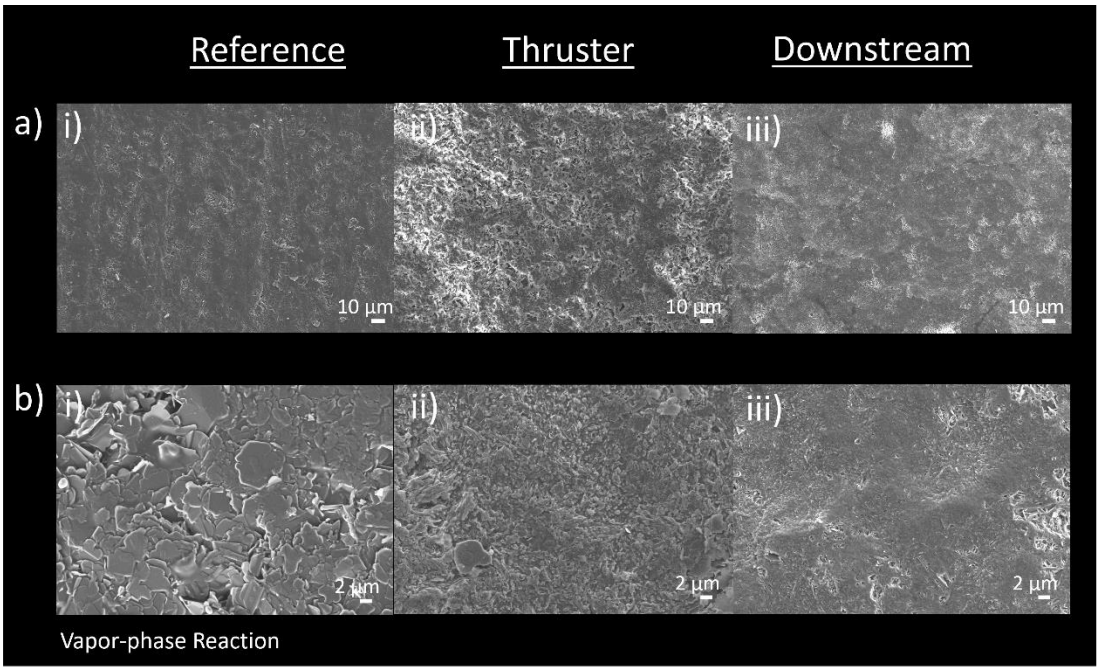

Figure 3.9. Mechanical wear of vapor-phase developed h-BN layer: a) surface microstructure of sample i) before exposure (Reference) and after ii) thruster and iii) downstream exposures; b) magnification of a).

After being exposed to a *thruster* environment, the surface appears to have eroded from the plasma, showing surface irregularities (Figure 3.9a(ii)), and partially oxidized h-BN flakes. These flakes appear to be oriented in different directions in Figure 3.9b(ii); however, a large majority are h-BN flat faces remain parallel to the surface, having not yet eroded off. Figure 3.9a(iii) shows a similar behavior in *downstream* environments, where a denser microstructure is again observed relative to Figure 3.5a(iii). Surface irregularities, in the

form of pits, are visible on the surface, however these irregularities are minimal compared to the porous morphologies seen in Figure 3.5a(iii). Having an initially smooth h-BN layer, as is produced by vapor-phase carbothermic reactions, avoids the ripple-effect issue seen in liquid-phase developed samples. Instead, the h-BN surface microstructure remains relatively unchanged during the plasma exposures, with minimal signs of mechanical wear and surface-level oxidation.

3.3.3.3 Chemical and Structural Composition

Table 3.4 describes a summary of the chemical changes that vapor-phase developed bimaterials experience when exposed to thruster and downstream environments. The accompanying Figure 3.10 shows EDS maps of the bimaterial surface.

Table 3.4. Elemental composition (Wt.%) of surface of liquid-phase developed h-BN.

Element	Reference (Wt.%)	Thruster (Wt.%)	Downstream (Wt.%)
B	42.5	31.4	41.9
N	41.6	34.0	46.4
O	1.4	3.7	2.3
C	14.2	26.6	7.0
Mo	0	3.9	2.2
Si	0.3	0.3	0.2

As before, reference samples are largely composed of B, N and C, with small amounts of O and Si from contamination. Mo and higher levels of O are detected in samples exposed to *thruster* and *downstream* environments, although these concentrations are notably lower than for liquid-phase produced h-BN (Table 3.3). This indicates that as-prepared smoother surfaces, with fewer surface irregularities, demonstrate improved resistance of the h-BN layer to Mo sputtering and surface level oxidation. Xe was not detected in any of the samples.

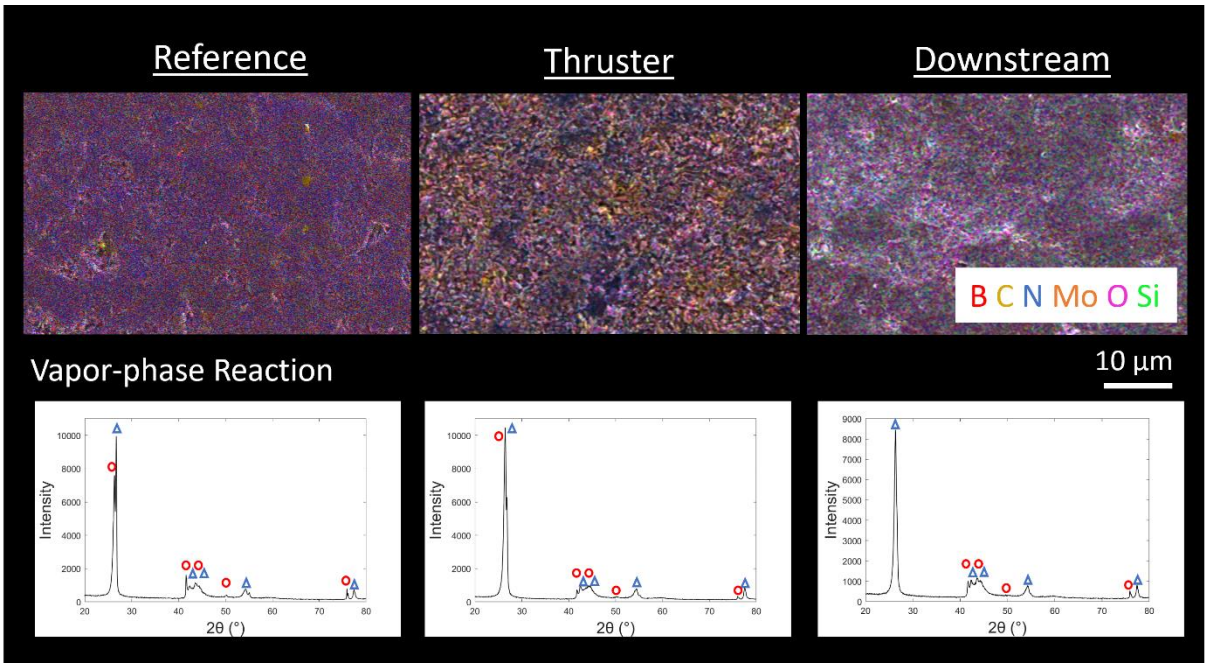

Figure 3.10. SEM-EDS maps showing elemental composition of h-BN surfaces, synthesized from vapor-phase carbothermic reaction, showing presence of h-BN (○) and graphite (△).

The corresponding XRD spectra in Figure 3.10 confirm that the composition of the bimaterial did not change after the exposures, with graphite and h-BN being the only crystalline materials detected. The decreased intensity of h-BN peaks is due to the thinning of the outer layer. Considering the denser microstructure of the h-BN layer, it is plausible to conclude that vapor-phase developed bimaterials performed better than their liquid-phase counterparts.

3.4 Summary

Graphite/h-BN bimaterials synthesized through vapor-phase carbothermic reactions performed comparatively better than bimaterials synthesized through liquid-phase carbothermic reactions. This is a consequence of the initial surface microstructure of the h-BN layer, which contains fewer surface irregularities when h-BN layers grow from the vapor-phase reactions. An abundance of surface irregularities, as seen in liquid-phase developed h-BN, results in a ripple-effect of damage to the outer layer, characterized by

variations in h-BN erosion rates due to the polycrystalline nature of the layer, which further promotes surface roughness. As a result of these surface irregularities, Mo impingement and carbon sputtering are further embedded into the h-BN layer, as noted in EDS results, resulting in a porous framework unlike the original microstructure. Such detrimental features are not visible when starting with smoother surfaces, as seen in vapor-phase developed h-BN layers, where EDS results document much lower concentrations of Mo, O and C. As such, the performance of vapor-phase grown layers is superior, with similar erosion rates to bulk h-BN with a sputtering yield of 0.0208 mm^3/C at 300 V.

These preliminary findings highlight the potential of using graphite/h-BN bimaterials as wall materials for Hall thruster chambers, specifically for bimaterials synthesized from vapor-phase carbothermic reactions.

References

[1] D.G. Zidar, J.L. Rovey, Hall-effect thruster channel surface properties investigation, Journal of Propulsion and Power. 28 (2012) 334–343. https://doi.org/10.2514/1.B34312.

[2] J.T. Yim, M.L. Falk, I.D. Boyd, Modeling low energy sputtering of hexagonal boron nitride by xenon ions, Journal of Applied Physics. 104 (2008) 123507. https://doi.org/10.1063/1.2987090.

[3] B.K. Parida, K.P. Sooraj, S. Hans, V. Pachchigar, S. Augustine, T. Remyamol, M.R. Ajith, M. Ranjan, Sputtering yield and nanopattern formation study of $BNSiO_2$ (Borosil) at elevated temperature relevance to Hall Effect Thruster, Nuclear Instruments and Methods in Physics Research Section B: Beam Interactions with Materials and Atoms. 514 (2022) 1–7. https://doi.org/10.1016/j.nimb.2022.01.001.

[4] A.J. Satonik, J.L. Rovey, G. Hilmas, Effects of plasma exposure on boron nitride ceramic insulators for hall-effect thrusters, Journal of Propulsion and Power. 30 (2014) 656–663. https://doi.org/10.2514/1.B34877.

[5] Y. Garnier, V. Viel, J.-F. Roussel, J. Bernard, Low-energy xenon ion sputtering of ceramics investigated for stationary plasma thrusters, Journal of Vacuum Science & Technology A: Vacuum, Surfaces, and Films. 17 (1999) 3246–3254. https://doi.org/10.1116/1.582050.

[6] Y. Garnier, V. Viel, J.F. Roussel, D. Pagnon, L. Magne, M. Touzeau, Investigation of xenon ion sputtering of one ceramic material used in SPT discharge chamber, in: 26th International Electric Propulsion Conference, IEPC Paper 1999-083, Kitakyushu, Japan, 1999.

[7] T. Tondu, J.P. Chardon, S. Zurbach, Sputtering yield of potential ceramics for hall effect thruster discharge channel, in: 32nd International Electric Propulsion Conference, IEPC Paper 2011-106, Wiesbaden, Germany, 2011.

[8] J.T. Yim, A survey of xenon ion sputter yield data and fits relevant to electric propulsion spacecraft integration, in: 35th International Electric Propulsion Conference, IEPC Paper 2017-060, Atlanta, Georgia, USA, 2017.

[9] M. Tartz, T. Heyn, C. Bundesmann, H. Neumann, Measuring sputter yields of ceramic materials, in: 31st International Electric Propulsion Conference, IEPC Paper 2009-240, Ann Arbor, Michigan, USA, 2009.

[10] M.W. Crofton, J.A. Young, Low energy Xe^{+} sputter yields for alumina, Hiperco 50, and boron nitride, American Institute of Physics Advances. 11 (2021) 125126. https://doi.org/10.1063/5.0067346.

[11] D.M. Goebel, R.R. Hofer, I.G. Mikellides, I. Katz, J.E. Polk, B.N. Dotson, Conducting Wall Hall Thrusters, IEEE Transactions on Plasma Science. 43 (2015) 118–126. https://doi.org/10.1109/TPS.2014.2321110.

[12] Combat (R) Boron Nitride Solids Product Data Sheet, (2022). https://www.bn.saint-gobain.com/sites/hps-mac3-cma-boron-nitride/files/2022-06/combat-bn-solids-ds.pdf (accessed July 25, 2022).

Chapter 4

ALUMINUM NITRIDE / BORON NITRIDE COMPOSITES

The contents of this chapter are also presented in "Oxidation resistance of AlN/BN via mullite-type $Al_{18}B_4O_{33}$" by C.S. Chari and K.T. Faber, which was published in the Journal of the European Ceramic Society in 2022 [1], with the exception of Section 4.6. which was carried out after publication. C.S. Chari led the experimental portion of the work. Faber supervised the experimental work. All authors were involved in designing the work and preparing the manuscript.

4.1 Introduction

Aluminum nitride/boron nitride (AlN/BN) composites are popular high-temperature ceramics, desired for their improved machinability and increased thermal shock resistance over traditional aluminum nitride (AlN). The inclusion of hexagonal boron nitride (BN) in the material lowers the toughness and compliance of the composite, making it easier to machine and thus more affordable to process. The mechanical properties and the dielectric behavior of AlN/BN composites are desirable for applications in the automotive and aerospace industries.

The presence of BN in the composite, however, poses challenges due to its oxidation into boria (B_2O_3), a highly reactive material that has reportedly created unwanted side products in other BN-bearing composites, such as SiC/BN [2]. Previous studies have explored this in depth, demonstrating how the oxidation products of SiC and BN (SiO_2 and B_2O_3, respectively) can react together in high-temperature environments over 1000 °C to form borosilicate glass, commonly found in oxidized SiC/BN/SiC ceramic-matrix composites (CMCs) [2,3]. With this in mind, it is an intuitive next step to study whether similar challenges could be expected in AlN/BN composites exposed to comparable conditions, where BN can oxidize into boria.

Boria exists as a liquid oxide at temperatures up to 1000 °C, after which its evaporation rate increases exponentially [4]. The viscosity of boria decreases with increasing

temperature, from 100 poise at 1000 °C to 40 poise at 1200 °C [5]. It is also hygroscopic; its evaporation rate intensifies in humid environments, as it is easily converted to boric acid in the presence of water [6]. Furthermore, boria is capable of reacting with other oxides, forming products that are less volatile, e.g., borosilicate and aluminum borate [4,7,8].

Earlier studies focusing on the fabrication of composites like Al_2O_3/BN [9–11], AlON/BN [12,13], AlN/B_2O_3 [14], AlN/HfB_2 [15], and AlN/TiB_2 [16], have noted that aluminum borate whiskers can form from the reaction between alumina and boria starting at temperatures of 1000 °C. Thus, we expect whiskers to also be detected in AlN/BN composites exposed to elevated temperatures in oxidizing environments. Interestingly, aluminum borate whiskers have also been used in other applications as reinforcements to enhance toughness in aluminum composites [17,18] and glass composites [19], given their low density (2.93-2.94 g/cm^3), high hardness (Mohs hardness of 7) and high Young's Modulus (400 GPa) [17,19]. Nevertheless, the role of aluminum borate whiskers and boria in the oxidation of AlN/BN composites has not been the focus of any comprehensive study.

In the current study, we explore how the presence of liquid boria alters the oxidation kinetics of AlN by comparing AlN to boria-coated AlN and AlN/BN composites. We examine how boria can provide AlN with added protection against oxidation. We also investigate the chemical composition and microstructure of the aluminum borate whiskers created in these material systems. Moreover, we shed light on how the whisker morphology evolves with exposures to high-temperature environments, and how this affects the oxidation protection of AlN as well as the flexural strength of heat-treated AlN/BN.

4.2 Materials and Methods

4.2.1 Materials and Processing

Commercially available sintered AlN and AlN/BN were used in this study. Sintered AlN bars (ST-200, Sienna Technologies) were cut into 6 mm x 8 mm x 8 mm sized coupons. ST-200 has a density of 3.3 g/cm^3 and a purity of 95%, with the remaining 5% being from the Y-rich binder. Sintered AlN/BN (Shapal Hi-M Soft, Precision Ceramics) were cut into 3 mm x 4 mm x 6 mm sized coupons. Shapal Hi-M Soft has a density of 2.88 g/cm^3, thermal expansion coefficient (from RT to 800 °C) of $5 \times 10^{-6}/°C$, and a purity just under 99%,

with trace amounts of O (0.9 wt.%), Ca (1300 ppm), C (300 ppm), Cr (<1 ppm), Mg (1 ppm), Ni (<2 ppm), Fe (8 ppm), Si (40 ppm) and Ti (20 ppm).

Boria-coated AlN was prepared by covering the topmost face of the ST-200 coupons with 0.019 ± 0.003 g/cm^2 of boric acid powder (H_3BO_3, Sigma-Aldrich) and heating the sample to 450 °C in stagnant air. H_3BO_3 powder was used instead of B_2O_3 due to the hygroscopic, volatile nature of the oxide. H_3BO_3 dehydrates into B_2O_3 at 300 °C, which then melts into a glassy film at 450 °C, below the oxidation temperature of the AlN substrate. The oxidation tests outlined in section 2.2 were carried out during the same heating cycle.

Circular discs of $Al_{18}B_4O_{33}$ were created by preparing water-based slurries of alumina powder (Al_2O_3, VWR) and boric acid powder (H_3BO_3, Sigma-Aldrich), using a molar ratio of Al_2O_3 to B_2O_3 of 1:1. The slurries were allowed to dry in custom-built aluminum molds, subsequently pressed into 2.4-2.9 mm thick discs with a diameter of 30 mm using a pneumatic press and a force of 40 kN. The green bodies were initially sintered in a high-temperature box furnace (CM Rapid Temp 1700 °C Furnace) at 1000 °C for 36 h to densify the body, and then further exposed to 1100 °C, 1200 °C or 1300 °C for 36 h to ensure the whiskers fully developed into their desired morphologies.

4.2.2 Oxidation Studies

The oxidation behavior of AlN (ST-200, Sienna Technologies) was investigated at temperatures varying from 800 °C to 1300 °C using a high-temperature box furnace (CM Rapid Temp 1700 °C Furnace) in stagnant air. The holding times at each temperature ranged from 5 h to 48 h. The heating and cooling rates were both 3 °C/min to minimize thermal shock effects. The individual experiments are further summarized in Table 4.1.

The oxidation experiments were then repeated with boria-coated AlN (ST-200, Sienna Technologies). The oxidation temperature range in this case was restricted from 1000 °C to 1300 °C, to ensure significant oxide growth while still limiting the amount of boria lost by evaporation. The holding times and ramp rates were identical to those used for the reference AlN samples.

The oxidation of AlN/BN composites (Shapal Hi-M Soft, Precision Ceramics) was studied using dry air (AI Z200, Airgas) to minimize the amount of water vapor influencing the

oxidation of BN. Studies have shown that BN can easily oxidize into boria vapor in the presence of water [20,21]. In order to investigate the interactions between liquid boria and alumina, a dry air environment with negligible amounts of water vapor (2 ppm H_2O) was chosen. The oxidation exposures studied ranged from 1200 °C to 1450 °C over 48 h or 60 h. We chose to focus on these exposure conditions because they resulted in stoichiometric amounts of both boria and alumina that were needed for aluminum borate growth.

Table 4.1. Summary of oxidation conditions for each experiment.

Materials System	Oxidation Temperature (°C)	Holding Times (h)
AlN (ST-200)	*800*	*12*
	1000	*5, 12, 24, 36, 48*
	1100	*5, 12, 24, 36, 48*
	1200	*5, 12, 24, 36, 48*
	1300	*5, 12, 24, 36, 48*
Boria-coated AlN (ST-200)	*1000*	*5, 12, 24, 36, 48*
	1100	*5, 12, 24, 36, 48*
	1200	*5, 12, 24, 36, 48*
	1300	*5, 12, 24, 36, 48*
AlN/BN (Hi-M Shapal Soft)	*1200*	*48*
	1250	*48, 60*
	1300	*48*
	1350	*48*
	1450	*48*

4.2.3 Characterization

Scanning electron microscopy and energy dispersive X-ray spectroscopy (SEM-EDS, ZEISS 1550VP FESEM, Carl Zeiss Microscopy GmbH, Jena, Germany) were used to detect the oxide layers of cross-sectioned samples, and to measure the whisker dimensions. The oxide thicknesses were measured after each exposure experiment using the image-processing tool ImageJ (National Institutes of Health). An average of 35 thickness

measurements were carried out for each sample over the length up to 800 μm, with measurements being made in evenly spaced intervals. The widths of the aluminum borate whiskers were also measured using ImageJ with an average of 100 whiskers being measured for each sample. The width was defined as the averaged thickness of the orthorhombic crystal, measured perpendicular to the direction of crystal growth. These measurements were taken near the mid-section of the whisker to avoid the narrow widths of the tips and better represent the whisker size. Note that due to the interlocking nature of the whiskers, it was not possible to determine the distribution of whisker lengths. The reported values of oxide thickness and whisker widths were determined using number averaging, with the error term representing one standard deviation.

X-ray powder diffraction (XRD, PANalytical X'Pert Pro) and transmission electron microscopy (TEM, TF-30, Tecnai) were also carried out to characterize the oxidized samples and aluminum borate crystals, respectively. Mass attenuation coefficients and penetration depths were calculated using PANalytical's HighScore Plus Software. Single crystal electron backscatter diffraction (HKL EBSD system, on the ZEISS 1550VP FESEM) was performed using a focused beam with a 70° tilted stage. The crystallographic orientation of the whiskers was determined by matching the experimental EBSD pattern with crystallographic information of $Al_{18}B_4O_{33}$ from Ihara et al. (1980) [22].

Ball-on-ring tests [23] were used to measure the effective strength of the discs. Four discs were tested for each temperature condition. In the configuration used, the radius of the circle of support points was 10.25 mm. Poisson's ratio used for alumina was 0.25 [24], while that for $Al_{18}B_4O_{33}$ was approximated as 0.25. In addition, 4-point bend tests were carried out following ASTM C1161-13 to measure the flexural strength of AlN/BN beams measuring 3 x 4 x 45 mm^3. A total of 10 specimens were measured for as-received beams, 5 for as-received and indented beams, 10 for indented beams exposed to dry air, 6 for indented beams exposed to dry argon. The cross-head rates for both mechanical tests were 0.5 mm/min. Note that dry argon (AR UHP200, Airgas) was chosen for the inert high-temperature exposure, which contained 1 ppm O_2 and 1 ppm H_2O.

4.3 Results and Discussion

4.3.1 Influence of Boria on the Oxidation of Aluminum Nitride

4.3.1.1 Oxidation of Aluminum Nitride

The oxidation kinetics of AlN were studied by tracking the growth of the Al_2O_3 layer as a function of time. This was achieved by measuring the thickness of the oxide layer of each experiment outlined in Table 4.1. Figure 4.1a illustrates the oxidation kinetics of AlN within the temperature range 1000 °C to 1300 °C.

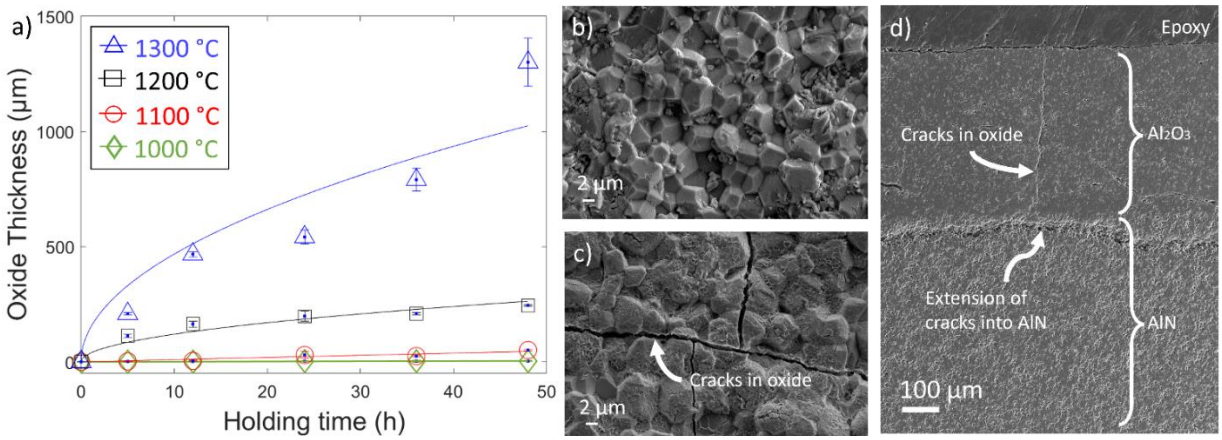

Figure 4.1. AlN oxidation: a) Oxide thickness of AlN versus holding times for oxidation exposures at 1000 °C, 1100 °C, 1200 °C, and 1300 °C. Scanning electron micrograph image of b) as-received AlN surface, c) oxidized AlN surface and d) oxidized AlN cross-section, following exposures to 1300 °C in air for 12 h.

The results and best fits displayed in Figure 4.1a suggest that the oxidation of AlN behaves linearly at 1000 °C and 1100 °C. This indicates that the growth rates of the oxide layer at these temperatures are constant and completely controlled by Reaction 4.1.

$$4AlN + 3O_2 \rightarrow 2Al_2O_3 + 2N_2 \qquad (4.1)$$

At higher temperatures, the results and best fits shown in Figure 4.1a imply that the oxidation behavior of AlN is parabolic at 1200 °C and 1300 °C. This suggests that the oxide layers formed at these temperatures are sufficiently thick to act as physical barriers that restrict oxygen diffusion to AlN. In parabolic oxidation, the rate of oxidation is no

longer controlled by Reaction 4.1, but instead is influenced by the diffusivity of oxygen into the bulk. More details of this behavior can be found in Appendix B.

The oxidation of AlN into Al_2O_3 has been examined in the past, and is shown to depend greatly on the properties of the starting material, such as the grain size, porosity and impurity content of the reported AlN [25–30]. The surface microstructure of the as-received AlN is shown in Figure 4.1b. In high-temperature environments over 800 °C, AlN can oxidize into Al_2O_3 with the evolution of nitrogen gas, as seen in Reaction 4.1. Previous studies have demonstrated that the evolving nitrogen gas creates pores within the oxide layer [25,28,29], facilitating paths for oxygen diffusion into the substrate. There is a significant difference between the coefficients of thermal expansion (CTE) of Al_2O_3 (9×10^{-6} /°C) and AlN (5×10^{-6} /°C), which results in a large thermal mismatch between the two layers on cooling from the oxidation temperature [26]. This can cause cracks to form in the porous Al_2O_3 layer, which can extend through its thickness as seen in Figure 4.1c,d. The appearance of cracks, in addition to pores, assists the transport of oxygen to AlN, allowing for continued and rapid oxidation with increasing temperature and exposure time.

4.3.1.2 Oxidation of Boria-coated Aluminum Nitride

In Figure 4.2a-d, we compare the oxidation of AlN with that of boria-coated AlN. At 1000 °C, seen in Figure 4.2a, the measured oxide thickness of boria-coated AlN is greater than the thicknesses measured for AlN at the same temperature due to the inclusion of boria as a coating in the former. The added liquid oxide increases the overall thickness of the oxide layer, which remains constant at 6 ± 2 μm for all holding times. The constant thickness reflects the low evaporation rate of boria at 1000 °C [4]. At 1100 °C, seen in Figure 4.2b, the oxide thicknesses for boria-coated AlN remains constant at 10 ± 2 μm for all the holding times, indicating that the low evaporation rate of boria is maintained at this temperature [4].

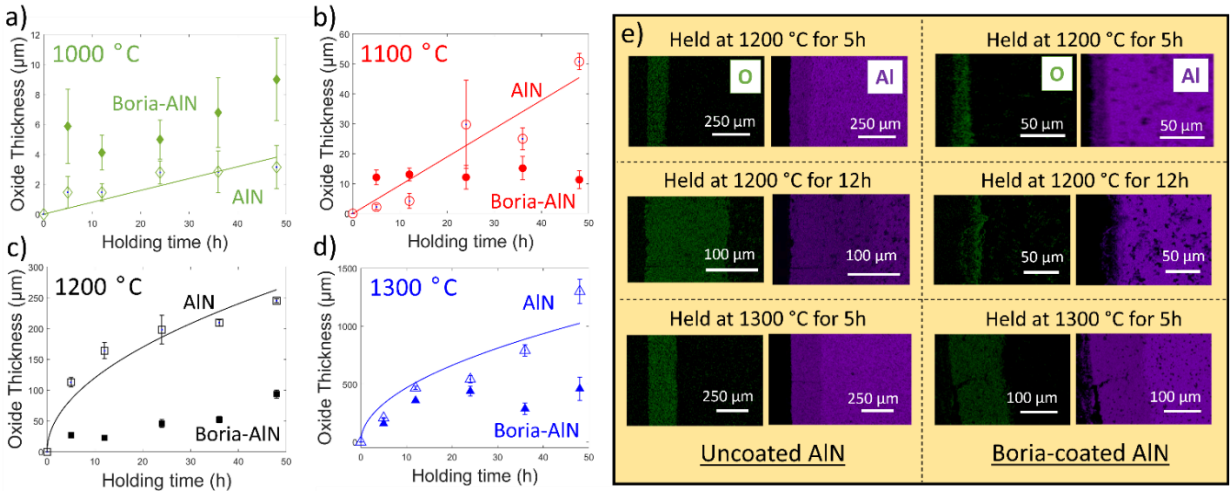

Figure 4.2. Oxide thickness of AlN (empty markers) and boria-coated AlN (filled markers) versus holding times for oxidation exposures at a) 1000 °C, b) 1100 °C, c) 1200 °C, and d) 1300 °C. e) SEM-EDS maps of oxidized coupons exposed to different oxidative conditions: AlN (left), boria-coated AlN (right).

At 1200 °C, seen in Figure 4.2c, the oxide thicknesses for the boria-coated AlN samples are superseded by the oxide layer thickness of corresponding AlN samples. Oxide thickness is reduced by as much as 86% with the inclusion of boria, demonstrating a protection against oxidation and against Al_2O_3 formation due the inclusion of the boria coating. This protection diminishes with increased holding time because of the significant evaporation rate of boria at 1200 °C [4]. Likewise at 1300 °C, seen in Figure 4.2d, the added boria continues to protect AlN against oxidation, as evidenced by the lower oxidation rate compared to uncoated AlN. However, this protection is not as effective as what was observed at 1200 °C because of the higher volatility of boria at 1300 °C compared to 1200 °C [4].

To further elucidate the observed oxidation behavior, X-ray diffraction spectra of boria-coated AlN coupons were collected after exposure. It was revealed that the oxide layers formed in every oxidation experiment contained varying mixtures of unreacted B_2O_3, Al_2O_3, and aluminum borate, as seen in Figure 4.3a. There are two stable phases of aluminum borate, $Al_4B_2O_9$ and $Al_{18}B_4O_{33}$ [31]. Both arise from the reaction between B_2O_3 and Al_2O_3.

$$2Al_2O_3 + B_2O_3 \rightarrow Al_4B_2O_9 \quad (4.2)$$

$$9Al_2O_3 + 2B_2O_3 \rightarrow Al_{18}B_4O_{33} \quad (4.3)$$

The $Al_{18}B_4O_{33}$ phase forms when there is a low concentration of boria and high concentration of alumina, while the $Al_4B_2O_9$ phase forms with higher concentrations of boria. Due to the volatile nature of boria, $Al_4B_2O_9$ transforms into $Al_{18}B_4O_{33}$ with increasing temperatures, commencing near 1040 °C [19,31]. Similarly, $Al_{18}B_4O_{33}$ converts to Al_2O_3 when boria completely volatizes out of the crystal [31].

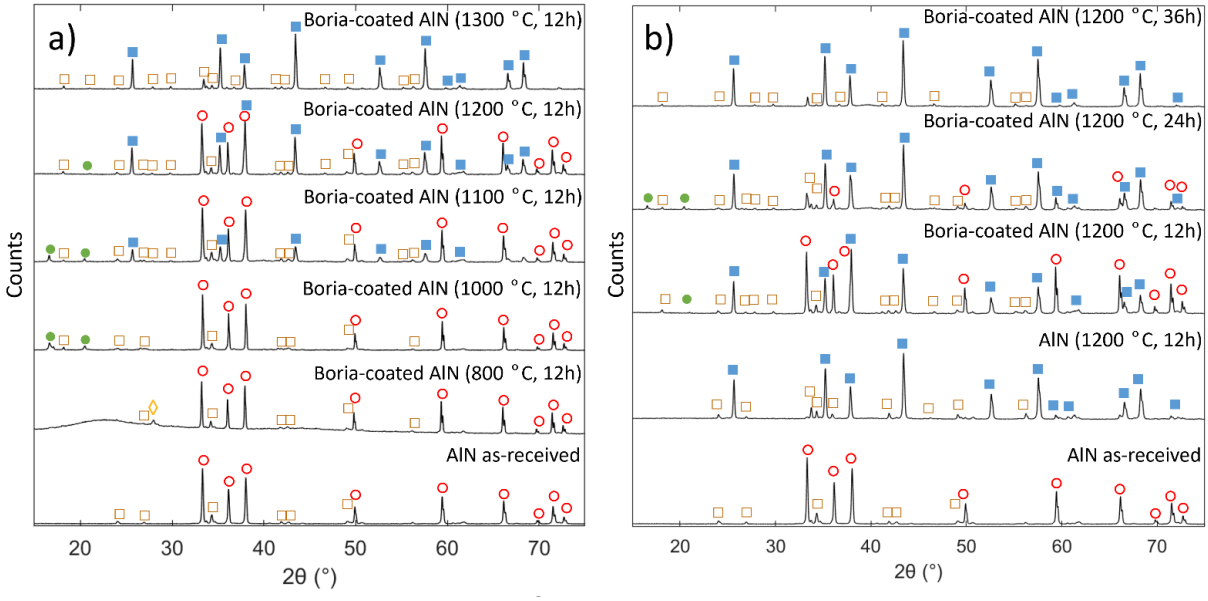

Figure 4.3. XRD spectra of a) boria-coated AlN at oxidation temperatures ranging from 800°C to 1300°C in contrast to as-received AlN, b) boria-coated AlN compared to AlN at an oxidation temperature of 1200 °C for 12 h, 24 h, and 36 h. Spectra show presence of AlN (○), $Al_{18}B_4O_{33}$ (●), boria (◊), YAG/YAP (□), Al_2O_3 (■).

Figure 4.3a shows that the $Al_{18}B_4O_{33}$ phase was present within the oxide layer of boria-coated AlN coupons after treatments at 1000 °C, 1100 °C and 1200 °C, indicating a low initial concentration of boria relative to alumina. The diffraction peaks that correspond to $Al_{18}B_4O_{33}$ decrease in intensity as the temperature increases. Simultaneously, Al_2O_3 peaks grow in intensity with increasing temperature, beginning at 1100 °C. This suggests that the $Al_{18}B_4O_{33}$ crystals start to convert to Al_2O_3 with the high-temperature evaporation of boria. This conversion appears to be complete by 1300 °C. Figure 4.3 also indicates the presence

of YAG (yttrium aluminum garnet) and YAP (yttrium aluminum perovskite), which originate from the commercially available sintered AlN. Y-rich additives are commonly added to high-temperature ceramics like AlN to improve their sinterability [32,33]. However, these Y-rich phases are not considered any further for this analysis.

A notable observation from the X-ray diffraction data is that the underlying AlN substrate is protected against oxidation by the addition of the boria coating. This protection is particularly obvious during 12 h holds at 1200 °C, seen in Figure 4.3b, where the AlN peaks are strong in boria-coated AlN coupons, but greatly diminished in uncoated AlN coupons. To verify this observation, we refer to the expected X-ray penetration depths for each system, assuming that 95% of the information collected pertains to the volume of the material from the surface to the penetration depth, and not the material below this layer [34]. In samples of boria-coated AlN that had been exposed to air for 12 h at 1200 °C, we see that the X-rays can penetrate the 23 ± 4 μm thick $Al_{18}B_4O_{33}$-rich oxide layer and probe the underlying AlN substrate as seen in Figure 4.3b. In contrast, for samples of uncoated AlN exposed to the same conditions, the X-ray penetration is limited within the 164 ± 13 μm thick Al_2O_3 layer, never reaching the underlying AlN substrate, seen in Figure 4.3b. This suggests that the addition of boria creates a superficial liquid barrier to oxygen diffusion that ultimately results in thinner oxide layers, and thus, a greater protection against oxidation. Figure 4.3b shows that the $Al_{18}B_4O_{33}$-rich oxide layer in boria-coated AlN only starts to oxidize into Al_2O_3 past 24 h exposures, when the trapped boria within $Al_{18}B_4O_{33}$ starts to evaporate.

Hence, we see that boria serves as a barrier to oxygen diffusion, protecting the underlying AlN substrate from being oxidized, while actively reacting with any created alumina to form aluminum borate on the surface of the samples, as seen in Reactions 4.2 and 4.3. Thus, we can deduce that it is a combination of Reactions 4.1-4.3 that results in an overall diminished thickness of the oxide layers seen in Figure 4.2a-e.

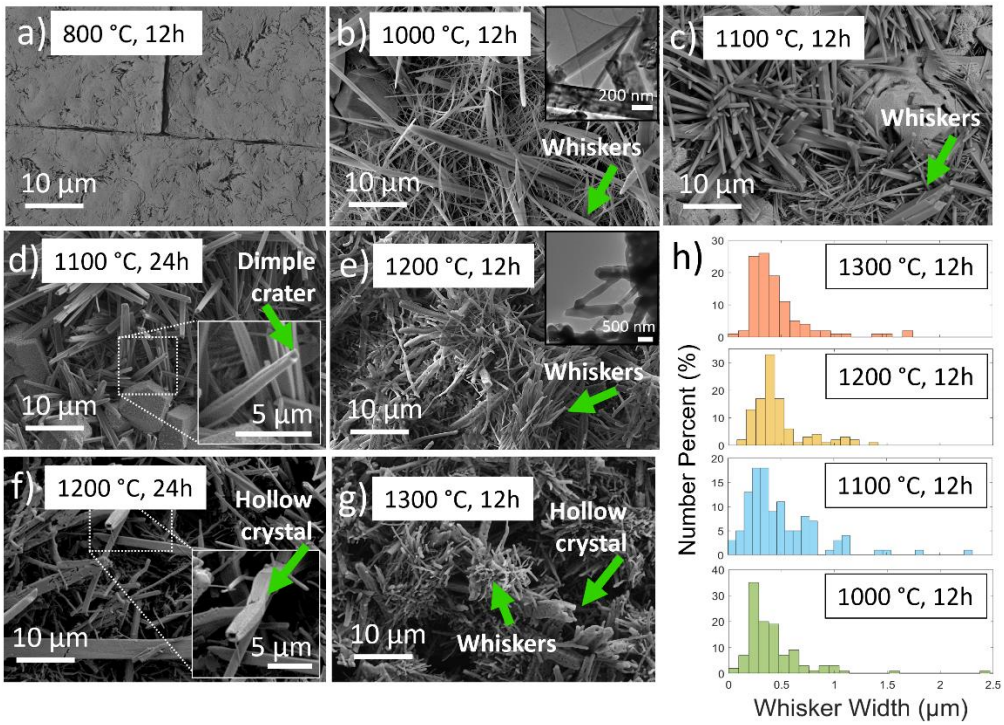

Figure 4.4. Scanning electron micrographs of boria-coated AlN after 12 h hold at described oxidation temperatures (a-g), including insets of transmission electron microscopy micrographs (b,e). Green arrows indicate features of interest, such as whiskers, dimple craters and hollow crystals. h) Histograms show whisker width distributions from images displayed in 4b,c,e,g.

The resulting surface microstructures of the boria-coated AlN coupons, observed using SEM, can be seen in Figure 4.4a-g. In contrast to the as-received AlN surface (Figure 4.1b), we can identify acicular crystals on these surfaces, indicating that $Al_{18}B_4O_{33}$ is present in whisker form. At 800 °C, boria melts into a thin amorphous film that covers the surface of the AlN coupon. The cracks that are seen in Figure 4.4a are a result of the thermal expansion mismatch that occurs during cooling of the glassy film to room temperature, as noted earlier. No whiskers are observed, indicating that boria has not yet reacted with any alumina that may be present from AlN oxidation. At 1000 °C, this is no longer the case, and we observe highly acicular crystals (Figure 4.4b) growing from many nucleation sites. The $Al_{18}B_4O_{33}$ whiskers can be seen again at 1100 °C (Figure 4.4c), appearing coarser and with a shape that is consistent with the orthorhombic morphology of $Al_{18}B_4O_{33}$. Exposing boria-coated AlN coupons to 1100 °C for an additional 12 h (Figure 4.4d), we observe that

$Al_{18}B_4O_{33}$ whiskers start to develop dimple craters on their tips (noted by green arrows), a feature that we will refer to later in this discussion.

At 1200 °C or higher (Figure 4.4e-g), the whiskers appear deformed due to the evaporation of boria. Porous Al_2O_3 whiskers, confirmed by XRD in Figure 4.3, result from the loss of boria, some of which have shrunk in size (Figure 4.4g), as noted by the shift in the whisker width distribution to smaller sizes in Figure 4.4h. Curiously, under prolonged exposure to high-temperature environments, tube-like hollow crystals can be seen in Figure 4.4f,g. The whiskers can be seen on both the micro and the nanoscale. Displayed in the insets in Figure 4.4b,e are bright field TEM images that show whiskers grown at 1000 °C and 1200 °C for 12 h. The morphology of the nanocrystals closely resembles their micro-sized counterparts.

4.3.2 Oxidation of AlN/BN Composites

X-ray diffraction patterns indicate that $Al_{18}B_4O_{33}$ crystals formed during the dry air exposures of AlN/BN composites, seen in Figure 4.5a. Unlike the previously discussed boria-coated AlN system, the formation of aluminum borate in the composite depends on the oxidation of AlN into alumina as well as the oxidation of BN into boria. During these experiments, the stoichiometric quantities of alumina and boria needed to produce $Al_{18}B_4O_{33}$ whiskers were developed between 1200 °C to 1300 °C, after exposures of 48 h or longer.

Figure 4.5 b-h shows SEM images of the as-received composite and the composite surface after being exposed to dry air from 1200 °C to 1450 °C, for holding times ranging from 48 h to 60 h, further described in Table 4.1. The images reflect the various stages of whisker growth produced from the reaction between boria and alumina. Early stages of $Al_{18}B_4O_{33}$ growth can be seen in Figure 4.5c on the surface of the oxidized AlN grains after 48 h long exposures to 1200 °C. The pores and crevices present between the AlN grains are due to the oxidation of the BN flakes into liquid boria. The growth of $Al_{18}B_4O_{33}$ acicular crystals can be seen in Figure 4.5d with an increase in temperature to 1250 °C for 48 h. As the temperature is increased further to 1300 °C (Figure 4.5e) or the exposure time is increased to 60 h (Figure 4.5f), we see a change in whisker morphological characteristics from solid to hollow crystals of $Al_{18}B_4O_{33}$, both longer and wider than the acicular crystals seen at

1250°C for 48 h (Figure 4.5d). Although the morphology of the crystals is significantly different in Figures 4.5d-g, the corresponding XRD data confirms that the aluminum borate phase present in every case is $Al_{18}B_4O_{33}$.

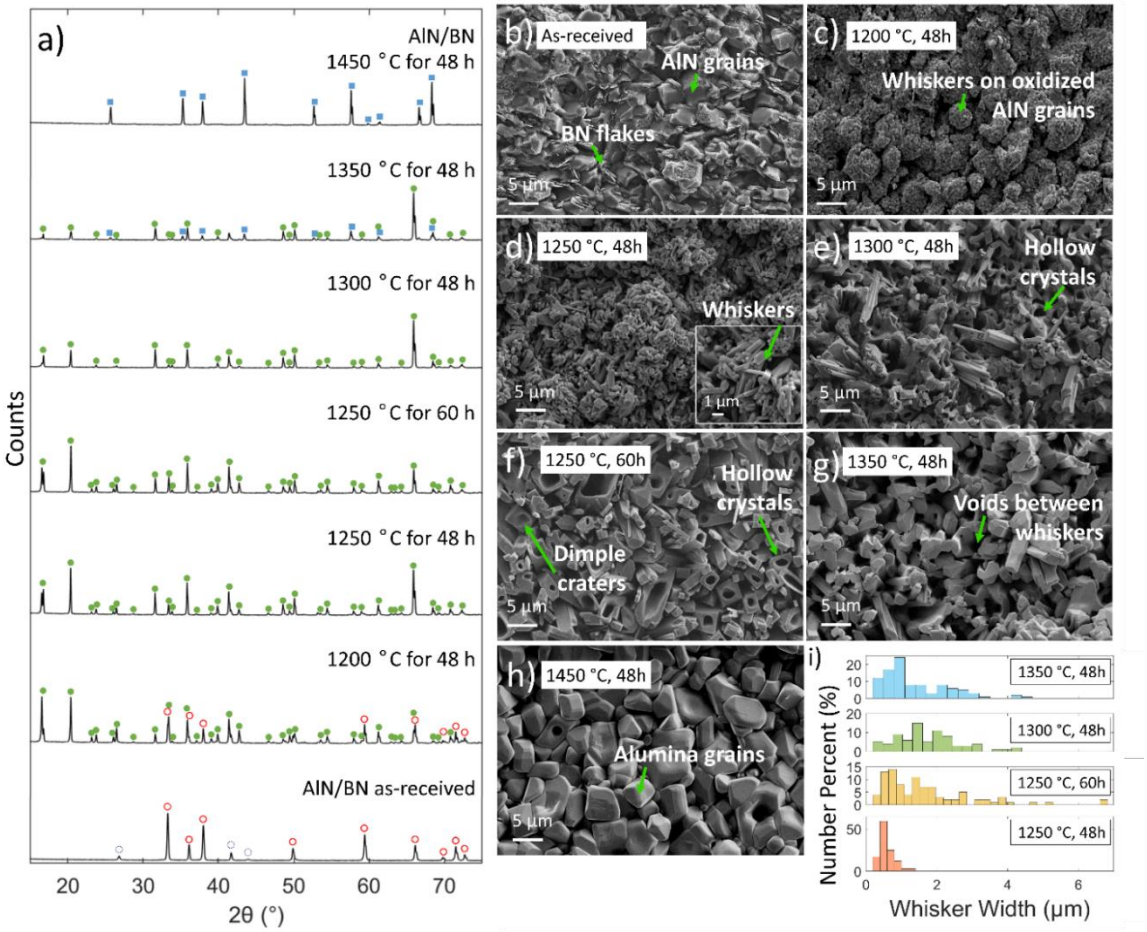

Figure 4.5. Chemical oxidation of AlN/BN: a) XRD spectra of oxidized AlN/BN composites in dry air from 1200°C to 1450°C, showing AlN (○), BN (◌), $Al_{18}B_4O_{33}$ (●), Al_2O_3 (■), in contrast to as-received AlN/BN. SEM images of b) as-received AlN/BN composite, (c-h) oxidized AlN/BN composites in dry air, including oxidation temperature and exposure time. i) Histograms show whisker width distributions from images displayed in 5d-g.

X-ray diffraction patterns (Figure 4.5a) show that $Al_{18}B_4O_{33}$ starts to convert to Al_2O_3 at 1350 °C. One possible explanation for the inter-whisker voids, seen in Figure 4.5g, is the collapse of hollow crystals. By 1450 °C seen in Figure 4.5h, the conversion is complete

and isotropic grains of Al_2O_3 cover the surface with no signs of $Al_{18}B_4O_{33}$. The whisker width distributions are summarized in Figure 4.5i. The distribution of whiskers exposed to 1200 °C for 48h is narrow, centered near 0.5 µm. In contrast, at higher holding times or temperatures, the distribution widens, predominantly from widths < 1 µm to > 5 µm. The broad distributions, seen in both Figures 4.5i and 4.4h, may be attributed to the scatter in nucleation times, coarsening, and whisker deterioration, the latter being due to the high-temperature transition of the whiskers into porous Al_2O_3.

Cross-sections of oxidized AlN/BN composites were analyzed using SEM-EDS to measure the thickness of the $Al_{18}B_4O_{33}$ oxide layer. In Figure 4.6a, the oxide thickness of AlN/BN after 48 h at 1200 °C (Figure 4.6b) and 1300 °C (Figure 4.6d) were included in the oxidation plot from Figure 4.2. From this comparison, it is clear that the oxidation protection previously discussed in boria-coated AlN coupons can also be seen in AlN/BN composites. The inclusion of liquid boria within the system, both through an applied coating or from BN, can impede the oxidation of AlN.

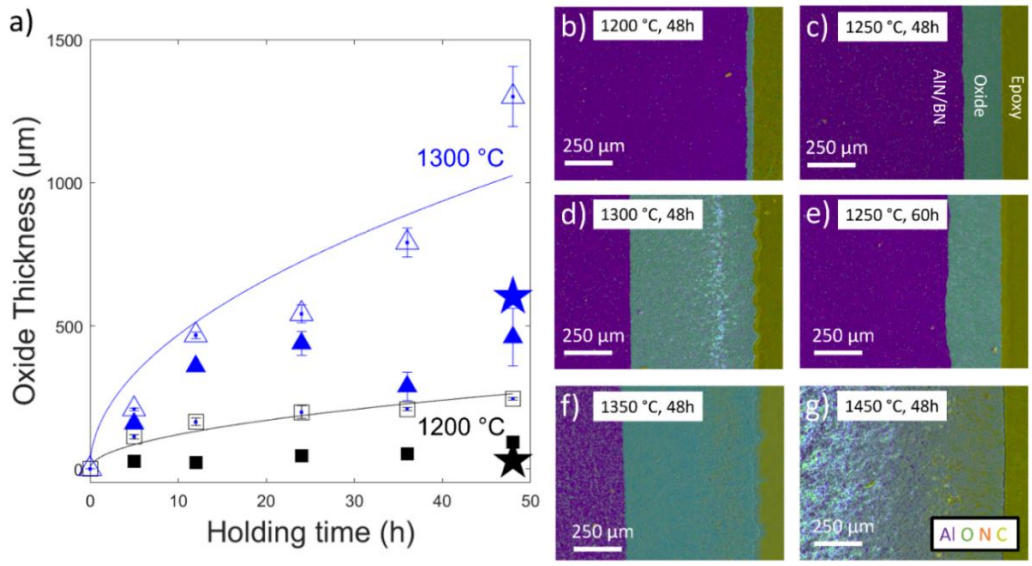

Figure 4.6. AlN/BN oxide layers: a) Oxidation plot from Figure 4.1 including data points from AlN (empty markers), boria-coated AlN (filled markers), and AlN/BN (★) at 1200 °C (black) and 1300 °C (blue). SEM-EDS maps of oxidized AlN/BN cross-sections b) held at 1200 °C for 48 h, c) 1250 °C for 48 h, d) 1300 °C for 48 h, e) 1200 °C for 60 h, f) 1350 °C for 48 h, and g) 1450 °C for 48 h.

The whisker morphology can also significantly influence the oxide layer's ability to protect the underlying composite. We see that the $Al_{18}B_4O_{33}$ whiskers (in Figure 4.5d) result in an oxide layer that is 184 ± 6 µm thick (Figure 4.6c). In contrast, the hollow crystals (in Figures 4.5f) lead to an oxide layer that is 262 ± 10 µm thick (Figure 4.6e). The increase in oxide thickness observed by exposing the composite to 1250 °C for an additional 12 h can be explained by the tubular morphology of the hollow crystals, observed in Figure 4.5f. Such crystals provide additional pathways for oxygen diffusion into the AlN/BN substrate via tunnels through the crystal. Similar observations can also be made of boria-coated AlN samples. Referring to Figure 4.2, the oxide layers of coupons with hollow crystals (Figure 4.4f,g) appear to be thicker than those of coupons with capped whiskers and dimples (Figure 4.4b-e). The thickness of the oxide layer is obviously also a function of temperature and time, yet it is worth noting that the whisker morphology could also influence the transport of oxygen into the AlN-rich material. With this in mind, the oxidation protection witnessed via the growth of $Al_{18}B_4O_{33}$ greatly depends on the whisker morphology.

Figure 4.6f suggests that the oxide layer developed after 48 h at 1350 °C is comparable to the same time at 1300 °C. The hollow crystals seen at 1300 °C create pathways that are still present at 1350 °C in the form of voids between coarsened $Al_{18}B_4O_{33}$ crystals. In contrast, Figure 4.6g demonstrates the full conversion of AlN/BN into porous Al_2O_3, and no protection against oxidation is observed in the absence of $Al_{18}B_4O_{33}$.

4.3.3 Aluminum Borate Crystal Microstructures

When boria-coated AlN coupons and AlN/BN composites are exposed to high-temperature oxidative environments, liquid boria can form and react with oxidized AlN to produce $Al_{18}B_4O_{33}$ (Reaction 4.2). Referring to the Al_2O_3-B_2O_3 phase diagram by Gielisee [31], seen in Figure 4.7a, the liquid oxide layer can contain dissolved aluminum borate and unreacted boria within the temperature range of 470 °C to 1035 °C. Once supersaturation is reached, $Al_{18}B_4O_{33}$ starts to crystallize out of the liquid oxide [35]. Based on SEM observations, nucleation and growth results in highly anisotropic whisker-like crystals.

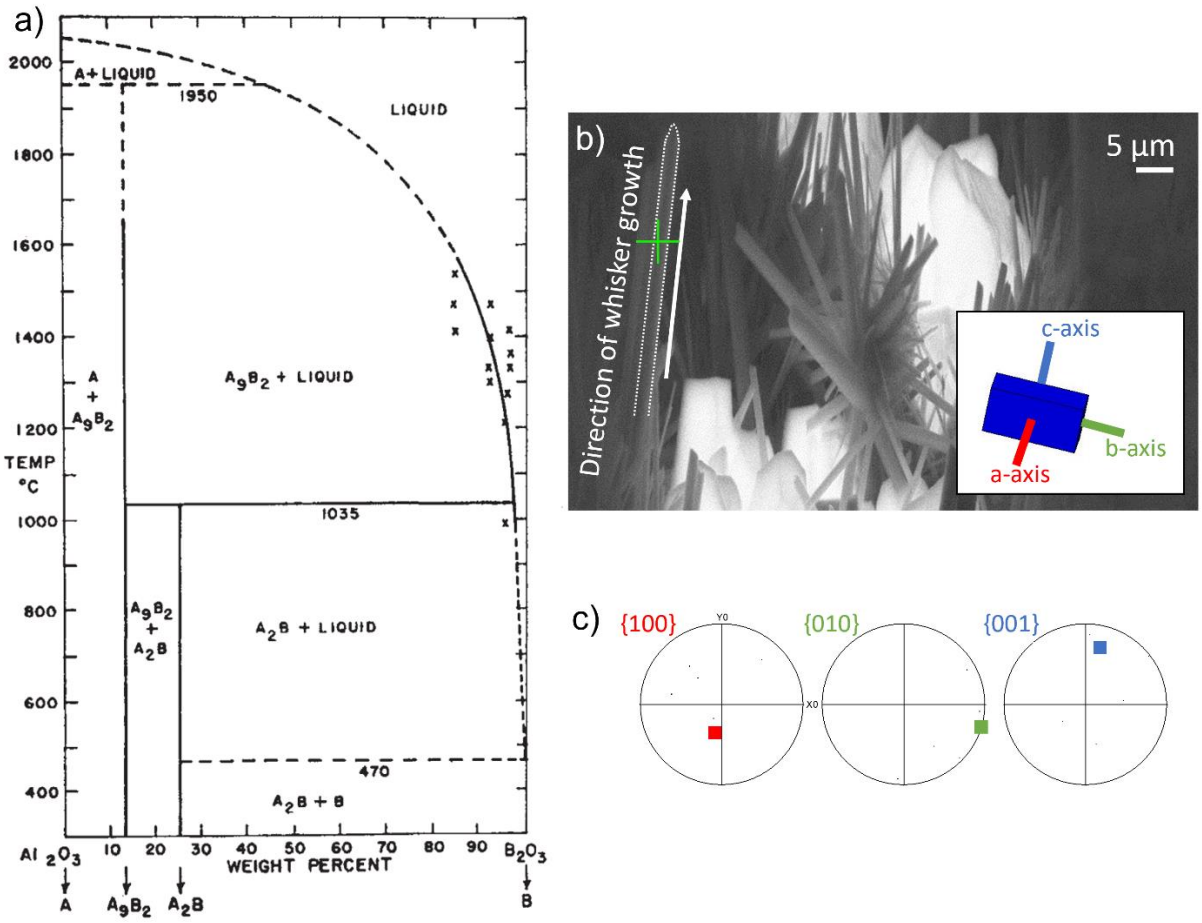

Figure 4.7. Crystal growth and orientation of $Al_{18}B_4O_{33}$ whiskers: a) Al_2O_3-B_2O_3 phase diagram reprinted with permission from Gielisse et al.[31]*, © Springer Nature (1962). b) Back-scattered electron image of $Al_{18}B_4O_{33}$ whiskers, where green cross shows point analyzed in EBSD, white dotted line shows outline of analyzed whisker, white arrow shows direction of crystal growth. Inset shows proposed orientation of crystallographic axes of outlined whisker. c) Corresponding pole figures from this analysis. Note that crystallographic information from Ihara et al. (1980) was used for indexing*[22]*.*

Electron backscatter diffraction was used to determine the direction of crystal growth. Figure 4.7b shows a back-scattered electron image of $Al_{18}B_4O_{33}$ whiskers, taken from the sample seen in Figure 4.4c. The indexed EBSD patterns (provided in Appendix B) and corresponding pole figures (Figure 4.7c) were used to determine that the direction of growth of the analyzed crystal was perpendicular to the (001) plane. Previous studies on

$Al_{18}B_4O_{33}$ whiskers have shown similar results, supporting that the direction of the anisotropic crystal growth of $Al_{18}B_4O_{33}$ is <001> [35,36].

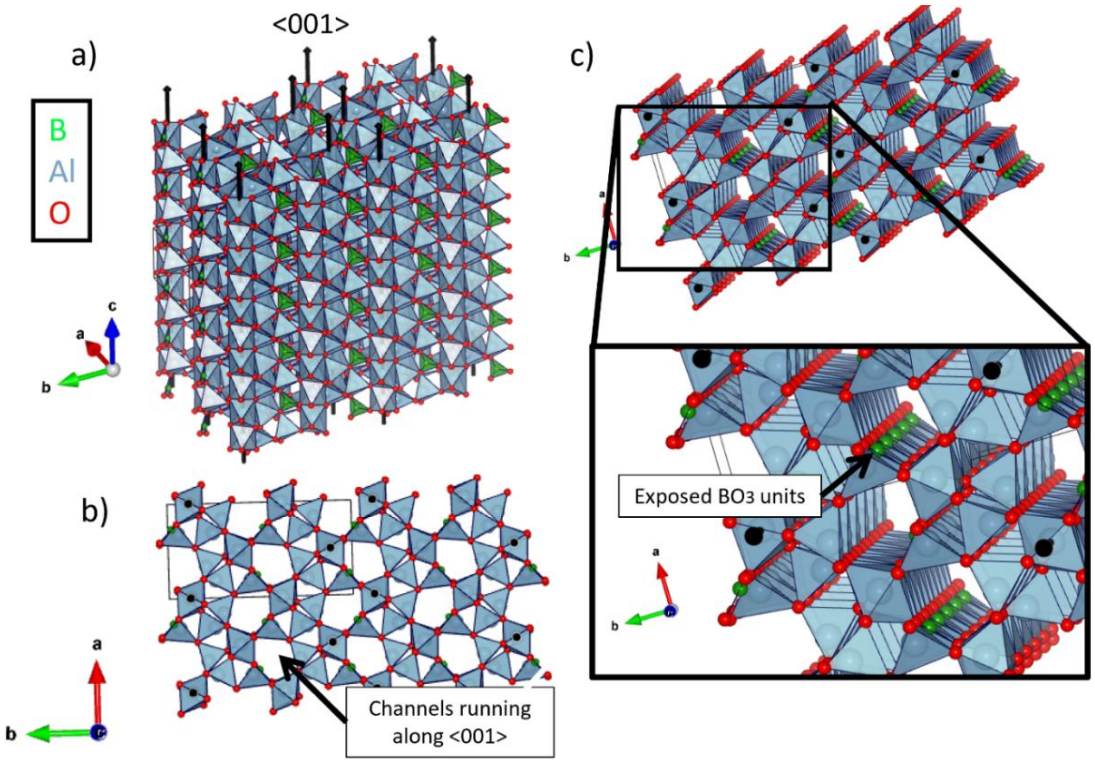

Figure 4.8. Super cell (3x3x6) of $Al_{18}B_4O_{33}$ with black arrows showing direction of crystal growth along <001>: a) side view, b) view of $Al_{18}B_4O_{33}$ along the (001) plane, showing channels through crystal, and c) close-up of exposed BO_3 units along the channels. Lattice parameters are defined as a = 0.7692 nm, b = 1.4973 nm, c = 0.5682 nm[22,37].

It is possible to link the acicular morphology of $Al_{18}B_4O_{33}$ to the fundamental structure of the single crystal. Referring to Figure 4.8a, uninterrupted chains of strong bonds run parallel to the c-axis of $Al_{18}B_4O_{33}$, including structural chains of AlO_6 octahedra, chains of AlO_4 tetrahedra, and chains of alternating AlO_4 tetrahedra and planar BO_3 groups. According to Hartman et al.'s periodic bond chain (PBC) theory, crystal growth in the direction of such continuous chains is preferred [38,39]. The theory states that crystal faces that are parallel to two or more strong chains dominate the crystal habit, and can grow from the vapor through spiral growth from a dislocation, or through layer-by-layer growth [39,40].

There is a separate yet critical observation that can be made when looking at the crystal structure of $Al_{18}B_4O_{33}$. Across the (001) plane shown in Figure 4.8b, we see empty channels running along <001>. Such channels directly expose planar BO_3 groups along the length of the crystal, seen in Figure 4.8b,c. This structure provides a pathway for high-temperature volatilization of trapped boria within the crystal structure, which can result in the breaking of PBC chains. The release of boria is considerable at temperatures over 1200 °C, when the evaporation rate [4] of boria is sufficient to initiate the transformation of $Al_{18}B_4O_{33}$ to porous Al_2O_3, as seen in Figures 4.3 and 4.4. The structural change observed with the loss of boria is significant, affecting the crystal's composition and microstructure.

From our observations, the morphology of the $Al_{18}B_4O_{33}$ whiskers evolves with increased exposure to high-temperature environments. For example, whiskers grown on AlN/BN composites at 1250 °C after 48 h appeared to be capped by pyramid tips. In contrast, in AlN/BN composites oxidized at 1250 °C for 60 h, dimples craters and hollow cores begin to emerge in the crystals, as shown in Figure 4.5f.

The occurrence of dimples and hollow cores in $Al_{18}B_4O_{33}$ is not fully understood. One possible reason for these morphological features can be ascribed to Frank's theory of capillary equilibria [41], a theory that assumes spiral crystal growth. Frank argued that hollow cores can form in single crystals to minimize the strain energy from screw dislocations. With increased exposure to high temperatures, a balance is sought between the surface tension and the line tension of the dislocation, which can lead to the creation of a free surface along the dislocation line that produces a hollow core in the crystal [40]. The diameter of the hollow core can be directly related to the strain energy of the dislocation, being a function of the square of the Burgers vector [42]. In Figure 4.5f, we see that the core diameters can range from ~0.5 µm to 6 µm. Based on Frank's theory, this would imply that there is a wide discrepancy in dislocation strain energies from whisker to whisker. Thus, there may be other factors contributing to the development of such large hollow cores.

A second possible cause could be the partial dissolution of $Al_{18}B_4O_{33}$ whiskers, potentially from excess boria in the environment. Studies on zeolites [43] and quartz [44] have described how voids and etch pits can form from the dissolution of these crystals in strong

bases and silica melts, respectively. Interestingly, these studies suggest that dissolution is most likely to occur in areas along boundaries, and where defect sites are abundant. The hollow cavities in $Al_{18}B_4O_{33}$ might therefore arise from the dissolution of dislocations within its core (e.g., screw dislocations) or of energetically unstable phases located in the core, through excess boria, a liquid oxide known to dissolve alumina [31,35]. In order to establish this, future studies might explore how easily $Al_{18}B_4O_{33}$ crystals dissolve in liquid boria, and if screw dislocations are truly responsible for the acicular growth of $Al_{18}B_4O_{33}$.

A third potential reason for these features relates back to PBC theory. At high temperatures, the breaking of PBCs from the loss of boria could induce a roughening transition that transforms steps (along the edges and corners of the crystal) into kinks [38]. The rough edges from the kinks could act as preferred sites for layered growth along <001> [45], causing the crystal to protrude out on its edges and corners, as seen in Figure 4.5f. Consequently, this preferred growth along the edges and corners could account for the formation of hollow cores within $Al_{18}B_4O_{33}$ which, as previously outlined and shown in Figure 4.6d-f, provide additional, yet undesirable, pathways for oxygen diffusion [40]. Though beyond the scope of the current work, these three hypotheses point to future experiments.

4.3.4 Self-healing in AlN/BN Composites

4.3.4.1 Effective Strength of Whiskers

Ball-on-ring tests were carried out to evaluate the effective strength of interlocking aluminum borate whiskers [23]. All discs were synthesized at 1000 °C for 36 h from a slurry of alumina and H_3BO_3 [46,47], and subsequently exposed to: 1100 °C for 36 h, 1200 °C for 36 h, or 1300 °C for 36h. The high-temperature conditions were chosen in order to investigate how the strength of the whiskers varies with evolving morphological features.

Figure 4.9 shows the microstructure of the three types of discs exposed to 1100 °C, 1200 °C, and 1300 °C compared to the as-synthesized material, along with their corresponding X-ray diffraction patterns. The whisker microstructures are noticeably similar to the surface of boria-coated AlN coupons seen in Figure 4.4. Figure 4.9a shows that the as-synthesized discs contain whiskers that are long and flat, with rough heads. This structure

is typical for acicular crystals, where the growth is anisotropic and favored in the direction of the highest surface area. The XRD data in Figure 4.9e suggest that the as-synthesized discs contain significant amounts of unreacted alumina and $Al_4B_2O_9$, where the latter has not yet fully crystallized into $Al_{18}B_4O_{33}$. Figure 4.9e reveals that $Al_{18}B_4O_{33}$ develops when the discs are exposed to 1100 °C or 1200 °C for 36h. Additionally, the absence of unreacted alumina under said conditions, seen in Figure 4.9e, points to the completion of Reaction 4.3 at 1100 °C for 36h. As a result of this completed reaction, Figure 4.9b shows a comparatively denser structure of interlocking $Al_{18}B_4O_{33}$ whiskers compared to Figure 4.9a.

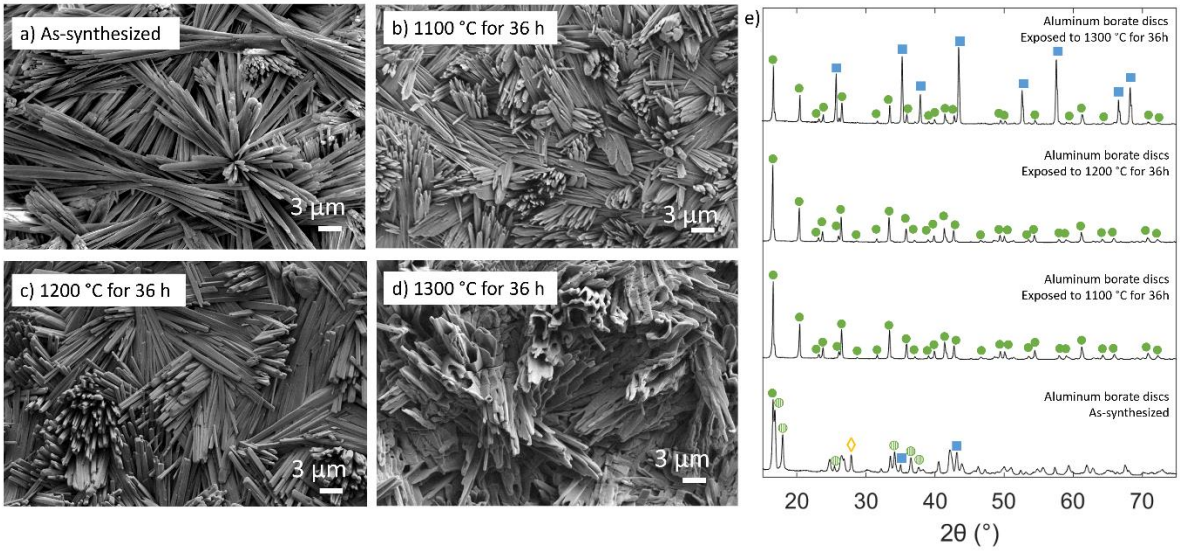

Figure 4.9. Aluminum borate discs: a) SEM microstructure of discs sintered at 1000 C for 36h; the discs were then exposed to b) 1100 C for 36h, c) 1200 C for 36h, and d) 1300 C for 36h. e) XRD spectra of samples seen in a)-d), showing $Al_{18}B_4O_{33}$ (●), $Al_4B_2O_9$ (◍), boria (◊), and Al_2O_3 (■).

Additionally, Figure 4.9c shows that the whiskers become coarser, with a shape consistent with the orthorhombic structure of $Al_{18}B_4O_{33}$ when the discs are exposed to 1200 °C for 36 h. Figure 4.9d and the corresponding XRD data indicate that hollow tubes of alumina start to develop during exposures to 1300 °C for 36 h, likely due to the significant evaporation of B_2O_3 at 1300 °C that causes $Al_{18}B_4O_{33}$ to convert to Al_2O_3, as previously discussed [1,4,31].

The effective strength (σ_f) of the discs was calculated using equation 4.4:

$$\sigma_f = \frac{3P(1+v)}{4\pi t^2} \times \left(1 + 2\left[\ln\left(\frac{a}{b}\right)\right] + \left[\frac{(1-v)a^2}{(1+v)R^2}\right]\left[1 - \frac{b^2}{2a^2}\right]\right) \quad (4.4)$$

where P is the load to failure, t is the thickness of the disc, v is the Poisson's ratio, a is the radius of the circle of support points, $b \approx t/3$ is the radius of the region of uniform loading at the disc center, and R is the radius of the disc.

Table 4.2. Summary of measured effective strength of aluminum borate discs.

Description of Exposure Conditions in Stagnant Air	Effective Strength (MPa)
1100 °C for 36h	5.9 ± 1.2
1200 °C for 36h	8.6 ± 1.3
1300 °C for 36h	4.4 ± 1.5

A summary of the measured effective strengths can be found in Table 4.2. The effective strength of discs exposed to 1100 °C for 36h was 5.9 ± 1.2 MPa. The relatively low magnitude is attributed to the interlocking nature of the acicular whiskers, which produces a porous framework. The effective strength of discs exposed to 1200 °C for 36h was 8.6 ± 1.3 MPa, which is statistically higher than the former, though still formidably low for a structural material. The relatively higher strength could be due to the coarser shape of the interlocking whiskers, which creates a more robust framework. The effective strength of discs exposed to 1300 °C for 36 h was 4.4 ± 1.5 MPa, demonstrating that the formation of hollow cores and degradation of $Al_{18}B_4O_{33}$ into alumina further degrades the porous structure, and lowers its effective strength.

4.3.4.2 Bend Strength of AlN/BN Composites

It was desired to probe how successful $Al_{18}B_4O_{33}$ whiskers could be at bridging and *healing* cracks on the surface of the composite. Previous studies on ceramic matrix composites containing SiC and h-BN have shown that self-healing, also referred to as self-sealing or crack-healing, can be achieved when such composites are exposed to oxidizing

atmospheres [2,48,49]. Under these conditions, h-BN can oxidize into liquid-phase B_2O_3, also termed the *healing agent*, which can travel into pre-existing cracks within the composite. Once in contact with the crack walls (which are made of SiC or SiO_2), the liquid oxide can react to form borosilicate. Upon cooling to room temperature, the volume expansion of the glass allows the oxidation product to seal the cracks and thus reinforce the material. Similar healing effects have also been seen in SiC/B_4C [50] and SiC/B_3C_2 [51] composites, as well as in ZrO_2/$MoSi_2$ through the formation of $ZrSiO_4$ as the load bearing material [52].

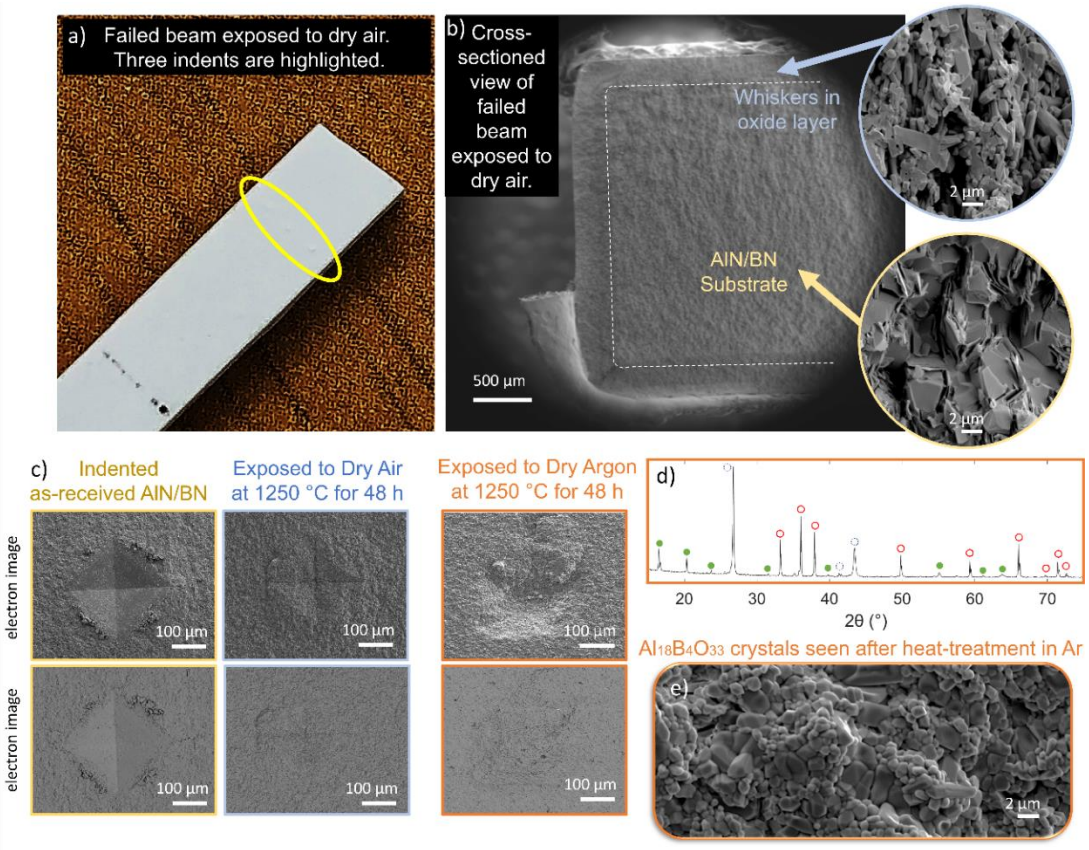

Figure 4.10. Images of healed AlN/BN beams exposed to dry air at 1250 °C for 48h after flexural test: surface (a) and cross-sectioned view (b). c) Indentations before treatment (yellow), after dry air heat-treatment (blue), and after dry argon heat-treatment (orange), showing both secondary electron (top) and backscattered electron (bottom) micrographs to better illustrate the absence of cracks from the indents after heat-treatment. d) XRD spectra and e) surface micrograph of beam exposed to dry argon at 1250 °C for 48 h, showing AlN (○), BN (○), and $Al_{18}B_4O_{33}$ (●).

The role of $Al_{18}B_4O_{33}$ on the mechanical strength of AlN/BN composites was thus investigated through a serious of 4-point bend flexural tests. A summary of the measured flexural strengths can be found in Table 4.3. In this experiment, the strength of as-received beams was compared to heat-treated beams, which were exposed to either dry air or dry argon. Cracks were induced on the surface of these beams by introducing three indentations along the center of the beam (created with loads of 196 N), an example of which is illustrated in Figure 4.10a. The bend strength of the as-received bars was measured to be 223 ± 29 MPa, with failure originating from random locations in every specimen. The flexural strength of the indented AlN/BN was measured to be 139 ± 23 MPa, with failure occurring repeatedly through the indentations.

Table 4.3. Summary of measured flexural strength of AlN/BN composites.

Description of AlN/BN Beams	Flexural Strength (MPa)	Failure Origin
As-received	223 ± 29	Random
Indented	139 ± 23	Indentation
Indented + exposed to dry air (1250 °C for 48 h)	83 ± 24	Random
Indented + exposed to dry argon (1250 °C for 48 h)	194 ± 27	Indentation

Indentations were similarly introduced in beams subjected to heat-treatment, prior to being treated. Figure 4.10b confirms that bars exposed to dry air at 1250 °C for 48 h developed whiskers on the surface of the beam. Given the results from Figure 4.5, this temperature and holding time was selected to maximize the whisker strength, considering that hollow crystals did not develop under these conditions. When measuring the flexural strength of these indented and heat-treated beams, the origin of failure was found to be random, derived from the porous nature of the interlocking whiskers, seen in Figure 4.10b. We observed that the cracks produced by the three indentations were indiscernible from the rest of the oxide layer (seen in Figure 4.10c) and were not the origin of failure. The porosity of this oxide layer meant that the flexural strength of the oxidized beams was measured to be 83 ± 24 MPa, much lower than the previous two results.

Indented AlN/BN bars were also exposed to dry argon at 1250 °C for 48h, to develop an understanding of the effects that heating in an inert atmosphere could have on the strength of the indented composite. The flexural strength was measured to be 194 ± 27 MPa, with failure occurring repeatedly through the indentations even though Figure 4.10c shows the absence of cracks emerging from the indents after heat-treatment. The flexural strength of AlN/BN after heat-treatment in argon was significantly higher than it was before the treatment. This result is indicative of either residual stress relief of the indentation cracks or self-healing through oxide growth, and thus prompted further chemical and microstructural investigation. X-ray diffraction seen in Figure 4.10d suggested that small quantities of $Al_{18}B_4O_{33}$ developed on the surface of the beams after heat-treatment in dry argon, despite the gas only containing 2 ppm of O_2 and H_2O combined. This result highlights the effectiveness of O_2 and H_2O in oxidizing h-BN and AlN, which might have been further promoted by B_2O_3 vapors in the system and the Al_2O_3 crucibles holding the samples. Scanning electron micrographs in Figure 4.10e show crystals of $Al_{18}B_4O_{33}$ forming on the surface of the beam, where the widths of the grains remain below 2 µm. It is thought that the improved flexural strength of AlN/BN heat-treated in dry argon originates from the development of small $Al_{18}B_4O_{33}$ crystals on the crack walls, which delayed the extension of the crack through friction between the walls and improved the strength of the fractured composite. Further, residual stress relief from the indentation stress field should also be considered as an additional factor. The increased strength of the composite could have arisen from annealing effects during dry argon exposure. Lawn demonstrates a more than doubling of the indentation strength through residual stress relief [53]. The occurrence of $Al_{18}B_4O_{33}$ in the system highly suggests that oxide growth is the principle mechanism for the healing of the indentation cracks, however more work needs to be done to better decouple the two factors and establish to what extent the residual stress relief has influenced the improved strength of the composite.

4.4 Summary and Implications

The oxidation kinetics of AlN were compared to that of boria-coated AlN, where it was shown that the inclusion of liquid boria resulted in the growth of thinner oxide layers containing $Al_{18}B_4O_{33}$. Based upon SEM-EDS and XRD results, the boria film protected the AlN substrate from oxidation by 1) acting as a barrier to oxygen diffusion and 2) reacting with freshly oxidized AlN to form $Al_{18}B_4O_{33}$ crystals, actively trapping boria into the oxide layer as it is incorporated within the $Al_{18}B_4O_{33}$ crystal structure. The porous oxide layer of $Al_{18}B_4O_{33}$ has a CTE similar to that of AlN and AlN/BN [8,26]. This offers a more compatible oxide layer for AlN ceramics than Al_2O_3, where thermal mismatch cracks are widely observed in the latter [26]. The $Al_{18}B_4O_{33}$ layer eventually transforms to Al_2O_3 with prolonged exposure to high-temperature environments, behaving as a transitional oxide layer that slows down the rate at which AlN oxidizes to Al_2O_3. Similar observations were revealed in AlN/BN composite structures, indicating that the inclusion of BN in the composite results in a similar oxidation retardance in high-temperature, dry air environments.

$Al_{18}B_4O_{33}$ whiskers display a variety of morphological features, with some crystals exhibiting dimples or hollow cores after prolonged exposure to high-temperature environments. This change in morphology is still not fully understood. Nevertheless, potential reasons were offered, including dislocation strain energy, dissolution, and promoted growth along the edges and corners. It was further shown that the crystal morphological features could greatly affect the oxidation protection of the composite, with hollow cores providing pathways for oxygen diffusion that could be damaging to the non-oxide. This, coupled with the transformation of $Al_{18}B_4O_{33}$ to Al_2O_3, indicates that the oxidation protection witnessed from the $Al_{18}B_4O_{33}$ layer is temporary, and depends on the duration and temperature of the exposure.

The effective strength of interlocking $Al_{18}B_4O_{33}$ whiskers was also evaluated and shown to vary with changing morphological features and composition, with coarse whiskers building stronger frameworks than hollow alumina tubes. It was also found that heat-treating fractured AlN/BN composites in dry argon produced small quantities of $Al_{18}B_4O_{33}$ crystals between crack walls that improved the material's flexural strength. These results

shed light to the healing abilities of AlN/BN when heat-treated, and show promise for the use of $Al_{18}B_4O_{33}$ as a load-bearing, porous ceramic joint.

Overall, the role of boria on the oxidation kinetics of AlN was revealed in detail, with helpful new insights into $Al_{18}B_4O_{33}$ growth and how the crystal morphological features can affect the oxidation protection and mechanical properties of AlN/BN composites.

References

[1] C.S. Chari, K.T. Faber, Oxidation resistance of AlN/BN via mullite-type $Al_{18}B_4O_{33}$, Journal of the European Ceramic Society. 42 (2022) 3437–3445. https://doi.org/10.1016/j.jeurceramsoc.2022.02.037.

[2] B.W. Sheldon, E.Y. Sun, S.R. Nutt, J.J. Brennan, Oxidation of BN-coated SiC fibers in ceramic matrix composites, Journal of the American Ceramic Society. 79 (1996) 539–543. https://doi.org/10.1111/j.1151-2916.1996.tb08163.x.

[3] E.J. Opila, R.C. Robinson, M.J. Verrilli, Borosilicate glass-induced fiber degradation of SiC/BN/SiC composites exposed in combustion environments, International Journal of Applied Ceramic Technology. 13 (2016) 434–442. https://doi.org/10.1111/ijac.12499.

[4] H. Hatta, T. Sohtome, Y. Sawada, A. Shida, High temperature crack sealant based on SiO_2-B_2O_3 for SiC coating on carbon–carbon composites, Advanced Composite Materials. 12 (2003) 93–106. https://doi.org/10.1163/156855103772658498.

[5] A. Napolitano, P.B. Macedo, E.G. Hawkins, Viscosity and density of boron trioxide, Journal of the American Ceramic Society. 48 (1965) 613–616. https://doi.org/10.1111/j.1151-2916.1965.tb14690.x.

[6] E. Pérez-Enciso, M.A. Ramos, S. Vieira, Low-temperature specific heat of different B_2O_3 glasses, Physical Review B. 56 (1997) 32–35. https://doi.org/10.1103/PhysRevB.56.32.

[7] J. Schlichting, Oxygen transport through glass layers formed by a gel process, Journal of Non-Crystalline Solids. 63 (1984) 173–181. https://doi.org/10.1016/0022-3093(84)90396-X.

[8] S.P. Ray, Preparation and characterization of aluminum borate, Journal of the American Ceramic Society. 75 (1992) 2605–2609. https://doi.org/10.1111/j.1151-2916.1992.tb05622.x.

[9] D. Goeuriot-Launay, G. Brayet, F. Thevenot, Boron nitride effect on the thermal shock resistance of an alumina-based ceramic composite, Journal of Materials Science Letters. 5 (1986) 940–942. https://doi.org/10.1007/BF01729282.

[10] Y. Li, G. Qiao, Z. Jin, Machinable Al_2O_3/BN composite ceramics with strong mechanical properties, Materials Research Bulletin. 37 (2002) 1401–1409. https://doi.org/10.1016/S0025-5408(02)00786-9.

[11] A. Abreal, D. Goeuriot, F. Thevenot, M. Lagace, B. Gueroult, M. Rigaud, Effect of Y_2O_3 addition on alumina-hex boron nitride composites, Journal of the European Ceramic Society. 15 (1995) 841–849. https://doi.org/10.1016/0955-2219(95)00056-Z.

[12] Shimpo A., Ueki M., Naka M., Mechanical properties of AlON-based composite ceramics at high temperature. (Part 1). Effect of oxidation on mechanical properties of AlON-BN composite ceramics., Journal of the Ceramic Society of Japan. 109 (2001) 127–131. https://doi.org/10.2109/jcersj.109.1266_127.

[13] H. Yamashita, A. Yamaguchi, Oxidation of aluminum oxynitride-boron nitride (AlON-BN) composite prepared by reaction sintering, Journal of the Ceramic Society of Japan. 109 (2001) 94–99. https://doi.org/10.2109/jcersj.109.1266_94.

[14] S. Kurita, Z.-Q. Zeng, H. Takebe, K. Morinaga, Reaction and phase relations in the AlN-B_2O_3 system, Materials Transactions, The Japan Institute of Metals and Materials. 35 (1994) 258–261. https://doi.org/10.2320/matertrans1989.35.258.

[15] D. Mattia, M. Desmaison-Brut, S. Dimovski, Y. Gogotsi, J. Desmaison, Oxidation behaviour of an aluminium nitride–hafnium diboride ceramic composite, Journal of the European Ceramic Society. 25 (2005) 1789–1796. https://doi.org/10.1016/j.jeurceramsoc.2004.12.011.

[16] S.V. Schneider, M. Desmaison-Brut, Yu.G. Gogotsi, J. Desmaison, Oxidation behaviour of a hot isostatically pressed TiB_2-AlN composite, Key Engineering Materials. 113 (1995) 49–58. https://doi.org/10.4028/www.scientific.net/KEM.113.49.

[17] K. Suganuma, T. Fujita, N. Suzuki, K. Niihara, Aluminium composites reinforced with a new aluminium borate whisker, Journal of Materials Science Letters. 9 (1990) 633–635. https://doi.org/10.1007/BF00721787.

[18] K. Suganuma, T. Fujita, G. Sasaki, N. Suzuki, Evaluation of strength and heat-resistance for aluminum-borate whisker reinforced AC8A aluminum alloy

composite, Journal of Japan Institute of Light Metals. (1991) 270–275. https://doi.org/10.2464/JILM.41.270.

[19] H.K. Lee, S. Zerbetto, P. Colombo, C.G. Pantano, Glass–ceramics and composites containing aluminum borate whiskers, Ceramics International. 36 (2010) 1589–1596. https://doi.org/10.1016/j.ceramint.2010.02.039.

[20] G.N. Morscher, D.R. Bryant, R.E. Tressler, Environmental durability of BN-based interphases (for SiC_f/SiC_m composites) in H_2O containing atmospheres at intermediate temperatures, in: Proceedings of the 21st Annual Conference on Composites, Advanced Ceramics, Materials, and Structures—A: Ceramic Engineering and Science Proceedings, John Wiley & Sons, Ltd, 1997: pp. 525–534. https://doi.org/10.1002/9780470294437.ch58.

[21] N. Jacobson, S. Farmer, A. Moore, H. Sayir, High-temperature oxidation of boron nitride: i, monolithic boron nitride, Journal of the American Ceramic Society. 82 (2004) 393–398. https://doi.org/10.1111/j.1551-2916.1999.tb20075.x.

[22] M. Ihara, K. Imai, K. Fukunaga, N. Yoshida, Crystal structure of boroaluminate, $9Al_2O_3$ $2B_2O_3$, Journal of the Ceramic Association, Japan. 88 (1980) 77–84.

[23] G. With, H.H.M. Wagemans, Ball-on-ring test revisited, Journal of the American Ceramic Society. 72 (1989) 1538–1541. https://doi.org/10.1111/j.1151-2916.1989.tb07702.x.

[24] F. Ren, E.D. Case, A. Morrison, M. Tafesse, M.J. Baumann, Resonant ultrasound spectroscopy measurement of Young's modulus, shear modulus and Poisson's ratio as a function of porosity for alumina and hydroxyapatite, Philosophical Magazine. 89 (2009) 1163–1182. https://doi.org/10.1080/14786430902915388.

[25] A. Bellosi, E. Landi, A. Tampieri, Oxidation behavior of aluminum nitride, Journal of Materials Research. 8 (1993) 565–572. https://doi.org/10.1557/JMR.1993.0565.

[26] H.-E. Kim, A. J. Moorhead, Oxidation behavior and flexural strength of aluminum nitride exposed to air at elevated temperatures, Journal of the American Ceramic Society. 77 (1994) 1037–1041. https://doi.org/10.1111/j.1151-2916.1994.tb07264.x.

[27] J.W. Lee, I. Radu, M. Alexe, Oxidation behavior of AlN substrate at low temperature, Journal of Materials Science: Materials in Electronics. 13 (2002) 131–137. https://doi.org/10.1023/A:1014377132233.

[28] A. Maghsoudipour, F. Moztarzadeh, M. Saremi, J.G. Heinrich, Oxidation behavior of AlN–Al_2O_3 composites, Ceramics International. 30 (2004) 773–783. https://doi.org/10.1016/j.ceramint.2003.10.004.

[29] C.-T. Yeh, W.-H. Tuan, Oxidation mechanism of aluminum nitride revisited, Journal of Advanced Ceramics 6 (2017) 27–32. https://doi.org/10.1007/s40145-016-0213-1.

[30] D. Suryanarayana, Oxidation kinetics of aluminum nitride, Journal of the American Ceramic Society. 73 (1990) 1108–1110. https://doi.org/10.1111/j.1151-2916.1990.tb05167.x.

[31] P.J.M. Gielisse, W.R. Foster, The system Al_2O_3–B_2O_3, Nature. 195 (1962) 69–70. https://doi.org/10.1038/195069a0.

[32] M. Coëffe-Desvaux, T. Tabares-Medina, N. Pradeilles, P. Marchet, M. Joinet, A. Maitre, New insight on the effect of yttria-based secondary phases on sintering and electrical behavior of aluminum nitride ceramics, Journal of Materials Engineering and Performance. (2022). https://doi.org/10.1007/s11665-022-06588-9.

[33] D. Huang, Z. Tian, W. Cui, L. Gao, Z. Liu, X. Diao, G. Liu, Effects of Y_2O_3 and yttrium aluminates as sintering additives on the thermal conductivity of AlN ceramic substrates, Ceramics International. 44 (2018) 20556–20559. https://doi.org/10.1016/j.ceramint.2018.07.178.

[34] B.D. Cullity, Elements of X-ray diffraction, Addison-Wesley Publishing Company, 1956.

[35] Y. Li, R.P.H. Chang, Synthesis and characterization of aluminum borate ($Al_{18}B_4O_{33}$, $Al_4B_2O_9$) nanowires and nanotubes, Materials Chemistry and Physics. 97 (2006) 23–30. https://doi.org/10.1016/j.matchemphys.2005.06.023.

[36] C. Cheng, C. Tang, X.X. Ding, X.T. Huang, Z.X. Huang, S.R. Qi, L. Hu, Y.X. Li, Catalytic synthesis of aluminum borate nanowires, Chemical Physics Letters. 373 (2003) 626–629. https://doi.org/10.1016/S0009-2614(03)00672-9.

[37] K. Momma, F. Izumi, VESTA 3 for three-dimensional visualization of crystal, volumetric and morphology data, Journal of Applied Crystallography. 44 (2011) 1272–1276. https://doi.org/10.1107/S0021889811038970.

[38] P. Hartman, W.G. Perdok, On the relations between structure and morphology of crystals. I, Acta Crystallographica. 8 (1955) 49–52. https://doi.org/10.1107/S0365110X55000121.

[39] P. Hartman, W.G. Perdok, On the relations between structure and morphology of crystals. II, Acta Crystallographica. 8 (1955) 521–524. https://doi.org/10.1107/S0365110X55001679.

[40] I. Sunagawa, Crystals: Growth, morphology, & perfection, Cambridge University Press, 2007. https://doi.org/10.1017/CBO9780511610349.

[41] F.C. Frank, Capillary equilibria of dislocated crystals, Acta Crystallographica. 4 (1951) 497–501. https://doi.org/10.1107/S0365110X51001690.

[42] K. Maiwa, M. Plomp, AFM observation of barium nitrate (111), and (100), faces: Spiral growth and two-dimensional nucleation growth, Journal of Crystal Growth. (1998) 214–223. https://doi.org/10.1016/S0022-0248(97)00446-6.

[43] Y. Wang, M. Lin, A. Tuel, Hollow TS-1 crystals formed via a dissolution–recrystallization process, Microporous and Mesoporous Materials. 102 (2007) 80–85. https://doi.org/10.1016/j.micromeso.2006.12.019.

[44] S.L. Brantley, S.R. Crane, D.A. Crerar, R. Hellmann, R. Stallard, Dissolution at dislocation etch pits in quartz, Geochimica et Cosmochimica Acta. 50 (1986) 2349–2361. https://doi.org/10.1016/0016-7037(86)90087-6.

[45] W.F. Berg, Crystal growth from solutions, Proceedings of The Royal Society of London. A164 (1938) 79–95. https://doi.org/10.1098/rspa.1938.0006.

[46] M.F. Hernández, G. Suárez, M. Cipollone, M.S. Conconi, E.F. Aglietti, N.M. Rendtorff, Formation, microstructure and properties of aluminum borate ceramics obtained from alumina and boric acid, Ceramics International. 43 (2017) 2188–2195. https://doi.org/10.1016/j.ceramint.2016.11.002.

[47] M.F. Hernández, G. Suárez, C. Baudin, P. Pena Castro, E.F. Aglietti, N.M. Rendtorff, Densification of lightweight aluminum borate ceramics by direct sintering of milled powders, Journal of Asian Ceramic Societies. 6 (2018) 374–383. https://doi.org/10.1080/21870764.2018.1539209.

[48] X. Luan, Y. Zou, X. Hai, H. Bai, Q. Zhang, R. Riedel, L. Cheng, Degradation mechanisms of a self-healing $SiC_{(f)}/BN_{(i)}/[SiC\text{-}B_4C]_{(m)}$ composite at high

temperature under different oxidizing atmospheres, Journal of the European Ceramic Society. 38 (2018) 3804–3813. https://doi.org/10.1016/j.jeurceramsoc.2018.05.001.

[49] L. Quemard, F. Rebillat, A. Guette, H. Tawil, C. Louchet-Pouillerie, Self-healing mechanisms of a SiC fiber reinforced multi-layered ceramic matrix composite in high pressure steam environments, Journal of the European Ceramic Society. 27 (2007) 2085–2094. https://doi.org/10.1016/j.jeurceramsoc.2006.06.007.

[50] M.B. Ruggles-Wrenn, M.D. Lee, Fatigue behavior of an advanced SiC/SiC ceramic composite with a self-healing matrix at 1300 °C in air and in steam, Materials Science and Engineering: A. 677 (2016) 438–445. https://doi.org/10.1016/j.msea.2016.09.076.

[51] Y. Liu, L. Zhang, L. Cheng, X.L.W. Yang, W. Zhang, Y. Xu, Q. Zeng, Preparation and oxidation resistance of 2D C/SiC composites modified by partial boron carbide self-sealing matrix, Materials Science and Engineering: A. 498 (2008) 430–436. https://doi.org/10.1016/j.msea.2008.08.022.

[52] F. Nozahic, C. Estournès, A.L. Carabat, W.G. Sloof, S. van der Zwaag, D. Monceau, Self-healing thermal barrier coating systems fabricated by spark plasma sintering, Materials & Design. 143 (2018) 204–213. https://doi.org/10.1016/j.matdes.2018.02.001.

[53] B. Lawn, Fracture of brittle solids, 2nd ed., Cambridge University Press, Cambridge, 1993. https://doi.org/10.1017/CBO9780511623127.

Chapter 5

ALUMINOSILICATE DEGRADATION IN ACIDIC ENVIRONMENTS

The contents of this chapter are part of a manuscript in preparation titled "From Acidic Soil to Acid Rain: Chemical Transformations of Clay Mineral Surfaces from Exposure to Sulfuric Acid" by C. S. Chari, J. E. Heimann, Z. Rosenzweig, J. W. Bennett and K. T. Faber. C. S. Chari led the experimental portion of the work, supervised by Faber. J. E. Heimann led the computational portion of the work, co-supervised by Bennett and Rosenzweig. All authors were involved in designing the work. All authors were involved in preparing the manuscript.

5.1. Introduction

Aluminosilicate minerals are found abundantly in nature under an array of different chemistries and crystal structures, from phyllosilicates like mica to tectosilicates like feldspar. Kaolinite ($Al_2Si_2O_5(OH)_4$) is an example of a layered phyllosilicate mineral that, due to its plasticity and common geographic occurrence, has been used throughout history as a main ingredient in the production of pottery [1]. This versatile clay mineral can dehydrate at high temperatures, forming amorphous metakaolin ($Al_2Si_2O_7$) above 600 °C and recrystallizing into a spinel-structure above 900 °C and mullite above 1000 °C [2,3]. Kaolinite and its high-temperature products are therefore important aluminosilicate minerals in the study of fired pottery including low-fired pottery, stoneware, and porcelain in the fields of archaeology and cultural heritage science.

The structure of kaolinite consists of stacked layers of silica tetrahedra bonded to alumina octahedra through shared oxygen ions. The layers are connected through hydrogen bonds originating from hydroxyl groups attached to the aluminum ions. Because of their structure, phyllosilicates such as kaolinite have also been widely featured in the biomedical sciences including cosmetics and pharmaceuticals [4–7]. The high adsorption capacity [4], antiseptic nature, and bioactive properties of this clay mineral make it particularly desirable for use in therapeutic delivery [5]. More specifically, nano-engineered clay sheets have become materials of interest in biomedical applications, demonstrating a strong need for a

comprehensive understanding of the surface chemistry of these two-dimensional (2D) clay minerals across a wide range of variable chemical environments that include both acidic and basic pH.

It is not well understood how these 2D aluminosilicate sheet-like structures behave under acidic conditions, let alone the atomistic changes that could happen at their exposed surfaces. This is a problem that also ties in with the geological origin of the clay mineral and the acidity of the soil in which it was generated and/or exposed. These variable conditions will influence the surface structure, and it has been shown that modifications of the surface chemistry of 2D materials have proven to be crucial for engineering tailored nanostructures and properties [8]. For example, incorporating specific functional groups on the surface could influence the electronegativity and adsorption affinity of the 2D material. Thus, chemical alterations at the surface of clay minerals could greatly modify the sought-after properties of the material, making it undesirable for certain applications. Through a different lens, this problem is also of great concern to the archeological sciences, where there is a limited understanding of the degradation mechanism of pottery exposed to acid rain or acidic soils [9–11].

Previous literature on the atmospheric weathering of feldspar has described acid leaching of alkalis and aluminum from the mineral surface, leaving behind a silica-terminated feldspar surface that appears to mitigate further corrosion [12]. A similar process, referred to as dealumination, has also been reported in the literature as being the primary industrial method for producing aluminum sulfate ($Al_2(SO_4)_3$), also known as alum, for wastewater treatment, using sulfuric acid and clay minerals like kaolinite and metakaolin [13,14]. The results of these studies are concerning, as they suggest that alumina-rich surfaces are not completely inert to degradation from acidic environments, as previously thought [15]. Nevertheless, there is currently no detailed understanding of how these processes occur on an atomic-scale, resulting in the need to discern how thermochemical changes from acid interactions can influence the aluminosilicate surface structure. Insights into these processes would be beneficial to the archaeological and cultural heritage sciences, and to the aforementioned industries that utilize naturally occurring clay minerals.

The current study seeks to gain a mechanistic understanding of the acid corrosion process of the phyllosilicates kaolinite and metakaolin using a combined experimental and computational approach. Surface sensitive-techniques like X-ray photoelectron spectroscopy (XPS) and Fourier transform infrared spectroscopy coupled with Attenuated Total Reflectance (ATR-FTIR) are used to experimentally examine chemical alterations of the clay minerals after a week-long exposure to sulfuric acid (H_2SO_4). The surface changes as well as the dealumination process are further investigated using density functional theory (DFT) to probe the adsorption of H_2SO_4 and other sulfur-containing adsorbates on an atomistic level. The results from the surface reactivity study are then combined with a thermodynamics model to better understand acid-induced transformations of the mineral surfaces. Ultimately, we compare the dealumination of kaolinite to metakaolin surfaces under a variety of pH conditions, revealing environmental requirements for preventing acid-based degradation of clay minerals and 2D oxide materials.

5.2. Methods

5.2.1. H_2SO_4 Exposure

5.2.1.1. Materials

Powders of kaolinite ($Al_2Si_2O_5(OH)_4$, Sigma Aldrich) were used in this study. Metakaolin powders were prepared by heat treating kaolinite to 850 °C for 3h using a high-temperature box furnace (CM Rapid Temp 1700 °C Furnace) in stagnant air. The ramp rates used were 3 °C/min for both heating and cooling.

Solutions of sulfuric acid (99.999% H_2SO_4, Sigma-Aldrich) were prepared in the following concentrations: 1 M (pH 0), 0.01 M (pH 2), 0.0001 M, (pH 4) and 0.000001 M (pH 6). Powders of kaolinite (0.1 g) were immersed into borosilicate vials containing 5-mL solutions of each H_2SO_4 concentration. Each vial contained a Pyrex-coated magnetic stir bar rotating at 350 rpm, included to ensure powders were uniformly exposed to the acid. The process was repeated for powders of metakaolin.

After one week of the acid bath exposure, powders were separated from the H_2SO_4 solutions using a porcelain Buchner funnel and filter paper (Whatman, Grade No. 1). The recovered powders were then washed with deionized water to remove excess sulfuric acid from their surface. The powders were then air dried before characterization.

The remaining H_2SO_4 solutions were kept after the acid bath exposures, and a white precipitate could be extracted from said solutions with the addition of ethanol. The characterized precipitate was obtained by adding 25-mL of ethanol dropwise to 5-mL of the 1M H_2SO_4 remaining from a metakaolin acid bath experiment. A Pyrex-coated magnetic stir bar was used to aid the extraction process, rotating at 350 rpm.

5.2.1.2. Characterization

X-ray photoelectron spectroscopy (Kratos Ultra XPS) was used to quantify the relative ratio of Si wt.% to Al wt.% at the surface of the aluminosilicate layers. This was achieved by measuring the Al 2p and Si 2p peaks at a pass energy of 20 eV, with a total of 40 scans per peak for each sample. The peaks were calibrated using the C 1s peak at 284.8 eV. Two samples were measured for each condition. The average is reported, with the error term representing one standard deviation. The captured data were analyzed using CasaXPS software. Fourier-transform infrared spectroscopy (Thermo-Nicolet iS50 FTIR) coupled with Attenuated Total Reflectance (DuraScope ATR unit) were used to monitor changes in the bond structure of the aluminosilicate layers on a surface-sensitive level and to characterize the precipitate. X-ray powder diffraction (XRD, Rigaku SmartLab) was used to identify the crystalline precipitate. The positions of the diffraction peaks were calibrated using Si powder as a standard. The XRD data were interpreted using reference diffraction patterns of hydrated $Al_2(SO_4)_3$ from the literature [16,17].

5.2.2. SO_2 Exposure

5.2.2.1. Materials

Green body tiles of kaolinite ($Al_2Si_2O_5(OH)_4$, Sigma Aldrich) were prepared via slip casting using a graphite mold, and subsequently air dried for at least one day before firing. The kaolinite tiles and powders were fired at temperatures ranging from 300 °C to 900 °C

for 3h using a high-temperature box furnace (CM Rapid Temp 1700 °C Furnace) in stagnant air. The ramp rates used were 3 °C/min for both heating and cooling.

An acid-resistant exposure chamber was constructed using a SiC tube and stainless-steel tubing, as illustrated in Figure 5.1. The SO_2 source was a mixture of air mixed with 1% SO_2 (1% Sulfur Dioxide Balance Air Size 150A, Airgas). Samples were exposed to SO_2 in the chamber for the duration of three days. Two water-filled conical flasks were used to collect SO_2 remains, trapping the off-gas inside the flasks as H_2SO_4. The exposure chamber and the flasks were kept inside a fume hood for improved ventilation in order to minimize any hazardous leaks.

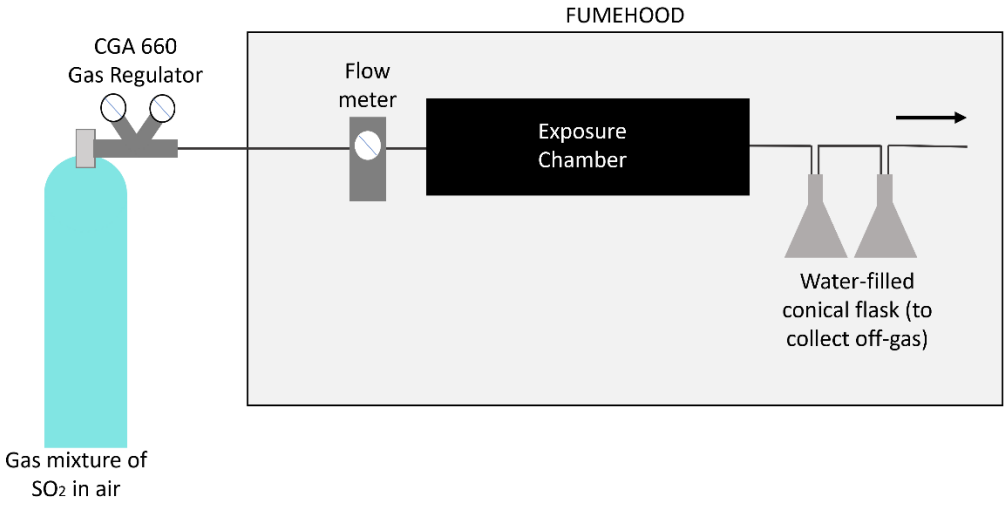

Figure 5.1. Schematic of SO_2 exposure set-up, showing gas regulator, flow meter, stainless-steel tubing, SiC tube acting as the exposure chamber, and two water-filled conical flasks.

5.2.2.2. Characterization

ATR-FTIR as well as XRD analyses were performed on the fired powders and tiles. Hardness measurements were carried out on the tiles using a Vickers indenter and a load of 2.94 N. Archimedes' technique was used to measure the open porosity of the fired tiles, using Eqn. 5.1:

$$\text{Porosity}\ (\%) = \frac{m_s - m_o}{m_s - m_{sat}} \tag{5.1}$$

where m_s is the mass of the tile suspended in water, m_o is the mass of the dry tile in air, and m_{sat} is the mass of the water-saturated tile in air.

5.2.3. Computational Details

5.2.3.1. Bulk Structures

All calculations described here employed periodic DFT methods [18,19] and were carried out using Quantum Espresso, an open-source software package [20,21]. All atoms were represented using GBRV-type ultrasoft pseudopotentials [22,23]. A plane-wave cutoff of 40 Ry and charge density cutoff of 320 Ry were employed for all calculations, in line with similar surface studies [24–26]. Bulk structural relaxations used a 6x6x6 k-point grid [27], and the energy convergence criteria for self-consistent relaxations is $5x10^{-6}$ eV. Geometry optimization of all surface-adsorbate interactions did not include fixing any layers; all atoms were allowed to fully relax [28]. All calculations were performed at the GGA level using the Wu-Cohen (WC) modified PBE-GGA exchange correlation functional for solids [29,30]. The atomistic pictures presented here were generated using XCrySDen [31].

5.2.3.2. Surface Models

Using the fully relaxed bulk kaolinite structure, a super cell repeat of 2x2x1 was generated. The supercell was cleaved along the [001] direction to create a supercell slab with only one kaolinite repeat in the [001] direction. In this surface slab, Al-O(H) octahedra were exposed as the top surface and Si-O(H) tetrahedra were exposed as the bottom surface. A side view picture along the [010] axis of the fully relaxed kaolinite is shown in Figure 5.2a, next to the top-down view along the [001] axis in Figure 5.2b.

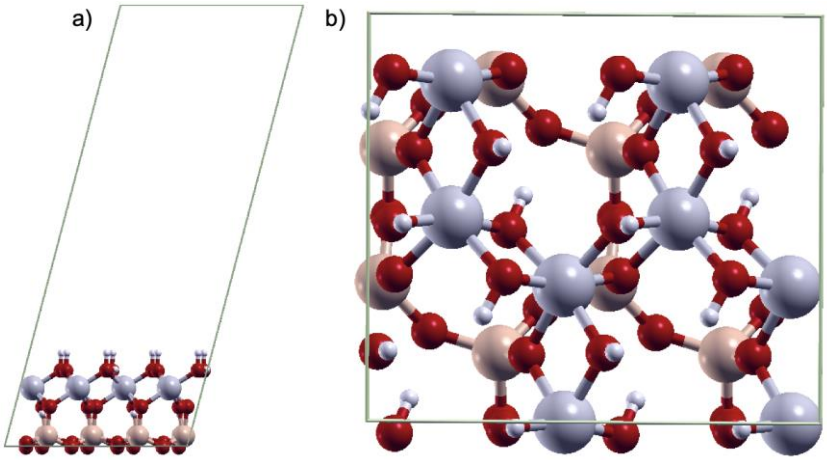

Figure 5.2. Fully relaxed kaolinite surface model: a) Side view along [010] axis, and b) top-down view along the [001] axis. Aluminum, silicon, oxygen, and hydrogen are shown in gray, peach, red, and white, respectively. The unit cell is shown in green.

5.2.3.3 DFT + Thermodynamics

Combining DFT models and thermodynamics corrections has been essential to mapping changes in surface structure onto experiments performed across a wide range of environmental conditions. The range has varied from ultrahigh vacuum [32–34] to regimes of definite temperature and pressure, with variable humidity [35] and the inclusion of either implicit [36] or explicit [37] solvation effects. To better understand surface responses beyond vacuum, specifically under aqueous conditions, the DFT and thermodynamics model must account for processes like making and breaking bonds as well as solvation and redox [38]. Here the DFT + Solvent Ion model [39] was employed to compute the pH-dependent thermodynamics associated with surface transformations including small molecule adsorption, ion release, and surface healing. This model can break an overall reaction cycle into elementary reaction steps which can be partitioned between theory (as DFT) and experiment (as tabulated data [40]) to compute overall ΔG_{tot}. It does so by combining DFT-computed total energies as ΔG_1 (making and breaking bonds) with experimentally determined changes in free energy in aqueous solutions as ΔG_2 (solvation and redox), where ΔG_2 contains Nernstian terms for changes in pH, applied potential, and concentration.

Zero-point energy (ZPE) correction terms were added to the DFT total energies of supercell surface slabs to obtain ΔG_1, as described in Refs. [24,25] and in the style of Ref. [39]. For the solvent ion term, $\Delta G_2 = \Delta G^0_{SHE} - n_e e U_{SHE}$ - $2.303 n_H$ + kT pH + kT ln $a(H_xAO_y)^{z-}$, where ΔG^0_{SHE} was the change in free energy of formation at standard state, eU_{SHE} was the applied potential relative to the standard hydrogen electrode, and $a(H_xAO_y)^{z-}$ were the concentrations of the dissolved constituent ions (assumed to be $1x10^{-6}$ M). The terms n_e and n_{H+} were the respective number of electrons and protons involved in the chemical reactions required for surface atom release.

Values of ΔG^0_f were obtained from Ref. [40]. At conditions of $eU_{SHE} = 0$ and $a = 1x10^{-6}$ M, DFT-calculable Pourbaix diagrams [41] showed that increasing pH from 0.5 to 6 changes the preferred aqueous species of Al from Al^{3+} to $AlOH^{2+}$ at pH 5. Over the same range of pH values, the preferred aqueous species of sulfur (S) changes from HSO_4^{-1} to SO_4^{2-} at pH 2. For this series, each oxygen atom present in the aqueous species required the addition of 1 ΔG^0_{SHE} (O), which was -2.46 eV, to the ΔG^0_f values obtained from Ref. [40]. This converted each ΔG^0_f into a ΔG^0_{SHE} per species, which was added into the expression for ΔG_2. The expressions for ΔG_2 for each species are shown in Section C.1.1 of Appendix C. They are given relative to the standard states of these elements (O_2 and H_2 gas). This is discussed further in Section S2 of the Supplementary Information of Ref. [42].

While the DFT + Solvent Ion model has already been used to investigate cation release from delafossites and carbonates [25,26,35,42–44] and adsorption of ions on mineral oxides [45,46], it has not yet been used to probe the effects of sulfurous adsorbates on kaolinite. Here, the model is used to compute the pH-dependent thermodynamics associated with the adsorption and release of sulfur-containing adsorbates on kaolinite, partially dehydrated kaolinite, and metakaolin surfaces in aqueous environments.

5.3. Results and Discussion

5.3.1 H_2SO_4 Exposure

5.3.1.1 Aluminosilicate Powders

Powders of kaolinite and metakaolin were studied using XPS to determine the relative ratio of Si to Al on the aluminosilicate surface. Figure 5.3a shows a typical survey spectrum for kaolinite and metakaolin powders, where the Al 2p peak (Figure 5.3b) and Si 2p peak (Figure 5.3c) were used to determine the Si/Al ratio (wt.%/wt.%) of samples exposed to different pH conditions. A more detailed summary of the spectra and collected data is outlined in the Appendix C.

Indicated in Figure 5.3d, the neutral (pH 7) reference powders of the aluminosilicates have comparable ratios to one another, where Si/Al is 1.40 ± 0.01 in kaolinite, and 1.38 ± 0.03 in metakaolin. Figure 5.3d demonstrates that this ratio changes significantly after the aluminosilicates are exposed to H_2SO_4 baths of different concentrations. In fact, there is a gradual increase in the Si-content at the surface of the powders with decreasing pH. The magnitude of this trend, however, varies greatly between kaolinite and metakaolin.

In kaolinite, the increase in the ratio of Si/Al is shallow, reaching a maximum value of 1.56 ± 0.01 when the pH of the acid bath is 0. This indicates that, under highly concentrated H_2SO_4 environments, there is a measurable loss of Al from kaolinite surfaces. Previous literature on the production of alum for water-treatment [13,14] indicates that this loss of Al is due to the formation of $Al_2(SO_4)_3$ during the acid exposure, described by:

$$Al_2Si_2O_5(OH)_{4(s)} + 3H_2SO_{4(aq)} \rightarrow Al_2(SO_4)_{3(aq)} + 2SiO_{2(s)} + 5H_2O_{(l)} \qquad (5.2)$$

Thus, within the first 1.4 nm from the surface (see Appendix C for estimation on analysis depth), the kaolinite powders are steadily dissociating and reacting to form $Al_2(SO_4)_3$ and SiO_2 with increasing acidity. We hypothesize that the sulfate salt dissolves in the acid bath solution, leaving behind a silica-rich surface layer on kaolinite that could be detected with XPS, as shown in Figure 5.3d.

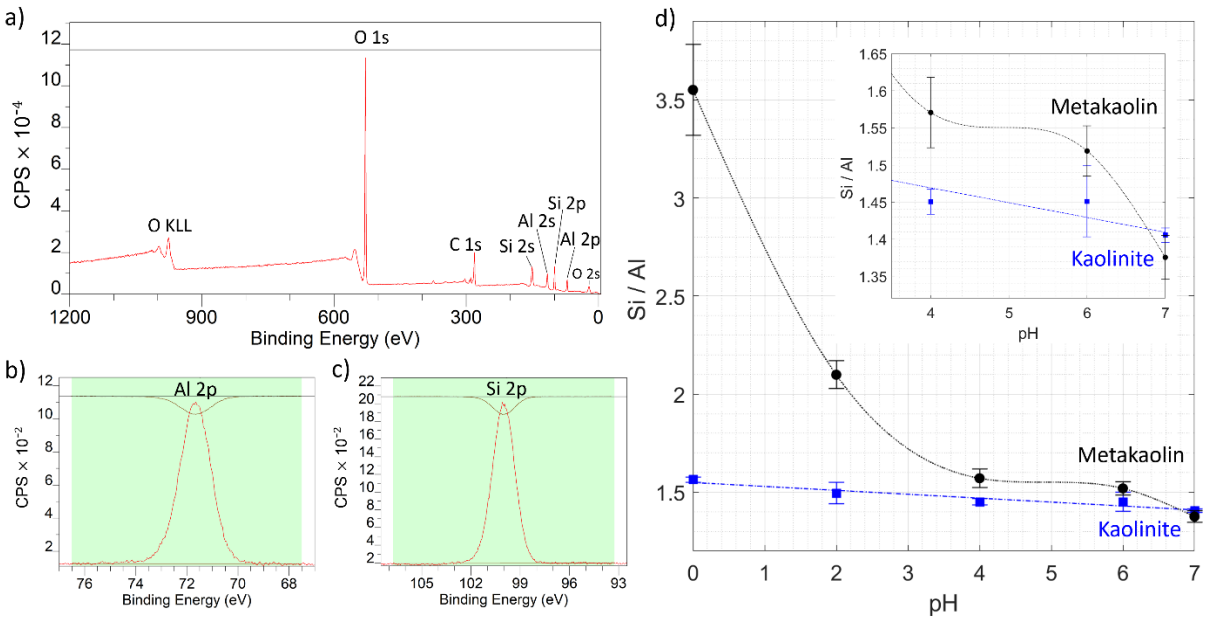

Figure 5.3. XPS data analysis: a) Representative XPS survey spectrum of the aluminosilicate powders, as well as representative spectra of the b) Al 2p peak and c) Si 2p peak. Example spectra shown in a)-c) are of reference kaolinite. d) Ratio of Si wt.% and Al wt.% as a function of pH for H_2SO_4 exposures of kaolinite (■) and metakaolin (●).

In metakaolin, an analogous chemical transformation is observed with exposures to H_2SO_4 solutions of pH 6 and 4, as seen in the inset in Figure 5.3d, where metakaolin appears to experience a marginally greater loss of Al than kaolinite. In fact, the Si/Al ratio of metakaolin at pH 6 is 1.52 ± 0.03, approximating the value seen in kaolinite at pH 0. As with kaolinite, previous literature [13,14] implies that the loss of Al from the metakaolin surface is due to the formation of $Al_2(SO_4)_3$ as follows:

$$Al_2Si_2O_{7(s)} + 3H_2SO_{4(aq)} \rightarrow Al_2(SO_4)_{3(aq)} + 2SiO_{2(s)} + 3H_2O_{(l)} \qquad (5.3)$$

Strikingly, the Si/Al ratio of metakaolin increases significantly to 2.10 ± 0.07 at pH 2 and then further to 3.55 ± 0.23 at pH 0 (Figure 5.3d). This suggests that the metakaolin surface is capable of silicifying to a larger extent than kaolinite surfaces and that Reaction (5.3) is favored at a pH lower than 4. It is important to note that S 2p peaks were not identified in

any of the XPS survey spectra, indicating that the sulfate salts likely dissolved in the acid bath to generate the silica-terminated surfaces on the aluminosilicate powders analyzed with XPS.

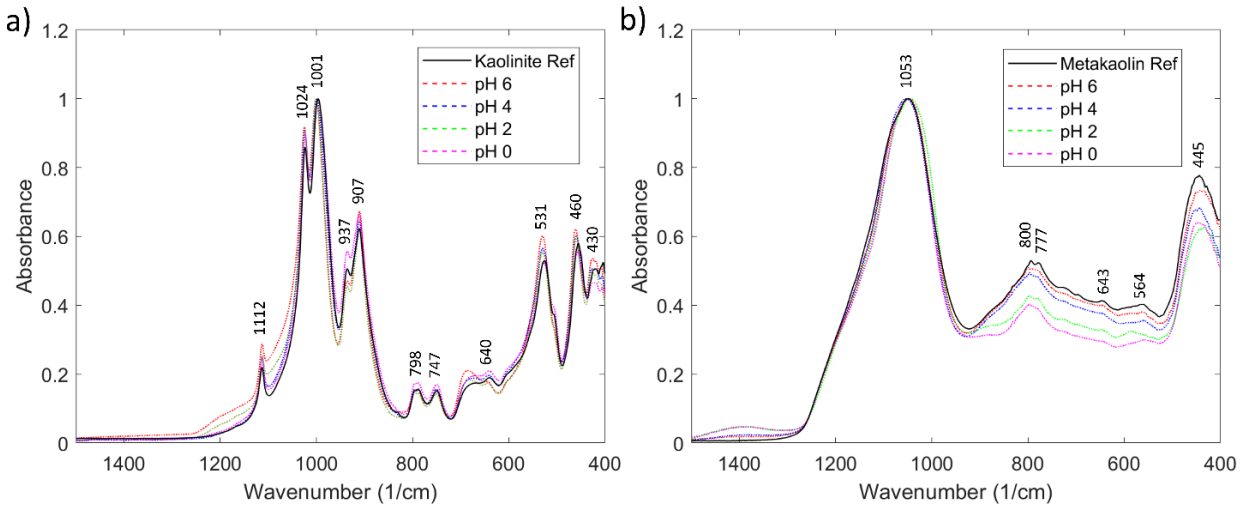

Figure 5.4. ATR-FTIR spectra of a) kaolinite and b) metakaolin, including signatures of reference powders and powders exposed to H_2SO_4 solutions of pH 6, 4, 2, and 0.

ATR-FTIR was then used to further understand the changes in the surface chemistry of kaolinite and metakaolin exposed to H_2SO_4. Figure 5.4a shows the chemical signatures of the reference kaolinite compared to kaolinite exposed to different concentrations of H_2SO_4 solutions. The positions of most sharp peaks remain constant in all samples, with similar absorbance intensities. These peaks correspond to Si-O bands at 1112 cm^{-1}, 1024 cm^{-1}, 1001 cm^{-1}, 460 cm^{-1} and 430 cm^{-1}; Al-OH bands at 937 cm^{-1} and 907 cm^{-1}; and Al-O-Si bands at 798 cm^{-1}, 747 cm^{-1}, 640 cm^{-1} and 531 cm^{-1}, which match closely with previous results from the literature [47]. It should be noted that a measurable shift towards larger wavenumbers is visible in Si-O bands located at both 460 cm^{-1} and 430 cm^{-1}. This slight shift indicates that exposures to acidic environments can alter the Si-O bond length, causing it to marginally decrease. However, the similarities in the intensities and positions of all other peaks suggest that, at large, the pH does not significantly impact the kaolinite structure. This echoes the XPS results seen in Figure 5.3d, where the trend of increasing Si/Al with acidity is shallow in kaolinite, demonstrating minimal chemical changes to the surface with minimal dealumination occurring.

In contrast, the chemical signature of the reference metakaolin compared to metakaolin exposed to different concentrations of H_2SO_4 solutions (Figure 5.4b) exhibits peaks that are much broader than those in the kaolinite spectra. This is due to the amorphous nature of metakaolin that results in a wider distribution of bond lengths of Si-O and Al-O-Si and an absence of Al-OH. The positions of such broad peaks remain similar in all samples; however, there is a clear variation in the absorbance of Si-O bands located near 445 cm^{-1}, where the absorption intensity steadily decreases with increasing acidity. This indicates the occurrence of acid-induced alterations to the metakaolin surface, much clearer than previously observed in kaolinite.

Additionally, there is a notable decrease in the absorbance of Al-O-Si bonds positioned at 800 cm^{-1}, 777 cm^{-1}, 643 cm^{-1} and approximately at 564 cm^{-1} as the acidity of the environment increases. This is indicative of Al-O-Si bond breaking with decreasing pH (increasing acidity), potentially due to dealumination as illustrated in Reaction (5.3). On closer inspection, Figure 5.4b reveals minimal signs of dealumination at pH 4 and 6. This is especially evident in contrast to the spectra at pH 2 and 0, where the breakage of Al-O-Si bonds is noticeable compared to the reference spectrum. Consistent with XPS data shown in Figure 5.3d, these results indicate that metakaolin degradation is enhanced at a pH environment lower than 4. Another notable observation is that the peaks associated with Si-O bonds, positioned at 1053 cm^{-1} and 445 cm^{-1}, have higher absorbance than the Al-O-Si bands at a pH of 2 or lower, implying that the metakaolin surface is becoming relatively richer in silica as dealumination progresses.

5.3.1.2 Remaining Acid Bath Solution

Upon the completion of the acid bath exposures, a white precipitate could be extracted from the H_2SO_4 solutions. ATR-FTIR was used to identify the precipitate, which was found to consist largely of amorphous silica, with peaks corresponding to Si-O bands centered at 1065 cm^{-1}, 797 cm^{-1}, and 453 cm^{-1} (Figure 5.5a), in agreement with values from the literature [48]. In addition, peaks centered at 1665 cm^{-1}, 1141 cm^{-1}, 673 cm^{-1}, as well as 605 cm^{-1} indicated the presence of $Al_2(SO_4)_3$. Peaks corresponding to residual ethanol (used in the extraction process) could also be identified at 1383 cm^{-1} (C-O), 2993 cm^{-1} (C-H), and 3366 cm^{-1} (O-H), the latter of which may also be from hydrated $Al_2(SO_4)_3$. These

results are corroborated by XRD (Figure 5.5b), which reveals that the precipitate is a mixture of amorphous silica and hydrated $Al_2(SO_4)_3$ generated by Reaction (5.3).

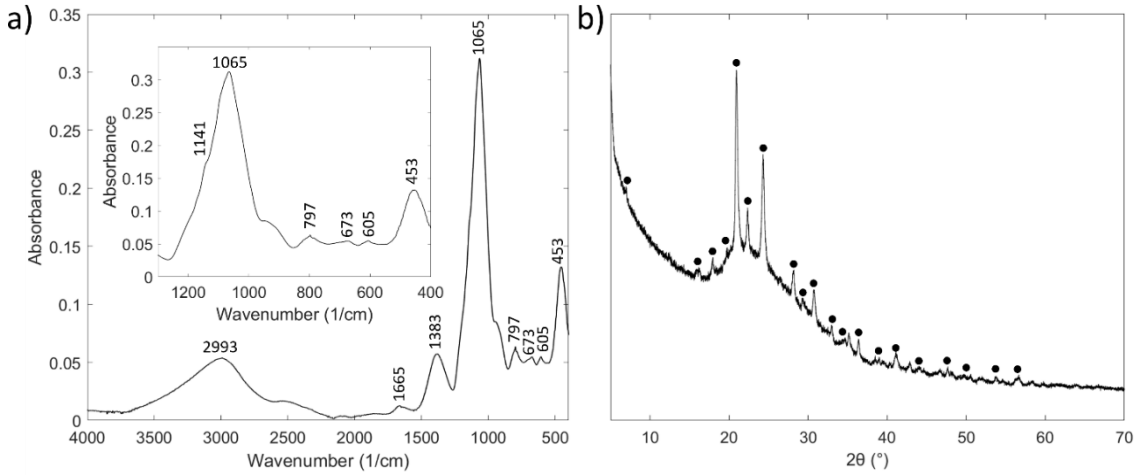

Figure 5.5. Spectra of precipitate obtained from exposing metakaolin to 1M H_2SO_4, including a) ATR-FTIR and b) XRD, showing amorphous silica background and hydrated $Al_2(SO_4)_3$ peaks (●).

The results of these findings imply that metakaolin, which is fundamentally heat-treated kaolinite, is prone to considerable chemical alterations from exposures to H_2SO_4, a pollutant that is frequently found in acidic soils and acid rain environments. Interactions between H_2SO_4 and the Al cations on metakaolin surfaces lead to Al-O-Si bond breakage as Al leaches out of the material in the form of $Al_2(SO_4)_3$, resulting in a silica-terminated surface (Figure 5.3d).

Our results also demonstrate that amorphous SiO_2 could be extracted from the remaining acid bath, pointing to the additional degradation of the silica-rich layer during the week-long experiment. It is possible that the experimental setup used here is partially responsible for this observation, as the powders were constantly stirred within the acid bath solutions for the duration of the experiment. This could cause the chemically altered surfaces to physically break by force. Despite the extraction of amorphous SiO_2, the results outlined in Figure 5.3d and Figure 5.4a-b show remarkable signs of a silica-rich passivation layer developing on the surface of metakaolin. Due to the chemical stability of silica, this passivation layer could mitigate further corrosion of the powders at a given pH environment.

5.3.2 SO_2 Exposure

5.3.2.1. Firing Temperature

From an archeological and conservation science perspective, the fundamental difference between kaolinite and metakaolin in their interactions with S-rich pollutants is an important finding that motivates further studies on the degradation of low-fired pottery. Primarily, it is important to investigate whether the dealumination process could impact not just powders, but also objects fired at different temperatures. To consider this, kaolinite powders and green bodied tiles were fired at temperatures ranging from 300 °C to 900 °C, and later exposed to vapors of SO_2.

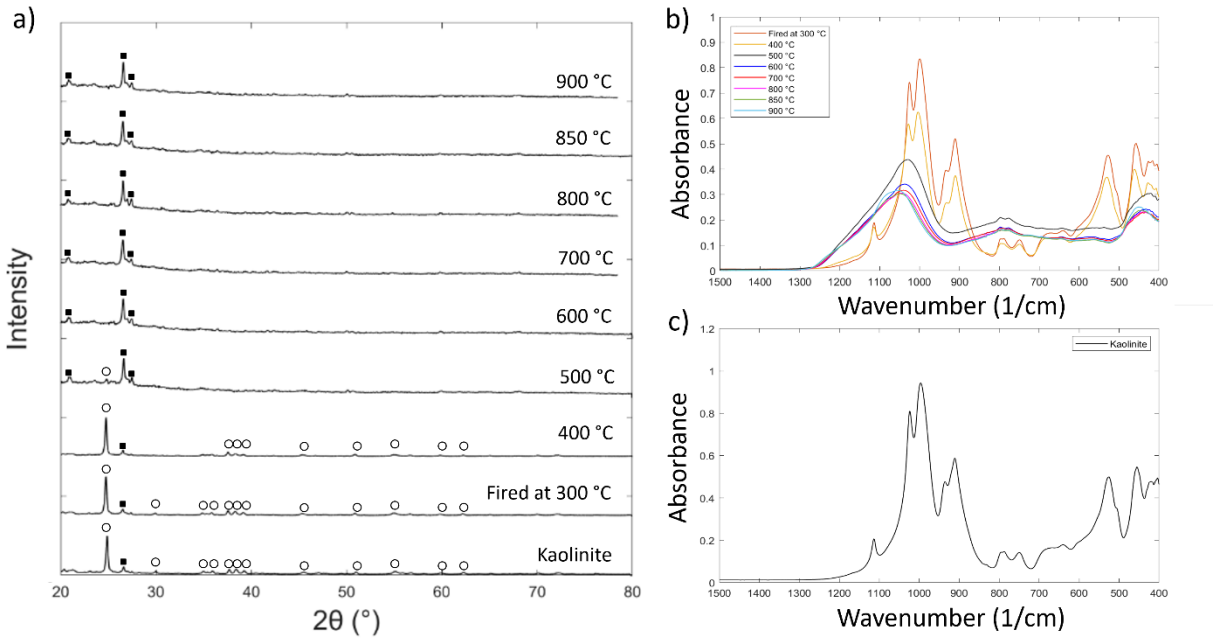

Figure 5.6. Spectra of heat-treated kaolinite, fired at temperatures ranging from 300 °C to 900 °C, including a) XRD and b) ATR-FTIR. c) ATR-FTIR spectra of as-purchased kaolinite. Note that XRD spectra shows presence of kaolinite (○) and quartz (■).

X-ray diffraction spectra shown in Figure 5.6a highlight the evolution of kaolinite into metakaolin. Samples fired at 300 °C and 400 °C have preserved the crystalline structure of kaolinite. Samples fired at 500 °C retain small amounts of the kaolinite structure, however at this temperature the majority of the material converts into amorphous metakaolin. Above 500 °C, traces of kaolinite are fully transformed into metakaolin, and the only crystalline

component detected is from the quartz traces that were originally present in the as-purchased kaolinite. Similarly, ATR-FTIR spectra in Figures 5.6b-c indicate that samples fired at 300 °C and 400 °C have a comparable structure to kaolinite, however with less intense Al-OH bands at 937 cm^{-1} and 907 cm^{-1}. At firing temperatures of 500 °C or higher, the spectrum starts to resemble the fingerprint of metakaolin, previously seen in Figure 5.4b. Notably, the position of Si-O bands at 1053 cm^{-1} appears to shift towards higher wavenumber as the firing temperature increases, illustrating the gradual conversion of the material into an amorphous structure. The XRD and ATR-FTIR spectra of the fired powders were identical to the spectra of the fired tiles.

The observations seen in Figure 5.6 allow us to categorize structures based on their firing temperature: (i) kaolinite is the raw clay, (ii) partially dehydrated kaolinite is observed at 300 °C and 400 °C, and (iii) metakaolin is observed at 500 °C or higher.

In order to examine how the mechanical properties of the tiles changed with firing temperature, the Vickers hardness of the fired tiles were measured, shown in Figure 5.7a-b. In general, the metakaolin tiles (500 °C and above) have a hardness comparable to talk (1 on the Mohs scale), with values rising exponentially above 800 °C due to sintering and densification effects. The hardness of the partially dehydrated kaolinite tiles (300 °C and 400 °C) are significantly lower, as a consequence of the hydroxylated sheet-like structure that facilitates the compression of the material. The porosity of the tiles, seen in Figure 5.7c, similarly depends on the firing temperature of the tile. The porosity of metakaolin tiles decreases down to 54.6 ± 1.3 % with increasing temperature, with the most porous tile being created at 500 °C. The porosity of the partially dehydrated kaolinite tile (400 °C) is comparatively higher, with values reaching 61.6 ± 2.9 %. Note that it was not possible to measure the porosity of the tile fired at 300 °C, due to it disintegrating in water upon immersion. It is expected that the high open porosities seen in all samples (Figure 5.7c) directly influence the low hardness of the tiles (Figure 5.7b).

In comparison, the expected hardness of low-fired pottery, more specifically that of low-fired earthenware objects, is cited as being close to 4 on the Mohs scale, however this is largely dependent on the composition of the original clay which might additionally contain feldspar and glass-forming materials like lime and quartz to aid with densification [49].

Our findings in Figure 5.7a-b provide a fundamental understanding of how the hardness of pure kaolinite tiles are affected by firing temperatures. The intention of this study is to provide a base assessment that can be built on in future experiments, when eventually more complex low-fired systems (e.g., containing additions of feldspar, mica, silica, iron oxides etc.) will be investigated.

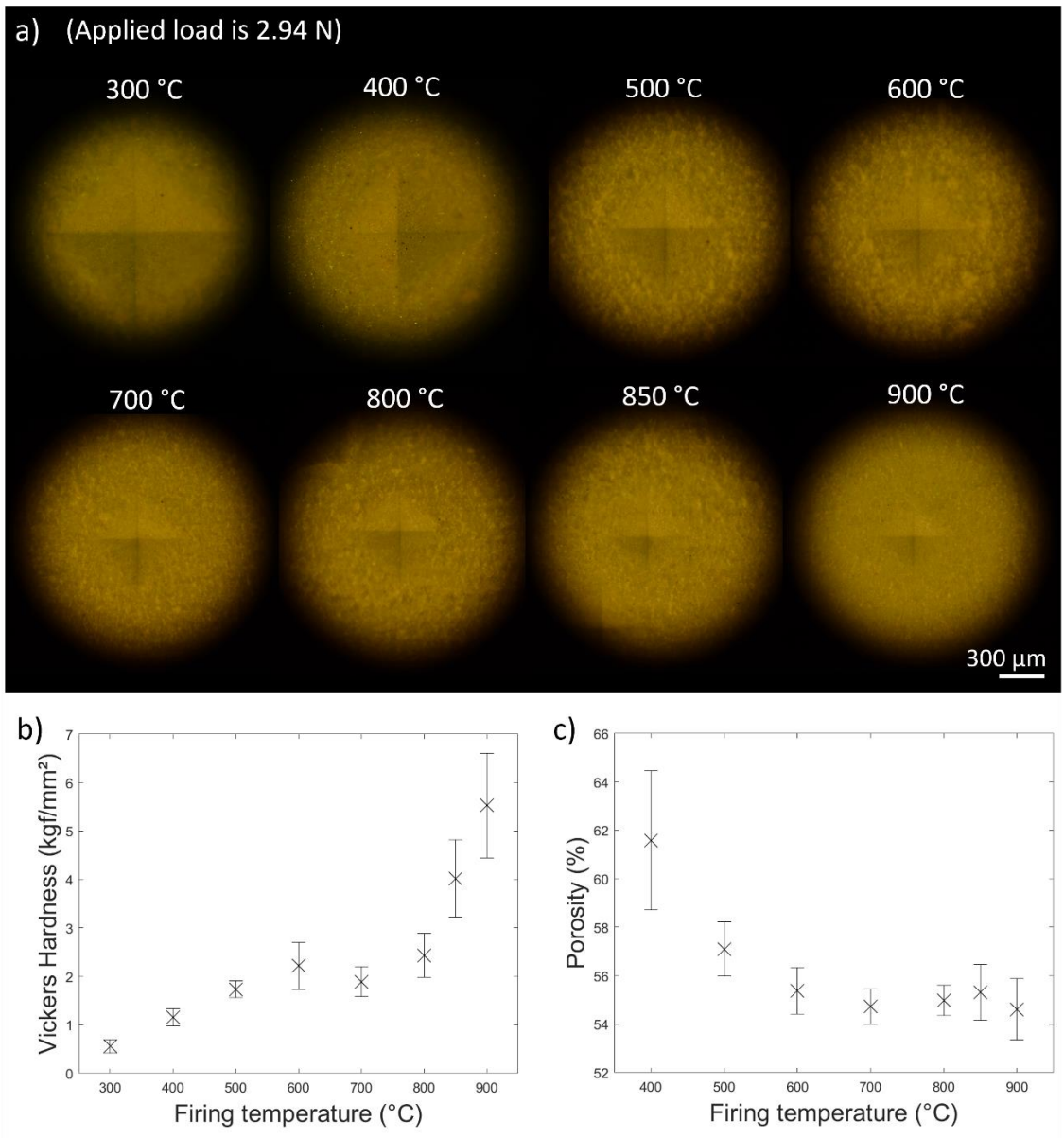

Figure 5.7. Hardness of tiles fired at temperatures ranging from 300 °C to 900 °C: a) micrograph of indentations and b) Vickers hardness. c) Porosity of tiles measured using Archimedes' technique.

The fired tiles were exposed to SO_2 mixed with air, as illustrated in Figure 5.1. Figure 5.8a shows the resulting ATR-FTIR spectra and compares it to the original spectra before the exposure. The spectrum of the partially dehydrated kaolinite sample (400 °C) is similar to the original, showing identical peak positions and absorption intensities, reminiscent of results seen in Figure 5.4a. In contrast, the spectra of the metakaolin samples (500 °C and above) show a shift in the Si-O bands, located near 1053 cm^{-1} and 438 cm^{-1}, towards higher wavenumbers after exposures to SO_2. This shift indicates that the tile surfaces (within 1 µm from the surface) are richer in silica after the SO_2 exposure, a result that could imply the occurrence of dealumination, as previously seen in Figure 5.3.

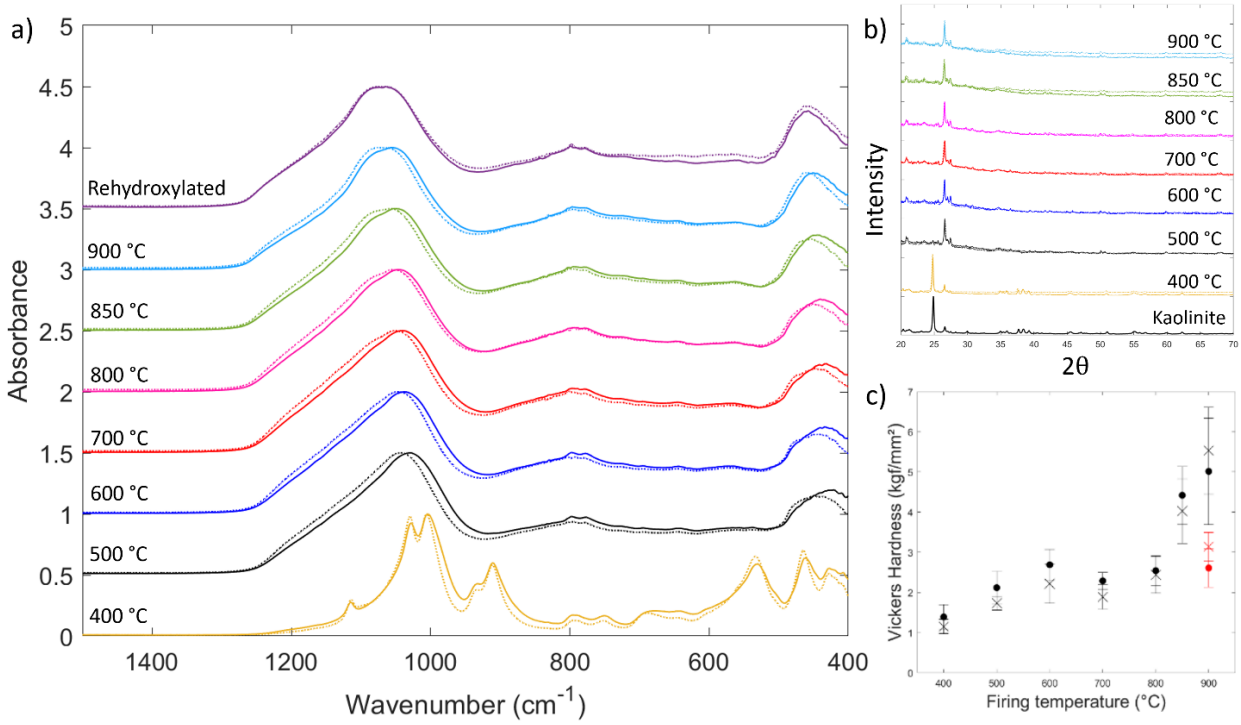

Figure 5.8. Spectra of heat-treated kaolinite, fired at temperatures ranging from 300 °C to 900 °C, before (|) and after (:) exposures to SO_2: a) ATR-FTIR and b) XRD. c) Vickers hardness of tiles before (×) and after (●) exposures to SO_2, including a rehydroxylated sample in red.

Note that the largest shift is observed at 500 °C, where high porosities were observed that could facilitate interactions between SO_2 and the aluminosilicate surface area. However, such a shift is not observed in Figure 5.4b, potentially due to the set-up of the acid bath

experiment where constant stirring caused the silica-rich passivation layer to break down, forming a white precipitate that became separated from the aluminosilicate powders. The absorption intensities of Al-O-Si bands in Figure 5.8 remain largely intact after the SO_2 exposure, suggesting that the pH of the SO_2 environment is approximately equal to 6, based on previous results from Figure 5.4b.

Nevertheless, $Al_2(SO_4)_3$ is not detected in the ATR-FTIR (Figure 5.8a) nor XRD (Figure 5.8b) spectra. It is not fully understood why $Al_2(SO_4)_3$ is not visible, however this might be due: 1) the sulfate salt is present in ppm quantities, which are difficult to detect, 2) the SO_2 concentration was too low, or the environment too dry, for dealumination to take place, 3) a different silicifying process is occurring that is not dealumination. Figure 5.8c shows the hardness of the tiles after the exposure, where it was found that the dry, acidic environment did not alter the hardness in any statistically significant way.

5.3.2.2. Rehydroxylation

In addition to probing the effects of firing temperature, porosity, and environmental pH, it was decided to investigate the effect of environmental humidity on the properties of a fired tile. A tile fired at 900 °C was immersed in water for a week, after which the hardness of the tile was remeasured, seen in Figure 5.8c in red. It was found that the hardness of the tile nearly halved in size after being exposed to extreme humidity. The intake of water into the porous body caused the sample to rehydroxylate and thus revert back to a clay-like consistency as denoted by the softening of the body.

The rehydroxylated tile was subsequently exposed to SO_2 for the duration of 3 days. Figure 5.8a shows the ATR-FTIR spectra of the tile before and after the exposure, demonstrating that the spectrum remained unchanged after the exposure. This is likely a result of preferred interactions between SO_2 and H_2O molecules to form H_2SO_4, temporarily protecting the aluminosilicate from reacting with SO_2 during this short 3-day long exposure. As a result, the rehydroxylated tile did not show any evidence of dealumination. In addition, the exposure to SO_2 mixed with air did not alter the hardness of the rehydroxylated tile in any statistically significant way.

5.3.3. Surface Reactivity Study

To further investigate the interaction of these aluminosilicate clay minerals with H_2SO_4 and other sulfur-containing adsorbates including SO_2, SO_3, and H_2SO_3, we modelled the relevant surface-adsorbate interfaces and calculated the corresponding adsorption energies E_{ads} as follows:

$$E_{ads} = E_{system} - (E_{adsorbent} + E_{adsorbate}) \tag{5.4}$$

where E_{system} is the energy of the interface with the surface (or adsorbent) and adsorbate interacting, $E_{\text{adsorbent}}$ is the energy of just the chosen surface, and $E_{\text{adsorbate}}$ is the energy of the specific adsorbate isolated in vacuum.

In the present work, we explored the reactivity of three clay mineral surfaces: native kaolinite with no defects, a partially dehydrated kaolinite surface ($-H_2O$), and metakaolin ($-2\ H_2O$). For native kaolinite and partially dehydrated kaolinite, the 2x2x1 periodic surface slab was generated as previously reported [50]. The partially dehydrated kaolinite surface was viewed as the first step in a two-part dehydration process in which one water molecule is removed from the surface in each step. Thus, to generate the metakaolin model, an additional water molecule was removed from the partially dehydrated kaolinite surface as shown in Figure 5.9, creating a first-approximation of an amorphous structure on a local level. An additional figure highlighting the location of the removed atoms is provided in the Appendix C.

Table 5.1 provides the calculated adsorption energies for the four chosen sulfur-containing adsorbates on the three surfaces. Depictions of all surface-adsorbate interfaces not shown in the present text or in Ref. [50] are provided in the Appendix C. As shown in Table 5.1, there is a distinct pattern in reactivity among the three surfaces: native kaolinite << partially dehydrated kaolinite < metakaolin. That is, sulfur-containing adsorbates interact least strongly (i.e., have the least negative adsorption energy) with kaolinite and most strongly (i.e., have the most negative adsorption energy) with metakaolin. The partially dehydrated kaolinite surface falls in the middle, generally with a larger difference between the adsorption energy of partially dehydrated surface and native kaolinite than between the partially dehydrated surface and metakaolin. Removing one or two water molecules from

kaolinite generates a more strained, buckled structure that has surface aluminum cations (gray atoms in Figure 5.9) in undercoordinated environments (4- or 5-coordinate) [51]. As evidenced by the calculated adsorption energies in Table 5.1, the dehydration process generates surfaces that are more reactive towards sulfur-containing adsorbates and, consequently, more susceptible to dealumination in the presence of H_2SO_4 (*vide infra*). These findings further support the experimental evidence of acid-induced alterations to the metakaolin surface presented in Figures 5.2d and 5.3. Furthermore, in light of these computational results, we propose that the observed differences in the experimentally determined reactivity of kaolinite and metakaolin are linked to the coordination of aluminum cations at the surface of the material.

Table 5.1. Adsorption energies on the native kaolinite, partially dehydrated kaolinite, and metakaolin surfaces.

Surface	E_{ads} SO_2 (eV)	E_{ads} SO_3 (eV)	E_{ads} H_2SO_3 (eV)	E_{ads} H_2SO_4 (eV)
Native Kaolinite	-0.74[a]	-1.71[a]	-1.46[a]	-1.34
Partially Dehydrated Kaolinite	-1.63	-3.05[a]	-3.16	-3.05
Metakaolin	-2.83	-3.84	-3.58	-4.47

[a]These values are taken from Ref. (50).

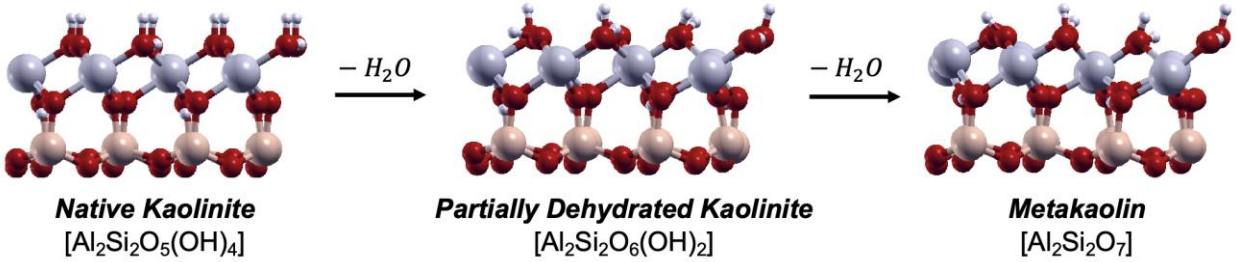

Figure 5.9. Scheme showing the two-step transformation of native kaolinite to metakaolin.

Figure 5.10 provides an in-depth comparison of the interactions observed between H_2SO_4 and the three clay mineral surfaces. Because the native kaolinite surface is fully hydroxylated, the main interaction type observed is hydrogen bonding between the surface hydroxyl groups and the oxygen atoms of the acid molecule. The basic surface also deprotonates the acid to generate a surface water and a hydrogen sulfate anion (HSO_4^-).

This deprotonation similarly occurs on the partially dehydrated surface. However, in both the partially dehydrated kaolinite and metakaolin surfaces, the predominant interaction is now the formation of new $Al_{surface}$-$O_{adsorbate}$ bonds. The formation of these bonds is at least partially explained by the presence of undercoordinated aluminum cations on the dehydrated surfaces, which, as previously noted, is proposed to contribute to the increased reactivity of the partially dehydrated kaolinite and metakaolin surfaces. These undercoordinated aluminum cations are not present on the native kaolinite surface. Consequently, we propose that the dehydration process generates undercoordinated aluminum sites, which in turn facilitates the formation of $Al_{surface}$-$O(S)_{adsorbate}$ bonds. The generation of these new Al-O(S) bonds suggests a mechanism of $Al_2(SO_4)_3$ formation and primes the surface for $Al_2(SO_4)_3$ release, which has been confirmed experimentally (*vide supra*). In the partially dehydrated kaolinite interface, the HSO_4^- anion is positioned so that one of the adsorbate oxygen atoms is located in between two undercoordinated aluminum centers. One new $Al_{surface}$-$O_{adsorbate}$ bond (2.11 Å) is formed, and a second longer interaction (2.29 Å) to a different aluminum cation is also present. Notably, the metakaolin surface doubly deprotonates the sulfuric acid molecule to generate two new surface hydroxyl groups and a bound SO_4 unit. The SO_4 unit once again is located in between two undercoordinated aluminum centers, here forming two strong $Al_{surface}$-$O_{adsorbate}$ bonds (1.92 and 1.99 Å) and completing the octahedral coordination spheres of the two aluminum centers.

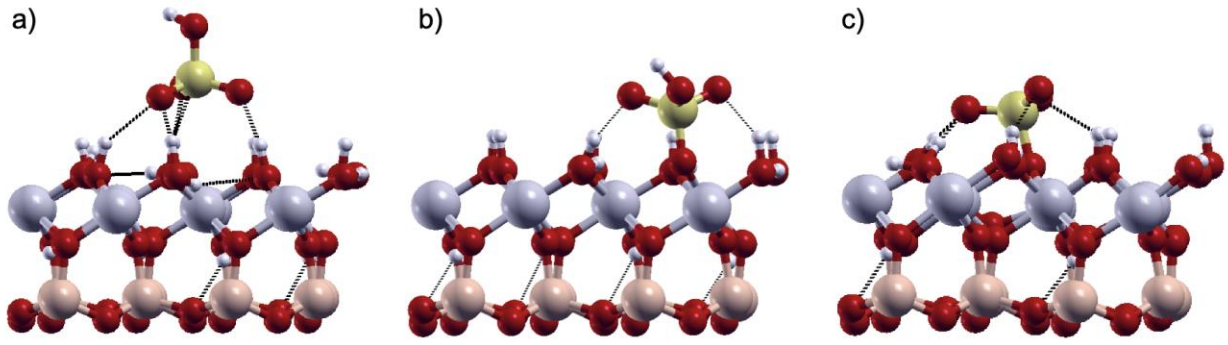

Figure 5.10. H_2SO_4 interacting with the a) native kaolinite, b) partially dehydrated kaolinite, or c) metakaolin surface.

5.3.4 Thermodynamic Analyses

As depicted in Figure 5.10, the interaction of small molecules containing a central S^{6+} cation can vary significantly with changes to the surface structure. Going from (a) to (b) in Figure 5.10, the dehydration of kaolinite led to surface transformations that interrupted surface bonds. To explore how these surface transformations could affect the adsorption and release properties of probe adsorbates, the following thermodynamics analysis was performed using SO_3 as the probe molecule: a) SO_3 was adsorbed to the mineral surface, creating new $S_{adsorbate}$-$O_{surface}$ bonds and effectively forming a surface-bound SO_4 molecule, b) Al and H_xSO_4 were released from the surface into solution, and finally c) the surface was healed with protons from surrounding H_2O. This three-step reaction process (adsorption, release, and healing) is shown in Figure 5.11 and resulted in a charge neutral defect surface. This process was mapped out for the pH range of 0.5 to 6. Over this pH range, there are two aqueous speciation changes to consider. Al changes from Al^{3+} (ΔG^0_{SHE} = -5.03 eV) to $AlOH^{2+}$ (ΔG^0_{SHE} = -4.73 eV) at pH 5, and S changes from HSO_4^{-1} (ΔG^0_{SHE} = +2.00 eV) to SO_4^{2-} (ΔG^0_{SHE} = +2.12 eV) at pH 2. The results of the overall cycle are depicted in Figure 5.12, which is a plot of ΔG_{tot} vs. pH, and the complete cycles are outlined in Section S1 of Appendix C.

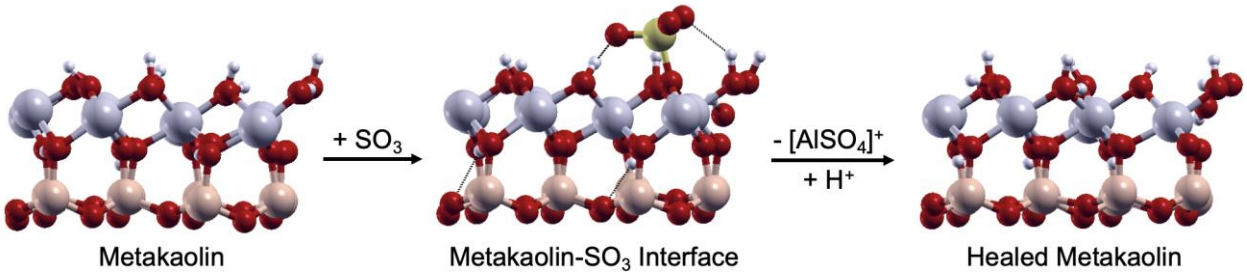

Figure 5.11. Representative scheme showing the three-step reaction cycle with metakaolin to generate a defect, charge neutral surface. The first reaction is adsorption, and the second reaction includes both the release and healing steps.

The SO_3 adsorption step on kaolinite, partially dehydrated kaolinite, and metakaolin surfaces has an E_{ads} value of -1.71, -3.05, and -3.84 eV, respectively (Table 5.1), indicating that SO_3 does not bind as strongly to a kaolinite surface with a full layer of Al-O(H) bonds when compared to a metakaolin surface that has lost multiple H_2O molecules. When SO_3

binds to these surfaces, it creates surface H_xSO_4 groups, which are energetically favorable. However, when released, this requires energy to break multiple Al-O surface bonds, which is partially compensated by a) releasing ions into solution and b) forming surface H-O-Al bonds when the surface is healed.

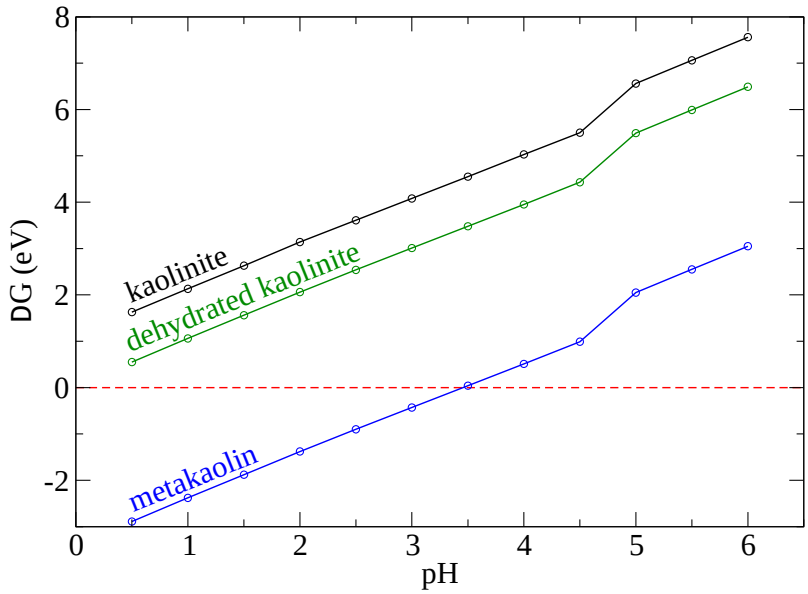

Figure 5.12. ΔG of the total cycle (adsorption, ion release, and surface healing) indicate that kaolinite and partially dehydrated kaolinite (with ΔG > 0 eV) will not behave like metakaolin (ΔG < 0 eV), which is predicted to dissolve in solutions with pH below 3.48. This pH value agrees with the experimental data indicating that metakaolin degradation is enhanced at pH environments lower than 4. The change in slope before pH 5 is caused by the change in Al speciation from Al^{3+}(aq) to $AlOH^{2+}$(aq).

In the cycles investigated here, both an aluminum cation and H_xSO_4 are released into solution in the second step (as Al^{3+}(aq) and HSO_4^{-1}(aq)), necessitating the addition of a proton from solution to heal the surface. For kaolinite, the sum of (free) energies for the cycles at pH 2 is -1.71 eV + 16.41–eV - 11.56 eV = +3.14 eV, while for metakaolin it is -3.84 eV + 14.02–eV - 11.56 eV = -1.38 eV. The first numbers in these summations are the adsorption energy values from Table 5.1, the second numbers are the ΔG_1 contributions from making and breaking bonds, and the third numbers are the ΔG_2 contributions from releasing ions into solution. As the number of atoms released to solution does not change,

the ΔG_2 contribution to the cycles are the same at pH 2 (-11.56 eV). The largest differences here are the two DFT computed pieces: E_{ads} and the breaking of bonds that occurs in the first two steps of the cycle. The metakaolin surface has a more favorable E_{ads} by 2.13 eV, and it is easier to release H_xSO_4 ions to solution (since there are fewer bonds to break) by 2.39 eV. These favorable contributions decrease the overall ΔG_{tot} by over 4 eV, which is the large difference between the black (kaolinite) and blue (metakaolin) trendlines in Figure 5.12. The results of the thermodynamics analyses match strongly with the experimental data shown in Figures 5.2d and 5.3, where metakaolin surfaces undergo significant chemical transformations at pH 2 and 0. The dehydrated surface of metakaolin has undercoordinated aluminum cations, which allow for the formation of $Al_{surface}$-$O(S)_{adsorbate}$ bonds when SO_3 (or H_2SO_4) enters an open coordination site. The new Al-O(S) bonds create $Al_x(SO_4)_y$ units on the surface, which can then be released into solution (as evidenced in ATR-FTIR and XRD results in Figure 5.5). In comparison, the aluminum cations on the kaolinite surface are fully coordinated, meaning a sulfur-containing adsorbate cannot find an open coordination site and bind to the aluminum to form a $Al_x(SO_4)_y$ unit. Consequently, kaolinite undergoes minimal structural changes from H_2SO_4 exposures due to the limited interactions between the Al and the sulfur-containing adsorbates.

5.4 Summary

Chemical alterations on the surface of the 2D clay materials, kaolinite and metakaolin were investigated through a combination of experimental and computational methods. Powder samples were exposed to H_2SO_4, and it was observed that both clay minerals undergo a loss of aluminum to some extent, with metakaolin experiencing the greater alteration. We used DFT methods to inform our exposure studies by exploring the thermodynamics of surface transformations that could lead to aluminum release. Our modeling efforts probed the interactions between the 2D clay mineral surfaces and H_2SO_4 as well as other sulfur-containing adsorbates, and these results were used in conjunction with experimentally determined changes in free energy via a DFT + Solvent Ion model to determine how surface hydration could affect the thermodynamics of material dissolution. Our DFT surface

reactivity studies demonstrated that the dehydrated surface of metakaolin interacted most strongly (i.e., had the most negative adsorption energy) with the chosen adsorbates and that only metakaolin would release ions, corresponding to aluminum sulfate salts, below pH values of approximately 3.5. Experimentally, interactions between exposed aluminum cations on the metakaolin surface and the sulfur-containing adsorbates resulted in the formation of hydrated $Al_2(SO_4)_3$. Most importantly, the agreement between theory and experiment for the onset pH values of Al release (determined to be below 3.5 and 4.0, respectively) and the finding that these processes would occur for metakaolin but not kaolinite are highlighted. The removal of these aluminum sulfate units generated a silica-terminated surface. Thus, the production and loss of aluminum sulfate could be detrimental to the clay mineral, affecting the surface properties and potentially limiting its use for certain applications.

Within archaeological and cultural heritage contexts, this study reveals potential issues for low-fired pottery exposed to acid rain or acidic soils. Our results show that chemical transformations can still be identified in metakaolin even at pH values of 4 and 6, albeit to a much lesser extent than pH 0 and 2. Namely, dealumination at $4 < pH < 6$ indicates the precipitation of $Al_2(SO_4)_3$. This sulfate salt, a known mordant, could facilitate the binding of stains onto the ceramic, which would be detrimental for the conservation of such objects [52]. Additionally, the precipitation of $Al_2(SO_4)_3$ within low-fired pottery could damage the porous object by causing internal cracks to form upon the crystallization of the sulfate salts.

The effects of firing temperature, porosity and humidity were further investigated to determine the stability of low-fired objects. The hardness of kaolinite tiles was shown to depend on all three aforementioned factors, emphasizing the need for careful control of both pH and humidity in current conservation protocols of low-fired pottery. It is recommended that future experiments combine SO_2 and humidity exposures together, to better simulate acid rain environments, and to reach more conclusive results than what has already been observed in dry SO_2 exposures. Future experiments should also focus on modeling more complex interpretations of low-fired aluminosilicate composites, to consider effects from additions of feldspar and glass-forming inclusions.

References

[1] W.D. Kingery, P.B. Vandiver, Ceramic masterpieces, The Free Press, New York NY, 1986.

[2] Y.-F. Chen, M.-C. Wang, M.-H. Hon, Phase transformation and growth of mullite in kaolin ceramics, Journal of the European Ceramic Society. 24 (2004) 2389–2397. https://doi.org/10.1016/S0955-2219(03)00631-9.

[3] P. Ptáček, F. Šoukal, T. Opravil, J. Havlica, J. Brandštetr, The kinetic analysis of the thermal decomposition of kaolinite by DTG technique, Powder Technology. 208 (2011) 20–25. https://doi.org/10.1016/j.powtec.2010.11.035.

[4] P.S.C. Silva, S.M.B. Oliveira, L. Farias, D.I.T. Fávaro, B.P. Mazzilli, Chemical and radiological characterization of clay minerals used in pharmaceutics and cosmetics, Applied Clay Science. 52 (2011) 145–149. https://doi.org/10.1016/j.clay.2011.02.013.

[5] A.K. Gaharwar, L.M. Cross, C.W. Peak, K. Gold, J.K. Carrow, A. Brokesh, K.A. Singh, 2D nanoclay for biomedical applications: Regenerative medicine, therapeutic delivery, and additive manufacturing, Advanced Materials. 31 (2019) 1900332. https://doi.org/10.1002/adma.201900332.

[6] A. López-Galindo, C. Viseras, P. Cerezo, Compositional, technical and safety specifications of clays to be used as pharmaceutical and cosmetic products, Applied Clay Science. 36 (2007) 51–63. https://doi.org/10.1016/j.clay.2006.06.016.

[7] M. das G. Silva-Valenzuela, M.M. Chambi-Peralta, I.J. Sayeg, F.M. de Souza Carvalho, S.H. Wang, F.R. Valenzuela-Díaz, Enrichment of clay from Vitoria da Conquista (Brazil) for applications in cosmetics, Applied Clay Science. 155 (2018) 111–119. https://doi.org/10.1016/j.clay.2018.01.011.

[8] Y. Guo, K. Xu, C. Wu, J. Zhao, Y. Xie, Surface chemical-modification for engineering the intrinsic physical properties of inorganic two-dimensional nanomaterials, Chemical Society Reviews. 44 (2015) 637–646. https://doi.org/10.1039/C4CS00302K.

[9] I.C. Freestone, Post-depositional changes in archaeological ceramics and glasses, in: Handbook of Archaeological Sciences, John Wiley & Sons, Ltd., 2001: pp. 615–626.

[10] P. Vandiver, Corrosion and conservation of ancient glass and ceramics, in: Corrosion of Glass, Ceramics and Ceramic Superconductors, Noyes Publications, Park Ridge, NJ, 1992.

[11] C.S.M. Allen, Recent developments in ceramic petrology, British Museum, London, 1991.

[12] J.V. Smith, Atmospheric weathering and silica-coated feldspar: Analogy with zeolite molecular sieves, granite weathering, soil formation, ornamental slabs, and ceramics, Proceedings of the National Academy of Sciences. 95 (1998) 3366–3369. https://doi.org/10.1073/pnas.95.7.3366.

[13] S.A. Hosseini, A. Niaei, D. Salari, Production of γ-Al_2O_3 from kaolin, Open Journal of Physical Chemistry. 01 (2011) 23–27. https://doi.org/10.4236/ojpc.2011.12004.

[14] Y. Zhao, Q. Zhang, W. Yuan, H. Hu, Z. Li, Z. Ai, Y. Li, High efficient coagulant simply by mechanochemically activating kaolinite with sulfuric acid to enhance removal efficiency of various pollutants for wastewater treatment, Applied Clay Science. 180 (2019) 105187. https://doi.org/10.1016/j.clay.2019.105187.

[15] A.E. Marquardt, E.M. Breitung, T. Drayman-Weisser, G. Gates, R.J. Phaneuf, Protecting silver cultural heritage objects with atomic layer deposited corrosion barriers, Heritage Science. 3 (2015) 37. https://doi.org/10.1186/s40494-015-0066-x.

[16] J.D. Hanawalt, H.W. Rinn, L.K. Frevel, Chemical analysis by x-ray diffraction, Industrial & Engineering Chemistry Analytical Edition. 10 (1938) 473. https://doi.org/10.1021/ac50125a001.

[17] P. Bayliss, Some properties of alunogen from New South Wales, American Mineralogist. 49 (1964) 1763–1766.

[18] P. Hohenberg, W. Kohn, Inhomogeneous electron gas, Physical Review. 136 (1964) B864–B871. https://doi.org/10.1103/PhysRev.136.B864.

[19] W. Kohn, L.J. Sham, Self-consistent equations including exchange and correlation effects, Physical Review. 140 (1965) A1133–A1138. https://doi.org/10.1103/PhysRev.140.A1133.

[20] P. Giannozzi, S. Baroni, N. Bonini, M. Calandra, R. Car, C. Cavazzoni, D. Ceresoli, G.L. Chiarotti, M. Cococcioni, I. Dabo, A. Dal Corso, S. de Gironcoli, S. Fabris, G. Fratesi, R. Gebauer, U. Gerstmann, C. Gougoussis, A. Kokalj, M. Lazzeri, L.

Martin-Samos, N. Marzari, F. Mauri, R. Mazzarello, S. Paolini, A. Pasquarello, L. Paulatto, C. Sbraccia, S. Scandolo, G. Sclauzero, A.P. Seitsonen, A. Smogunov, P. Umari, R.M. Wentzcovitch, QUANTUM ESPRESSO: a modular and open-source software project for quantum simulations of materials, Journal of Physics: Condensed Matter. 21 (2009) 395502. https://doi.org/10.1088/0953-8984/21/39/395502.

[21] P. Giannozzi, O. Andreussi, T. Brumme, O. Bunau, M. Buongiorno Nardelli, M. Calandra, R. Car, C. Cavazzoni, D. Ceresoli, M. Cococcioni, N. Colonna, I. Carnimeo, A. Dal Corso, S. de Gironcoli, P. Delugas, R.A. DiStasio, A. Ferretti, A. Floris, G. Fratesi, G. Fugallo, R. Gebauer, U. Gerstmann, F. Giustino, T. Gorni, J. Jia, M. Kawamura, H.-Y. Ko, A. Kokalj, E. Küçükbenli, M. Lazzeri, M. Marsili, N. Marzari, F. Mauri, N.L. Nguyen, H.-V. Nguyen, A. Otero-de-la-Roza, L. Paulatto, S. Poncé, D. Rocca, R. Sabatini, B. Santra, M. Schlipf, A.P. Seitsonen, A. Smogunov, I. Timrov, T. Thonhauser, P. Umari, N. Vast, X. Wu, S. Baroni, Advanced capabilities for materials modelling with Quantum ESPRESSO, Journal of Physics: Condensed Matter. 29 (2017) 465901. https://doi.org/10.1088/1361-648X/aa8f79.

[22] K.F. Garrity, J.W. Bennett, K.M. Rabe, D. Vanderbilt, Pseudopotentials for high-throughput DFT calculations, Computational Materials Science. 81 (2014) 446–452. https://doi.org/10.1016/j.commatsci.2013.08.053.

[23] D. Vanderbilt, Soft self-consistent pseudopotentials in a generalized eigenvalue formalism, Physical Review B. 41 (1990) 7892–7895. https://doi.org/10.1103/PhysRevB.41.7892.

[24] J.W. Bennett, D. Jones, X. Huang, R.J. Hamers, S.E. Mason, Dissolution of complex metal oxides from first-principles and thermodynamics: Cation removal from the (001) surface of $Li(Ni_{1/3}Mn_{1/3}Co_{1/3})O_2$, Environmental Science & Technology. 52 (2018) 5792–5802. https://doi.org/10.1021/acs.est.8b00054.

[25] J.W. Bennett, D.T. Jones, R.J. Hamers, S.E. Mason, First-principles and thermodynamics study of compositionally tuned complex metal oxides: Cation release from the (001) surface of Mn-rich lithium nickel manganese cobalt oxide,

Inorganic Chemistry. 57 (2018) 13300–13311. https://doi.org/10.1021/acs.inorgchem.8b01855.

[26] J.W. Bennett, D.T. Jones, B.G. Hudson, J. Melendez-Rivera, R.J. Hamers, S.E. Mason, Emerging investigator series: first-principles and thermodynamics comparison of compositionally-tuned delafossites: Cation release from the (001) surface of complex metal oxides, Environmental Science: Nano. 7 (2020) 1642–1651. https://doi.org/10.1039/C9EN01304K.

[27] H.J. Monkhorst, J.D. Pack, Special points for Brillouin-zone integrations, Physical Review B. 13 (1976) 5188–5192. https://doi.org/10.1103/PhysRevB.13.5188.

[28] K.W. Corum, X. Huang, J.W. Bennett, S.E. Mason, Systematic density functional theory study of the structural and electronic properties of constrained and fully relaxed (001) surfaces of alumina and hematite, Molecular Simulation. 43 (2017) 406–419. https://doi.org/10.1080/08927022.2017.1285402.

[29] J.P. Perdew, K. Burke, M. Ernzerhof, Generalized gradient approximation made simple, Physical Review Letters. 77 (1996) 3865–3868. https://doi.org/10.1103/PhysRevLett.77.3865.

[30] Z. Wu, R.E. Cohen, More accurate generalized gradient approximation for solids, Physical Review B. 73 (2006) 235116. https://doi.org/10.1103/PhysRevB.73.235116.

[31] A. Kokalj, Computer graphics and graphical user interfaces as tools in simulations of matter at the atomic scale, Computational Materials Science. 28 (2003) 155–168. https://doi.org/10.1016/S0927-0256(03)00104-6.

[32] K.M. Rosso, U. Becker, M.F. Hochella, Atomically resolved electronic structure of pyrite {100} surfaces: An experimental and theoretical investigation with implications for reactivity, American Mineralogist. 84 (1999) 1535–1548. https://doi.org/10.2138/am-1999-1007.

[33] K.M. Rosso, U. Becker, M.F. Hochella, The interaction of pyrite {100} surfaces with O_2 and H_2O: Fundamental oxidation mechanisms, American Mineralogist. 84 (1999) 1549–1561. https://doi.org/10.2138/am-1999-1008.

[34] S.E. Mason, C.R. Iceman, T.P. Trainor, A.M. Chaka, Density functional theory study of clean, hydrated, and defective alumina surfaces, Physical Review B. 81 (2010) 125423. https://doi.org/10.1103/PhysRevB.81.125423.

[35] X. Huang, J.W. Bennett, M.N. Hang, E.D. Laudadio, R.J. Hamers, S.E. Mason, *Ab initio* atomistic thermodynamics study of the (001) surface of $LiCoO_2$ in a water environment and implications for reactivity under ambient conditions, The Journal of Physical Chemistry C. 121 (2017) 5069–5080. https://doi.org/10.1021/acs.jpcc.6b12163.

[36] A. Klamt, The COSMO and COSMO-RS solvation models, WIREs Computational Molecular Science. 8 (2018). https://doi.org/10.1002/wcms.1338.

[37] M.D. Kundrat, J. Autschbach, Ab initio and density functional theory modeling of the chiroptical response of glycine and alanine in solution using explicit solvation and molecular dynamics, Journal of Chemical Theory and Computation. 4 (2008) 1902–1914. https://doi.org/10.1021/ct8002767.

[38] G. Brown, V. Henrich, W. Casey, D. Clark, C. Eggleston, A.F.A. Felmy, D. Goodman, M. Gratzel, G. Maciel, M. McCarthy, K. Nealson, D. Sverjensky, M. Toney, J. Zachara, Metal oxide surfaces and their interactions with aqueous solutions and microbial organisms, US Department of Energy Publications. (1999). https://digitalcommons.unl.edu/usdoepub/197.

[39] X. Rong, A.M. Kolpak, Ab initio approach for prediction of oxide surface structure, stoichiometry, and electrocatalytic activity in aqueous solution, The Journal of Physical Chemistry Letters. 6 (2015) 1785–1789. https://doi.org/10.1021/acs.jpclett.5b00509.

[40] D.D. Wagman, Selected values of chemical thermodynamic properties, Institute for Materials Research, National Bureau of Standards, 1965.

[41] K.A. Persson, B. Waldwick, P. Lazic, G. Ceder, Prediction of solid-aqueous equilibria: Scheme to combine first-principles calculations of solids with experimental aqueous states, Physical Review B. 85 (2012) 235438. https://doi.org/10.1103/PhysRevB.85.235438.

[42] R.T. Grimes, J.A. Leginze, R. Zochowski, J.W. Bennett, Surface transformations of lead oxides and carbonates using first-principles and thermodynamics calculations,

Inorganic Chemistry. 60 (2021) 1228–1240. https://doi.org/10.1021/acs.inorgchem.0c03398.

[43] J.T. Buchman, E.A. Bennett, C. Wang, A. Abbaspour Tamijani, J.W. Bennett, B.G. Hudson, C.M. Green, P.L. Clement, B. Zhi, A.H. Henke, E.D. Laudadio, S.E. Mason, R.J. Hamers, R.D. Klaper, C.L. Haynes, Nickel enrichment of next-generation NMC nanomaterials alters material stability, causing unexpected dissolution behavior and observed toxicity to *S. oneidensis* MR-1 and *D. magna*, Environmental Science: Nano. 7 (2020) 571–587. https://doi.org/10.1039/C9EN01074B.

[44] A. Abbaspour-Tamijani, J.W. Bennett, D.T. Jones, N. Cartagena-Gonzalez, Z.R. Jones, E.D. Laudadio, R.J. Hamers, J.A. Santana, S.E. Mason, DFT and thermodynamics calculations of surface cation release in $LiCoO_2$, Applied Surface Science. 515 (2020) 145865. https://doi.org/10.1016/j.apsusc.2020.145865.

[45] A.A. Tamijani, J.L. Bjorklund, L.J. Augustine, J.G. Catalano, S.E. Mason, Density functional theory and thermodynamics modeling of inner-sphere oxyanion adsorption on the hydroxylated α-Al_2O_3 (001) surface, Langmuir. 36 (2020) 13166–13180. https://doi.org/10.1021/acs.langmuir.0c01203.

[46] L.J. Augustine, A. Abbaspour Tamijani, J.L. Bjorklund, H.A. Al-Abadleh, S.E. Mason, Adsorption of small organic acids and polyphenols on hematite surfaces: Density Functional Theory + thermodynamics analysis, Journal of Colloid and Interface Science. 609 (2022) 469–481. https://doi.org/10.1016/j.jcis.2021.11.043.

[47] A. Tironi, M.A. Trezza, A.N. Scian, E.F. Irassar, Kaolinitic calcined clays: Factors affecting its performance as pozzolans, Construction and Building Materials. 28 (2012) 276–281. https://doi.org/10.1016/j.conbuildmat.2011.08.064.

[48] J. Madejová, FTIR techniques in clay mineral studies, Vibrational Spectroscopy. 31 (2003) 1–10. https://doi.org/10.1016/S0924-2031(02)00065-6.

[49] P.B. Vandiver, O. Soffer, B. Klima, J. Svoboda, The origins of ceramic technology at Dolni Věstonice, Czechoslovakia, Science. 246 (1989) 1002–1008.

[50] J.E. Heimann, R.T. Grimes, Z. Rosenzweig, J.W. Bennett, A density functional theory (DFT) investigation of how small molecules and atmospheric pollutants

relevant to art conservation adsorb on kaolinite, Applied Clay Science. 206 (2021) 106075. https://doi.org/10.1016/j.clay.2021.106075.

[51] J. Davidovits, Geopolymers: Ceramic-like inorganic polymers, Journal of Ceramic Science and Technology. (2017). https://doi.org/10.4416/JCST2017-00038.

[52] B. Pouliot, L. Fair, R. Wolbers, Re-thinking the approach: Techniques explored at winterthur for the stain reduction of ceramics, (2013) 15.

Chapter 6

SYNTHESIS AND CHARACTERIZATION OF LUSTER GLAZES

The contents of this chapter are also presented in "Nanoscale engineering of gold particles in 18th century Böttger lusters and glazes" by C. S. Chari, Z. W. Taylor, A. Bezur, S. Xie and K. T. Faber, which was published in the Proceedings of the National Academy of Sciences in 2022 [1]. C. S. Chari led the experimental portion of the work on the reproductions. A. Bezur led the experimental portion of the work on the historic samples, with assistance from S. Xie. Faber supervised all experimental work. In addition, Z. W. Taylor led the theoretical portion of the work, supervised by Faber and co-supervised by Chari. Chari, Faber and Bezur were involved in designing the work. All authors were involved in preparing the manuscript.

6.1 Introduction

The story of Böttger luster starts with the ambitious avarice of a porcelain-crazed monarch: Augustus the Strong, Elector of Saxony (1694-1733). In the 17th century, Chinese porcelain was widely sought after by European aristocrats for its unrivalled delicacy and translucence. The original recipe of hard-paste porcelain, composed mostly of acicular mullite crystals and quartz grains in a glassy matrix, was closely guarded by Chinese potters for centuries, enhancing the value of this luxury product. The arcanum for porcelain was deeply coveted by European nobility along with the ability to transmute ordinary metals into gold. The latter pursuit led Augustus the Strong to summon the alchemist Johann Friedrich Böttger to his palace in Dresden in 1702, in a bold attempt to discover the formula for the philosopher's stone. Unfortunately for Böttger, the task was undeniably impossible, resulting in a series of failed experiments, unsuccessful attempts to flee, and his forceful recaptures [2].

Böttger's luck turned around in 1708, when he was able to appease Augustus the Strong by successfully producing the first Continental European hard-paste porcelain, also referred to as white gold [2,3]. In contrast to Chinese porcelain, Böttger porcelain contained high amounts of lime and low amounts of quartz, making it stronger and more resistant to thermal

shock than contemporary porcelain formulations [4]. The Meissen Manufactory, established in 1710 by Augustus the Strong and continuing to date, transitioned from producing calcium-rich Böttger porcelain to making potassium-rich Meissen porcelain around 1730 when feldspar replaced calcined alabaster as a flux [4,5].

Figure 6.1. Teapot from Meissen Porcelain Manufactory, Art Institute of Chicago 1991a-b: a) full view, b) close-up of teapot showing Böttger luster.

During its first decade of existence, the Meissen Manufactory struggled to produce overglaze polychrome decorations that were compatible with the high temperatures needed to fire porcelain - just over 1350 °C [4,6]. Following countless experiments, the factory eventually became famous for developing a purple, iridescent overglaze decoration known as Böttger luster [7], also referred to as the mother-of-pearl glaze, opal glaze and (somewhat confusingly) "copper color" [6,8], seen as the purple decoration in Figure 6.1 in the cartouche surrounding the central decoration. Recent translations of historical recipes from the Meissen Manufactory reveal that the hue and iridescence of the glaze could be due to gold embedded in the top glaze layer [6,9]. The luster glaze is distinct from Purple of Cassius, a contemporaneous purple colorant used at Meissen to achieve hues ranging from purple to pink that is non-iridescent and composed of gold nanoparticles well-dispersed in a tin-containing and lead-rich glassy matrix [10–12]. The recipe for Böttger luster lacks tin, though it is also based on a lead-rich glassy matrix. Böttger luster also differs from colloidal gold-

based glasses, glazes and enamels with red to violet colors prepared with arsenic salts and used in Bernard Perrot's workshop, pre-dating Meissen's polychrome wares [13,14].

The formation of metal nanoparticles in overglaze decorations to create lustrous effects has been employed by artisans since 9th century CE Mesopotamia, most prominently used in Spain and Italy from the 14th to the 16th centuries [15]. The luster layer is typically applied by depositing a mixture of metal salts and oxides to the surface of a glazed ceramic and then heating the piece to 600 °C in a reducing atmosphere, achieved by adding smoking substances into the kiln that inhibit the flow of oxygen, e.g., burning wood. This process allows the metal ions to diffuse into the glaze and reduce into metal nanoparticles close to the surface. It is important to note that all previously reported examples of lusterware use mixtures of silver and copper nanoparticles to create gold- and red-colored lusters [15–21]. This study is the first, to our knowledge, to specifically focus on purple-colored luster glazes produced with gold nanoparticles.

The focus of this research is to characterize historic Böttger luster and compare this to a purple overglaze enamel produced at Meissen using Purple of Cassius. To further understand the materials and methods used in the original Meissen Manufactory we attempt to reproduce the luster-glazed porcelain. Analytical techniques such as energy-dispersive X-ray spectroscopy (EDX), X-ray diffraction (XRD), and ultraviolet-visible spectroscopy (UV-Vis) coupled with imaging methods such as scanning electron microscopy (SEM) and scanning transmission electron microscopy (STEM) are applied to provide insight into the composition and structure of the lusterware layers. Finally, we use experimentally determined size distributions of gold nanoparticles in Böttger luster and Purple of Cassius and consult models of Mie scattering and particle array interference to explain how the distribution, if properly tailored, gives rise to lusters through distinct optical effects.

6.2 Materials & Methods

6.2.1 Characterization of the historic Meissen samples and reproductions

Fragments (0.5 x 0.5 mm^2) of decorative surface layers were obtained from Meissen porcelain dated to the 18th century. Two gold containing decorative samples were studied:

one was a lustrous sample from a Meissen porcelain teapot (DC.0508, from the study collection of the Winterthur Museum, Garden and Library, 18th century) and the other a piece of purple enamel from a cup (DC.0510, Winterthur collection, 18th century).

TEM samples were prepared with focused ion beam (FIB). Cross-sectional slices with electron transparency were extracted from the purple regions, revealing the multi-layered structure of the surface decoration. The distribution of nanoparticles as well as the glaze chemistry were determined via scanning transmission electron microscopy (JEOL JEM-2100 FasTEM). The operating voltage was 200 kV. The chemistry of the glaze was studied using EDX coupled with the STEM. INCA software was employed for EDX acquisition and analysis.

Reproductions were analyzed using an array of imaging and chemical characterization methods. A camera was used to capture the iridescence of the samples at the macroscale (Nikon D7500, AF-S Micro Nikkor 40mm Lens, Nikon, Tokyo, Japan). The surface microstructure and overview cross-section of the lusterware samples were imaged using scanning electron microscopy (ZEISS 1550VP FESEM, Carl Zeiss Microscopy GmbH, Jena, Germany). The elemental compositions of the individual layers were determined using energy dispersive X-ray spectroscopy (Oxford X-Max SDD X-ray Energy Dispersive Spectrometer). The cross-section of the luster layer was imaged using scanning electron microscopy (Nova 200 NanoLab, Thermo Fisher, U.S.A) and the elemental compositions were determined using energy dispersive X-ray spectroscopy (Bruker Quantax X-ray Energy Dispersive Spectrometer). The chemical composition of the reproduced Böttger porcelain and purple luster layer was measured using X-ray diffraction (Panalytical X'Pert Pro-diffractometer) with a Cu source at 45 kV and 40 mA, scanned from 20° to 80° 2θ.

Ultraviolet-visible spectroscopy of the historic Böttger luster sample was carried out with a normal illumination/ normal collection setup using a 200 µm diameter single fiber illumination leg and a single fiber collection leg of the same diameter (Ocean Optics BIF200-UV/VIS), a halogen light source (Ocean Optics DH-2000-BAL), and an Ocean Optics spectrometer (OCEAN-FX-XR1-ES, XR1-500 line/mm grating blazed at 250 nm) to collect 20 averaged spectra, each at 1000 ms collection time, controlled by OceanView software.

For the recreation sample, a normal illumination/normal collection setup was used using a 400 µm diameter 6-fiber illumination leg and a single fiber collection leg of the same diameter (Ocean Insight QR400-7-SR-BX), a halogen light source, a Shamrock spectrometer (SR-193i-B2, S/N SR-2502) and a silicon CCD Camera (IDUS D4420A-OE, S/N CCD-19533, May 2016) to collect spectra controlled by Andor Solis software.

6.2.2 Production of Purple Lusters

Details of the recipes used to create Böttger porcelain and the Böttger base glaze can be found in Appendix D. For the luster glaze, modifications were made from the original Böttger recipe [6,9] to avoid working with gold(I) hydrazide. First, a lead-rich glaze slurry was prepared from raw materials, including lead bisilicate (U.S. Pigment Corporation, South Elgin, IL, USA), kaolinite (Sigma-Aldrich, St. Louis, MO, USA), potash feldspar (Custer, South Dakota, USA), calcium carbonate (Alfa Aesar, Ward Hill, MA, USA) and quartz (Sigma-Aldrich, St. Louis, MO, USA), which were suspended in water and ball-milled for 2 h. Table 6.2 summarizes the raw materials used to create all three lead-rich glazes. Exact oxide compositions of the fired glazes can be found in Table D.3 in Appendix D.

The raw slurry was then applied with a brush as a thin layer of less than 25 µm on the surface of the previously base-glazed porcelain. The freshly glazed piece was then fired at 900 °C for 2 hours in air with a ramp rate of 2 °C/min. The melting point of the lead-rich layer was designed to be below 1100 °C to avoid any intermixing between this layer and the base glaze (which begins to soften at 1100 °C). Previous studies on lead oxide-alumina-silica glazes have reported that additions of PbO can lower the melting temperature of the system [22]. Three compositions of the lead-rich were investigated, referred to as: Baseline (based on STEM-EDX results of historic Meissen samples, modified so that it could begin to melt at 600 °C), High Ca/K (a Ca-rich version of Baseline) and High Pb (a Pb-rich version of Baseline). Details of their compositions are outlined in Table D.3. The three variations each produced a clear and smooth surface after firing, and were rich in silicon, calcium, and lead. The thickness of the applied lead-rich glaze played a critical role in obtaining the correct color and luster. Applying layers less than 25 µm was desired to avoid the growth of silica

or mullite crystals within the lead-rich glaze, which could alter the optical properties of the glaze.

To introduce gold ions into the glaze, an aqueous solution of gold(III) chloride was applied to the fired lead-rich glaze. The piece was then heated to 600 °C with a ramp rate of 2 °C/min, and held at that temperature for 30 min with flowing argon gas, creating an inert atmosphere. The lead-rich glazes start to soften at this temperature, facilitating the diffusion of the gold ions into the glaze where they are reduced to produce gold nanoparticles.

6.2.3 Spectroscopic Simulations of Lusters

Evaluating the effects of Mie scattering involved the solution of the Maxwell equations around spherical particles by expanding the problem in an infinite series of spherical harmonics [23,24]. While this provided an analytical solution, numerical approximations were necessary to evaluate that solution, and Python scripts such as PyMieScatt [25] were used to evaluate the extinction, absorption, and scattering efficiencies of nanoparticles both individually and in a size-density distribution. Kubelka-Munk theory [26] was then used to approximate the scattering and reflectivity of a suspension of nanoparticles of infinite thickness from the coefficients given by PyMieScatt [25,26]. This process is used to approximate the matte color purely due to the nanoparticles in a hypothetical infinite suspension and not their layered distribution. The absorption and scattering coefficients of the material, K and S, respectively, are based on the nanoparticle density and properties of the material. More precisely, they are defined as:

$$K = \beta_{abs} = \int_0^\infty \pi r^2 Q_{abs}(r, \lambda, n_{matrix}) \rho(r) dr \tag{6.1}$$

$$S = \beta_{sca} = \int_0^\infty \pi r^2 Q_{sca}(r, \lambda, n_{matrix}) \rho(r) dr \tag{6.2}$$

where r is the metal nanoparticle radius, $Q_{abs}(r, \lambda, n_{matrix})$ and $Q_{sca}(r, \lambda, n_{matrix})$ are the Mie absorption and scattering coefficients, respectively, and $\rho(r)$ is the volume density describing the concentration of nanoparticles in the glassy matrix.

The reflectivity of a suspension of nanoparticles of infinite thickness is then defined as:

$$R_\infty = \frac{K + S - \sqrt{(K+S)^2 - S^2}}{S} \tag{6.3}$$

Approximating the disordered periodic structure of the nanoparticles as a perfect 2D square array of identical lossy particles, subjected to normal incidence of light, we applied the approach proposed by Garcia de Abajo [27] to model the luster; effectively this is the wavelength at which intensely reflective resonances occur from a uniform lattice with well-defined particle size and periodicity.

$$R = |r|^2 \tag{6.4}$$

$$r = \frac{\frac{2\pi i k}{A}}{\frac{1}{\alpha_E} - G_{xx}(0)} \tag{6.5}$$

$$\frac{1}{\alpha_E} = \frac{1}{\alpha_E^{es}} - \frac{2ik^3}{3} \tag{6.6}$$

$$\alpha_E^{es} = b^3 \frac{\epsilon - 1}{\epsilon + 2} \tag{6.7}$$

$$G_{xx}(0)a^3 \approx \frac{4\pi^2\sqrt{2}}{\sqrt{\lambda/a - 1}} - 118 \tag{6.8}$$

In this model, the periodicity is a, nanoparticle radius is b, and the nanoparticle's complex permittivity is a constant ϵ. With these parameters, $A = a^2$ the area of the lattice unit cell, and the magnitude of the light wavevector k, the reflection coefficient r and thus reflectance R can be calculated. Note that introducing disorder into this system, as is more realistic, would broaden and decrease the intensity of the resonant peaks in the reflectance spectra, but would not eliminate them [27–29].

6.3 Results and Discussion

6.3.1 Historic Glazes

6.3.1.1 Böttger Luster

Historic Böttger luster was examined by probing the cross-section of a lusterware sample (taken from a Meissen porcelain teapot, DC0508, from the study collection of the Winterthur Museum, Garden and Library), using STEM.

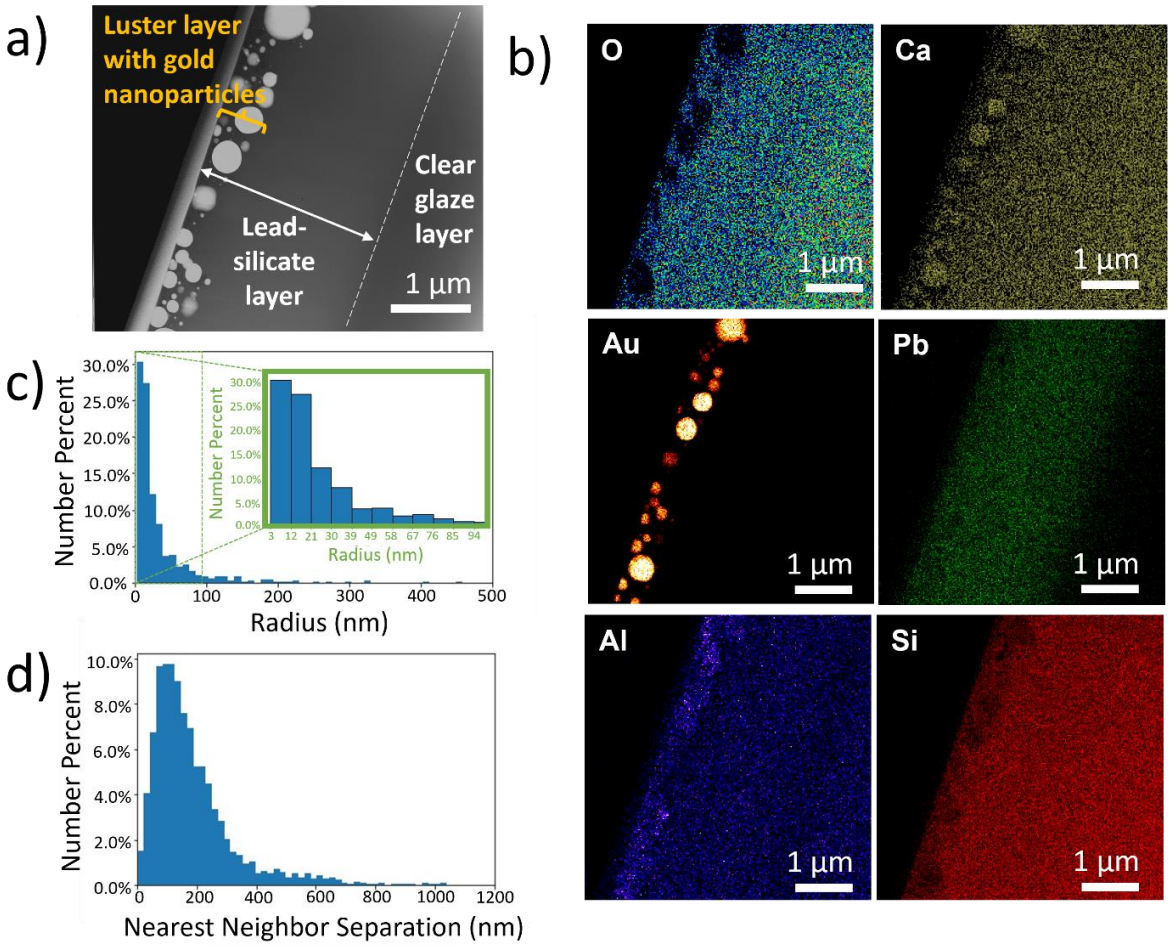

Figure 6.2. Analysis of historic Böttger luster: a) STEM image of historic Böttger luster, showing spherical Au nanoparticles near the surface, b) corresponding EDX maps of several elements, c) distribution of gold nanoparticle sizes with detail included as inset, d) distribution of the nearest neighbor separation of gold nanoparticles.

The STEM micrograph, shown in Figure 6.2a, reveals that Böttger luster includes an approximately 0.3 to 0.8 μm thick layer, called the luster layer, containing gold nanoparticles dispersed within a lead silicate glaze, which by itself is approximately 2.6 μm thick. The EDX maps seen in Figure 6.2b show that the luster layer is rich in gold, aluminum, lead and calcium. The gold nanoparticles are located close to the surface of the lead-rich glaze, with a wide distribution of particle sizes and nearest neighbor separations as seen in Figure 6.2c,d. The nanoparticle radius was measured using Image J (National Institutes of Health) analysis and found to be 34 ± 47 nm using number averaging. The error term represents one standard deviation; see Appendix D for more details on the error analysis.

Underneath the lead-rich glaze seen in Figure 6.2 is the clear base Böttger glaze. Apart from the gold nanoparticles, no additional pigments are present in the lead-rich glaze or the Böttger glaze. Therefore, it is likely that the luster layer alone is responsible for the color and iridescence. As defined in Figure 6.2a, the oxide compositions of the luster layer, lead-rich layer and Böttger glaze layer were measured quantitively using EDX and are presented in Table 6.1. The composition of the luster layer's lead silicate matrix is similar to the copper/pink colorant on object AR1 of Domoney et al. (2012), an 18th century Meissen porcelain vase dated between 1725-1733 thought to be decorated with Böttger luster [10].

Böttger luster is closely related to other forms of lusterware caused by different metal nanoparticles, such as silver and copper [15,19,21,30,31]. Of note, tin is not present in Böttger luster as indicated by the measurements in Table 6.1. This makes Böttger luster distinct from another glaze colorant based on gold nanoparticles, Purple of Cassius, which is used to produce non-iridescent glazes with purple and pink hues.

6.3.1.2 Purple of Cassius

In parallel with historic Böttger luster, a historic Meissen purple enamel sample (taken from a cup, DC.0510, Winterthur collection) was also examined by studying its cross-section using STEM-EDX, shown in Figure 6.3a,b. The purple enamel revealed a similar multi-layered structure to Böttger luster, with a 200 nm thick layer containing gold nanoparticles. The gold nanoparticle radius is 16 ± 11 nm by number averaging, much smaller than the

sizes seen in Böttger luster. The error term represents one standard deviation. The homogeneous nanoparticle size distribution seen in the purple enamel sample is similar to that observed in historical Gold Ruby glass [32,33]. Bar charts showing the distribution of gold nanoparticle sizes and the distance between neighboring particles are shown in Figure 6.3c,d.

The gold nanoparticle layer is located within an approximately 1 μm thick lead silicate layer. Similar to the Böttger luster, the lead-rich glaze sits over a high-temperature base glaze. The oxide compositions of the gold nanoparticle-rich region, the lead-rich layer and the base glaze layer were measured quantitively using EDX (Figure 6.3b) and are presented in Table 6.1.

The base glazes seen in the purple enamel sample and in the Böttger luster sample have similar compositions, which is expected considering that both pieces originate from the Meissen Manufactory in the 18th century. In contrast, the lead-rich glaze in the purple enamel sample is richer in PbO and CaO than the luster sample. Traces of iron are present within the glaze, which could imply the presence of small Fe_2O_3 particles that could contribute to the red tones of the purple enamel [34]. However, the purple color likely originates from the gold nanoparticle-containing layer, which is also rich in aluminum, lead, calcium, and tin. Unlike Böttger luster, the gold nanoparticles in the purple enamel sample are surrounded by a tin-rich matrix. The presence of tin suggests that the gold nanoparticles had been added as Purple of Cassius, a famous purple colorant since ancient times.

Specifically, Purple of Cassius, a precipitate of tin(IV) oxide and colloidal gold, can be prepared using a mixture of tin(II) and tin(IV) chlorides, and gold(III) chloride, as shown by several previous studies [35–37]. Tin(II) chloride serves as a reducing agent that facilitates the reduction of gold ions into metal nanoparticles [38]. The gold nanoparticles pigment can be fused with glaze-making components to create purple and pink overglaze decorations [36,39]. Because such gold nanoparticles are formed prior to firing, and therefore do not require nucleation within the glaze during the firing process, they are smaller and more uniform in size and particle dispersion.

Table 6.1. Composition (wt.%) of lead glazes and clear Böttger glazes, omitting Au content.

	Al_2O_3	SiO_2	CaO	Na_2O	K_2O	PbO	SnO_2	As_2O_3***	Other*
Historic Böttger Luster Layer (<800 nm)**	13.6	61.7	2.6	0	0.1	21.7	0	0	0.3
Historic Böttger Lead-rich Layer (~2.6 µm)**	16.2	63.2	2.8	0	0.3	17.4	0	0	0.1
Copper/Pink Colorant from Object AR1, (Ref. 10)**	8.99	60	6.79	0.73	1.65	15.4	0	0.55	5.89
Historic Clear Böttger Glaze (close to Pb-rich layer)	18.78	78.39	2.16	0	0.55	0	0	0	0.12
Historic Clear Böttger Glaze (further from Pb-rich layer)	20.71	76.23	2.59	0	0.34	0	0	0	0.13
Historic Purple Glaze Gold Layer (200-300 nm)**	9.2	37.5	3.2	0	0.3	36.4	12.2	0	1.2
Historic Purple Glaze Lead-rich Layer (~1 µm)**	11.9	47.2	4	0	0.2	36	0	0	0.7
Historic Purple Glaze Clear Böttger Glaze	18.05	75.17	5.04	0	1.23	0	0	0	0.51
Reproduction Lead-rich Layer After Firing – Baseline**	5.4	39.6	7.3	0.3	0.5	46.8	0	0	0.1
Reproduction Lead-rich Layer After Firing – High Ca/K**	3.9	33.4	23.1	0.1	0.7	38.7	0	0	0.1
Reproduction Lead-rich Layer After Firing – High Pb**	2.6	38.6	4.2	0.4	1.2	52.9	0	0	0.1

*Other includes trace amounts of oxides of Mg, Fe, Cr, Ti, P

** Recalculated and normalized to exclude Au from the total, to represent the lead-rich matrix surrounding the Au nanoparticles. Note that the original reported Au content in this colorant is 45.4 wt.%

*** Spectral overlaps between the following X-ray lines make it challenging to reliably determine and quantify the presence of minor amounts of arsenic, especially considering the high quantity of gold reported by Domoney et al.[10] for objects AR1: Mg K/As L, Pb Lα/As Kα, and Au Lβ/As Kβ

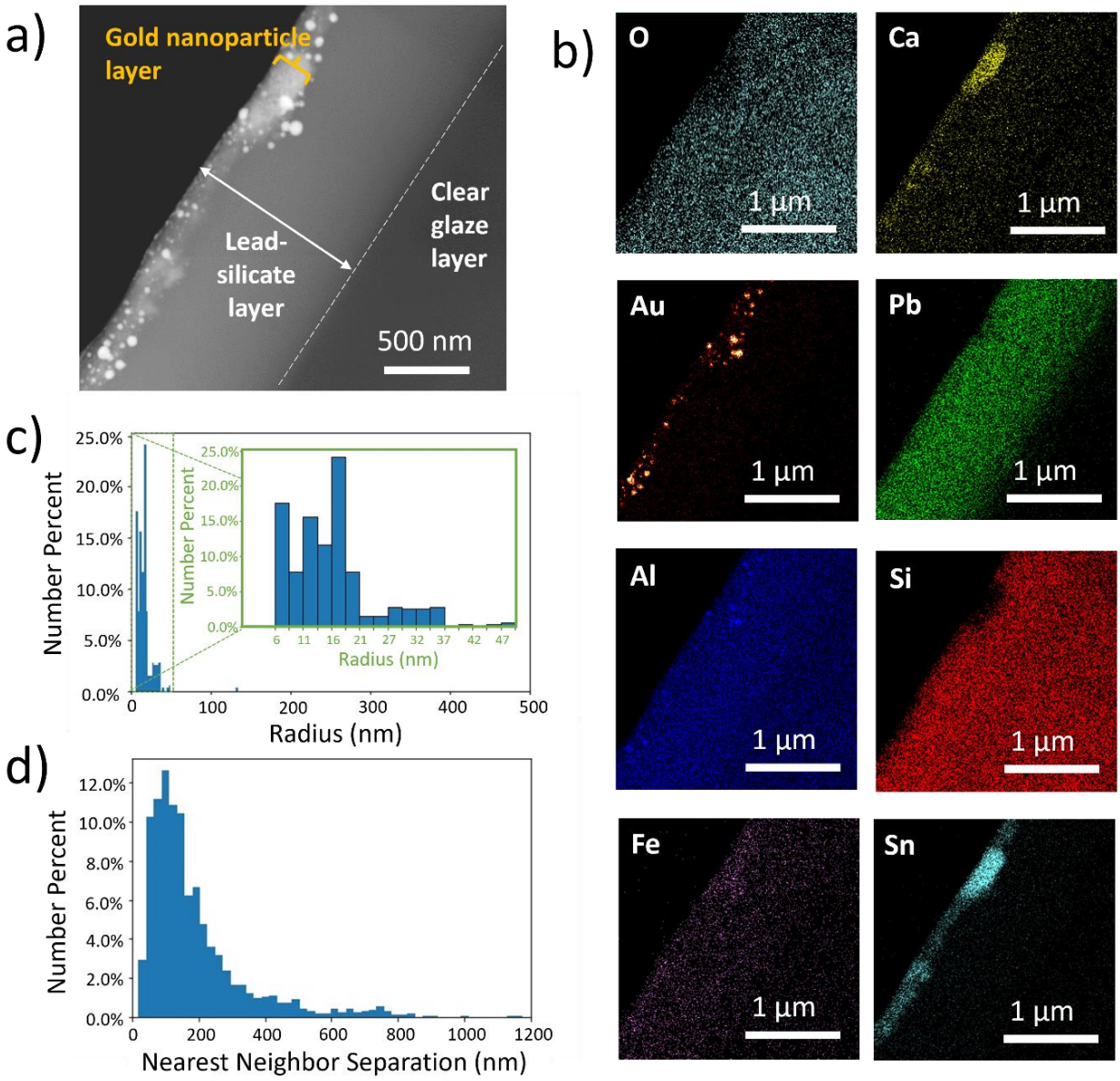

Figure 6.3. Analysis of historic Purple of Cassius: a) STEM image of historic Meissen purple enamel sample, showing spherical Au particles near the surface, b) corresponding EDX maps of several elements, c) distribution of gold nanoparticle sizes with detail included as inset, d) distribution of the nearest neighbor separation of gold nanoparticles.

6.3.2 Analysis of Reproductions

Böttger porcelain and the base Böttger glaze were reproduced based on recipes by Kingery and Vandiver [4], further described and characterized in Appendix D. Unlike Böttger

porcelain and the Böttger glaze, there is limited information available on the lead-rich glazes used in the Meissen Manufactory in the 18th century. Lead was popularly added to lower the melting temperature of pottery glazes in this period, allowing the glaze to uniformly cover the ceramic piece by firing it at a much lower temperature than would be required for unleaded silicate-based glazes. In this study, three recipes of lead glazes were investigated, referred to as Baseline, High Ca/K and High Pb (described in Materials and Methods). The compositions of the lead glazes were chosen so that they could soften at the luster forming temperature of 600 °C. The oxide compositions of the fired glazes can be found in Table 6.1.

Recently translated records and recipes for overglaze enamels by Johann Gregorius Höroldt, who became renowned for porcelain decoration at the Viennese Du Paquier Manufactory prior to joining Meissen, reveal that the unstable explosive *aurum fulminans*, essentially gold(I) hydrazide, was used to introduce gold ions into the lead glaze to create the luster layer [9]. Additionally, previous research suggests that a flux of powdered leaded glass was used in preparing the historic overglazes [9,40]. In this study, modifications were made to the original recipe to avoid the safety concerns associated with handling gold(I) hydrazide and processing lead-rich powders. Instead, we used a solution of gold(III) chloride, a substance readily available to Meissen workers in the 18th century, as the source of gold ions. Gold dissolves in aqua regia to form chloroauric acid ($HAuCl_4$), which dissociates into gold(III) chloride and HCl. Since gold is the most electronegative among all transition metals, gold(III) chloride or $HAuCl_4$ are readily reduced to gold at relatively low temperatures in oxygen deficient atmospheres. Furthermore, we prepared a slurry with the raw components needed to create a lead-silicate matrix, further described in Materials and Methods, instead of preparing and handling a frit of pretreated lead-rich powders.

Photographs of the samples, shown in Figure 6.4a, reveal that the Baseline composition of the lead-rich glaze produced the most iridescent sample. The High Ca/K glazed sample contained regions where the metallic luster was visible, however the luster was not as consistent as that seen with the Baseline glaze. SEM images show that both glazes contain gold nanoparticles on their surface.

Table 6.2. Raw materials (g) used in lead-rich glaze reproductions.

	Baseline	High Ca/K	High Pb
Quartz	0.40	0	0
Feldspar	1	1.60	0.57
Clay	0.68	0.16	0.15
Calcium carbonate	1	1.10	0.44
Lead bisilicate	6	5.40	7

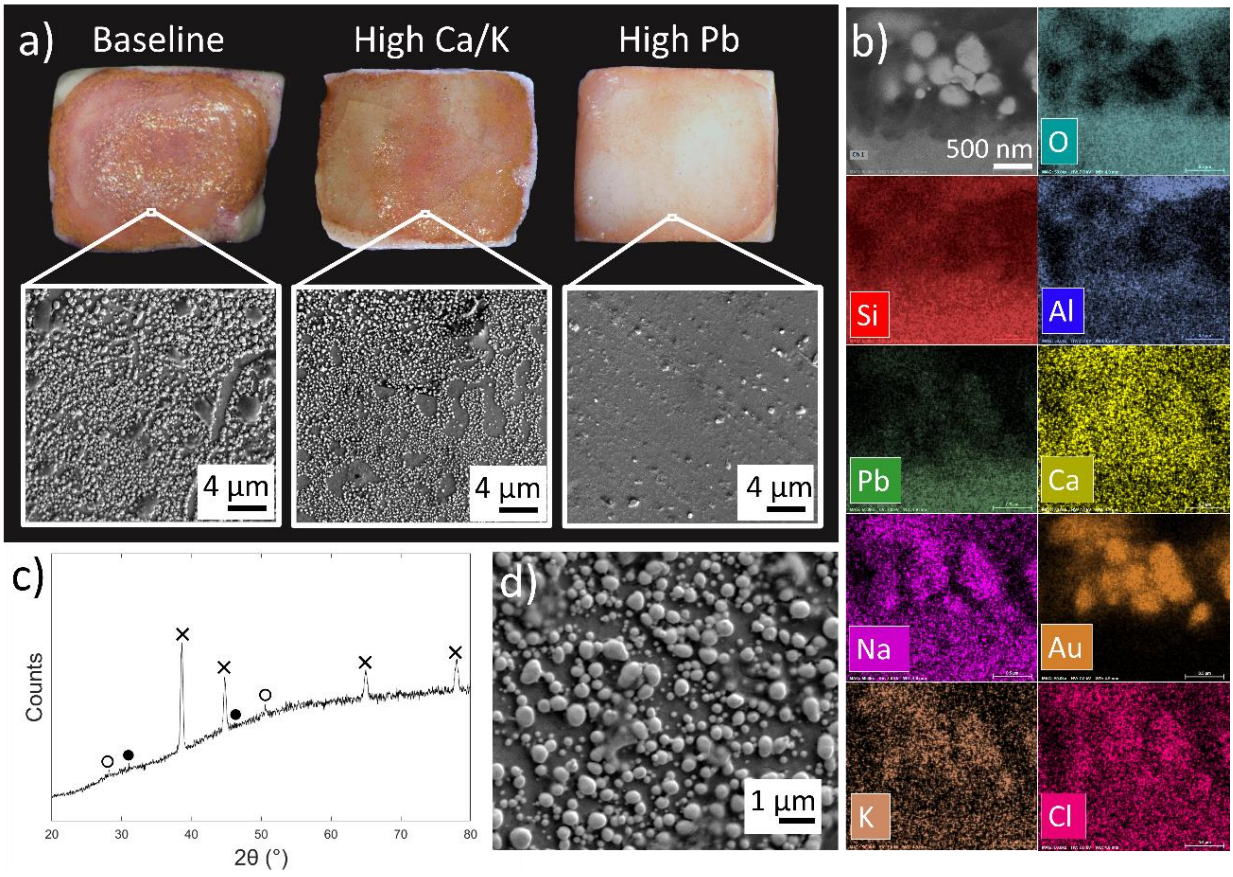

Figure 6.4. Analysis of reproductions: a) Photographs of purple luster reproductions, comparing three different compositions of the lead-silicate layer with corresponding SEM-EDX images of the surfaces of each lead glaze. b) SEM-EDX images of cross-section of Baseline sample. c) XRD pattern of Baseline sample indicating the presence of Au nanoparticles (×), NaCl (●) and KCl (○). d) SEM images of surface of Baseline sample, showing Au nanoparticles on the surface of the luster layer.

The High Pb glazed sample, although colored pink due to the presence of gold nanoparticles, exhibited no luster from the naked eye. SEM images suggest that this could be due to the shortage of gold nanoparticles on the surface of the High Pb glaze, possibly due to the higher lead content and therefore lower melting temperature of the glaze.

The SEM-EDX maps presented in Figure 6.4b show that the gold-containing locations within the luster layer are also rich in sodium, potassium, and chlorine. We hypothesize that the alkali ions, both K^+ and Na^+, were leached from the sanidine-type feldspar, which was a main ingredient of the lead-rich slurry [41]. These alkali ions may have diffused towards the metal-bearing chloride to form KCl and NaCl salts around the gold nanoparticles. This is different from what is seen in historic Böttger luster, where the gold-source is gold (I) hydrazide and not gold (III) chloride. Nevertheless, we observe that the gold ions still reduce to metallic gold and coarsen similarly to what was seen in Böttger luster. Furthermore, the gold-free locations contain silicon, aluminum, oxygen, and traces of lead, showing that the nanoparticles are located within a $PbO\text{-}SiO_2\text{-}Al_2O_3$ matrix, reminiscent of what was previously seen in historic Böttger luster.

The X-ray diffraction pattern shown in Figure 6.4c verifies that the luster glaze is composed of gold nanoparticles in a glassy matrix, with minor peaks attributed to the presence of salts. Figure 6.4d shows a close-up of the particle array observed on the surface of the Baseline lead glaze. The average nanoparticle radius was measured to be 89 ± 52 nm using number averaging, which falls within the range observed in historic Böttger luster. The error term represents one standard deviation. Applying the luster layer using gold(III) chloride therefore gave comparable results to the original application method using gold(I) hydrazide, ultimately producing purple luster. Despite differences in the chemistry of the matrix, we see that in both cases gold-bearing compounds can grow into gold nanoparticles of varying sizes.

6.3.3 Optical Effects

Nanoparticles may contribute to the coloration of a sample through several mechanisms. Plasmonic effects exist for nanoparticles under ~15 nm in radius due to resonant oscillation of a nanoparticle's electrons with incident light waves [30,42–44]. The nanoparticles in the

Böttger luster and Purple of Cassius samples are generally larger than the scale at which plasmonic effects occur. Rather, they fall into the regime of Mie scattering, which is a largely geometric effect for nanoparticles upwards of ~15 nm that produce a purple hue [25,26,42,45]. In an infinite suspension of nanoparticles, this would fully describe the behavior, however, these glazes produce a structured distribution of nanoparticles in space, as well as in size. Namely, nanoparticles are localized to the surface of the glazes in an approximately uniform spatial distribution, ~100 nm inter-nanoparticle separation distances for both glazes (Figures 6.2d and 6.3d). This can give rise to diffraction from a particle array, similar to that of diffraction gratings [46,47]. This phenomenon can result in luster, or iridescence, as the interaction of light with such structures is angle-dependent, giving different colors in different lighting. To understand why Böttger luster is iridescent while Purple of Cassius is not, simulations based on simple models of particle array interference were conducted using the experimentally determined nanoparticle size and spacing distributions [27].

When producing Böttger luster from gold-bearing salts, a large distribution of gold nanoparticle sizes is observed due to the occurrence of multiple nucleation sites during firing. The simulations indicated that Böttger luster is a result of the combined effects of: i) Mie scattering of small nanoparticles (in the radius range of 15-250 nm) producing hue without luster, and ii) disordered nanoparticle array interference of large nanoparticles (~100 nm radius) with large periodicity (on the order of several hundred nanometers) producing luster in the visible spectrum. These findings were based on the gold particle sizes seen in Figure 6.2. More specifically, hue without iridescence is dominated by the Mie scattering of the many small nanoparticles of ~25 nm in radius.

Purple of Cassius is formed by mixing tin chloride with gold chloride, resulting in colloidal gold and tin oxide. The metal nanoparticles form before being applied as a colorant, resulting in controlled particle growth and better particle dispersion. As such, these small (~20 nm radius), more uniform nanoparticles produce no array interference in the visible spectrum. Instead, there is only Mie scattering of the small nanoparticles within the tin-rich layer, which produces a color without any lustrous effect. These findings were based on the gold particle sizes seen in Figure 6.3. With this knowledge, a successful lustrous reproduction would be

expected to have a polydisperse distribution of gold nanoparticles, with enough gold content to nucleate large nanoparticles and many smaller ones near the surface, but not so high as to create a “thick film” of gold, as is seen in gilding.

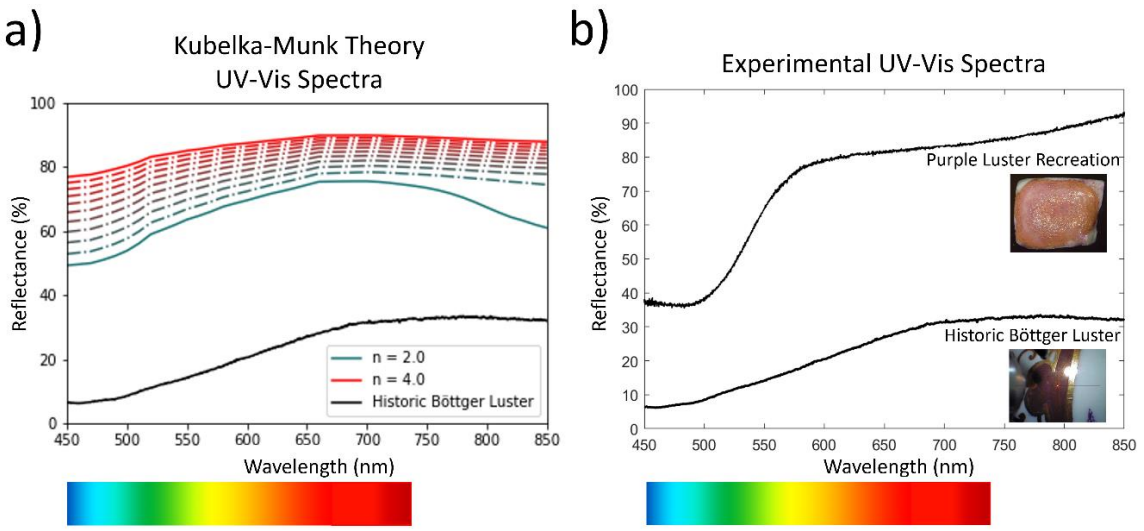

Figure 6.5. Color of Böttger luster: a) Kubelka-Munk theoretical UV-Vis spectra showing reflectance of an infinitely thick nanoparticle layer (also referred to as reflectivity) as a function of wavelength, along with the experimentally obtained UV-Vis spectrum of historic Böttger luster. b) Experimental UV-Vis spectra of Böttger luster, including recreated and historic samples. Note: the intermediate lines in the theoretical plots are spaced $\Delta n=0.2$ apart.

Shown in Figure 6.5a, simulations of the hue, based on Kubelka-Munk Theory, were compared to the UV-Vis reflectance spectrum of historic Böttger luster. Spectra are displayed for indices of refraction (n) ranging between $2 < n < 4$, to illustrate how small deviations of the refractive index of the lead-rich matrix can influence the reflectivity of the glaze. Our results align with the empirical observation that nanoparticles in the radius range of ~15-250 nm produce a purple coloration. Resonant reflectance can occur at wavelengths slightly larger than the array’s periodicity, with smaller nanoparticles giving sharper peaks [27]. Therefore, Böttger luster’s very largest nanoparticles, which are widely separated, create broad peaks in the visible reflectance spectrum, generating luster in addition to the underlying coloration from Mie scattering. Conversely, the smaller nanoparticles (less than

15 nm), which have much smaller periodicity, produce narrow peaks in the ultraviolet reflectance spectra and do not contribute to visible optics.

UV-Vis spectroscopy was also used to compare a historic sample of Böttger luster to our purple luster recreation, seen in Figure 6.5b. Experimental results are consistent with the observed colors of the glazes, where our purple reproduction strongly reflects red-yellow with traces of green and blue, while the darker purple of the historic Böttger luster sample reflects more blue light. The reproduction is more reflective than the historic sample, possibly because the lead glaze of the recreation contains 46.8 wt.% PbO while the historic sample contains 21.7 wt.% PbO. In fact, the reflectivity of pure PbO increases dramatically around 500 nm wavelength, which could account for the sharp increase in reflectance observed in the purple luster reproduction at that wavelength [48]. Our results suggest that the optical properties of Böttger luster are governed by the highly reflective, gold-containing lead glaze, and have little to do with the underlying clear Böttger glaze and porcelain body.

6.4 Summary

By characterizing historic samples of Böttger luster, we confirmed experimentally that the iridescence and purple color of Böttger luster originates from an array of gold nanoparticles situated near the surface of the glazed porcelain. This was validated using models of Mie scattering and disordered nanoparticle array interference. Böttger luster exhibits metallic sheen as well as iridescence despite only containing a single layer of nanoparticles, unlike silver- and copper-based lusterware that have multiple bands of nanoparticles separated by a glassy region.

Böttger luster was compared to Purple of Cassius, a more frequently used purple colorant, composed of colloidal gold within a tin-rich glassy matrix. STEM-EDX analyses of cross-sections of Böttger luster and Purple of Cassius glazes reveal information on how the gold nanoparticles are created and distributed within each glaze, implying vital differences between their application methods. In Böttger luster, as with other types of lusterware, the metal nanoparticles develop in the top glaze through a firing step that allows metal ions to

diffuse, nucleate and grow into particles of several sizes inside the glaze. In Purple of Cassius, the gold nanoparticles are precipitated using tin(II) chloride prior to being incorporated into the leaded frit that is applied to create an overglaze enamel, providing a more homogenous particle dispersion and smaller particle sizes.

Purple luster was created through the evaluation of three lead glazes, and analyzed using SEM-EDX, XRD, and UV-Vis. It was determined that the iridescent reproductions contain gold nanoparticles in a lead glaze, like the structure seen in historic Böttger luster. Thus, we have demonstrated that purple luster can be produced following modern-day safety standards, applying gold(III) chloride as the source of gold ions along with minimal processing of lead-rich powders, albeit with the formation of alkali salts in a matrix that is chemically different from historic Böttger luster.

The techniques used by alchemists in the 18th century Meissen Manufactory were likely the fruit of repeated trials in their tireless attempts to appease Augustus the Strong. Yet, with the aid of contemporary scientific analytical and imaging techniques, we have revealed that the purple colorants of Meissen owe their color and shine to the hidden chemistry, kinetics, and optical effects occurring in their decorative glazes.

References

[1] C.S. Chari, Z.W. Taylor, A. Bezur, S. Xie, K.T. Faber, Nanoscale engineering of gold particles in 18th century Böttger lusters and glazes, Proceedings of the National Academy of Sciences. 119 (2022) e2120753119. https://doi.org/10.1073/pnas.2120753119.

[2] J. Gleeson, The Arcanum: The extraordinary true story, Warner Books, Inc., New York NY, 1998.

[3] M. Spataro, N. Meeks, M. Bimson, A. Dawson, J. Ambers, Early porcelain in seventeenth-century England: Non-destructive examination of two jars from Burghley House, The British Museum Technical Research Bulletin. 3 (2009) 37–46.

[4] W.D. Kingery, P.B. Vandiver, Ceramic masterpieces, The Free Press, New York NY, 1986.

[5] A. Bezur, F. Casadio, Du Paquier Porcelain: Artistic expression and technological mastery. A scientific evaluation of the materials, in: Fired by Passion. Vienna Baroque Porcelain of Claudius Innocentius Du Paquier, Arnoldsche, 2009.

[6] N. Zumbulyadis, "...with a dreadful bang": A chemical history of Bottger lustre, Keramos. 222 (2013) 3–16.

[7] D. Lübke, Böttger-lüster, Keramos. 185 (2004) 13–22.

[8] R. Seyffarth, Johann Gregor Höroldt als chemiker und techniker, Mitteilungsblatt / Keramik-Freunde der Schweiz. 39 (1957). https://doi.org/10.5169/SEALS-394953.

[9] N. Zumbulyadis, Decorating with explosives: The use of aurum fulminans as a purple pigment, Bulletin for the History of Chemistry. 39 (2014) 7–17.

[10] K. Domoney, A.J. Shortland, S. Kuhn, Characterization of 18th-century Meissen porcelain using SEM-EDS, Archaeometry. 54 (2012) 454–474. https://doi.org/10.1111/j.1475-4754.2011.00626.x.

[11] F. Casadio, A. Bezur, K. Domoney, K. Eremin, L. Lee, J.L. Mass, A. Shortland, N. Zumbulyadis, X-ray fluorescence applied to overglaze enamel decoration on eighteenth- and nineteenth-century porcelain from central Europe, Studies in Conservation. 57 (2012) S61–S72. https://doi.org/10.1179/2047058412Y.0000000047.

[12] N. Zumbulyadis, V. Van Thienen, Changes in the body, glaze and enamel compositions of early Meissen porcelain, 1723–c.1740, Archaeometry. 62 (2020) 22–41. https://doi.org/10.1111/arcm.12502.

[13] P. Colomban, B. Kırmızı, B. Zhao, J.-B. Clais, Y. Yang, V. Droguet, Investigation of the pigments and glassy matrix of painted enamelled Qing dynasty chinese porcelains by noninvasive on-site raman microspectrometry, Heritage. 3 (2020) 915–940.

[14] C. Louis, O. Pluchery, Gold nanoparticles in the past: Before the nanotechnology era, Gold Nanoparticles for Physics, Chemistry and Biology. 1 (2012).

[15] I. Borgia, B. Brunetti, A. Giulivi, A. Sgamellotti, F. Shokouhi, P. Oliaiy, J. Rahighi, M. Lamehi-Rachti, M. Mellini, C. Viti, Characterisation of decorations on Iranian (10th–13th century) lustreware, Applied Physics A. 79 (2004) 257–261. https://doi.org/10.1007/s00339-004-2519-z.

[16] P. Colomban, The use of metal nanoparticles to produce yellow, red and iridescent colour, from bronze age to present times in lustre pottery and glass: solid state chemistry, spectroscopy and nanostructure, Journal of Nano Research. 8 (2009) 109–132. https://doi.org/10.4028/www.scientific.net/JNanoR.8.109.

[17] I. Borgia, B. Brunetti, I. Mariani, A. Sgamellotti, F. Cariati, P. Fermo, M. Mellini, C. Viti, G. Padeletti, Heterogeneous distribution of metal nanocrystals in glazes of historical pottery, Applied Surface Science. 185 (2002) 206–216. https://doi.org/10.1016/S0169-4332(01)00659-6.

[18] P. Fredrickx, D. Hélary, D. Schryvers, E. Darque-Ceretti, A TEM study of nanoparticles in lustre glazes, Applied Physics A. 79 (2004) 283–288. https://doi.org/10.1007/s00339-004-2515-3.

[19] J. Molera, M. Mesquida, J. Perez-Arantegui, T. Pradell, M. Vendrell, Lustre recipes from a Medieval workshop in Paterna, Archaeometry. 43 (2001) 455–460. https://doi.org/10.1111/1475-4754.00028.

[20] G. Padeletti, P. Fermo, Production of gold and ruby-red lustres in Gubbio (Umbria, Italy) during the Renaissance period, Applied Physics A. 79 (2004) 241–245. https://doi.org/10.1007/s00339-004-2513-5.

[21] S. Padovani, D. Puzzovio, C. Sada, P. Mazzoldi, I. Borgia, A. Sgamellotti, B.G. Brunetti, L. Cartechini, F. D'Acapito, C. Maurizio, F. Shokoui, P. Oliaiy, J. Rahighi, M. Lamehi-Rachti, E. Pantos, XAFS study of copper and silver nanoparticles in glazes of medieval middle-east lustreware (10th–13th century), Applied Physics A. 83 (2006) 521–528. https://doi.org/10.1007/s00339-006-3558-4.

[22] R.F. Geller, E.N. Bunting, Report on the systems lead oxide-alumina and lead oxide- alumina-silica, Journal of Research of the National Bureau of Standards. 31 (1943) 255–270.

[23] A. Chhatre, P. Solasa, S. Sakle, R. Thaokar, A. Mehra, Color and surface plasmon effects in nanoparticle systems: Case of silver nanoparticles prepared by microemulsion route, Colloids and Surfaces A: Physicochemical and Engineering Aspects. 404 (2012) 83–92. https://doi.org/10.1016/j.colsurfa.2012.04.016.

[24] W.J. Wiscombe, Improved Mie scattering algorithms, Applied Optics. 19 (1980) 1505. https://doi.org/10.1364/AO.19.001505.

[25] B. Sumlin, Functions for forward Mie calculations of homogeneous spheres — PyMieScatt 1.7.5 documentation., (n.d.). https://pymiescatt.readthedocs.io/en/latest/forward.html#functions-for-single-particles.

[26] H.G. Hecht, The interpretation of diffuse reflectance spectra, Journal of Research of the National Bureau of Standards Section A: Physics and Chemistry. 80A (1976) 567–583. https://doi.org/10.6028/jres.080A.056.

[27] F.J. García de Abajo, Colloquium: Light scattering by particle and hole arrays, Reviews of Modern Physics. 79 (2007) 1267–1290. https://doi.org/10.1103/RevModPhys.79.1267.

[28] D. Pacifici, H.J. Lezec, L.A. Sweatlock, R.J. Walters, H.A. Atwater, Universal optical transmission features in periodic and quasiperiodic hole arrays, Optics Express. 16 (2008) 9222–9238. https://doi.org/10.1364/OE.16.009222.

[29] F. Przybilla, C. Genet, T.W. Ebbesen, Long vs short-range orders in random subwavelength hole arrays, Optics Express. 20 (2012) 4697–4709. https://doi.org/10.1364/OE.20.004697.

[30] J. Lafait, S. Berthier, C. Andraud, V. Reillon, J. Boulenguez, Physical colors in cultural heritage: Surface plasmons in glass, Comptes Rendus Physique. 10 (2009) 649–659. https://doi.org/10.1016/j.crhy.2009.08.004.

[31] G. Padeletti, P. Fermo, Italian Renaissance and Hispano-Moresque lustre-decorated majolicas: Imitation cases of Hispano-Moresque style in central Italy, Applied Physics A. 77 (2003) 125–133. https://doi.org/10.1007/s00339-002-2048-6.

[32] M. Verita, P. Santopadre, Analysis of gold-colored Ruby Glass tesserae in Roman church mosaics of the 4th to 12th centuries, Journal of Glass Studies. 52 (2010) 11–24.

[33] F.E. Wagner, S. Haslbeck, L. Stievano, S. Calogero, Q.A. Pankhurst, K.-P. Martinek, Before striking gold in gold-ruby glass, Nature. 407 (2000) 691–692. https://doi.org/10.1038/35037661.

[34] F. Gol, Z.G. Saritas, S. Cıbuk, C. Ture, E. Kacar, A. Yilmaz, M. Arslan, F. Sen, Coloring effect of iron oxide content on ceramic glazes and their comparison with the similar waste containing materials, Ceramics International. (2021).

[35] L.B. Hunt, The true story of Purple of Cassius: The birth of gold-based glass and enamel colours, Gold Bull. 9 (1976) 134–139. https://doi.org/10.1007/BF03215423.

[36] W.D. Kingery, P.B. Vandiver, The 18th century changes in technology and style from the famille verte palette to the famille rose palette, Technology and Style. (1986) 363–82.

[37] A. Ruivo, C. Gomes, A. Lima, M.L. Botelho, R. Melo, A. Belchior, A. Pires de Matos, Gold nanoparticles in ancient and contemporary ruby glass, Journal of Cultural Heritage. 9 (2008) 134–137. https://doi.org/10.1016/j.culher.2008.08.003.

[38] S. Haslbeck, K.P. Martinek, L. Stievano, F.E. Wagner, Formation of gold nanoparticles in gold ruby glass: The influence of tin, Hyperfine Interactions. 165 (2005) 89–94. https://doi.org/10.1007/s10751-006-9246-0.

[39] M.E.F. Reboulleau, M.D. Magnier, A. Romain, H. Bertran, Nouveau manuel complet de la peinture sur verre, sur porcelaine et sur email, L. Mulo, 1900.

[40] D. Lübke, Keramische Fachbegriffe für die Analyse von frühem Meissner Porzellan, Rach Verlag Bramsche, Germany, 2014.

[41] E. Menendez, R. Garcia-Roves, B. Aldea, Incidence of alkali release in concrete dams. Evaluation of alkalis releasable by feldspars., in: MATEC Web Conference, 2018.

[42] P. Mulvaney, Not all that's gold does glitter, MRS Bulletin. 26 (2001) 1009–1014. https://doi.org/10.1557/mrs2001.258.

[43] L. Novotny, B. Hecht, Ch 12: Surface Plasmons. in Principles of nano-optics, in: Principles of Nano-Optics, Cambridge University Press, n.d.: pp. 369–413.

[44] O. Benson, Ch 7: Plasmonics. in Elements of Nanophotonics, in: HUZU, 2019.

[45] X. Fan, W. Zheng, D.J. Singh, Light scattering and surface plasmons on small spherical particles, Light: Science & Applications. 3 (2014) 1–14.

[46] V. Reillon, S. Berthier, C. Andraud, Optical properties of lustred ceramics: Complete modelling of the actual structure, Applied Physics A. 100 (2010) 901–910. https://doi.org/10.1007/s00339-010-5791-0.

[47] H. Hirayama, K. Kaneda, H. Yamashita, Y. Monden, An accurate illumination model for objects coated with multilayer films, Computers & Graphics. 25 (2001) 391–400. https://doi.org/10.1016/S0097-8493(01)00063-2.

[48] S. Zou et al., A new reaction between common compounds: Lead reacts with formaldehyde, ChemComm. 50 (2014) 6316–6318.

Chapter 7

CONCLUSIONS AND FUTURE WORK

The objective of this thesis was to investigate the processing-microstructure-performance relationship of ceramics, specifically with regard to the degradation of ceramic surfaces. Throughout this thesis, this relationship was examined using a series of material case studies, including (i) advanced high-temperature ceramics composed of h-BN rich composites, and (ii) historic ceramics, ranging from low-fired pottery to porcelain. This work provided details for the design and manufacturing of novel high-performing ceramics used in electric propulsion while simultaneously referring to ceramics of the past to understand how their surfaces have altered over their lifetime. An emphasis was drawn on ways of mitigating degradation from mechanical wear and chemical erosion by controlling processing conditions and, when possible, environmental exposures, so as to aid in the sustainability of the materials.

We first designed and manufactured novel dielectric and emissive bimaterials for Hall thruster chambers with a more desirable fracture behavior than the state-of-the-art bulk h-BN; these bimaterials were composed of graphite with h-BN surface layers. The carbothermic reaction used to synthesize the bimaterials was evaluated considering both the liquid-phase and vapor-phase reactions taking place, given the high volatility of B_2O_3 above 1650 °C. It was found that the reacting phase of B_2O_3 influenced the surface microstructure and thickness of the h-BN layer, as well as the size of the interface between the layers, giving insight into the processing-microstructure relationship of this system. The interfacial fracture toughness of the bimaterial, notably, did not depend on the reacting phase of B_2O_3, and the porous nature of the h-BN layer ensured a strong adhesion between the coupled materials. The bimaterial was exposed to thruster environments to assess its performance and degradation in electric propulsion systems. It was found that the initial microstructure and presence of surface irregularities played a defining role in the response of the ceramic to surface impingement from Mo and Xe ions, with smoother surfaces synthesized from vapor-phase B_2O_3 performing the strongest. These findings highlight the

potential of using graphite/h-BN bimaterials as wall materials for Hall thruster chambers, specifically for bimaterials synthesized from vapor-phase carbothermic reactions.

A key concern in the current understanding of this materials system is the polycrystallinity and porosity of the h-BN layer, which results in different erosion rates of the layer dependent on the local orientation of the h-BN flakes. It is suggested that future work concentrate on methods of homogenizing the h-BN flake orientation, by (i) using a uniaxial hot press or hydraulic press post-processing to densify the h-BN layers and reorient the flakes, (ii) using temperatures higher than 1700 °C during the carbothermic synthesis to improve densification effects, (iii) investigating alternative synthesis routes that minimize the evolution of $CO_{(g)}$, perhaps by forming an initial h-BN "seed" layer covering the graphite body at 1600 °C, and then further growing the h-BN layer at 1700 °C in the presence of excess $B_2O_{3(g)}$ and $N_{2(g)}$ in a two-step reaction.

Our second materials system was a composite made of AlN and h-BN. The microstructure of the composite was monitored under varying high-temperature oxidative environments to evaluate the degradation mechanism of the material. A passivation layer composed of $Al_{18}B_4O_{33}$ formed on the surface of the material, which retarded the oxidation of the underlying AlN substrate. It was found that the protection provided by the passivation layer relied on the microstructure and morphology of the $Al_{18}B_4O_{33}$ crystals, with the protection being threatened by the development of hollow cores in the crystals, which aided the transport of oxygen into the substrate. The chemical composition and mechanical properties of the acicular crystals were found to degrade with increasing temperature into a porous Al_2O_3 framework at temperatures higher than 1300 °C due to the volatility of B_2O_3. In addition, small crystals of $Al_{18}B_4O_{33}$ were shown to exhibit self-healing of the indented AlN/BN composite by providing friction through crack walls that led to improved flexural strengths. These results show promise for the use of $Al_{18}B_4O_{33}$ as a reinforcement material.

It is suggested that future work concentrate on (i) the use of $Al_{18}B_4O_{33}$ as porous ceramic joints or load-bearing reinforcements for composite structures, (ii) the growth mechanism of $Al_{18}B_4O_{33}$ crystals through additional microscopic studies, to understand if the crystal grows spirally from a dislocation or through an alternative process, and (iii) the dissolution

of $Al_{18}B_4O_{33}$ in B_2O_3 melts, to understand if this contributes to hollow core formation in high-temperature environments.

The third material system studied consisted of clay minerals typically found in low-fired pottery; kaolinite ($Al_2Si_2O_5(OH)_4$) and metakaolin ($Al_2Si_2O_7$). Through a combined experimental and computational approach, it was found that heat-treated kaolinite, referred to as metakaolin, was more susceptible to degradation than kaolinite, through a process referred to as dealumination. The exposed Al cations in the metakaolin structure could react with S-rich pollutants, including H_2SO_4, H_2SO_3, SO_2, and SO_3, leading to the precipitation of $Al_2(SO_4)_3$ and amorphous SiO_2. Thus, it was found that the extent of degradation of clay-based pottery in acidic soils or acid rain depended on the firing temperature of the samples, with metakaolin forming between 500 °C and 900 °C, and kaolinite or partially dehydrated kaolinite forming at 400 °C or below. This study provides an example of how processing conditions like firing temperature can directly affect the degradation of the material on an atomistic level, with consequences scaling-up to a microscopic level through the development of the mordant $Al_2(SO_4)_3$.

It is recommended that future work focus on (i) exploring if similar degradation mechanisms to dealumination are observed when clay tiles are exposed to a mixture of SO_2 and H_2O, which is a more realistic simulation of acid rain than our initial dry SO_2 attempt, (ii) probing if dealumination is promoted in samples that are more porous, and if so relating this back to firing temperatures within the metakaolin range, (iii) studying tiles of varying thicknesses to see how ununiform heating throughout a sample could result in interior bodies that are richer in kaolinite and surfaces that are richer in metakaolin, which could result in variations of dealumination throughout the thickness of the sample (on the order of ~10 μm). This could be studied using tomography and X-ray spectroscopy through synchrotron collaborations (e.g., X-ray Raman spectral mapping and spectroscopy), (iv) investigating to what extent the mordant $Al_2(SO_4)_3$ can facilitate the binding of stains onto the ceramic, perhaps using organic pigments as “stains”, with the additional use of fractography to study how the crystallization of the sulfate salts within the open pores could lead to fracture, (v) studying more complex systems to not just consider the clay

components of pottery, but also additives like feldspar, silica, mica, iron oxides, and even Ca-rich inclusions.

The fourth and final material system studied in this thesis was hard-paste porcelain and lead glazes from the Meissen Manufactory. Referring to original recipes from Meissen from the 18th century, recreations of Böttger porcelain and the purple colorant "Böttger luster" were synthesized and compared to historic samples. The optical effects governing the appearance of the purple glaze were related back to the surface microstructure of the lead glaze, which featured arrays of Au nanoparticles. Comparing the glaze to a contemporaneous purple colorant, Purple of Cassius, the distribution of the metal nanoparticle sizes, and nearest neighbor distances were used to understand the optical differences between the two glazes, and the origin of purple luster. By researching historic production methods and techniques, critical information was discovered on the processing-microstructure relationship of these system. Mainly, Purple of Cassius was prepared by synthesizing colloidal gold using tin(II) chloride, which resulted in homogenous, small particles that formed *prior* to the firing step, while Böttger Luster was prepared by applying gold salts on top of glazed surfaces, resulting in a mix of large and small gold particles that formed *during* the firing step. This chapter providing an example of how innovative and sustainable materials can be created using modern technologies inspired by the past.

Related to this study, future work could focus on (i) studying the chemical and mechanical properties of Böttger porcelain, regarded as the most thermal-shock resistant porcelain ever produced, using experimental recreations and computational models to understand how its behavior differs from porcelains made in the Far East, (ii) investigating if the shift in 1730 within the Meissen Manufactory from Böttger porcelain (Ca-rich) to Meissen porcelain (K-rich) resulted in significant changes to the mechanical properties of the porcelain, including its thermal-shock resistance and toughness, (iii) studying other colorants used from Meissen, including Höroldt's "iron-red" glaze, of which original recipes have recently been translated, and also Höroldt's cobalt blue glaze.

Appendix A

GRAPHITE/HEXAGONAL BORON NITRIDE BIMATERIALS

A.1 Urea-Based Routes for Synthesizing h-BN Layer

Initial studies on the formation of h-BN layers focused on the high-temperature reaction of B_2O_3 with N-containing compounds like urea ($CO(NH_2)_2$), which decomposes into ammonia (NH_3) at 350 °C. These amide reactions required the initial formation of turbostratic BN (t-BN), which developed at 950 °C from the reaction between B_2O_3 and NH_3 [1–4]. The structure of t-BN consists of two-dimensional layers of hexagonal boron nitride that are slightly misaligned with one another, producing a structure that is not as ordered as h-BN [2]. Nevertheless, t-BN can crystallize into h-BN at 1500 °C [4], acting as an intermediate phase to h-BN formation that requires relatively low temperatures (950 °C) to grow.

Experiments were carried out to test the incorporation of t-BN into the precursor powder melt, otherwise consisting of B_2O_3 and h-BN. Figure A.1 shows two precursor melt compositions that were investigated. The composition used in Figure A.1a, based on the findings by Thomas [2], did not result in a visible h-BN layer. The corresponding XRD spectrum shows the presence of only the graphite body. A different composition was investigated, as shown in Figure A.1b, this time with slightly higher quantities of B_2O_3. It was found that this precursor composition did develop a h-BN layer on the graphite body, however this layer was found to be around 50 μm thin, and patchy in appearance. The surface microstructure of the h-BN layer was porous, containing small (~1 μm) sized flakes. The porosity could have been due to the relatively low synthesis temperature of 1550 °C as well as off-gassing from CO due to Eqn. 2.1.

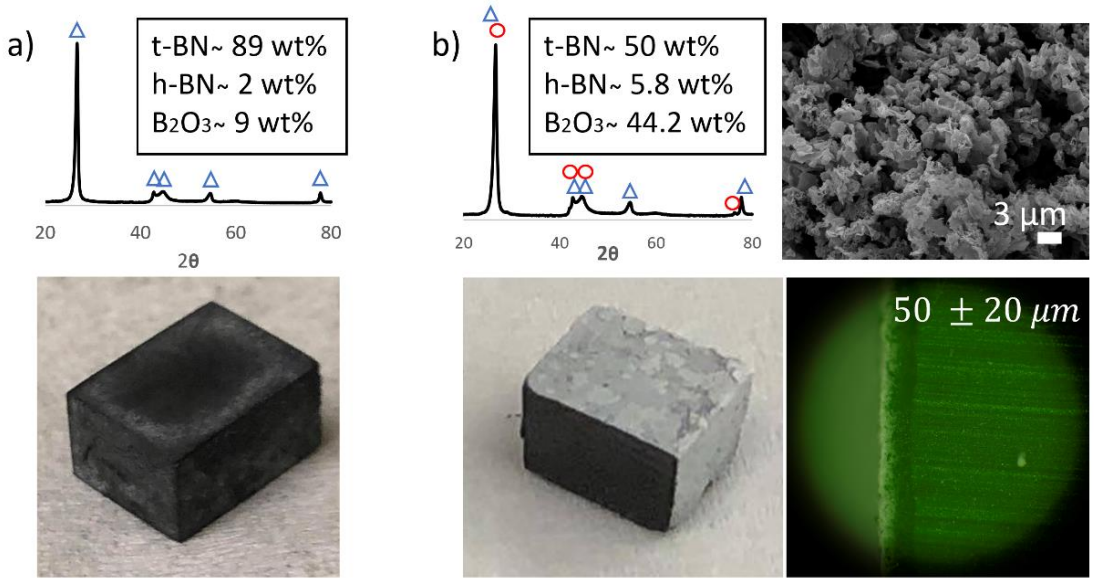

Figure A.1 Graphite/h-BN samples made using urea-based route: a) XRD spectrum and image of graphite/h-BN bimaterial synthesized from melt containing t-BN (89 wt%), h-BN (2 wt%), and B_2O_3 (9 wt%), at 1550 °C for 12 h. b) XRD spectrum and image of graphite/h-BN bimaterial synthesized from melt containing t-BN (50 wt%), h-BN (5.8 wt%), and B_2O_3 (44.2 wt%) at 1550 °C for 12 h, including electron micrograph of h-BN layer surface, and cross-sectioned image of bimaterial showing h-BN layer thickness of 50 ± 20 µm.

Apart from the ununiform h-BN layers, an additional problem encountered with this route was that the concentration of urea used to form t-BN was limited during the reaction. Although a lid was placed on top of the crucible, the off-gassing of NH_3 from decomposing urea caused the lid to come off the crucible, which allowed NH_3 vapors to leave the crucible before the t-BN forming temperature of 950 °C was even reached. This made it challenging to produce t-BN from the amide reaction. Flowing NH_3 vapors through the tube furnace would have facilitated t-BN formation, however this is also a hazardous gas to work with in the laboratory. Carbothermic reactions were thus investigated more closely for two reasons: i) they would only require the flow of N_2 vapors and not NH_3, ii) Figure A.1 suggests that high concentrations of B_2O_3 lead to thicker h-BN layers, so it was decided to make the precursor powders as rich in B_2O_3 and h-BN as possible, as described in Materials and Methods in Chapter 2.

A.2 Equilibrium Partial Pressure Calculations

Thermochemical information on the reactions featured in Chapter 2 are provided below.

$$B_2O_{3(l)} + 3C_{(s)} + N_{2(g)} \rightarrow 2BN_{(s)} + 3CO_{(g)} \quad (2.1)$$

The standard Gibbs free energy change in Joules for Eqn. 2.1 was calculated to be:

$$\Delta G^{o}_{(2.1)} = 2{,}550 - (130 \times T)$$

using thermochemical data from Chase [5].

$$2B_2O_{3(l)} + 7C_{(s)} \rightarrow B_4C_{(s)} + 6CO_{(g)} \quad (2.2)$$

The standard Gibbs free energy change in joules for Eqn. 2.2 was calculated to be:

$$\Delta G^{o}_{(2.2)} = 946{,}000 - (605 \times T)$$

using thermochemical data from Chase [5].

$$B_2O_{3(l)} + 2C_{(s)} \rightarrow 2BO_{(g)} + CO_{(g)} \quad (2.3)$$

$$B_2O_{3(l)} + 3C_{(s)} \rightarrow 2B_{(g)} + 3CO_{(g)} \quad (2.4)$$

$$B_2O_{3(l)} \rightarrow B_2O_{3(g)} \quad (2.5)$$

$$2B_{(g)} + \frac{1}{2}N_{2(g)} \rightarrow BN \quad (2.6)$$

The equilibrium partial pressures of the gaseous species in a closed system can be estimated by determining the equilibrium constants, *K*, of these reactions. The standard Gibbs free energy change in joules for Eqns. 2.3 to 2.6 are as follows:

$$\Delta G^{o}_{(2.3)} = 1{,}106{,}840 - (473.42 \times T)$$

$$\Delta G^{o}_{(2.4)} = 2{,}025{,}980 - (763 \times T)$$

$$\Delta G^{o}_{(2.5)} = 359{,}995 - (186.2 \times T)$$

$$\Delta G^{o}_{(2.6)} = -820{,}780 + (235.43 \times T)$$

Note that $\Delta G^{o}_{(2.3)}$, $\Delta G^{o}_{(2.4)}$ and $\Delta G^{o}_{(2.6)}$ were taken from Aydoğdu et al [6] from data compiled by Turkdogan [7], while $\Delta G^{o}_{(2.5)}$ was taken from Yoon et al [8]. Equilibrium constants could then be calculated at a given temperature through the following relationship: $K_{(i)} = \exp\left(-{}^{\Delta G^{o}_{(i)}}/_{T}\right)$. The equilibrium partial pressures were thus calculated by finding the simultaneous solution of the following equations:

$$K_{(2.3)} = P_{BO}^{2} \times P_{CO}$$

$$K_{(2.4)} = P_{B}^{2} \times P_{CO}^{3}$$

$$K_{(2.5)} = P_{B_2O_3}$$

$$K_{(2.6)} = \frac{1}{P_B \times {P_{N_2}}^{1/2}}$$

where $P_{CO} + P_B + P_{BO} + P_{N_2} + P_{B_2O_3} = 1$.

$$\frac{1}{2}\mathrm{N_{2(g)}} + \frac{1}{2}\mathrm{B_2O_{3(l)}} \rightarrow \mathrm{BN_{(s)}} + \frac{3}{4}\mathrm{O_{2(g)}} \qquad (2.7)$$

The standard Gibbs Free Energy change in joules for Eqn. 2.7 is $\Delta G^{o}_{(2.7)} = 364{,}000 - (17.4 \times T)$, where $K_{(2.7)} = \frac{{P_{O_2}}^{3/4}}{{P_{N_2}}^{1/2}}$ (units of atm$^{-1/4}$)

$$3\mathrm{B_4C_{(s)}} + \mathrm{B_2O_{3(l)}} + 7\mathrm{N_{2(g)}} \rightarrow 14\mathrm{BN} + 3\mathrm{CO} \qquad (2.10)$$

The standard Gibbs free energy change in Joules for Eqn. (2.10) was calculated to be $\Delta G^{o}_{(2.10)} = -2{,}820{,}000 - (-906 \times T)$ using thermochemical data from Chase [5], where $K_{(2.10)} = \frac{{P_{CO}}^{3}}{{P_{N_2}}^{7}}$ (units of atm^{-4}).

A.3 Relative Concentration of Vapor-Phase Species in h-BN forming Carbothermic Reaction

Knowing the equilibrium partial pressures of CO, BO, B, N_2 and B_2O_3 as shown in Figure 2.5, and the volume of the crucible as 0.024 L, the mole % and wt % of the gaseous species could be estimated using the ideal gas law, seen in Figures A.2 and A.3, respectively.

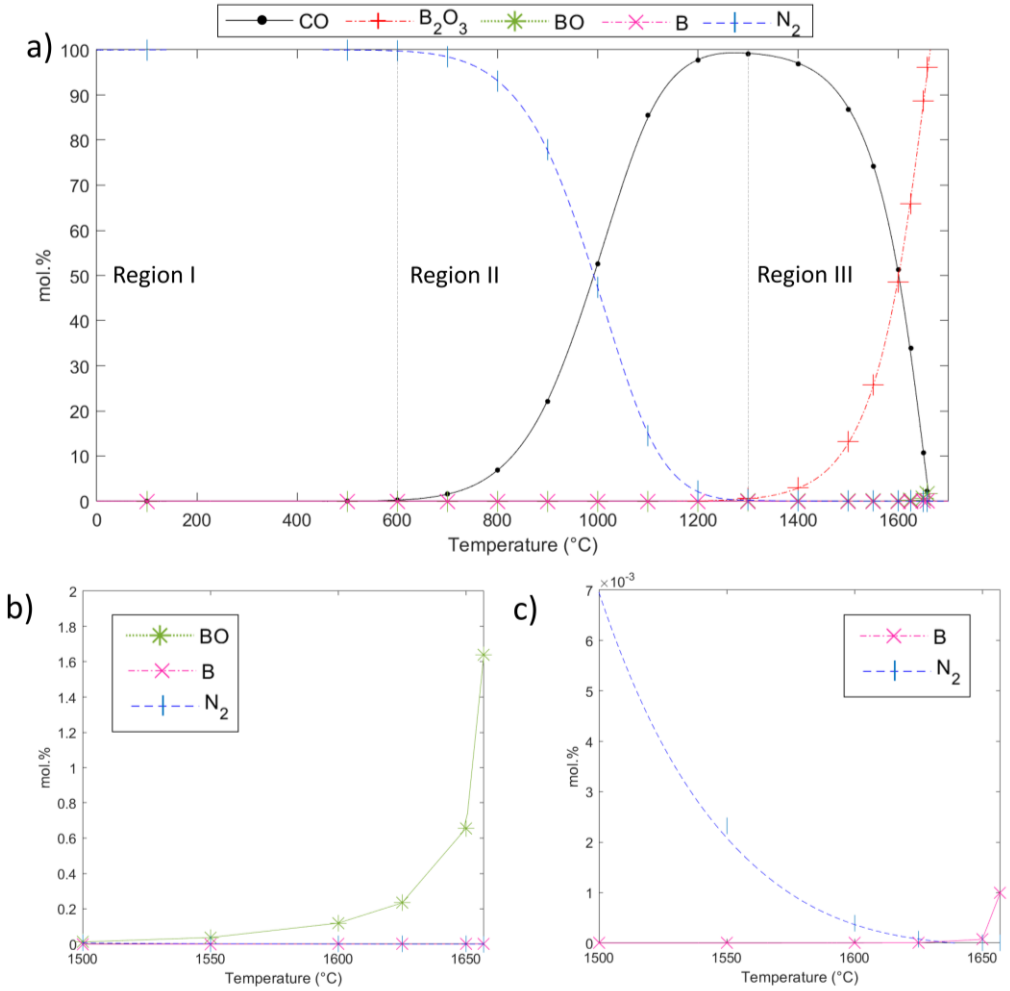

Figure A.2 Mole % of CO, BO, B, B_2O_3 and N_2 in a closed system as a function of temperature: a) showing three distinct regions largely populated by N_2, CO, and B_2O_3, respectively. b) Close-up of a) showing increase in BO concentration with temperature. c) Close-up of a) showing increase in B concentration with temperature.

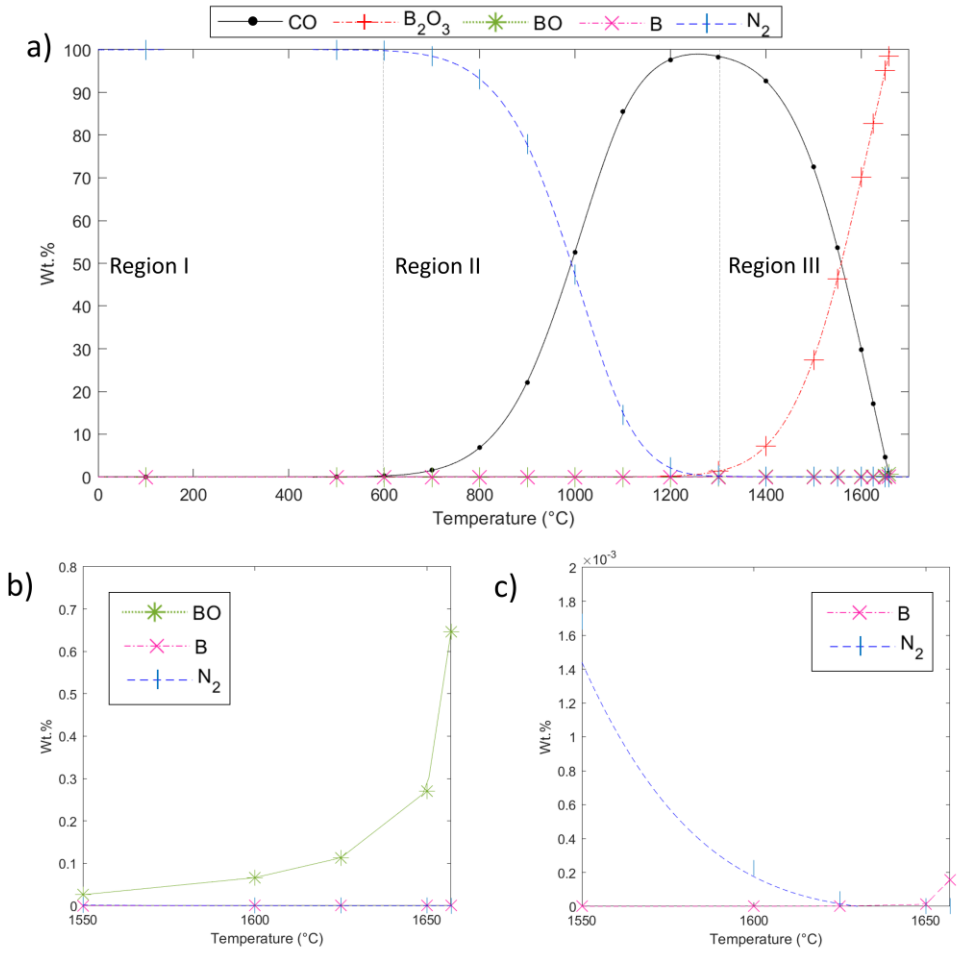

Figure A.3 Weight % of CO, BO, B, B_2O_3 and N_2 in a closed system as a function of temperature: a) showing three distinct regions largely populated by N_2, CO, and B_2O_3, respectively. b) Close-up of a) showing increase in BO concentration with temperature. c) Close-up of a) showing increase in B concentration with temperature.

A. 4. Diffusion Profiles at the Interface of Graphite/h-BN

The most dispersed interface is seen when the reaction is carried out for 8 h at 1650 °C, which shows evidence of B_4C formation in this sample, as was previously seen with X-ray spectra (Figure 2.7c) and supported by the SEM-EDS map in Figure 2.2b. As the temperature and reaction time increase, the size of the interfacial region decreases significantly; the interface between the layers becomes better defined as reaction (2.1) progresses. Please note that the residual C-content detected within the h-BN layer is likely due the cross-sectioned samples being carbon-coated for electron imagining analyses.

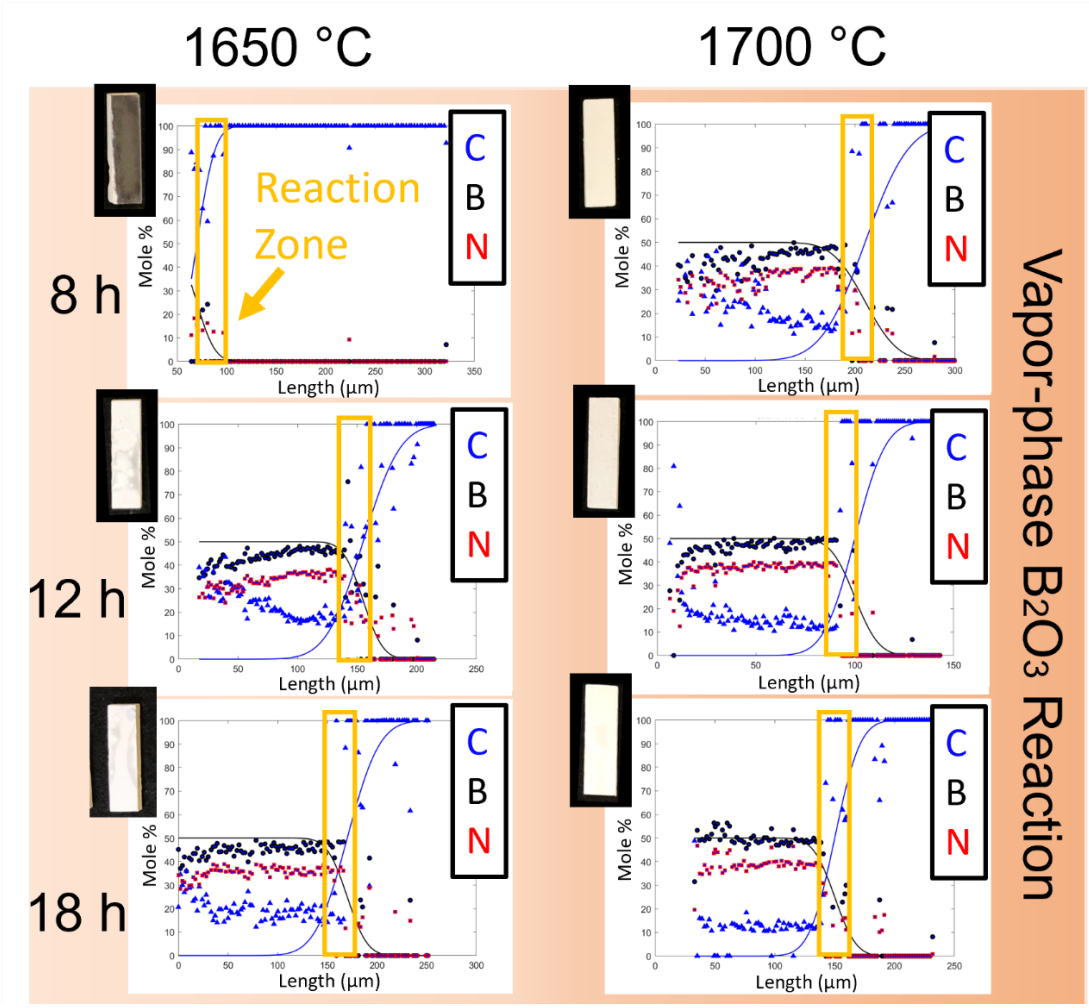

Figure A.4. Diffusion profile showing elemental composition (mole %) of the interface for vapor-phase B_2O_3 (orange) developed h-BN. Insets show photographs of the surface of graphite/h-BN bimaterials.

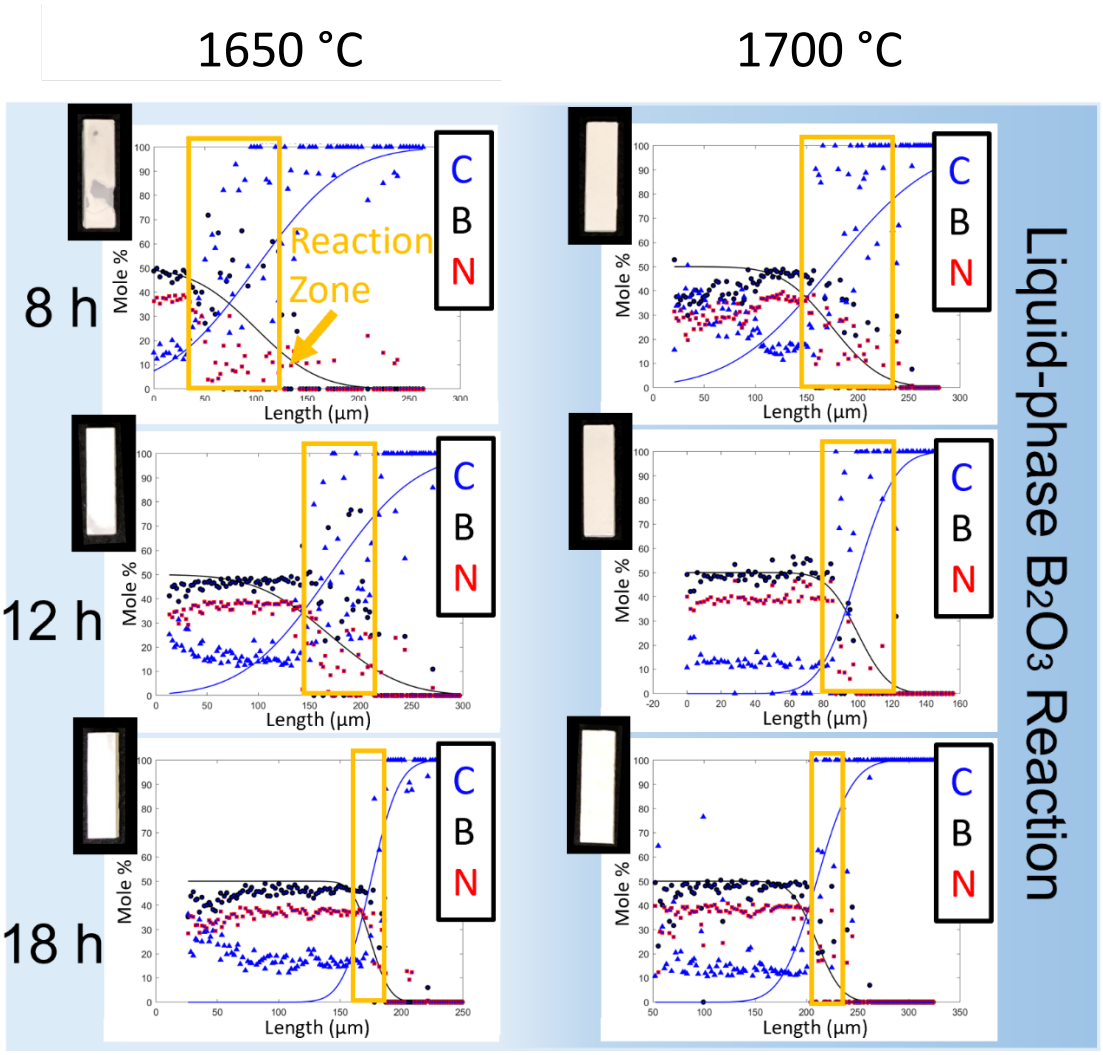

Figure A.5. Diffusion profile showing elemental composition (mole %) of the interface for liquid-phase B_2O_3 (blue) developed h-BN. Insets show photographs of the surface of graphite/h-BN bimaterials.

A. 5. Results of Bimaterial Thermal Cycle Tests

Figure A.6 shows examples of the h-BN surface before and after undergoing 10 thermal cycles up to 250 °C for 30 min. Both optical microscope images and SEM images are included. No spallation or cracking from thermal cycling was observed. Uneven surfaces around the center hole are from drilling artifacts. Uneven h-BN surface was from processing conditions, relying on liquid-phase B_2O_3 reactions with graphite.

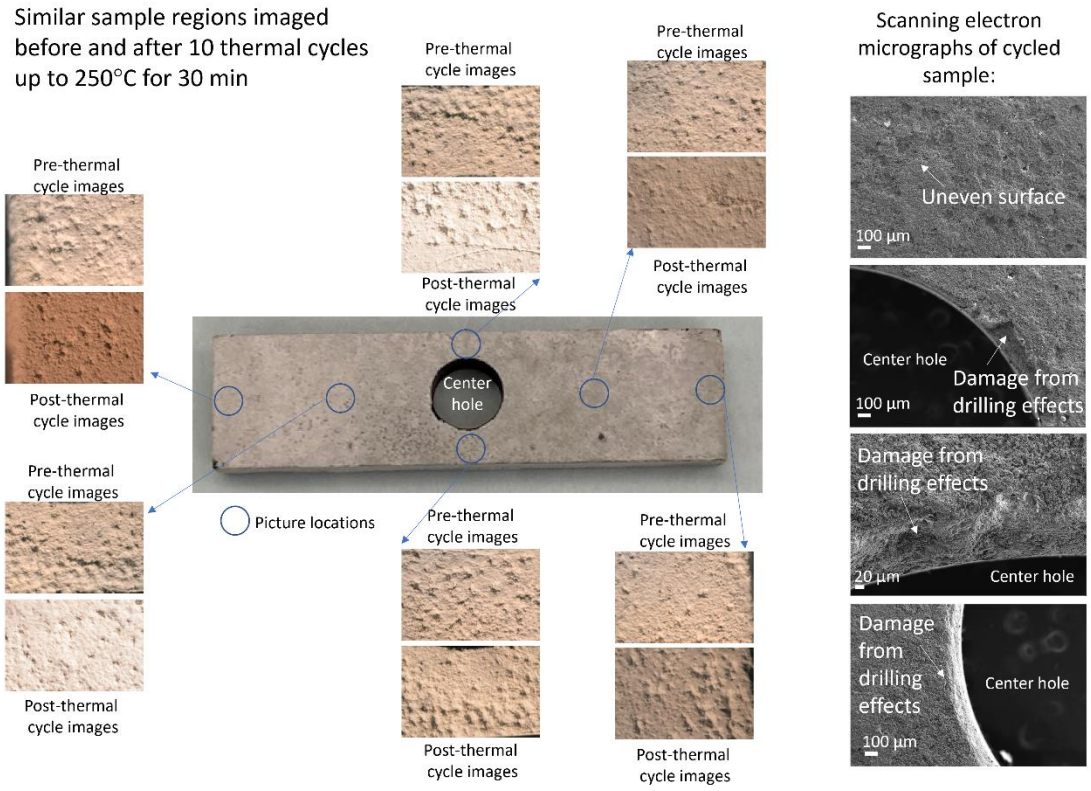

Figure A.6 Bimaterial sample regions imaged before and after thermal cycle test, including examples of micrographs taken with SEM showing uneven surfaces near center hole from drilling effects.

A. 6. Erosion Prediction for State-of-the-art h-BN

Table A.1. Constants for H9 Thrusters

$J_{300V/15A}$	Current density (1 m) @ 300 V / 15A	7 mA/cm^2
$J_{300V/20A}$	Current density (1 m) @ 300 V / 20A	8.75 mA/cm^2
$Y_{hBN\ @\ 300\ V}$	BN sputtering yield @ 300 V	0.020789209 mm^3/C
$J_{400V/15A}$	Current density (1 m) @ 400 V / 15A	9.5 mA/cm^2
$Y_{hBN\ @\ 400\ V}$	BN sputtering yield @ 400 V	0.023399083 mm^3/C
$J_{500V/15A}$	Current density (1 m) @ 500 V / 15A	10 mA/cm^2
$Y_{hBN\ @\ 500\ V}$	BN sputtering yield @ 500 V	0.025129888 mm^3/C

The erosion rate of h-BN could be determined from the constants shown in Table A.1 as follows:

$$\text{hBN Erosion Rate } \left[\frac{\mu m}{hr}\right] = J \times Y_{hBN} \times 0.00001 \times 3600 \times 1000$$

$$= J \times Y_{hBN} \times 36$$

A summary of the calculated h-BN erosion rates is provided in Table A. 2.

Table A.2. Summary of h-BN Erosion Rates

Thruster Condition	300 V / 15 A	300 V / 20 A	400 V / 15 A	500 V / 15 A
BN Erosion Rate [μm/hr]	5.2	6.5	8.0	9.0

Standard exposures can be described as 2 hours at 300 V / 15 A conditions, and 2 hours at 300 V / 20 A conditions. Thus, the total erosion of h-BN can be estimated as follows:

$$\text{hBN Erosion } [\mu\text{m}] = (2 \times 5.2) + (2 \times 6.5) = 23.6\ \mu\text{m}$$

If we were to directly use the thruster conditions of the experiment (referring to Table 3.1), the exposure could be described as 1.57 hours at 300 V / 15 A conditions, 0.63 hours at 400 V / 15 A conditions, and 8.5 h at 500 V / 15 A. Thus, the total expected erosion of h-BN during this 10.7 hour-long exposure would be:

$$\text{hBN Erosion } [\mu\text{m}] = (1.57 \times 5.2) + (0.63 \times 8.0) + (8.5 \times 9.0) = 89.7\ \mu\text{m}$$

As described in profilometry and SEM-EDS results in Chapter 3, graphite/h-BN bimaterials do not reach as high a magnitude of erosion as $89.7\ \mu\text{m}$. So, based on this erosion calculation, the bimaterials actually perform better than what would be expected for state-of-the-art bulk h-BN.

References

[1] T.E. O'Connor, Synthesis of boron nitride, Journal of the American Chemical Society. 84 (1962) 1753–1754. https://doi.org/10.1021/ja00868a065.

[2] J. Thomas, N.E. Weston, T.E. O'Connor, Turbostratic boron nitride, thermal transformation to ordered-layer-lattice boron nitride, Journal of the American Chemical Society. 84 (1962) 4619–4622. https://doi.org/10.1021/ja00883a001.

[3] M. Hubáček, M. Ueki, Chemical reactions in hexagonal boron nitride system, Journal of Solid State Chemistry. 123 (1996) 215–222. https://doi.org/10.1006/jssc.1996.0171.

[4] S. Alkoy, C. Toy, T. Gönül, A. Tekin, Crystallization behavior and characterization of turbostratic boron nitride, Journal of the European Ceramic Society. 17 (1997) 1415–1422. https://doi.org/10.1016/S0955-2219(97)00040-X.

[5] M.W. Chase Jr., NIST-JANAF Themochemical Tables, Fourth Edition, American Chemical Society, 1998.

[6] A. Aydoğdu, N. Sevinç, Carbothermic formation of boron nitride, Journal of the European Ceramic Society. 23 (2003) 3153–3161. https://doi.org/10.1016/S0955-2219(03)00092-X.

[7] E.T. Turkdogan, Physical chemistry of high temperature technology, Academic Press Inc, New York, 1980.

[8] S.J. Yoon, A. Jha, Vapour-phase reduction and the synthesis of boron-based ceramic phases, Journal of Materials Science. 30 (1995) 607–614. https://doi.org/10.1007/BF00356318.

Appendix B

ALUMINUM NITRIDE/BORON NITRIDE COMPOSITES

The contents of this Appendix are also presented in "Oxidation resistance of AlN/BN via mullite-type $Al_{18}B_4O_{33}$" by C.S. Chari and K.T. Faber, which was published in the Journal of the European Ceramic Society in 2022 [1], with the exception of Section 4.6. which was carried out after publication. C.S. Chari led the experimental portion of the work. Faber supervised the experimental work. All authors were involved in designing the work and preparing the manuscript.

B.1 Oxidation Kinetics of AlN

The parabolic (K) and linear rate constants (k) were measured from the AlN oxidation plots in Figure 4.1 using MATLAB as a fitting tool. The rate constant at 1000 °C is 2.2×10^{-9} cm/s, at 1100 °C is 2.6×10^{-8} cm/s, at 1200 °C is 4.0×10^{-9} cm^2/s, at 1300 °C is 6.1×10^{-8} cm^2/s.

As previously discussed, the diffusivity of O atoms to the substrate controls the rate of AlN oxidation. Within the oxide layer, there is interdiffusion between O atoms and Al atoms, where Al atoms have a higher diffusivity than O atoms. Knowing this, it is reasonable to assume that the oxidation rate is in fact controlled by the faster of the two species; controlled by Al atoms rather than O atoms. As such, we can use the oxidation plots from Figure 4.1a to estimate the diffusivity of Al within the porous oxide layer. We refer to previous models by D. W. Readey [2], which link the parabolic rate constant of the metal ion to the free energy of formation of the oxide and the diffusivity of the metal ion, as seen in equation B.1

$$K = \frac{L^2}{t} = -\frac{2 \times D \times \Delta G_{Al_2O_3}}{R \times T} \tag{B.1}$$

where L is the oxide thickness (cm), t is the exposure time (s), D is the diffusivity of the metal ion ($\frac{cm^2}{s}$), and T is the temperature in K. The free energy of formation was calculated

using the enthalpy of formation and the entropy of formation of Al_2O_3 and AlN. The free energy can be corrected to consider that the oxidation was carried out in air, as shown in equation B.2

$$\Delta G_{Al_2O_3} = \Delta G^{o}_{Al_2O_3} - \frac{1}{2} \times R \times T \times ln(p_{O_2}) \tag{B.2}$$

where $\Delta G^{o}_{Al_2O_3}$ ($\frac{J}{mol}$) is the free energy of formation of the oxide from AlN in pure oxygen, $\Delta G_{Al_2O_3}$ ($\frac{J}{mol}$) is the free energy of formation of the oxide from AlN in air, and p_{O_2} in air is 21 kPa. Using thermochemistry data published by NIST [3], $\Delta G_{Al_2O_3}$ could be estimated (-1418 $\frac{kJ}{mol}$ at 1200 °C, -1422 $\frac{kJ}{mol}$ at 1300 °C) and the effective diffusivity was calculated to be 1.7×10^{-11} $\frac{cm^2}{s}$ at 1200 °C, and 2.8×10^{-10} $\frac{cm^2}{s}$ at 1300 °C. These effective diffusivities, describing aluminum ions within alumina, are much greater than the values predicted from the literature [4–6], illustrating the high level of porosity within the oxide layer that results from the evolution of nitrogen gas during AlN oxidation.

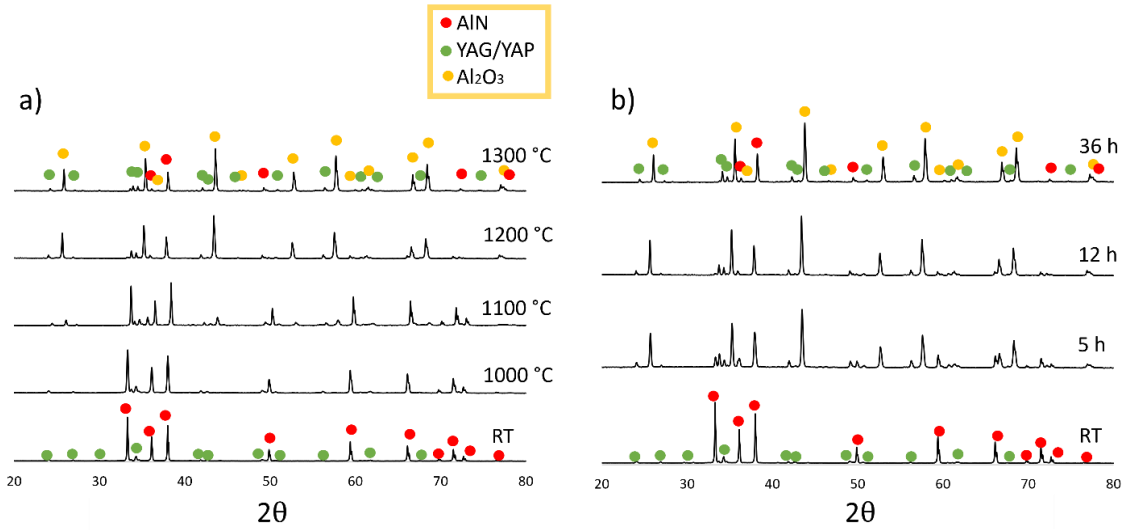

Figure B.1. X-Ray Diffraction patterns of oxidized AlN coupons a) held for 12 h at varying temperatures, b) held at 1200 °C for different times. The unoxidized, room temperature (RT). AlN coupon is included as a control.

X-ray diffraction (XRD) patterns of the oxidized AlN coupons, shown in figure B.1, verify that the layered material mainly consists of Al_2O_3 and AlN. Small amounts of YAG and YAP are detected from the sintering aids added to the commercially available sintered AlN. The results show no presence of aluminum oxynitride (AlON), despite the suggestion of previous reports [7] that AlON is a precursor to Al_2O_3 in the oxidation of AlN. The XRD patterns show the relative growth in Al_2O_3 concentration as the oxidation temperature and time is increased. Figure B.2 illustrates the microstructure of oxidized AlN grains, displaying an increasingly cracked and porous Al_2O_3 structure with increasing temperatures.

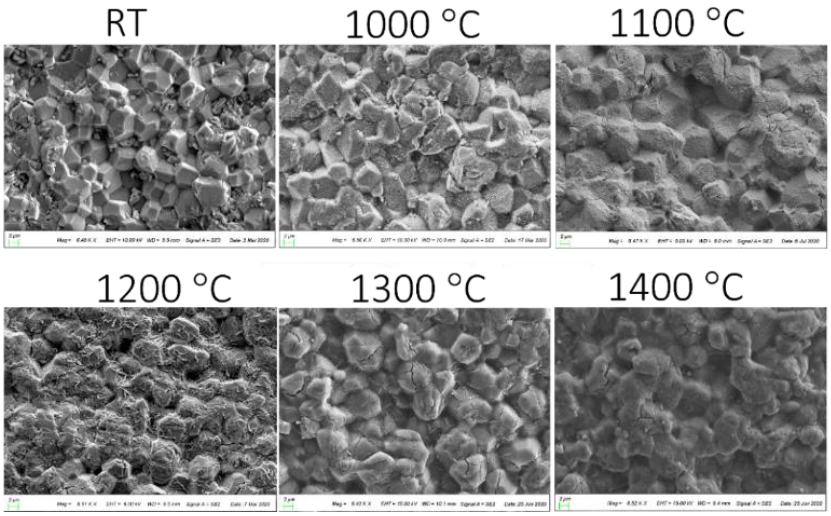

Figure B.2 Scanning electron micrographs of oxidized AlN coupons held for 12 h at varying temperatures. The unoxidized, room temperature (RT) AlN coupon is included as a control.

B.2 Hollow Minerals in Nature

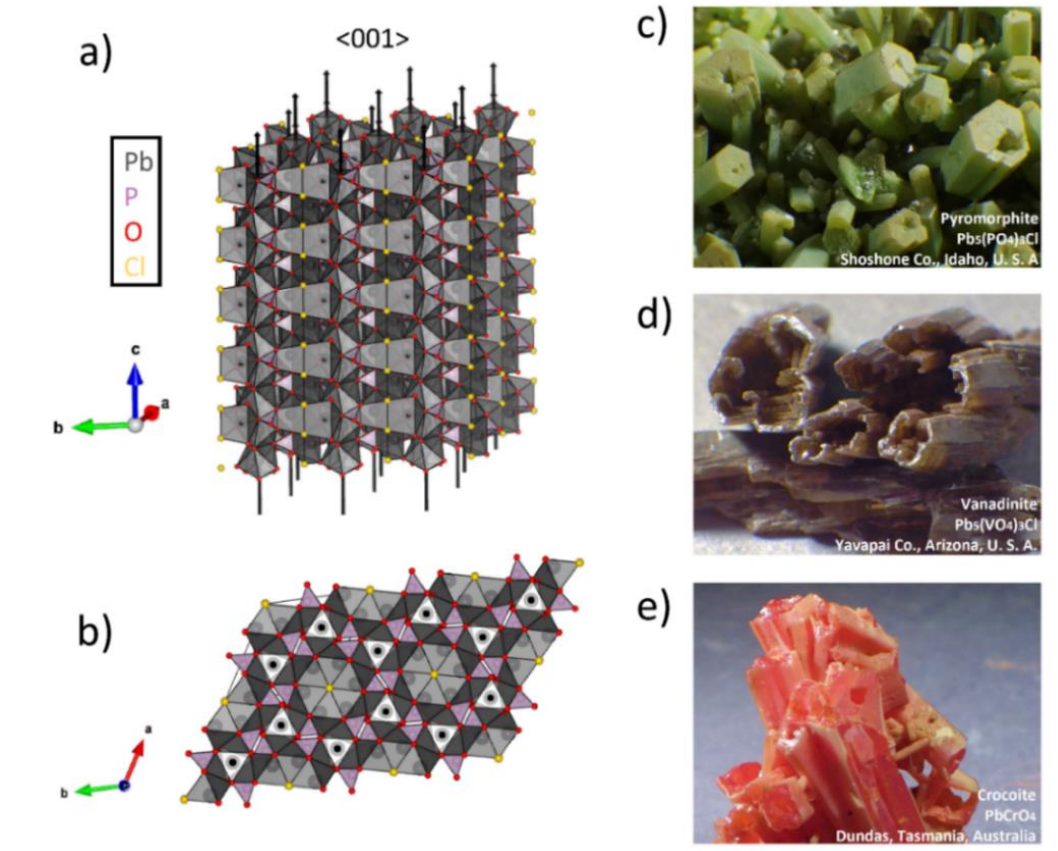

Figure B.3. Super cell (2x3x5) of pyromorphite with black arrows showing direction of crystal growth along <001>: a) side view, b) view from (001) plane [8]*. Images of hollow c) pyromorphite (CIT-11192), d) vanadinite (CIT-9070), e) crocoite (H-271), from the Mineral Room collection at the Division of Geology and Planetary Science Analytical Facility at Caltech.*

Hollow cores are commonly found in naturally occurring lead apatite minerals. Spiral growth has been observed in apatites crystallized from magmas, fluids and vapors [9,10]. An example of a hollow lead apatite is pyromorphite ($Pb_5(PO_4)_3Cl$) [11], illustrated in Figures B.3a-c. Its crystal structure consists of uninterrupted strong chains of Pb-Cl and Pb-PO_4 running along the direction of the anisotropic crystal growth <001> [12]. There is an undeniable similarity between this crystal system and $Al_{18}B_4O_{33}$. Thus, some possible analogous explanations for the hollow core formation are i) the minimization of the strain

energy from screw dislocations, ii) dissolution, enhanced in areas where dislocations are present such as the core, and iii) the breaking of PBCs due to the volatile nature of PbO, which can escape from the crystal at high temperatures (PbO begins to evaporate at 600 °C), causing preferred growth along edges and corners of the crystal. Equivalent observations can be made for other lead-bearing minerals, like vanadinite (shown in Figure B.3d) and crocoite (shown in Figure B.3e), which can also develop hollow cores.

B.3 Electron Backscatter Diffraction Patterns

The proposed crystallographic orientation of the whisker outlined in Figure 4.7a was determined by matching the electron backscatter diffraction (EBSD) pattern (shown in Figure B.4) of said crystal with information from Ihara et al. [13]. It was determined that the direction of crystal growth was along <001>.

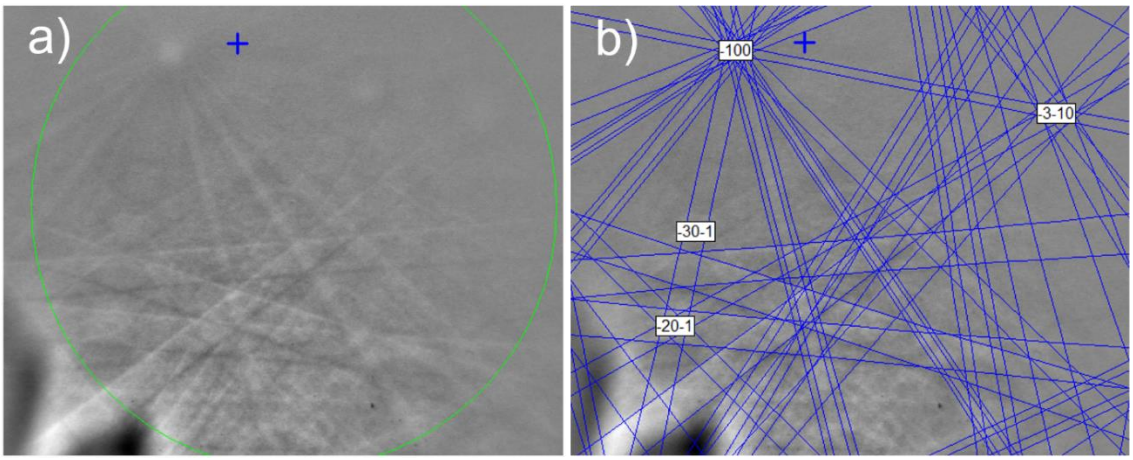

B.4. EBSD pattern of analyzed point from Figure 4.7a: a) before indexing, b) indexed EBSD pattern.

References

[1] C.S. Chari, K.T. Faber, Oxidation resistance of AlN/BN via mullite-type $Al_{18}B_4O_{33}$, Journal of the European Ceramic Society. 42 (2022) 3437–3445. https://doi.org/10.1016/j.jeurceramsoc.2022.02.037.

[2] Dennis E. Readey, Kinetics in Materials Science and Engineering, CRC Press, Taylor & Francis Group, Boca Raton, FL, 2017. https://doi.org/10.1201/9781315381985.

[3] M.W. Chase Jr., NIST-JANAF Themochemical Tables, Fourth Edition, American Chemical Society, 1998.

[4] C.-T. Yeh, W.-H. Tuan, Oxidation mechanism of aluminum nitride revisited, Journal of Advanced Ceramics. 6 (2017) 27–32. https://doi.org/10.1007/s40145-016-0213-1.

[5] R.M. Cannon, W.H. Rhodes, A.H. Heuer, Plastic Deformation of Fine-Grained Alumina (Al_2O_3): I, Interface-Controlled Diffusional Creep, Journal of the American Ceramic Society. 63 (1980) 46–53. https://doi.org/10.1111/j.1151-2916.1980.tb10648.x.

[6] A.H. Heuer, Oxygen and aluminum diffusion in α-Al_2O_3: How much do we really understand?, Journal of the European Ceramic Society. 28 (2008) 1495–1507. https://doi.org/10.1016/j.jeurceramsoc.2007.12.020.

[7] A. Bellosi, E. Landi, A. Tampieri, Oxidation behavior of aluminum nitride, Journal of Materials Research and Technology 8 (1993) 565–572. https://doi.org/10.1557/JMR.1993.0565.

[8] Y.S. Dai, J.M. Hughes, Crystal-structure refinements of vanadinite and pyromorphite, The Canadian Mineralogist. 27 (1989) 189–192.

[9] J. Rakovan, Growth and Surface Properties of Apatite, Reviews in Mineralogy and Geochemistry. 48 (2002) 51–86. https://doi.org/10.2138/rmg.2002.48.3.

[10] S. Amelinckx, Spiral growth patterns on apatite crystals., Nature. 169 (1952) 841–842. https://doi.org/10.1038/169841a0.

[11] R. Green, Pyromorphite, Rocks and Minerals. 51 (1976) 130–133. https://doi.org/10.1080/00357529.1976.11762760.

[12] R.A. Terpstra, P. Bennema, P. Hartman, C.F. Woensdregt, W.G. Perdok, M.L. Senechal, F faces of apatite and its morphology: Theory and observation, Journal of Crystal Growth. 78 (1986) 468–478. https://doi.org/10.1016/0022-0248(86)90149-1.

[13] M. Ihara, K. Imai, K. Fukunaga, N. Yoshida, Crystal structure of boroaluminate, $9Al_2O_3$ $2B_2O3$, Journal of the Ceramic Association, Japan. 88 (1980) 77–84.

Appendix C

ALUMINOSILICATE DEGRADATION IN ACIDIC ENVIRONMENTS

The contents of this Appendix are part of a manuscript in preparation titled "From Acidic Soil to Acid Rain: Chemical Transformations of Clay Mineral Surfaces from Exposure to Sulfuric Acid" by C. S. Chari, J. E. Heimann, Z. Rosenzweig, J. W. Bennett and K. T. Faber. C. S. Chari led the experimental portion of the work, supervised by Faber. J. E. Heimann led the computational portion of the work, co-supervised by Bennett and Rosenzweig. All authors were involved in designing the work and preparing the manuscript.

C.1 DFT + Thermodynamics Analysis of Kaolinite, Partially Dehydrated Kaolinite, and Metakaolin

C.1.1. Experimental Thermodynamic Data Used

a) $Al_{(s)} \rightarrow Al^{3+}_{(aq)} + 3e^-$: ΔG^0_f=-5.03 eV, ΔG^0_{SHE}=-5.03 eV
$\Delta G_2 (Al^{3+}) = -3eU_{SHE} + 0.0257 \ln(Al^{3+})$-5.03 eV

b) $Al_{(s)}+H_2O \rightarrow AlOH^{2+}_{(aq)} + H^+ + 3e^-$: ΔG^0_f=-7.19 eV, ΔG^0_{SHE}=-4.73 eV

$\Delta G_2 (AlOH^{2+}) = -3eU_{SHE} + 0.0257 \ln(AlOH^{2+}) - 0.059*pH - 4.73$ eV

c) $S_{(s)} + 4\ H_2O_{(l)} \rightarrow HSO_4^{1-}{}_{(aq)} + 7H^+ + 6e^-$: ΔG^0_f=-7.84 eV, ΔG^0_{SHE}=+2.00 eV
$\Delta G_2 (HSO_4^{1-}) = -6eU_{SHE} + 0.0257 \ln(HSO_4^{1-}) - 0.413*pH + 2.00$ eV

d) $S_{(s)} + 4\ H_2O_{(l)} \rightarrow SO_4^{2-}{}_{(aq)} + 8H^+ + 6e^-$: ΔG^0_f=-7.72 eV, ΔG^0_{SHE}=+2.12 eV

$\Delta G_2 (SO_4^{2-}) = -6eU_{SHE} + 0.0257 \ln(HSO_4^{1-}) - 0.472*pH + 2.12$ eV

e) $2\ O_{2(g)} + 8\ H^+ + 8\ e^- \rightarrow 4\ H_2O_{(l)}$: ΔG^0_{SHE}=-2.46 eV
$\Delta G_2 (O) = \Delta G^0_{SHE} + 0.118*pH$

f) $1/2\ H_{2\ (g)} \rightarrow H^+ + 1e^-$: ΔG^0_{SHE}=0 eV
$\Delta G_2 (H^+) = -0.059*pH$

C.1.2. Thermodynamic Cycles Investigated

C.1.2.1. Kaolinite

Step 1: Adsorption of SO_3 on kaolinite

Kaolinite + SO_3 → Kaolinite-SO_3
E_{ads}: -1.71 eV
(Forms SO_4 bonded to surface; has one proton transfer; all neutral molecules - No need for Solvent-Ion Model here)

Step 2: Ion Release

DG_1 (DFT, making and breaking bonds)

a) Kaolinite-SO_3 (K-S) → defect-Kaolinite (d-K^{-2}) + $Al_{(s)}$ + $S_{(S)}$ +2 O_2 (g) + 1/2 $H_{2(g)}$

DG_2 (Experiment, hydration and redox)

b) $Al_{(s)} \rightarrow Al^{3+}_{(aq)} + 3e^-$

c) $S_{(s)} + 4\ H_2O_{(l)} \rightarrow SO_4^{2-}{}_{(aq)} + 8H^+ + 6e^-$

d) $2\ O_{2(g)} + 8\ H^+ + 8\ e^- \rightarrow 4\ H_2O_{(l)}$

e) $1/2\ H_{2\ (g)} \rightarrow H^+ + 1e^-$

Step 2 DG_{tot}: Add a) through e), get:
K-S → d-K^{-2} + Al^{3+} + SO_4^{2-} + H^+ + $2e^-$

Step 3: Surface Healing

DG_1 (DFT, making and breaking bonds)

f) defect-Kaolinite (d-K^{-2}) + H_2(g) → healed defect Kaolinite (hd-K)

DG_2 (Experiment, hydration & redox)

g) $2H^+ + 2e^- \rightarrow H_{2\ (g)}$

Step 3 DG_{tot}: Add f) to g), get:
d-K^{-2} + $2H^+$ + $2e^-$ → hd-K

Total Cycle:

Add DG_{tot} of Step 2 & Step 3:

K-S → $d\text{-}K^{-2} + Al^{3+} + SO_4^{2-} + H^+ + 2e^-$

$d\text{-}K^{-2} + 2H^+ + 2e^-$ → hd-K

$K\text{-}S + 1H^+ \rightarrow hd\text{-}K + Al^{3+} + SO_4^{2-}$

DG_1 (DFT, making and breaking bonds)

dE = E(h-dK) -E(K-S) + E(Al) + E(S) + 4E(O) – E(H) = +16.19 eV

Add ZPE-TDS = +0.22 eV for change in 1 O-H on surface, **so DG_1 = +16.41 eV**

$DG_2 = DG\ ^0_{SHE} – n_e(eU_{SHE})$ -2.303 $n_{H+}\ k_BT\ pH + k_BT\ ln\ a(H_xAO_y^{-z})$

DG_2 (Experiment, hydration & redox @ varied pH)

$DG_2 = DG(Al) + DG(S) +4DG(O) -DG(H)$

DG_2 (pH 2) -12.45; **For total add -1.71 + 16.41 -11.56 = + 3.14 eV @ pH 2**
DG_2 (pH 5) -10.35; **For total add -1.71 + 16.41 -8.14 = + 6.56 eV @ pH 5**

This is not a favorable cycle.

S1.1.2. Partially Dehydrated (dehyd) Kaolinite

Step 1: Adsorption of SO_3 on dehydrated kaolinite

dehyd-Kaolinite + SO_3 → dehyd-Kaolinite-SO_3
E_{ads}: -3.05 eV
(Forms SO_4 bonded to surface; no proton transfer; all neutral molecules - No need for Solvent-Ion Model here)

Step 2: Ion Release

DG_1 (DFT, making and breaking bonds)

a) dehyd-Kaolinite-SO_3 (dK-S) → defect-dehyd-kaolinite ($d\text{-}dK^{-1}$) + $Al_{(s)}$ + $S_{(S)}$ +2 O_2 (g)

DG_2 (Experiment, hydration & redox)

b) $Al_{(s)} \rightarrow Al^{3+}_{(aq)} + 3e^-$

c) $S_{(s)} + 4\ H_2O_{(l)} \rightarrow SO_4^{2-}{}_{(aq)} + 8H^+ + 6e^-$

d) $2\ O_{2(g)} + 8\ H^+ + 8\ e^- \rightarrow 4\ H_2O_{(l)}$

Step 2 DG_{tot}: Add a) to d), get:
dK-S → dd-K^{-1} + Al^{3+} + SO_4^{2-} + $1e^-$

Step 3: Surface Healing

DG_1 (DFT, making and breaking bonds)

e) defect-dehyd-kaolinite (d-dK^{-1}) + 1/2 H_2(g) → healed defect dehyd-Kaolinite (hd-dK)

DG_2 (Experiment, hydration & redox)

f) $H^+ + 1e^- \rightarrow 1/2\ H_{2\ (g)}$

Step 3 DG_{tot}: add e) and f) to get:
d-dK^{-1} + H^+ + $1e^-$ → hd-dK

Total Cycle:

Add DG_{tot} of Step 2 & Step 3:

dK-S → dd-K^{-1} + Al^{3+} + SO_4^{2-} + $1e^-$

dd-K^{-1} + H^+ + $1e^-$ → hd-dK

---

dK-S + $1H^+$ → hd-dK + Al^{3+} + SO_4^{2-}

DG_1 (DFT, making and breaking bonds)

dE = E(h-dK) -E(K-S) + E(Al) + E(S) + 4E(O) – E(H) = +16.46 eV

Add ZPE-TDS = +0.22 eV for change in 1 O-H on surface, **so DG_1 = +16.68 eV**

$DG_2 = DG\ ^0_{SHE} – n_e(eU_{SHE})$ -2.303 $n_{H+}\ k_BT\ pH + k_BT\ ln\ a(H_xAO_y^{-z})$

DG_2 (Experiment, hydration & redox @ varied pH)

$DG_2 = DG(Al) + DG(S) +4DG(O) -DG(H)$

DG_2 (pH 2) -12.45; **For total add -3.05 + 16.68 -11.56 = +2.06 eV @ pH 2**
DG_2 (pH 5) -10.35; **For total add -3.05 + 16.68 -8.14 = +5.49 eV @ pH 5**

This is not a favorable cycle.

C.1.1.3. Metakaolin

Step 1: Adsorption of SO_3 on metakaolin

Metakaolin + SO_3 → Metakaolin-SO_3
E_{ads}: -3.84 eV
(Forms SO_4 bonded to surface; no proton transfer; all neutral molecules - No need for Solvent-Ion Model here)

Step 2: Ion Release

DG_1 (DFT, making and breaking bonds)

a) Metakaolin-SO_3 (M-S) → defect-Metakaolin (d-M^{-1}) + $Al_{(s)}$ + $S_{(S)}$ +2 O_2 (g)

DG_2 (Experiment, hydration & redox)

b) $Al_{(s)} \rightarrow Al^{3+}_{(aq)} + 3e^-$

c) $S_{(s)} + 4\ H_2O_{(l)} \rightarrow SO_4^{2-}{}_{(aq)} + 8H^+ + 6e^-$

d) $2\ O_{2(g)} + 8\ H^+ + 8\ e^- \rightarrow 4\ H_2O_{(l)}$

Step 2 DG_{tot}: Add a) to d), get:

M-S → d-M^{-1} + Al^{3+} + SO_4^{2-} + $1e^-$

Step 3: Surface Healing

DG_1 (DFT, making and breaking bonds)

e) defect-Metakaolin (d-M^{-1}) + 1/2 H_2(g) → healed defect Metakaolin (hd-M)

DG_2 (Experiment, hydration & redox)

f) $H^+ + 2e^- \rightarrow 1/2\ H_{2\,(g)}$

Step 3 DG_{tot}: add e) and f) to get:

$d\text{-}M^{-1} + H^+ + 1e^- \rightarrow$ hd-M

Total Cycle:

Add DG_{tot} of Step 2 & Step 3:

M-S $\rightarrow$ $d\text{-}M^{-1} + Al^{3+} + SO_4^{2-} + 1e^-$

$d\text{-}M^{-1} + H^+ + 1e^- \rightarrow$ h-dM

$M\text{-}S + 1H^+ \rightarrow$ h-dM + Al^{3+} + SO_4^{2-}

DG_1 (DFT, making and breaking bonds)

dE = E(h-dK) -E(K-S) + E(Al) + E(S) + 4E(O) – E(H) = +13.80 eV

Add ZPE-TDS = +0.22 eV for change in 1 O-H on surface, **so DG_1 = +14.02 eV**

$DG_2 = DG\ ^0_{SHE} - n_e(eU_{SHE}) - 2.303\ n_{H+}\ k_BT\ pH + k_BT\ \ln a(H_xAO_y^{-z})$

DG_2 (Experiment, hydration & redox @ varied pH)

$DG_2 = DG(Al) + DG(S) + 4DG(O) - DG(H)$

DG_2 (pH 2) -12.45; **For total add -3.84 + 14.02 -11.56 = - 1.38 eV @ pH 2**
DG_2 (pH 5) -10.35; **For total add -3.84 + 14.02 -8.14 = +2.05 eV @ pH 5**

This is a favorable cycle at low pH (pH < 3.48)

C.2 XPS Data Collection

An overview of the collected XPS spectra is found below. Pass energy used was 20 eV. A total of forty scans were taken per peak analyzed, including Al 2p and Si 2p. Two samples were measured for each condition. The average is reported, with the error term representing one standard deviation. The peaks were calibrated using the C 1s peak at 284.8 eV. Survey spectra in the following pages show the absence of S 2p peaks in all samples studied. If present, S 2p would be located at 164 eV.

Table C.1. Kaolinite XPS data showing relative wt.% of Al 2p and Si 2p, and their respective binding energies (eV).

	Al (wt.%)	**Si (wt.%)**	**Al (eV)**	**Si (eV)**
Ref - Site 1	41.68929	58.31071	74.45	102.8
Ref - Site 2	41.45482	58.54518	74.55	103
pH 6 - Site 1	40.24474	59.75526	74.55	102.9
pH 6 - Site 2	41.36778	58.63222	74.55	102.95
pH4 - Site 1	40.41201	59.58799	74.8	102.75
pH 4 - Site 2	40.8082	59.1918	74.6	102.5
pH 2 - Site 1	40.70475	59.29525	74.65	103.05
pH2 - Site 1	39.47859	60.52141	74.85	103.1
pH 0 - Site 1	38.85189	61.14811	74.75	102.95
pH0 - Site 2	39.14309	60.85691	74.8	103.1

Table C.2. Metakaolin XPS data showing relative wt.% of Al 2p and Si 2p, and their respective binding energies (eV).

	Al (wt.%)	**Si (wt.%)**	**Al (eV)**	**Si (eV)**
Ref - Site 1	41.72843	58.27157	74.9	102.8
Ref - Site 2	42.46913	57.53087	74.8	102.85
pH 6 - Site 1	39.32512	60.67488	74.85	102.8
pH 6 - Site 2	40.08289	59.91711	74.75	102.65
pH4 - Site 1	38.39684	61.60316	74.75	102.7
pH 4 - Site 2	39.4137	60.5863	74.75	102.75
pH 2 - Site 1	31.75974	68.24026	74.6	102.65
pH2 - Site 1	32.80333	67.19667	74.6	102.7
pH 0 - Site 1	21.20421	78.79579	75.1	103.2
pH0 - Site 2	22.79781	77.20219	74.85	103.1

Table C.3. Kaolinite survey spectra, showing O KLL, O 1s, O 2s, C1s, Al 2s, Al 2p, Si 2s, and Si 2p.

Sample – Site 1		Sample – Site 2	
pH 7	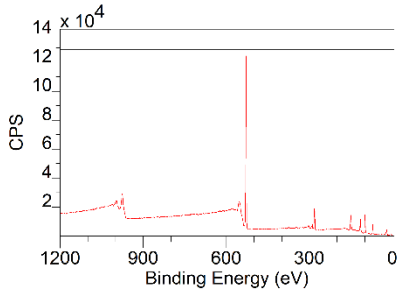	**pH 7**	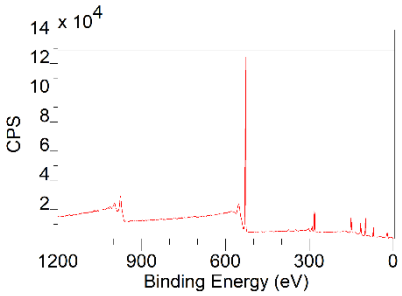
pH 6	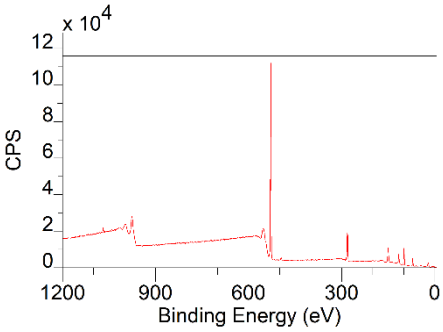	**pH 6**	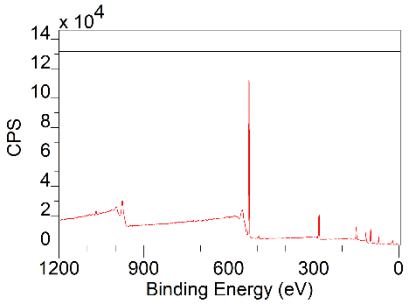
pH 4	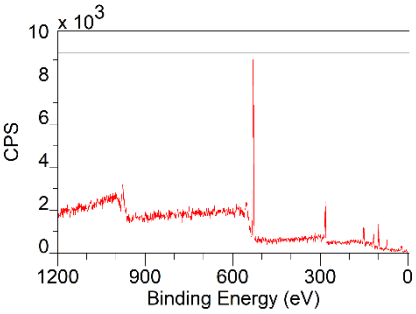	**pH 4**	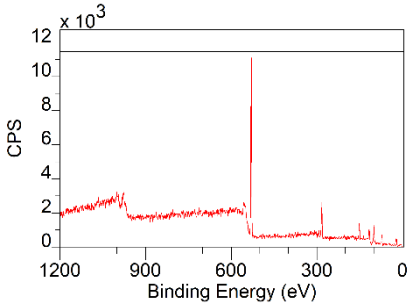
pH 2	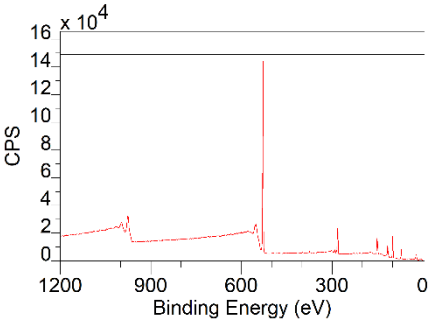	**pH 2**	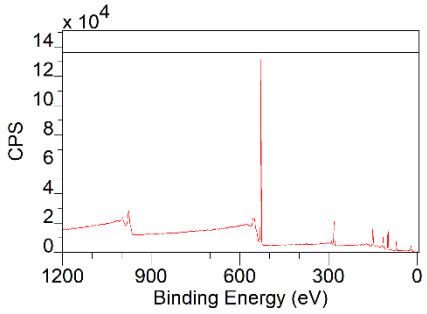

pH 0	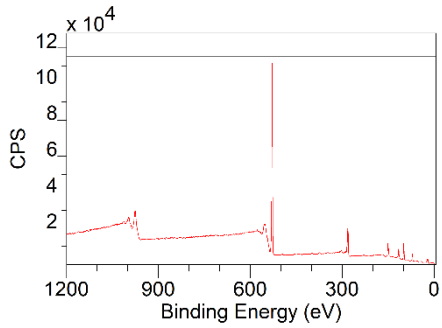	**pH 0**	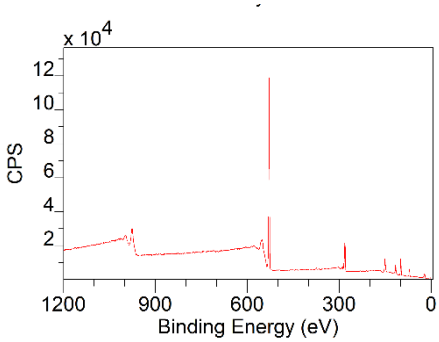

Table C.4. Metakaolin survey spectra, showing O KLL, O 1s, O 2s, C1s, Al 2s, Al 2p, Si 2s, and Si 2p.

Sample – Site 1		**Sample – Site 2**	
pH 7	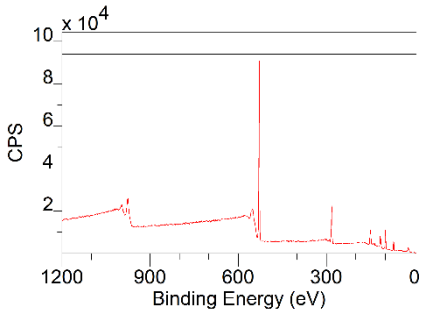	**pH 7**	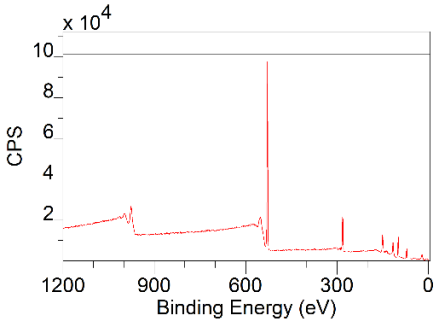
pH 6	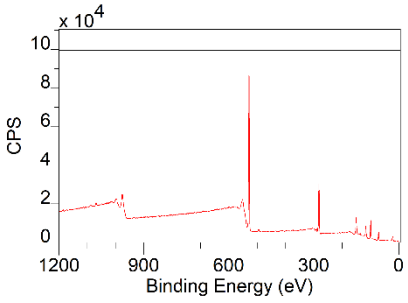	**pH 6**	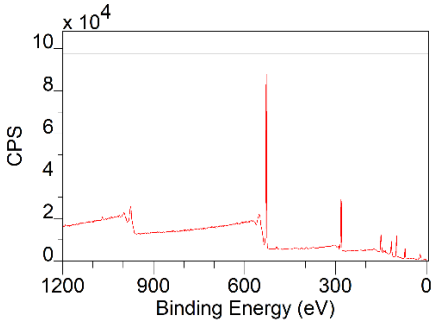
pH 4	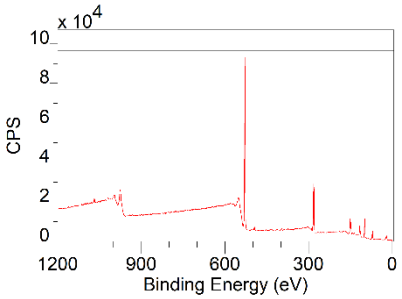	**pH 4**	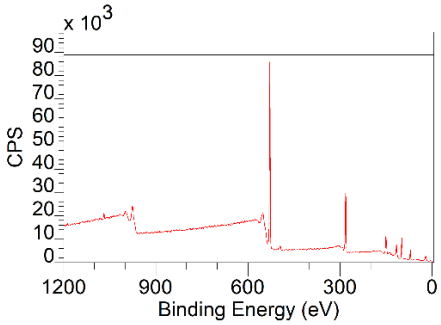

pH 2

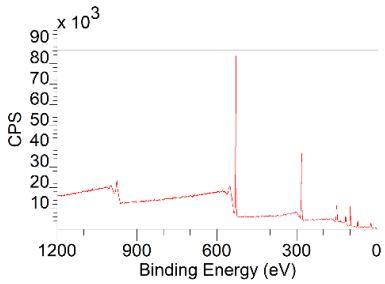

pH 2

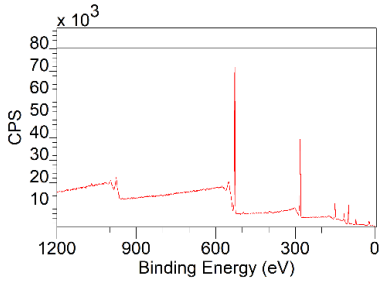

pH 0

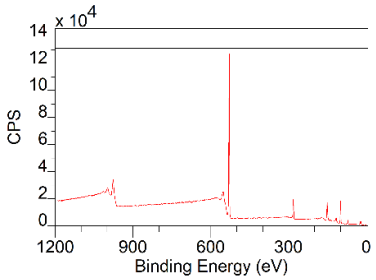

pH 0

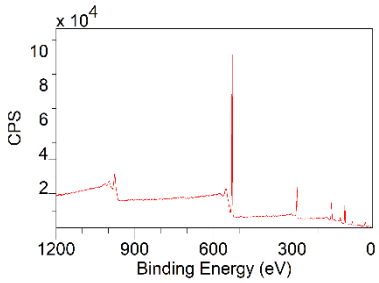

C.3 XPS Analysis Depth Estimation

The inelastic mean free path (λ) in nm could be estimated using the following universal relationship in Seah and Dench, 1979:

$$\lambda = \frac{143}{E^2} + 0.054 \times \sqrt{E}$$

where E is the electron energy in eV. Knowing that the accelerating voltage of the instrument is 1400 eV, the kinetic energy of the electrons ejected could be approximated as 1301 eV for Si 2p (1400 eV – 99 eV) and 1327 eV for Al 2p (1400 eV – 73 eV). These values result in $\lambda \approx 2$ nm.

The analysis depth (d) could then be estimated using the following relationship, as the take-off angle of the analyzed electrons (θ) was 45° in our analysis.

$$d = \lambda \times \sin(\theta)$$

Following these calculations, the analysis depth was estimated to be 1.4 nm.

C.4 Additional Figures of Kaolinite Dehydration Process

Figure C.1 below compares the top-down view of the three surfaces (kaolinite, partially dehydrated kaolinite, and metakaolin) along the [001] axis. The hydroxyl (-OH) group removed in each dehydration step is circled in orange, and the proton removed is circled in pink.

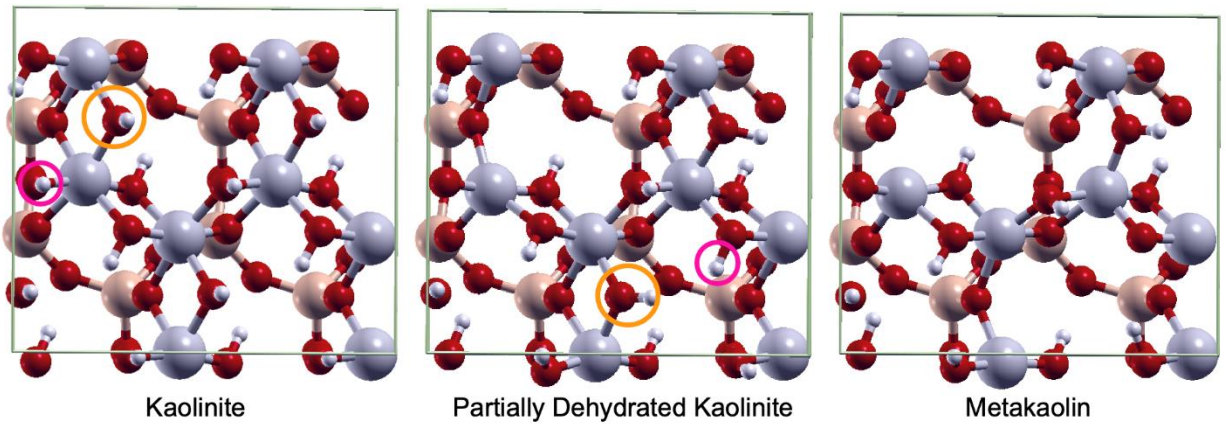

Figure C.1. Top-down view of the three surfaces highlighting the hydroxyl groups (orange circles) and protons (pink circles) removed in each dehydration step.

C.5 Surface-Adsorbate Interfaces

Figures C.2 and C.3 below depict the relaxed surface-adsorbate interfaces not provided in the text or in Heimann *et al.*, 2021. All figures were generated using XCrySDen (Kokalj, 2003).

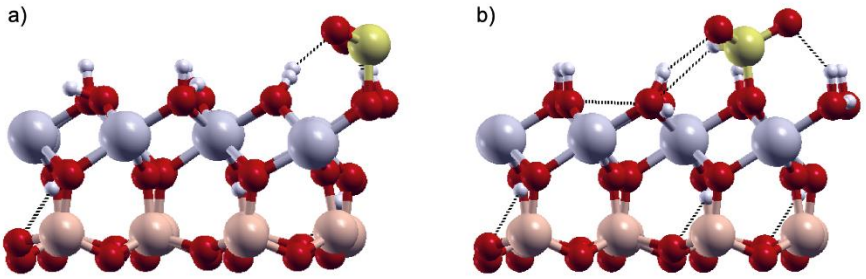

Figure C.2. a) Partially dehydrated kaolinite-SO_2 interface. b) Partially dehydrated kaolinite-H_2SO_3 interface.

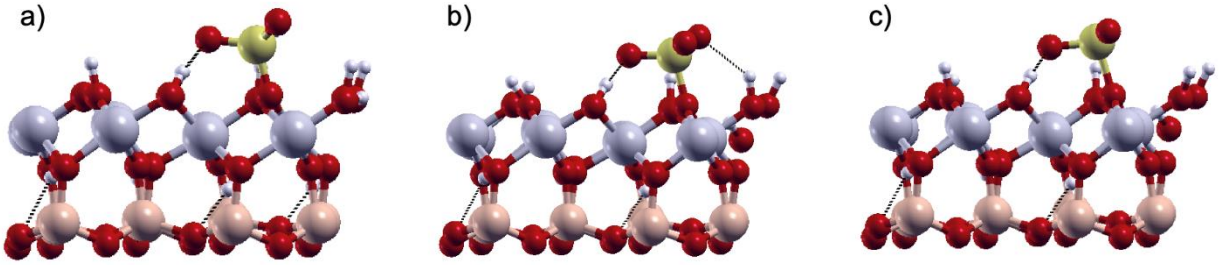

Figure C.3. a) Metakaolin-H_2SO_3 interface. b) Metakaolin-SO_3 interface. c) Metakaolin-SO_2 interface.

References

[1] J.E. Heimann, R.T. Grimes, Z. Rosenzweig, J.W. Bennett, A density functional theory (DFT) investigation of how small molecules and atmospheric pollutants relevant to art conservation adsorb on kaolinite, Applied Clay Science. 206 (2021) 106075. https://doi.org/10.1016/j.clay.2021.106075.

[2] A. Kokalj, Computer graphics and graphical user interfaces as tools in simulations of matter at the atomic scale, Computational Materials Science. 28 (2003) 155–168. https://doi.org/10.1016/S0927-0256(03)00104-6.

[3] M.P. Seah, W.A. Dench, Quantitative electron spectroscopy of surfaces: A standard data base for electron inelastic mean free paths in solids, Surface and Interface Analysis. 1 (1979) 2–11. https://doi.org/10.1002/sia.740010103.

Appendix D

SYNTHESIS AND CHARACTERIZATION OF LUSTER GLAZES AND PORCELAIN FROM MEISSEN

The contents of this Appendix are also presented in "Nanoscale engineering of gold particles in 18th century Böttger lusters and glazes" by C. S. Chari, Z. W. Taylor, A. Bezur, S. Xie and K. T. Faber, which was published in the Proceedings of the National Academy of Sciences in 2022 [1]. C. S. Chari led the experimental portion of the work on the reproductions. A. Bezur led the experimental portion of the work on the historic samples, with assistance from S. Xie. Faber supervised all experimental work. In addition, Z. W. Taylor led the theoretical portion of the work, supervised by Faber and co-supervised by Chari. Chari, Faber, and Bezur were involved in designing the work. All authors were involved in preparing the manuscript.

D.1 Comments on Composition of Base Böttger Glaze in Historic Meissen Samples

It should be noted from Table 6.1 that the measured compositions of the Böttger glaze have calcium concentrations much lower than expected based on previous reports by Kingery and Vandiver [2]. In fact, the measured composition of the Böttger glaze is close to the composition that was previously reported for Böttger porcelain [2]. There are two possible causes for this. First, it could be argued that no high-temperature base glaze layer between the lead glaze layer and the porcelain substrate exists in this particular piece, and that the lead-rich glaze might have been applied directly onto Böttger porcelain in this specific sample. Second, the measured composition of the Böttger glaze could imply a diffuse interface between the Böttger glaze and porcelain substrate, showing a combination of both layers. This diffuse interface would arise if the Böttger glaze was applied to a previously bisque-fired porcelain substrate, which interacts with the glaze during the porcelain firing step. With higher calcium content, the glaze layer melts more readily, and this flux with high mobility acts to homogenize the composition of the glaze and further influence the composition in the upper portion of the porcelain.

D.2 Böttger Porcelain and Böttger Glaze Reproduction

The recipes for Böttger porcelain and the base Böttger glaze were established from stoichiometries reported by Kingery and Vandiver [2]. Tiles of Böttger porcelain were created by preparing a water-based slurry of 40.30 g kaolinite, 3.45 g feldspar (both K-rich sanidine and Na-rich oligoclase could be used), 3.65 g calcium carbonate, and 2.60 g quartz suspended in 45 g of deionized water. The proportions of each material were chosen to match the oxide composition of Böttger porcelain from previous studies [3]. The oxide composition of our porcelain recreation can be found in Table D.1. Referring to Kingery and Vandiver's cited work, Böttger porcelain is shown to be at the dividing line of two different phase fields: mullite plus liquid, and mullite plus silica plus liquid. Adding small amounts of alkali from the addition of lime and feldspars can extend the liquid region, lowering the firing temperature to 1350 °C. Once mixed, the slurry was cast into tiles and dried thoroughly in air. Samples were then bisque fired at 900 °C for one hour in air with a ramp rate of 2 °C/min before applying the base glaze, known as the Böttger glaze.

Table D.1. Böttger Porcelain Body Composition in wt.%

	Al_2O_3	SiO_2	CaO	Na_2O	K_2O	Other*
Bezur [4]	34.8	56	6.6	0	1.5	1.1
Schulle [3]	33	61	4.8	0.2	0.1	0.9
Reproduction Raw Materials (SEM-EDX)**	35.8	56.4	5.1	0.8	1.8	0.1
Reproduction After Firing (SEM-EDX)**	33.6	56.6	5.6	0.8	2.3	1.1

*Other includes traces of oxides of Fe, Cr, Ti, P

**Na & Ca-rich feldspar used in raw materials

Table D.2. Böttger Glaze Composition in wt.%

	Al_2O_3	SiO_2	CaO	Na_2O	K_2O	Other*
Historic Böttger Glaze - Top (STEM-EDX)	18.8	78.4	2.2	0	0.6	0
Historic Böttger Glaze - Bottom (STEM-EDX)	20.7	76.2	2.6	0	0.34	0.16
Kingery [2]	14	62	24	unknown	unknown	0
Reproduction After Firing (SEM-EDX)**	14.9	60.2	18.3	0.5	1.1	5

*Other includes traces of oxides of Fe, Cr, Ti, P

**Na & Ca-rich feldspar used in raw materials

The composition of the base glaze was initially chosen based on previous experiments by Kingery and Vandiver [2], and can be found in Table D.2. However, small quantities of feldspar were also added to increase the flow characteristics of the glaze, and to better match the glassy phase of the porcelain body. To make the base glaze, a slurry of 7.50 g kaolinite, 0.60 g feldspar, 8.50 g calcium carbonate, and 9 g quartz was suspended in 20 g of deionized water and applied to the bisque-fired porcelain. The glazed piece was then fired for 2 hours at 1350 °C in air with a ramp rate of 2 °C/min. The thickness of the Böttger glaze layer varied from 450 µm to 200 µm and did not appear to affect the color or luster of the reproductions. The base glaze exhibited a smooth finish with no visible cracks after being applied to the porcelain and fired, indicating compatible thermal expansion coefficients between the two layers.

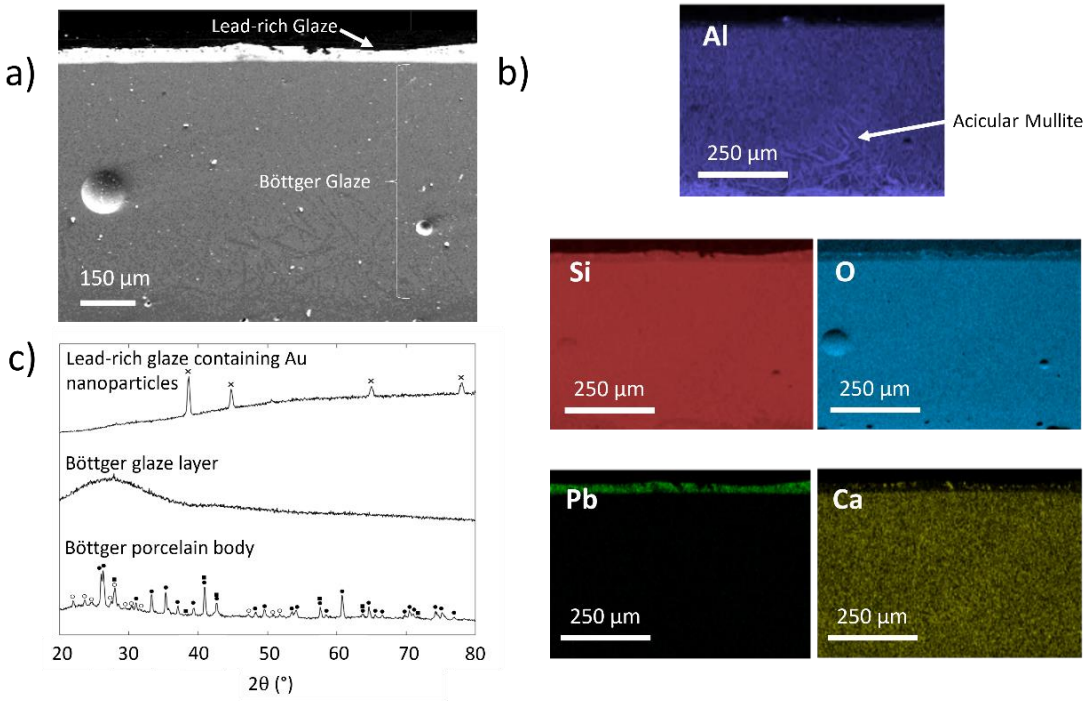

Figure D.1. Layered composition of reproduction: a) SEM image of cross-sectioned reproduction showing both the base Böttger glaze and lead-rich glaze, b) EDX mapping of several elements in cross-sectioned purple lusterware reproduction, c) XRD patterns of reproductions indicating the presence of $3Al_2O_3.2SiO_2$ (●), silica (■), aluminosilicate (○), Au nanoparticles (×).

Cross-sections of the samples were examined using scanning electron microscopy, as shown in Figure D.1a, and the oxide compositions of the reproduced Böttger porcelain, Böttger glaze and lead-rich luster layers were calculated based upon EDX elemental mapping. The full oxide composition of our reproductions can be found in Table D.1 and Table D.2. The base Böttger glaze shown in Figures D.1b is rich in silicon, aluminum, oxygen and calcium. X-ray diffraction patterns of the base glazed porcelain, seen in Figure D.1c, show an amorphous pattern due to the glassy nature of this Si-rich glaze. In contrast, the X-ray diffraction patterns of the unglazed Böttger porcelain body confirmed that the hard-paste porcelain contained acicular mullite ($3Al_2O_3.2SiO_2$) and quartz grains in a glassy matrix, as well as Ca-rich aluminosilicates expected in early Böttger porcelain. The acicular crystals are a product of decomposing metakaolin and feldspars at temperatures over 1000 °C. Interlocking mullite crystals can be seen emerging from the porcelain body, at its interface with the base Böttger glaze in Figure D.1b.

D.3 Role of Alkali Ions in Luster Forming Step

Two different types of feldspars were used to produce the lead glazes: Na- and Ca-rich oligoclase (Key Stone, South Dakota, USA) and K-rich sanidine (Custer, South Dakota, USA). The oxide compositions of the two sets of glazes are found in Table D.3. The similarities between samples made with K-rich feldspar and those made with Na and Ca-rich feldspar reveal important information on how the gold ions diffuse into the luster glaze. Previous investigations of lusterware made from Ag and Cu nanoparticles argue that an ion exchange mechanism is required to form a luster layer, between alkali ions found in the glaze (Na^+ and K^+) and the metal cations applied to the surface of the glaze [5–7]. Such studies suggest that similarities in the diffusivities between Cu^+ and K^+, and between Ag^+ and Na^+, cause the ion pairs to couple together, facilitating the diffusion of the metal ions into the glaze. The current study is the first detailed investigation of lusterware produced by gold nanoparticles. Thus, it is important to examine whether an ion exchange mechanism between gold ions and K+ is preferred over Na+, or vice versa. The optical similarities between samples made with K-rich feldspar and those made with Na and Ca-rich feldspar, seen in Figure D.2, suggest that both alkali ions are similarly involved in this luster-forming, ion exchange mechanism with gold ions. From our observations, there is no clear preference for one alkali ion over the other.

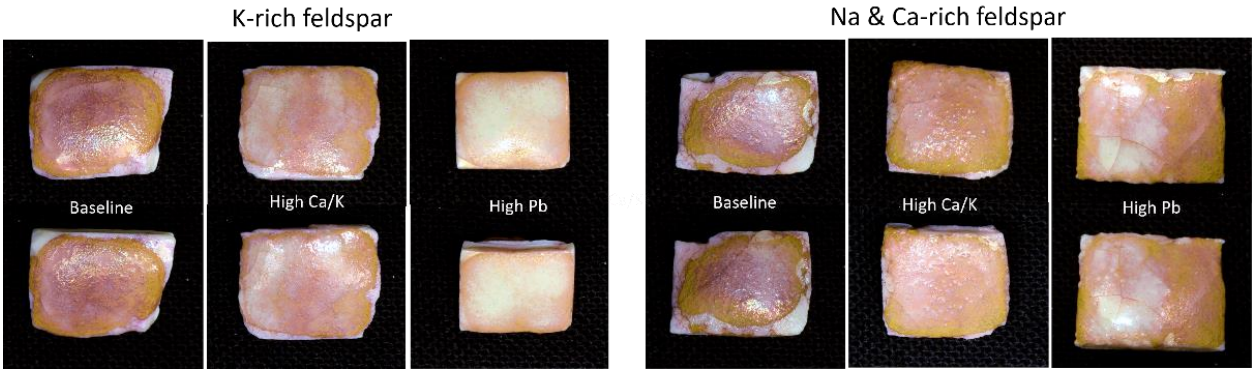

Figure D.2. Photographs of luster glaze reproductions made with K-rich feldspar and Na & Ca-rich feldspar, shown at different angles. The three iterations of glazes are included for both feldspars used: Baseline, High Ca/K and High Pb.

Table D.3. Raw compositions (wt.%) of lead-rich glaze reproductions made with different feldspars

	Al_2O_3	SiO_2	CaO	Na_2O	K_2O	PbO	K/Na
Na & Ca-rich Feldspar Baseline	5	40.8	6.8	1.2	0.2	46	0.17
Na & Ca-rich Feldspar High Ca/K	4.2	39.5	8.4	2.3	0.1	45.5	0.04
Na & Ca-rich Feldspar High Pb	1.9	36.6	3.2	0.7	0.1	57.5	0.14
K-rich Feldspar Baseline	5	40.6	6.5	0.2	1.9	45.8	9.5
K-rich Feldspar High Ca/K	4.4	39	7.9	0.3	3.1	45.3	10.33
K-rich Feldspar High Pb	1.9	36.5	3.1	0.1	1.1	57.3	11

D.4 Comments on ImageJ Measurements and Error Analysis

ImageJ was used to establish the particle sizes and particle separation distances shown in Figures 6.2c,d and 6.3c,d. A total of 684 nanoparticles were measured for Böttger luster distributions, and a total of 319 nanoparticles were measured for Purple of Cassius distributions. Repeated measurements of the same nanoparticle will give approximately the same results, with some fluctuations. In this study, those error terms were neglected for the sake of clarity. The reported standard deviation is simply the standard deviation of all nanoparticle radii.

There exist two other sources of bias within the system. The first is that for the very smallest nanoparticles (and this is particularly true with the Purple of Cassius glaze samples), the STEM images begin to pixelate, discretizing the measurable radii at the smallest scales; hence the “jagged” and chaotic structure of the nanoparticle radii distribution of the Purple of Cassius glaze shown in Figure 6.3a’s inset. The second source of bias is the implicit

assumption that the nanoparticles are (a) perfectly spherical and (b) exactly bifurcated into two hemispheres by the STEM image: (a) was addressed primarily by attempting to fit an ellipsoid of equivalent area to the nanoparticles, which will act as its own source of error, but that error should be unbiased as it both over- and under-estimates true measurements; (b) assumes then that each circular image of a nanoparticle in the STEM image represents the entire nanoparticle so that the radius calculated from the area is equivalent to the true radius of the sphere. Realistically, a random cut through a nanoparticle will sometimes give a cross-section smaller than the diametric cross-section, so the measured radius will accordingly be smaller than the true radius. The result will be that we systematically underestimate nanoparticle radii. That being said, this statistical underestimation will evolve to a scale-invariant multiplicative pre-factor that will be constant across samples and nanoparticles, so Purple of Cassius glaze and Böttger luster can be directly compared "apples-to-apples" and the true shape of their nanoparticle radii distribution will likewise be unaffected (simply stretched by the same amount along the x-axis).

D.5 Comments on Thin-film Interference Effects

Nanoparticles located near the surface of the glazes may also give rise to thin-film interference, which is analogous to the coloration of oil on water [8,9]. Like diffraction from a particle array, this phenomenon can also result in iridescence. Thin-film interference effects were investigated in our simulations, where an approximation was made to treat the layer of discrete nanoparticles as a homogenous layer for treatment by thin-film interference models. The Maxwell-Garnett approximation volume-averaged the optical properties of the nanoparticles, using literature values for gold and mullite-like media [10]. With this assumption, Hirayama's ray-based model for multilayer thin-films, later adapted by Reillon, was applied to obtain a predicted normal-incidence reflectance spectrum based on nanoparticle layer thickness and density [8,9]. This spectrum was then visualized through CIE 1931 XYZ color matching functions available in Mathematica [10–12]. Our simulations established that the concentrated layer of gold nanoparticles near the surface of the glaze did not contribute to thin-film interference. Such a high-density gold layer is incapable of creating a purple coloration except at ~10 nm layer thickness using experimentally measured optical properties and several models [8–10,13,14].

References

[1] C.S. Chari, Z.W. Taylor, A. Bezur, S. Xie, K.T. Faber, Nanoscale engineering of gold particles in 18th century Böttger lusters and glazes, Proceedings of the National Academy of Sciences. 119 (2022) e2120753119. https://doi.org/10.1073/pnas.2120753119.

[2] W.D. Kingery, P.B. Vandiver, Ceramic masterpieces, The Free Press, New York NY, 1986.

[3] W. Schulle, B. Ullrich, Ergebisse gefugeanalytischer Untersuchungen an Boettgerporzellan, Silikat Technik. 33 (1982) 44–47.

[4] A. Bezur, F. Casadio, Du Paquier Porcelain: Artistic expression and technological mastery. A scientific evaluation of the materials, in: Fired by Passion. Vienna Baroque Porcelain of Claudius Innocentius Du Paquier, Arnoldsche, 2009.

[5] A. Miotello, G. De Marchi, G. Mattei, P. Mazzoldi, A. Quaranta, Clustering of silver atoms in hydrogenated silver-sodium exchanged glasses, Applied Physics A: Materials Science & Processing. 70 (2000) 415–419. https://doi.org/10.1007/s003390051059.

[6] A. Miotello, G. De Marchi, G. Mattei, P. Mazzoldi, Ionic transport model for hydrogen permeation inducing silver nanocluster formation in silver-sodium exchanged glasses, Applied Physics A: Materials Science & Processing. 67 (1998) 527–529. https://doi.org/10.1007/s003390050816.

[7] T. Pradell, J. Molera, J. Roque, M. Vendrell-Saz, A.D. Smith, E. Pantos, D. Crespo, Ionic-Exchange Mechanism in the Formation of Medieval Luster Decorations, Journal of the American Ceramic Society. 88 (2005) 1281–1289. https://doi.org/10.1111/j.1551-2916.2005.00223.x.

[8] V. Reillon, S. Berthier, C. Andraud, Optical properties of lustred ceramics: Complete modelling of the actual structure, Applied Physics A. 100 (2010) 901–910. https://doi.org/10.1007/s00339-010-5791-0.

[9] H. Hirayama, K. Kaneda, H. Yamashita, Y. Monden, An accurate illumination model for objects coated with multilayer films, Computers & Graphics. 25 (2001) 391–400. https://doi.org/10.1016/S0097-8493(01)00063-2.

[10] P.B. Johnson, R.W. Christy, Optical Constants of the Noble Metals., Physical Review B. 6 (1972) 4370–4379.

[11] Convert spectral distribution to RGB color., Mathematica Stack Exchange. (n.d.). https://mathematica.stackexchange.com/questions/57389/convert-spectral-distribution-to-rgb-color.

[12] Color and Vision Research Labs. CVRL main., (2006). http://www.cvrl.org/.

[13] N. Stefanou, V. Yannopapas, A. Modinos, Heterostructures of photonic crystals: frequency bands and transmission coefficients., Computer Physics Communications 113 (1998) 49–77.

[14] N. Stefanou, V. Yannopapas, A. Modinos, MULTEM 2: A new version of the program for transmission and band-structure calculations of photonic crystals., Computer Physics Communications 132 (2000) 189–196.